A Computational Investigation of the Fluid Dynamics of a Three-Dimensional, Compressible, Mixing Layer with Strong Streamwise Vorticity

by

Jonathan Kindred Elliott

B.A.I. Mechanical Engineering, B.A. Mathematics, Trinity College, Dublin (1987)

SUBMITTED IN PARTIAL FULFILLMENT OF THE
REQUIREMENTS FOR THE DEGREE OF

Master of Science
in
Aeronautics and Astronautics
at the
Massachusetts Institute of Technology

June, 1990

Signature of Author _____
Department of Aeronautics and Astronautics
February, 1990

Certified by _____
Dr. Choon S. Tan
Thesis Supervisor

Accepted by _____
Professor Harold Y. Wachman
Chairman, Departmental Graduate Committee

A COMPUTATIONAL INVESTIGATION OF THE FLUID DYNAMICS OF A THREE-DIMENSIONAL, COMPRESSIBLE, MIXING LAYER WITH STRONG STREAMWISE VORTICITY

by

Jonathan Kindred Elliott

Submitted to the Department of Aeronautics and Astronautics

in June 1990 in partial fulfillment of the

requirements for the Degree of Master of Science in

Aeronautics and Astronautics

Abstract

A three-dimensional Euler solver employing Zalesak's multidimensional flux-limiter in a Flux-Corrected Transport (FCT) algorithm has been developed and used for the analysis of flow phenomena in a three-dimensional lobed mixer. In particular, results from the computed flow in a subsonic low penetration mixer, a supersonic low penetration mixer, a subsonic high penetration mixer and a supersonic high penetration mixer are used to investigate the effects of compressibility and lobe geometry on the generation of streamwise vorticity and the subsequent downstream evolution of the vortex sheet. The main results of this work are: (1) over the range of Mach numbers examined ($M \leq 2.0$) compressibility has only a marginal effect on the generation and evolution of the vortex sheet, (2) the dependence of the secondary circulation on the geometry can be estimated through the use of the simple scaling law developed by Barber, Paterson and Skebe in [3], and (3) the vortex sheet shed from the mixer lobe trailing edge exhibits a tendency to roll-up into a discrete, approximately circular, vortical region.

Acknowledgements

I would first like to thank my advisor, Dr. Choon Sooi Tan, for being a constant source of inspiration and encouragement during the course of this project. The effort he put into editing the thesis was greatly appreciated even though at times it may have seemed that this was not so. My thanks also go to Professor Greitzer for his encouragement, the incisiveness of his comments throughout and for the fine job of editing that he did. The contributions of Professor Frank Marble to the fluid dynamic aspects of the research were also invaluable.

My friend and colleague in lobed mixer research, Yuan Qiu, deserves special mention for the hours of discussions and for running the Trefftz plane calculations.

Thanks are certainly in order to the following people from the Laboratory for Computational Physics in the Naval Research Laboratory: Stephen Zalesak, for the hours of consultative advice on the details of the multidimensional FCT algorithm; Elaine Oran, for providing the LCPFCT subroutine and other software; Fernando Grinstein and Gopal Patnaik for their helpful discussions concerning the LCPFCT algorithm.

Thanks also to Nikolaos Gatsonis for arguing the advantages of using Zalesak's implementation and for providing the two-dimensional, Cartesian flux limiter and his other advice on the numerics.

I would also like to mention some of the GTL crowd: Earl Renaud, for help with computer and fluid dynamic aspects; Dan Gysling; Pete Silkowski; Andreas Schulmeyer; Eric Strang; Rob Plumley; Seung Jin Song; Bill Steptoe; George Pappas.

This project was supported by the Naval Air Systems Command, under NAVAIR Contract N00019-88-C-0229, project manager, George Derderian. Support for the author was provided by the Air Force Research in Aero Propulsion Technology (AFRAPT) program, AFOSR-85-0288 E. This support was greatly appreciated.

Contents

List of Figures

Nomenclature

a	Amplitude of mixer
a, b	Exponents in grid generation forcing terms
A	Antidiffusive flux
c	Sound speed
c	Complex phase velocity, $c_r + ic_i$
c_p	Pressure coefficient, $(P - P_{-\infty})/\frac{1}{2}\rho U^2_{-\infty}$
c_p, c_v	Specific heat at constant volume and pressure
C	Fraction that multiplies antidiffusive flux
$C_{xx}, C_{xy}, etc.$	Coefficients used to implement solid wall boundary condition
e, f, g	Inviscid flux vectors
e_s, f_s, g_s	Source components of the inviscid flux vectors
E_t	Total energy per unit volume
$E_{i+\frac{1}{2},j,k}$	Inner product of flux vectors with area vector on ξ faces $((e,f,g)\cdot\vec{S})_{i+\frac{1}{2},j,k}\Delta t$.
$F_{i,j+\frac{1}{2},k}$	Inner product of flux vectors with area vector on η faces $((e,f,g)\cdot\vec{S})_{i,j+\frac{1}{2},k}\Delta t$.
$G_{i,j,k+\frac{1}{2}}$	Inner product of flux vectors with area vector on ζ faces $((e,f,g)\cdot\vec{S})_{i,j,k+\frac{1}{2}}\Delta t$.
G	Amplification factor
H_0	Total Enthalpy
J	Jacobian of the transformation from physical to computational space

k_D Transport coefficient for diffusion of molecules

k_m Wave number

L Length scale characteristic of transverse variation of basic current

L_m Mixer length

L_ξ, L_η, L_ζ Time integration operation in the $\xi-$, $\eta-$ and $\zeta-$ directions for directional timestep splitting.

M Mach number

$\hat{n}$ Unit normal vector (n_x, n_y, n_z)

N Molecular number density

P Pressure

P, Q Grid generation forcing terms

P_t Total pressure

P^-, P^+ Sum of all andiffusive fluxes leaving/into cell (i, j, k)

Q^-, Q^+ Maximum allowable decrease/increase in $\mathbf{w}$ at cell (i, j, k)

r^+, r^- Riemann invariants

R^-, R^+ Least-upper-bound on fraction that must multiply all antidiffusive fluxes leaving/into cell at (i, j, k)

s Entropy

s_i Interface length

S	Cell face area
t	Time
T	Temperature
TE	Truncation error
$\vec{v}$	Velocity vector (v_x, v_y, v_z)
$\hat{v}$	Contravariant velocity
V	Cell volume
V	Velocity scale characteristic of transverse variation of basic current, $V_{upper} - V_{lower}$
$\bar{V}$	Mean axial velocity, $\frac{1}{2}(V_{upper} + V_{lower})$
w	Typical scalar
$\mathbf{w}$	State vector
x, y, z	Cartesian coordinates
α	Disturbance wavelength
α	Lobe penetration angle
β	$k_m \Delta x$
β	Shock angle
γ	Ratio of specific heats
$\gamma_{4_{lobe}}, \gamma_{4_{duct}}$	Coefficients for fourth order artificial diffusion
γ	Spanwise gradient of circulation, $\partial\Gamma/\partial s$

Γ Circulation

Γ^* Nondimensional circulation, $\frac{\Gamma}{U_{-\infty}\lambda}$

Δs Incremental distance

Δt Size of timestep

Δx $x_{i+\frac{1}{2}} - x_{i-\frac{1}{2}}$

ϵ Internal energy per unit volume

ϵ Local Courant number

ϵ Relative error in grid generation scheme

ε Root-mean-square state vector difference

η Disturbance amplitude

θ Deflection angle

κ Coefficient of diffusion

λ Lobe wavelength

μ Mach angle

μ Diffusion coefficient for Boris-Book limiter

ν Antidiffusion coefficient for Boris-Book limiter

ν_1, ν_2 Prandtl-Meyer functions

ν_2 Coefficient for second difference diffusion used in low order method

ξ, η, ζ Coordinates in computational space

ρ Density

τ Circular arc thickness ratio

ϕ Phase angle

ϕ_e Exact phase angle

ψ Passive scalar $N_{lower}/(N_{upper} + N_{lower})$

$\omega_x, \omega_y, \omega_z,$ components of vorticity

ω_P, ω_Q Relaxation factors for forcing terms in grid generation scheme

Superscripts

a, b Correspond to minimum/maximum allowable value of w^{n+1}

ad Antidiffusive

c Corrected

d Diffusive

fd Finite difference approximation

H High order

L Low order

n Temporal index

t Transported

td Transported-and-diffused

$*$ Average of predicted and nth timelevel values

$*$	Nondimensional
$'$	Predicted value

Subscripts

amb	Ambient
b	Face at boundary
$face$	Cell face
fct	Calculated by FCT scheme
g	Guard cell
$high$	Calculated by high order scheme
i, j, k	Computational space indices
I	Cell adjacent to boundary
low	Calculated by low order scheme
s	Corresponding to tip of splitter plate
te	Trailing edge
$upper, lower$	Upper and lower streams
$-\infty$	freestream

Chapter 1

Introduction

In two-dimensional shear layers, the dominant component of the vorticity vector is normal to the velocity field. Three-dimensionality in these types of mixing layers is not a key feature of the flow and takes a long time to develop [1,39]. The basic mechanism by which mixing is achieved is through the large scale fluid motions associated with the Kelvin-Helmholtz instability and the subsequent nonlinear rollup. The only parameters that can be used to alter the mixing properties of the shear layer are related to the velocity difference (through the factor $(V_1 - V_2)/(V_2 + V_1)$), the convective Mach number, $M_c = (V_1 - V_2)/2a$ (for equal soundspeeds) and, if two different fluids are used, the density ratio, (ρ_2/ρ_1) and (γ_2/γ_1). Available experimental data and theoretical analyses [47,37] of the compressible two-dimensional shear layer, however, have demonstrated that the growth rate of the Kelvin-Helmholtz instability decreases rapidly above a convective Mach number of about 0.7 or so. Because of this, it may be difficult to obtain efficient molecular mixing of fuel and air, for example, at the supersonic Mach numbers found in a scramjet.

The purpose of lobed mixers (of which a typical geometry is shown in Figure 1.1) is to introduce strong streamwise vorticity into the shear layer so that the flow becomes inherently three-dimensional. The production of streamwise vorticity is achieved in a fashion analogous to its generation by a wing of finite length. As a result of the transverse penetration of the lobed mixer into the stream, the mixer lobes have a pressure difference across them and thus an associated bound vorticity. Due to the spanwise variations of the geometry, the loading and bound vorticity strength also vary in the spanwise direction, so that streamwise vortex lines, emanating from the trailing edge, must occur. Thus the lobed mixer can be viewed as the periodic juxtapositioning of a wing and an identical inverted wing. In a flow configuration where the stream on one side of the lobed mixer has a total pressure that is different from that on the other side, the resulting

downstream shear layer will consist of streamwise vorticity associated with the three-dimensionality of the mixer and spanwise vorticity associated with the variation in total pressure. The strength and distribution of the streamwise vorticity are parameters that can be used to alter the mixing properties of the three-dimensional shear layer in addition to the two-dimensional shear layer parameters mentioned above. Because of this, the three-dimensional shear layers generated by lobed mixers are very different from the conventional two-dimensional shear layer.

Lobed mixers are in widespread usage in aircraft engines where one of the initial applications was for jet noise reduction. As shown for the turbofan engine in Figure 1.2, the streamwise vorticity generated by the mixer serves to mix the core and bypass airstreams such that lower effective jet velocity and shear layer intensity result. Hence an accompanying noise reduction is achieved. Lobed mixers have also been used to mix the exhaust gases from turbojet engines with the freestream atmospheric air. This also results in reduced noise level. In addition, if the stagnation enthalpies of the core and bypass streams are significantly different (whch is usually the case in turbofan engines), the mixer configuration shown in Figure 1.1 can result in thrust augmentation [2] and hence lower specific fuel consumption. There is reason to believe that the streamwise vorticity enhanced mixing observed at low Mach numbers will also be found in supersonic three-dimensional shear layers. The reasoning behind this argument is that even though flow in the streamwise direction is supersonic, the cross-stream flow is subsonic and compressibility effects may be small. The potential of lobed mixers for ejector pumping systems and as a means of improving airfoil stall margins and lift-to-drag ratios are also being investigated. Thus it is of engineering significance to develop the scientific basis for the design of optimum mixer configurations, e.g. one that produces a given mixing in the shortest length/time or maximum mixing in a given length/time, with minimum losses.

Previous research efforts include experimental investigations that established mixing is dominated by the secondary flow generated by the lobed mixer [4] and pinpointed the inviscid mechanisms that create the secondary flowfield [3]. However, in the latter case, measurements were

limited to downstream of the trailing edge with flow visualization being used on the surface of the lobed mixer. The role of the lobed mixer in mixing supersonic flow jets has also been examined [6]. Numerical investigations have been carried out for flow downstream of the lobed mixer [7,5] but these relied on experimental or other data for use as the inlet boundary conditions and the potential interaction between lobed mixer and downstream mixing duct was not modelled. Recently numerical investigations have been reported that generate solutions for the entire flowfield [8,9]. The first approach uses a full Navier-Stokes solver and the geometry corresponds to a specific high bypass-ratio turbofan engine. The second approach uses the two-equation $\kappa - \epsilon$ eddy viscosity turbulence model in the incompressible elliptic equations of fluid flow and the geometry, again, corresponds to a turbofan engine.

The research issues that need to be addressed before one can begin to develop the engineering and scientific basis for the design of an optimum mixer are:

(1) the extent to which three-dimensionality plays a role in the performance of lobed mixers as a mixing and thrust augmentation device in a propulsion system

(2) the roles of streamwise *and* spanwise vorticity in a three-dimensional shear layer

(3) the effects of compressibility

(4) the dependence of the mixing on the trailing edge vorticity field

(5) the effects of the different geometrical parameters such as amplitude-to-wavelength ratio, $a(x,z)/\lambda$, and mixer length L on establishing this vorticity field.

One objective of the present work was to develop a CFD tool capable of generating an accurate solution of the three-dimensional Euler equations for the flow in the entire domain, both around the lobed mixer and in the downstream mixing duct and over the subsonic, transonic and supersonic Mach number ranges. With the aid of this CFD tool, the generation of streamwise vorticity by the

lobed mixer is evaluated and the effects of compressibility on the mixing parameters are assessed. To this end, a Flux-Corrected Transport (FCT) code using Zalesak's multidimensional flux limiter (see Section 2.5) was developed for use with three-dimensional numerical grids with general curvilinear coordinates. To the author's knowledge, it is the first implementation of Zalesak's limiter in three-dimensional curvilinear coordinates. This algorithm can handle different geometries and is capable of modelling flows with total pressure variation at inflow, although time limitations precluded the investigation of these types of flows.

The development of the numerical algorithm is the subject of Chapter Two. Two-dimensional numerical solutions for standard test cases (which capture most of the flow phenomena to be expected in the three-dimensional case) are presented in Chapter Three. Fully three-dimensional solutions for two different lobed mixers in subsonic and supersonic freestreams are presented in Chapter Four. Chapter Five emphasises the conclusions of the investigation while the subject of Chapter Six is recommendations for future work.

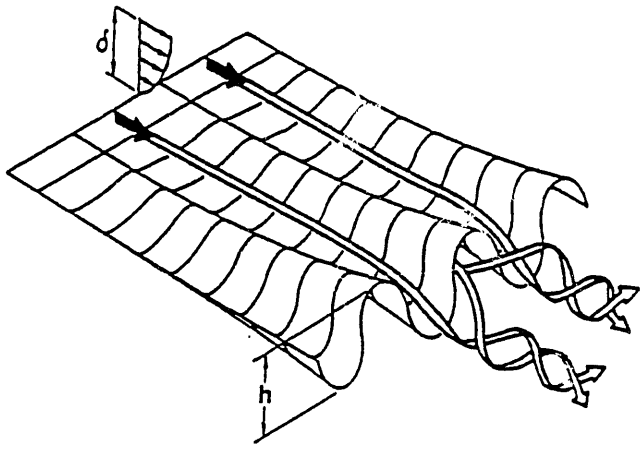

Figure 1.1: Typical lobed mixer

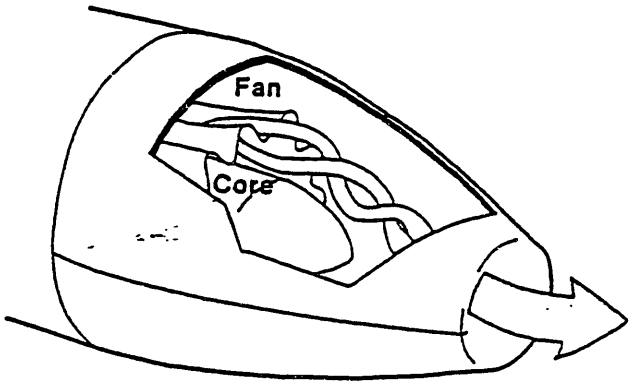

Figure 1.2: Lobed mixer as found in a turbofan

Chapter 2

Computational Algorithm

In this chapter, the governing equations for an inviscid flow are introduced, along with their three-dimensional finite-volume discretized form. Two algorithms for their solution are presented. One is suitable for applications in which a general orthogonal numerical grid (such as Cartesian or Cylindrical Polar) can be used. The other has no orthogonality restriction and can be used with any curvilinear grid as long as the grid is structured. Both use the principle of Flux-Corrected Transport [17,18,19,21]. The first (which will be referred to henceforth as Boris-Book FCT) was developed by Boris and Book and has undergone extensive validation [17,18,19,26,27],etc. The second algorithm (which will be referred to henceforth as FVFCT (Finite Volume Flux-Corrected Transport) utilizes the principles of Zalesak's multidimensional flux limiter [21] and was developed by the author. It is the first finite volume implementation of FCT in general curvilinear coordinates that the author is aware of.

2.1 Finite Volume Discretization of the Euler Equations

The Euler equations in integral form are (from Conservation of Mass, Momentum and Energy)

$$\frac{\partial}{\partial t}\int_V \mathbf{w}dV + \oint_S \mathbf{w}\vec{v}\cdot\hat{n}dS + \oint_S (\mathbf{e}_s,\mathbf{f}_s,\mathbf{g}_s)\cdot\hat{n}dS = 0 \tag{2.1}$$

where,

$$\mathbf{w} = \begin{bmatrix} \rho \\ \rho v_x \\ \rho v_y \\ \rho v_z \\ E_t \end{bmatrix} ; \ \mathbf{e}_s = \begin{bmatrix} 0 \\ P \\ 0 \\ 0 \\ Pv_x \end{bmatrix} ; \ \mathbf{f}_s = \begin{bmatrix} 0 \\ 0 \\ P \\ 0 \\ Pv_y \end{bmatrix} ; \ \mathbf{g}_s = \begin{bmatrix} 0 \\ 0 \\ 0 \\ P \\ Pv_z \end{bmatrix} \tag{2.2}$$

$$\hat{n} = (n_x, n_y, n_z) \tag{2.3}$$

$$\vec{v} = (v_x, v_y, v_z) \tag{2.4}$$

and E_t is the total energy per unit volume

$$E_t = \epsilon + \frac{1}{2}\rho(v_x^2 + v_y^2 + v_z^2) \tag{2.5}$$

Assuming a calorically perfect gas, the internal energy is given by

$$\epsilon = \rho c_v T = \frac{P}{\gamma - 1} \tag{2.6}$$

which closes the system. To put the Euler equations in conservation law form we first write them as

$$\frac{\partial}{\partial t}\int_V \mathbf{w} dV + \oint_S (\mathbf{e}, \mathbf{f}, \mathbf{g}) \cdot \hat{n} dS = 0 \tag{2.7}$$

where,

$$\mathbf{e} = \begin{bmatrix} \rho v_x \\ \rho v_x^2 \\ \rho v_x v_y \\ \rho v_x v_z \\ (E_t + P)v_x \end{bmatrix} ; \ \mathbf{f} = \begin{bmatrix} \rho v_y \\ \rho v_y v_x \\ \rho v_y^2 \\ \rho v_y v_z \\ (E_t + P)v_y \end{bmatrix} ; \ \mathbf{g} = \begin{bmatrix} \rho v_z \\ \rho v_z v_z \\ \rho v_z v_y \\ \rho v_z^2 \\ (E_t + P)v_z \end{bmatrix} \tag{2.8}$$

Using the Divergence Theorem and the fact that V is an arbitrary volume we get the familiar conservation law form

$$\frac{\partial \mathbf{w}}{\partial t} + \frac{\partial \mathbf{e}}{\partial x} + \frac{\partial \mathbf{f}}{\partial y} + \frac{\partial \mathbf{g}}{\partial z} = 0 \tag{2.9}$$

Spatial discretization is performed using a conservative finite-volume method. This allows shocks to be "captured" without special treatment in the neighbourhood of discontinuities. This is possible because the finite-volume form discretizes the integral form of the Euler equations rather

than the differential form. The integral form is applicable everywhere while the differential form is not valid in the neighbourhood of discontinuities.

The spatial discretization of Equation (2.1) based on the finite volume method reduces to a system of ordinary differential equations in the flow variables at each cell centre of the numerical grid. This numerical grid consists of a number of hexahedral cells each of which forms its own control volume around which the semi-discretized form of Equation (2.1) must be satisfied. Flow variables are defined at cell centers (i,j,k) from which the face values can be found by averaging the corresponding adjacent cell center values

$$\rho_{i+\frac{1}{2},j,k} = \frac{1}{2}(\rho_{i,j,k} + \rho_{i+1,j,k}) \tag{2.10}$$

(Zalesak [25] has proposed a method for increasing the spatial order of accuracy by including more cell center values in the equation for $\rho_{i+\frac{1}{2},j,k}$ but for nonuniform three-dimensional grids, the complexities of the formulation are prohibitive and this method was not used.) As mentioned previously, the semi-discrete finite volume form is then a system of ordinary differential equations of the form

$$\frac{d\mathbf{w}}{dt} = -\frac{1}{V_{i,j,k}} \sum_{face=1}^{6} (\mathbf{e},\mathbf{f},\mathbf{g})_{face} \cdot \vec{S}_{face} \tag{2.11}$$

or

$$\frac{d\mathbf{w}}{dt} = -\frac{1}{V_{i,j,k}} \sum_{face=1}^{6} (\hat{v}^n_{face}(\mathbf{w})^n_{face} + (\mathbf{e}_s,\mathbf{f}_s,\mathbf{g}_s)_{face} \cdot \hat{n}_{face})|S_{face}| \tag{2.12}$$

where $face = 1$ represents the face located at $(i-\frac{1}{2},j,k)$, $face = 2$ that located at $(i+\frac{1}{2},j,k)$, $face = 3$ that located at $(i,j-\frac{1}{2},k)$, etc., the unit normals are always taken to be directed outwards and

$$\hat{v}^n_{face} = \vec{v}^n_{face} \cdot \hat{n}_{face} \tag{2.13}$$

The normal vector $\hat{n}$ is found from

$$\hat{n}_{face} = \frac{\vec{S}_{face}}{|\vec{S}face|} \tag{2.14}$$

and the area vector $\vec{S}$ is found from the cross product of the displacement vectors with endpoints at the midpoints of each side of the face (see Figure 2.1)

$$\vec{S}_{face} = \vec{s_1} \times \vec{s_2} \tag{2.15}$$

$$\vec{s_1} = \frac{1}{2}(\vec{r_c} + \vec{r_d} - \vec{r_a} - \vec{r_b}) \tag{2.16}$$

$$\vec{s_2} = \frac{1}{2}(\vec{r_c} + \vec{r_b} - \vec{r_a} - \vec{r_d}) \tag{2.17}$$

where $\vec{r_a}$ is the position vector of the node located at a. The volume of cell (i,j,k) is found from the vector triple product of the displacement vectors with endpoints at the midpoint of each face (see Figure 2.2)

$$V = (\vec{t_1} \times \vec{t_2}) \cdot \vec{t_3} \tag{2.18}$$

$$\vec{t_1} = \frac{1}{4}(\vec{r_c} + \vec{r_d} + \vec{r_h} + \vec{r_g} - \vec{r_a} - \vec{r_b} - \vec{r_f} - \vec{r_e}) \tag{2.19}$$

$$\vec{t_2} = \frac{1}{4}(\vec{r_c} + \vec{r_b} + \vec{r_f} + \vec{r_g} - \vec{r_d} - \vec{r_a} - \vec{r_e} - \vec{r_h}) \tag{2.20}$$

$$\vec{t_3} = \frac{1}{4}(\vec{r_e} + \vec{r_f} + \vec{r_g} + \vec{r_h} - \vec{r_a} - \vec{r_b} - \vec{r_c} - \vec{r_d}) \tag{2.21}$$

As a consistency check, it is instructive to perform the spatial discretization through the application of a generalized transformation of the Euler equations from the physical domain (x, y, z) to the computational domain (ξ, η, ς). The semi-discrete form becomes (reference [28] shows the details of the manipulations)

$$\begin{aligned} \frac{dw}{dt} &= -\frac{1}{J}(((e,f,g)\cdot(J\xi_x, J\xi_y, J\xi_z))_\xi + ((e,f,g)\cdot(J\eta_x, J\eta_y, J\eta_z))_\eta + \\ &\quad ((e,f,g)\cdot(J\varsigma_x, J\varsigma_y, J\varsigma_z))_\varsigma) \end{aligned} \tag{2.22}$$

where J is the Jacobian and $\xi_x, \eta_x, \varsigma_x, etc.$ are the metrics of the transformation. It can be easily shown that the discretized form of this equation is identical to the finite volume discretization, Equation (2.12) and that the correspondences between the finite volume and computational space coordinates discretizations are

$$V_{i,j,k} \leftrightarrow J_{i,j,k} \tag{2.23}$$

$$\vec{S}_{i+\frac{1}{2},j,k} \leftrightarrow J(\xi_x, \xi_y, \xi_z)_{i+\frac{1}{2},j,k} \tag{2.24}$$

$$\vec{S}_{i,j+\frac{1}{2},k} \leftrightarrow J(\eta_x, \eta_y, \eta_z)_{i,j+\frac{1}{2},k} \tag{2.25}$$

$$\vec{S}_{i,j,k+\frac{1}{2}} \leftrightarrow J(\zeta_x, \zeta_y, \zeta_z)_{i,j,k+\frac{1}{2}} \tag{2.26}$$

An important property of the area discretization given in Equation (2.15) is that the sum of any component of $\vec{S}$ around all six faces of a hexahedral cell is equal to zero. This means that uniform flow stays uniform to within roundoff for even the most distorted numerical grids and that grid dependent errors are eliminated.

2.2 Flux-Corrected Transport

For the numerical solution of the Euler equations, one must account for the finite speed of propagation of pressure waves and the possibile formation of discontinuities (e.g. shocks, vortex sheets) arising as the flow field evolves with time. (Discontinuities may also occur in incompressible inviscid flows in the form of density interfaces as well as vortex sheets which are often found in the wakes shed off sharp trailing edged bodies.) Unless appropriately treated, the resulting numerical solution can overshoot and undershoot in the neighbourhood of the discontinuity. This is the well-known Gibbs phenomenon and is associated with approximating a discontinuous function by a smooth continuous function. The spurious ripples associated with the phenomenon can contaminate the solution leading to numerical instability. Increasing resolution in the neighbourhood of the discontinuity does not help because the ripples simply move closer to the discontinuity. Oscillations can also result from numerical dispersion. These arise because, at the discontinuity, the third derivative can be large, while away from the discontinuity, the solution is smooth so that behind the discontinuity there is an algebraically decaying oscillation.

Invariably, non-physical artificial viscosity is added to the algorithm to prevent the occurence of spurious oscillations in the vicinity of the discontinuity. This is usually in the form of second

or fourth order damping. Although this can successfully deal with the ripples around shocks, it also introduces a new error to the rest of the solution. (For the particular problem being discussed in this thesis (i.e., mixing layers with streamwise vorticity) it will also cause the rapid decay of the vortex sheet as it leaves the trailing edge of the mixer.) Characteristic-based schemes for the Euler equations have been reported [10,11,12,13] that avoid the need to impose artificial viscosity. However, these algorithms are still in the early stages of development and much work still has to be done before robustness can be claimed.

FCT deals with the problem of oscillations near discontinuities by mathematically enforcing monotonicity in the numerical solution. It does this by ensuring that no non-physical extrema develop in the solution. This is achieved by computing the net transportive flux as a nonlinearly weighted average of a flux calculated using a low order (and highly diffusive) scheme and a flux calculated using a high order scheme. The averaging is such that the high order flux is weighted as highly as possible without creating overshoots or undershoots. The high order scheme tends to dominate in smooth regions of the flowfield while the low order method dominates in the neighbourhood of large gradients. This weighting procedure is known as "flux-correction" or "flux-limiting".

Sod [14] presented an elucidating interpretation of the original FCT algorithm due to Boris and Book [17]. He considered a first order diffusive difference scheme which can be represented by

$$w_t + f(w)_x = \Delta t[g(w, \Delta t/\Delta x)w_x]_x \tag{2.27}$$

where $g(w, \Delta t/\Delta x)$ is the coefficient of the diffusion term. FCT can then be considered to be a modification of Equation (2.27) represented by

$$w_t + f(w)_x = \Delta t[(g(w, \Delta t/\Delta x) - r(w, \Delta t/\Delta x))w_x]_x \tag{2.28}$$

The antidiffusion term is introduced by operator splitting. The first step consists of solving Equation (2.27) to give the "transported-and-diffused" solution.

$$w_i^{td} = Lw_i^n \tag{2.29}$$

The antidiffusion step then gives the state vector at the next time level

$$w_i^{n+1} = Aw_i^{td} = ALw_i^n \tag{2.30}$$

Sod points out that

$$g(w, \Delta t/\Delta x) - r(w, \Delta t/\Delta x) \geq 0 \tag{2.31}$$

is required for stability. The fluxes used in the antidiffusion step are corrected to ensure that there is no extrema creation or accentuation. We shall now proceed to present the details of the Boris-Book FCT algorithm.

2.3 One-Dimensional Boris-Book FCT

The theory of Flux-corrected transport (FCT) was initially developed to solve one dimensional transport equations (such as the one-dimensional continuity equation) by Boris and Book [17], [18], [19] and was later extended to solve multidimensional problems through the use of directional timestep-splitting [29]. However, severe limitations have been found in the use of directional timestep splitting approach for the computation of three-dimensional flowfields using nonorthogonal grids. This will be dealt with in more detail later in this section. As the original Boris-Book FCT is used in two-dimensional shear layer calculations and for diagnostic purposes, the original FCT algorithm is described in some detail here. In addition, a complete understanding of the intricacies of Boris-Book FCT is helpful before embarking on an effort of developing an FCT scheme for three-dimensional shear layer calculations. Because FCT can be loosely defined as the means of creating a weighted average of a low order and a high order scheme, it can be implemented in various ways. This can be seen in its early development [20]. Of the Boris-Book algorithms, Phoenical FCT appears to be optimal in terms of amplitude and phase errors in various test cases. In addition it can be implemented with relative ease. It was therefore logical to choose Phoenical FCT with directional timestep-splitting applications for two-dimensional shear layer calculations.

Phoenical FCT consists of the following sequential stages (an orthogonal grid is assumed and w represents any one of the scalar components that together comprise the state vector **w** for the Euler equations)

(1) Compute the diffusive fluxes

$$F^d_{i+\frac{1}{2}} = \nu_{i+\frac{1}{2}} V_{i+\frac{1}{2}} (w^n_{i+1} - w^n_i) \tag{2.32}$$

(2) Compute the transported solution

$$w^t_i = w^n_i - \frac{\Delta t}{V_{i+\frac{1}{2}}} (v_{i+\frac{1}{2}} w^n_{i+\frac{1}{2}} S_{i+\frac{1}{2}} - v_{i-\frac{1}{2}} w^n_{i-\frac{1}{2}} S_{i-\frac{1}{2}} + Source_{i+\frac{1}{2}} - Source_{i-\frac{1}{2}}) \tag{2.33}$$

where, for the continuity equation

$$Source_{i+\frac{1}{2}} = 0$$

for the momentum equation

$$Source_{i+\frac{1}{2}} = P_{i+\frac{1}{2}} S_{x_{i+\frac{1}{2}}}$$

for the energy equation

$$Source_{i+\frac{1}{2}} = P_{i+\frac{1}{2}} \vec{v}_{i+\frac{1}{2}} \cdot \vec{S}_{i+\frac{1}{2}}$$

(3) Compute the antidiffusive fluxes

$$A^{ad}_{i+\frac{1}{2}} = \mu_{i+\frac{1}{2}} V_{i+\frac{1}{2}} (w^t_{i+1} - w^t_i) \tag{2.34}$$

(4) Compute the "transported-and-diffused" solution

$$w^{td}_i = w^t_i + \frac{1}{V_i} (F^d_{i+\frac{1}{2}} - F^d_{i-\frac{1}{2}}) \tag{2.35}$$

(5) Limit the antidiffusive fluxes

$$A^c_{i+\frac{1}{2}} = s_{i+\frac{1}{2}} max(0, min(|F^{ad}_{i+\frac{1}{2}}|, s_{i+\frac{1}{2}} V_{i+1} (w^{td}_{i+2} - w^{td}_{i+1}), s_{i+\frac{1}{2}} V_i (w^{td}_i - w^{td}_{i-1}))) \tag{2.36}$$

where

$$s_{i+\frac{1}{2}} = sign(w_{i+1}^{td} - w_i^{td})$$

(6) Apply the limited antidiffusive fluxes

$$w_i^{n+1} = w_i^{td} - \frac{1}{V_i}(A_{i+\frac{1}{2}}^c - A_{i-\frac{1}{2}}^c) \tag{2.37}$$

For Phoenical FCT, Boris and Book [20] chose as diffusion and antidiffusion coefficients, respectively

$$\nu_{i+\frac{1}{2}} = \frac{1}{6} + \frac{1}{3}\epsilon_{i+\frac{1}{2}}^2 \tag{2.38}$$

$$\mu_{i+\frac{1}{2}} = \frac{1}{6} - \frac{1}{6}\epsilon_{i+\frac{1}{2}}^2 \tag{2.39}$$

where for a uniform grid

$$\epsilon_{i+\frac{1}{2}} = \frac{v_{i+\frac{1}{2}}\Delta t}{\Delta x} \tag{2.40}$$

and for a nonuniform grid

$$\epsilon_{i+\frac{1}{2}} = \frac{\hat{v}_{i+\frac{1}{2}} S_{i+\frac{1}{2}} \Delta t}{V_{i+\frac{1}{2}}} \tag{2.41}$$

which reduce the relative phase errors in convection on a locally uniform grid to fourth order. These values will be used throughout this research for applications involving one-dimensional Boris-Book FCT with timestep splitting.

There are several features of the above algorithm that warrant remark. To ensure monotonicity, the values assigned to the diffusion coefficients would necessarily cause the provisional values w_i^{td} to be strongly diffused. Secondly, the diffusive and antidiffusive fluxes are zeroth order so that diffusion and antidiffusion are no longer proportional to $\frac{\partial^2 w}{\partial x^2}$ for nonuniform grids. Consequently, the damping decreases in fine regions of the grid.

It should be noted that step (5) ensures that the limited antidiffusive fluxes will not create new extrema nor accentuate existing ones in the "transported-and-diffused" solution w_i^{td}. This can be illustrated by studying the eight possible configurations of w_i^{td} in the vicinity of a positive $A_{i+\frac{1}{2}}$.

Fig 2.3 shows the normal situation in which $A_{i+\frac{1}{2}}$ has the same sign as the local gradient of w_i^{td} and will therefore tend to steepen the gradient (this is in contrast to a diffusive flux which would reduce the gradient). Examination of equation (2.36) reveals that when either $(w_i^{td} - w_{i-1}^{td})$ or $(w_{i+2}^{td} - w_{i+1}^{td})$ has a sign opposite to $A_{i+\frac{1}{2}}$ a negative quantity will appear inside the parenthesis to nullify $A_{i+\frac{1}{2}}$. In such a situation the high order flux would have been given zero weighting, which is in line with the intentions of the limiter since the antidiffusive flux would have accentuated the already existing extrema in cases (2), (3) and (4) in Fig 2.3. In case (1), there is no extremum in the w^{td} profile, so equation (2.36) will just limit the antidiffusive flux, $(A_{i+\frac{1}{2}})$ to prevent the formation of a new extremum; this is so since $A_{i+\frac{1}{2}}$ will not be selected from the inner parenthesis if $A_{i+\frac{1}{2}}$ exceeds either $V_{i+1}(w_{i+2}^{td} - w_{i+1}^{td})$ or $V_i(w_i^{td} - w_{i-1}^{td})$.

Cases (5)-(8) in Fig 2.3 are the same as (1)-(4) except that $w_{i+1}^{td} - w_i^{td}$ has the opposite sign. (Therefore the antidiffusive flux has actually become a diffusive flux.) Since $w_{i+1}^{td} - w_i^{td}$ does not enter into the equation (2.36) the results are exactly the same. Zalesak explains that cases (5)-(8) arise very rarely and that when they do, the errors introduced by (2.36) represent the correct action to take (since additional diffusion of the the w^{td} profile is undesirable).

As mentioned earlier, one-dimensional Boris-Book FCT can be used to construct a multidimensional algorithm through the use of directional timestep splitting in each coordinate direction. This is straightforward when an orthogonal grid is used. The flux terms on the right-hand-side of (2.10) are separated into those representing fluxes in the same computational space direction (ξ, η, ς). Sequence (1)-(6) is then carried out sequentially for each direction using the updated values of w_i^{td} for each step. Hence, the time integration of the Euler Equations would take the following form:-

$$w_{i,j}^{n+1} = L_\xi(\Delta t) L_\eta(\Delta t) L_\varsigma(\Delta t) w_{i,j}^n \tag{2.42}$$

where $L_\xi, L_\eta, L_\varsigma$ represent the operations that carry out steps (1) through (6) above in the computational direction indicated in the subscript. For a uniform grid, the temporal order of accuracy can be increased by making the sequence of operations symmetric [30]. One of the many permutations

is:-

$$w_{i,j}^{n+1} = L_\xi(\frac{\Delta t}{2})(L_\eta(\frac{\Delta t}{2})L_\varsigma(\Delta t)L_\xi(\frac{\Delta t}{2})(L_\eta(\frac{\Delta t}{2})w_{i,j}^n \tag{2.43}$$

The main drawback of directional timestep splitting is that problems develop when the algorithm is used with nonorthogonal curvilinear coordinates. The source of the problem can be readily identified by applying the scheme to the computation of uniform flow through a channel with straight walls but using a non-uniform grid. The resulting numerical solution indicates that the flow does not stay uniform. Deviations from uniform flow increase with the number of iterations until they reached an asymptotic steady state, with the largest deviation occuring in the most distorted cells. This scheme clearly yields an erroneous solution. One can perceive how this problem arises by examining the conservation of momentum equation for the ξ-direction stage of the timestep splitting sequence for uniform flow in the x-direction

$$\begin{aligned}(\rho v_x)_{i,j,k}^{n+1} &= (\rho v_x)_{i,j,k}^n - \frac{\Delta t}{V_{i,j,k}} \\ &\quad (\rho v_x^2 + P)^n(S_{x_{i-\frac{1}{2},j,k}} + S_{x_{i+\frac{1}{2},j,k}})\end{aligned} \tag{2.44}$$

For there to be no change in $(\rho v_x)_{i,j,k}^n$ we require

$$S_{x_{i-\frac{1}{2},j,k}} = -S_{x_{i+\frac{1}{2},j,k}} \tag{2.45}$$

and it can be shown that this is so for cartesian, spherical polar and cylindrical polar coordinates; however it is not necessarily true for curvilinear coordinates. As a result, errors are introduced. These errors are compounded by the fact that the diffusion-antidiffusion process then acts on the intermediate flow variables which have been affected by these erroneous, grid-dependent fluxes. For this reason we recommend the use of directional timestep splitting only to applications with orthogonal grids.

This appears to be an appropriate point to comment on the advantages of using a nonorthogonal, curvilinear, numerical grid. As stated earlier, the main objective of this research is to devise a computational tool that can generate an accurate numerical solution to the Euler equations in the

physical domain of a convoluted lobed mixer and in the downstream mixing duct. The complex topography of the lobed mixer does not permit the use of a Cartesian grid that conforms naturally to the physical boundaries. Therefore, a Cartesian grid would entail the use of rather complicated two-dimensional interpolation techniques. In addition to these complexities, interpolation provides an additional source of error at the locations that provide the dominant influence on the character of the solution [31]. These inaccuracies are worst when the boundary has high curvature or when large gradients are present in the vicinity of the boundary. Both of these are the case for the flowfield of the lobed mixer. Furthermore, with a Cartesian grid it is difficult to pack grid points into regions where the largest gradients exist (such as at the trailing edge of the lobed mixer and in the mixing layer as it evolves downstream) without also packing grid points needlessly into regions where the high resolution is not required. These difficulties are eliminated when a nonorthogonal, body-aligned, curvilinear grid can be generated with, for example, a scheme that calculates curvilinear coordinates as the solution of an elliptic partial differential system. Hence a body-aligned grid was chosen, and it thus became necessary to develop an Euler solver that does not resort to directional timestep-splitting.

2.4 Zalesak's Extension of Boris-Book FCT to Multidimensions

Zalesak [21] summarized the theory of FCT in a simple generalized format and presented a new algorithm for implementing Boris-Book FCT in multidimensions without any directional timestep splitting. This particular algorithm is computationally somewhat more expensive; in spite of this, its use for simulating flow in a domain with a general curvilinear grid is preferable to the use of directional timestep-splitting. The three-dimensional Euler equations, with finite volume spatial discretization and simple forward time temporal discretization are

$$w_{i,j,k}^{n+1} = w_{i,j,k}^{n} - \frac{1}{V_{i,j,k}}(E_{i+\frac{1}{2},j,k}^{n} - E_{i-\frac{1}{2},j,k}^{n} + F_{i,j+\frac{1}{2},k}^{n} - F_{i,j-\frac{1}{2},k}^{n} + G_{i,j,k+\frac{1}{2}}^{n} - G_{i,j,k-\frac{1}{2}}^{n}) \quad (2.46)$$

where

$$E^n_{i+\frac{1}{2},j,k} = ((e,f,g)\cdot\vec{S})^n_{i+\frac{1}{2},j,k}\Delta t$$

$$F^n_{i,j+\frac{1}{2},k} = ((e,f,g)\cdot\vec{S})^n_{i,j+\frac{1}{2},k}\Delta t$$

$$G^n_{i,j,k+\frac{1}{2}} = ((e,f,g)\cdot\vec{S})^n_{i,j,k+\frac{1}{2}}\Delta t$$

For two dimensions, $V_{i,j,k}$ becomes an area and the projected areas, (S_x, S_y, S_z) become projected distances. The FCT algorithm then proceeds as follows:-

(1) Compute the low order fluxes, $E^L_{i+\frac{1}{2},j,k}, F^L_{i,j+\frac{1}{2},k}, G^L_{i,j,k+\frac{1}{2}}$ by a low order, monotonicity-preserving scheme;

(2) Compute the high order fluxes, $E^H_{i+\frac{1}{2},j,k}, F^H_{i,j+\frac{1}{2},k}, G^H_{i,j,k+\frac{1}{2}}$ by a high order scheme;

(3) Define the antidiffusive fluxes

$$A_{i+\frac{1}{2},j,k} = E^H_{i+\frac{1}{2},j,k} - E^L_{i+\frac{1}{2},j,k} \tag{2.47}$$

$$A_{i,j+\frac{1}{2},k} = E^H_{i,j+\frac{1}{2},k} - E^L_{i,j+\frac{1}{2},k} \tag{2.48}$$

$$A_{i,j,k+\frac{1}{2}} = E^H_{i,j,k+\frac{1}{2}} - E^L_{i,j,k+\frac{1}{2}} \tag{2.49}$$

(4) Compute the low order time-advanced solution

$$w^{td}_{i,j,k} = w^n_{i,j,k} - \frac{1}{V_{i,j,k}}(E^L_{i+\frac{1}{2},j,k} - E^L_{i-\frac{1}{2},j,k} + F^L_{i,j+\frac{1}{2},k} - F^L_{i,j-\frac{1}{2},k} + G^L_{i,j,k+\frac{1}{2}} - G^L_{i,j,k-\frac{1}{2}}) \tag{2.50}$$

(5) Limit the antidiffusive fluxes

$$A^c_{i+\frac{1}{2},j,k} = C_{i+\frac{1}{2},j,k}A_{i+\frac{1}{2},j,k} \tag{2.51}$$

$$A^c_{i,j+\frac{1}{2},k} = C_{i,j+\frac{1}{2},k}A_{i,j+\frac{1}{2},k} \tag{2.52}$$

$$A^c_{i,j,k+\frac{1}{2}} = C_{i,j,k+\frac{1}{2}}A_{i,j,k+\frac{1}{2}} \tag{2.53}$$

with

$$0 \leq C_{i+\frac{1}{2},j,k} \leq 1$$

$$0 \leq C_{i,j+\frac{1}{2},k} \leq 1$$

$$0 \leq C_{i,j,k+\frac{1}{2}} \leq 1$$

(6) Apply the limited antidiffusive fluxes

$$w_{i,j,k}^{n+1} = w_{i,j,k}td - \frac{1}{V_i}(A^c_{i+\frac{1}{2},j,k} - A^c_{i-\frac{1}{2},j,k} + A^c_{i,j+\frac{1}{2},k} - A^c_{i,j-\frac{1}{2},k} + A^c_{i,j,k+\frac{1}{2}} - A^c_{i,j,k-\frac{1}{2}}) \quad (2.54)$$

The critical step in this sequence is step (5). Zalesak suggested that step(5) may just consist of the original Boris-Book limiter (see Equation (2.36)) acting on $A_{i+\frac{1}{2},j,k}, A_{i,j+\frac{1}{2},k}, A_{i,j,k+\frac{1}{2}}$ separately with all corrected antidiffusive fluxes being applied simultaneously in step (6). This approach does away with the need for using directional timestep splitting. However this procedure may result in a quite diffusive algorithm since the Boris-Book limiter looks in each coordinate direction separately for extrema. Even though a quantity may be an extremum with respect to one coordinate direction, it may not be an extremum with respect to all coordinate directions. Therefore, the Boris-Book limiter will limit antidiffusive fluxes needlessly in some cases.

2.5 Zalesak's Fully Multidimensional Flux Limiter

Zalesak proposed an implementation of step (5) above that takes into account all fluxes acting towards or away from a cell (i,j,k) and searches for extrema in all coordinate directions. It should be pointed out initially that the purpose of the limiter is to ensure that the corrected antidiffusive fluxes, $A^c_{i+\frac{1}{2},j,k}, A^c_{i,j+\frac{1}{2},k}, A^c_{i,j,k+\frac{1}{2}}$ acting in concert shall not cause

$$w_{i,j,k}^{n+1} = w_{i,j,k}td - \frac{1}{V_i}(A^c_{i+\frac{1}{2},j,k} - A^c_{i-\frac{1}{2},j,k} + A^c_{i,j+\frac{1}{2},k} - A^c_{i,j-\frac{1}{2},k} + A^c_{i,j,k+\frac{1}{2}} - A^c_{i,j,k-\frac{1}{2}})$$

to exceed some maximum value $w_{i,j,k}^{max}$ nor fall below some minimum value $w_{i,j,k}^{min}$. The method for the determination of $w_{i,j,k}^{max}$ and $w_{i,j,k}^{min}$ will be explained subsequently. The process is divided into two stages: the first limits the antidiffusive fluxes to ensure that no maxima are created nor accentuated while the second limits those provisionally corrected antidiffusive fluxes so that no minima are created nor accentuated. The algorithm proceeds as follows:-

(1) Calculate the sum of all antidiffusive fluxes into cell (i,j,k). (Negative contributions due to fluxes directed away from the cell should not be included in this sum since they may be cancelled by the flux-correction process in an adjacent cell and a worst case scenario should be assumed.)

$$\begin{aligned} P_{i,j,k}^{+} &= max(0, A_{i-\frac{1}{2},j,k}) - min(0, A_{i+\frac{1}{2},j,k}) + \\ &\quad max(0, A_{i,j-\frac{1}{2},k}) - min(0, A_{i,j+\frac{1}{2},k}) + \\ &\quad max(0, A_{i,j,k-\frac{1}{2}}) - min(0, A_{i,j,k+\frac{1}{2}}) \end{aligned} \tag{2.55}$$

(2) Calculate the maximum allowable increase in mass (or momentum, or energy) in cell (i,j,k)

$$Q_{i,j,k}^{+} = (w_{i,j,k}^{max} - w_{i,j,k}^{td})V_{i,j,k} \tag{2.56}$$

(3) Calculate the least-upper-bound on the fraction that must multiply all antidiffusive fluxes into cell (i,j,k) to guarantee no overshoot in $w_{i,j,k}^{n+1}$

$$R_{i,j,k}^{+} = \begin{cases} min(1, Q_{i,j,k}^{+}/P_{i,j,k}^{+}) & P_{i,j,k}^{+} > 0 \\ 1 & P_{i,j,k}^{+} = 0 \end{cases} \tag{2.57}$$

(4) Limit the fluxes so that no maxima are created nor accentuated

$$A_{i+\frac{1}{2},j,k}^{'} = \begin{cases} R_{i,j,k}^{+} A_{i+\frac{1}{2},j,k} & A_{i+\frac{1}{2},j,k} < 0 \\ R_{i+1,j,k}^{+} A_{i+\frac{1}{2},j,k} & A_{i+\frac{1}{2},j,k} > 0 \end{cases} \tag{2.58}$$

(5) Calculate the sum of all antidiffusive fluxes away from cell (i,j,k).

$$\begin{aligned} P^{-}_{i,j,k} &= max(0, A_{i+\frac{1}{2},j,k}) - min(0, A_{i-\frac{1}{2},j,k}) + \\ & max(0, A_{i,j+\frac{1}{2},k}) - min(0, A_{i,j-\frac{1}{2},k}) + \\ & max(0, A_{i,j,k+\frac{1}{2}}) - min(0, A_{i,j,k-\frac{1}{2}}) \end{aligned} \tag{2.59}$$

(6) Calculate the maximum allowable increase in mass (or momentum, or energy) in cell (i,j,k)

$$Q^{-}_{i,j,k} = (w^{td}_{i,j,k} - w^{min}_{i,j,k})V_{i,j,k} \tag{2.60}$$

(7) Calculate the least-upper-bound on the fraction that must multiply all antidiffusive fluxes away from cell (i,j,k) to guarantee no undershoot in $w^{n+1}_{i,j,k}$

$$R^{-}_{i,j,k} = \begin{cases} min(1, Q^{-}_{i,j,k}/P^{-}_{i,j,k}) & P^{+}_{i,j,k} > 0 \\ 1 & P^{+}_{i,j,k} = 0 \end{cases} \tag{2.61}$$

(8) Limit the fluxes so that no maxima are created nor accentuated

$$A^{c}_{i+\frac{1}{2},j,k} = \begin{cases} R^{+}_{i,j,k} A'_{i+\frac{1}{2},j,k} & A'_{i+\frac{1}{2},j,k} > 0 \\ R^{+}_{i+1,j,k} A'_{i+\frac{1}{2},j,k} & A'_{i+\frac{1}{2},j,k} < 0 \end{cases} \tag{2.62}$$

Following the example of the Boris-Book limiter, Zalesak also proposes to cancel the antidiffusive flux if it has a sign opposite to the gradient in w^{td}:-

$$\begin{aligned} A_{i+\frac{1}{2},j,k} = 0 \qquad & \text{if} \quad A_{i+\frac{1}{2},j,k}(w^{td}_{i+1,j,k} - w^{td}_{i,j,k}) < 0 \\ & \text{and either} \quad A_{i+\frac{1}{2},j,k}(w^{td}_{i+2,j,k} - w^{td}_{i+1,j,k}) < 0 \\ & \text{or} \quad A_{i+\frac{1}{2},j,k}(w^{td}_{i,j,k} - w^{td}_{i-1,j,k}) < 0 \end{aligned} \tag{2.63}$$

The following choice for $w^{max}_{i,j,k}$ and $w^{min}_{i,j,k}$ was used for most of the calculations carried out using Zalesak's limiter.

$$w^{a}_{i,j,k} = max(w^{n}_{i,j,k}, w^{td}_{i,j,k}) \tag{2.64}$$

$$w^{max}_{i,j,k} = max(w^a_{i,j,k}, w^a_{i+1,j,k}, w^a_{i-1,j,k}, w^a_{i,j+1,k}, w^a_{i,j-1,k}, w^a_{i,j,k+1}, w^a_{i,j,k-1}) \tag{2.65}$$

$$w^b_{i,j,k} = min(w^n_{i,j,k}, w^{td}_{i,j,k}) \tag{2.66}$$

$$w^{min}_{i,j,k} = min(w^b_{i,j,k}, w^b_{i+1,j,k}, w^b_{i-1,j,k}, w^b_{i,j+1,k}, w^b_{i,j-1,k}, w^b_{i,j,k+1}, w^b_{i,j,k-1}) \tag{2.67}$$

The Zalesak limiter is less likely to correct the antidiffusive fluxes than the Boris-Book limiter because it will check in all three computational dimensions for a maximum and a minimum. This causes the allowable variation in $w^{n+1}_{i,j,k}$ to be larger and so the antidiffusive fluxes will not be limited as much. In other words, Zalesak's limiter tends to give a higher weighting to the high order fluxes than Boris' limiter. Nevertheless, in some cases, such as when the quantity of interest is being convected in a direction perpendicular to a large gradient in that quantity, (for example, a contact discontinuity or a *vortex sheet*), it is desirable to check each of the coordinate directions separately as spurious ripples in the direction perpendicular to the gradient can arise. This is because the flux limiter will not correct antidiffusive fluxes that produce values of w^{n+1} that lie within the bounds imposed by w^{min} and w^{max}. When the gradient is large in the direction perpendicular to the direction of convection, the evaluation of w^{min} and w^{max} is dominated by the presence of this gradient. Hence, although a value of w^{n+1} may constitute a violation of monotonicity with respect to the direction perpendicular to the large gradient, the antidiffusive fluxes causing this violation of monotonicity will pass through the multidimensional limiter uncorrected. This means that there is essentially no flux correction in the perpendicular direction. In these cases, it would appear to be preferable to use the Boris-Book limiter (but not with timestep splitting). However the flexibility of Zalesak's limiter is such that it is possible to implement it in such a fashion that it will limit the antidiffusive fluxes in each coordinate direction separately, in the same manner as the Boris-Book limiter. It also has the added advantage of being capable of searching both $w^{td}_{i,j,k}$ and $w^n_{i,j,k}$ for extrema.

2.6 High Order Scheme

The high order scheme selected for use with the Zalesak limiter to calculate the high order fluxes $\mathbf{E}^H_{i+\frac{1}{2},j,k}$, $\mathbf{F}^H_{i,j+\frac{1}{2},k}$ and $\mathbf{G}^H_{i,j,k+\frac{1}{2}}$ was the Leapfrog-Trapezoidal Method [32,33]. This is a predictor/corrector type scheme in which the predictor step is leapfrog and the corrector step is trapezoidal. The algorithm proceeds as follows. First, the leapfrog discretization of Equation (2.12) gives the predicted state vector $\mathbf{w}'_{i,j,k}$:-

$$\mathbf{w}'_{i,j,k} = \mathbf{w}^{n-1}_{i,j,k} - \frac{2}{V_{i,j,k}}(\mathbf{E}^n_{i+\frac{1}{2},j,k} - \mathbf{E}^n_{i-\frac{1}{2},j,k} + \mathbf{F}^n_{i,j+\frac{1}{2},k} - \mathbf{F}^n_{i,j-\frac{1}{2},k} + \mathbf{G}^n_{i,j,k+\frac{1}{2}} - \mathbf{G}^n_{i,j,k-\frac{1}{2}}) \quad (2.68)$$

with the fluxes evaluated as follows:

$$\mathbf{E}^n_{i+\frac{1}{2},j,k} = \frac{\Delta t}{4}((\vec{v}_{i+1,j,k} + \vec{v}_{i,j,k}) \cdot \vec{S}_{i+\frac{1}{2},j,k})(\mathbf{w}_{i+1,j,k} + \mathbf{w}_{i,j,k}) + Sources \quad (2.69)$$

$$\mathbf{F}^n_{i,j+\frac{1}{2},k} = \frac{\Delta t}{4}((\vec{v}_{i,j+1,k} + \vec{v}_{i,j,k}) \cdot \vec{S}_{i,j+\frac{1}{2},k})(\mathbf{w}_{i,j+1,k} + \mathbf{w}_{i,j,k}) + Sources \quad (2.70)$$

$$\mathbf{G}^n_{i,j,k+\frac{1}{2}} = \frac{\Delta t}{4}((\vec{v}_{i,j,k+1} + \vec{v}_{i,j,k}) \cdot \vec{S}_{i,j,k+\frac{1}{2}})(\mathbf{w}_{i,j,k+1} + \mathbf{w}_{i,j,k}) + Sources \quad (2.71)$$

The trapezoidal stage then corrects the leapfrog prediction to give the state vector at the next time level $w^{n+1}_{i,j,k}$ with the following equation

$$\mathbf{w}^{n+1}_{i,j,k} = \mathbf{w}^n_{i,j,k} - \frac{1}{V_{i,j,k}}(\mathbf{E}^*_{i+\frac{1}{2},j,k} - \mathbf{E}^*_{i-\frac{1}{2},j,k} + \mathbf{F}^*_{i,j+\frac{1}{2},k} - \mathbf{F}^*_{i,j-\frac{1}{2},k} + \mathbf{G}^*_{i,j,k+\frac{1}{2}} - \mathbf{G}^*_{i,j,k-\frac{1}{2}}) \quad (2.72)$$

where,

$$\mathbf{E}^*_{i+\frac{1}{2},j,k} = \frac{1}{2}(\mathbf{E}^n_{i+\frac{1}{2},j,k} + \mathbf{E}'_{i+\frac{1}{2},j,k}) \quad (2.73)$$

etc. and,

$$\mathbf{E}' = \mathbf{E}(\mathbf{w}') \,. \quad (2.74)$$

The advantages of the leapfrog-trapezoidal method are that it is conservative, virtually non-dissipative (and stable when implemented with FCT) and it is computationally quite efficient. Its temporal accuracy is 2nd order while the spatial accuracy is 2nd order for a uniform grid but deteriorates to 1st order when the stretching between adjacent cells becomes large. One of the

drawbacks is that the leapfrog step requires the state vectors from two time levels, which increases memory requirements. The scheme is bootstrapped by assuming that the state vector at the first time level $\mathbf{w}^0$ is equal to the state vector at the previous time level, $\mathbf{w}^{-1}$. Since we are interested in steady state solutions attained after the initial conditions are convected out of the computational domain, the inaccuracies associated with this approximation and with the guess for the initial state vector $\mathbf{w}^0$ will not significantly affect the final solution. For restarts, time levels from the previous two time levels are stored to ensure a smooth continuation of the calculation.

The differential approximation to the discretized wave equation based on the leapfrog scheme is

$$w_t + cw_x = \frac{c(\Delta x)^2}{6}(\epsilon^2 - 1)w_{xxx} - \frac{c(\Delta x)^4}{120}(9\epsilon^4 - 10\epsilon^2 + 1)w_{xxxxx} \tag{2.75}$$

where ϵ is the CFL number as before. Some information can be extracted from this linearized case. The leading term in the truncation error contains the odd derivative w_{xxx} and so the solution will exhibit predominantly dispersive errors. There are no even derivatives in the modified equation so the linearized solution will have no dissipative error. This can be seen from the fact that the amplification factors are identically equal to one

$$G = \pm\sqrt{1 - \epsilon^2 \sin^2\beta} - i\epsilon \sin\beta \tag{2.76}$$

where $\beta = k_m \Delta x$ and $k_m$is the wave number. The relative phase error is

$$\frac{\phi}{\phi_e} = \frac{\arctan(-\epsilon \sin\beta / \pm\sqrt{(1 - \epsilon^2 \sin^2\beta)})}{-\beta\epsilon} \tag{2.77}$$

This brings us to the main disadvantage of the leapfrog method, i.e., that two independent solutions develop as the solution proceeds (since $w^{n+1}_{i,j,k}$ does not depend on $w^n_{i,j,k}$). Closely related to this, there are two amplification factors for the scheme, as can be seen from Equation (2.76) and Equation (2.77) where one is the amplification factor for the physical mode and the other is the amplification factor for the computational mode. The magnitude of both is always identically equal

to one for the leapfrog method. This can be seen by examination of the above expression for the amplification factors.

The complex amplification factor for the leapfrog-trapezoidal method is

$$G = (1 - (\epsilon \sin\beta)^2 - \frac{1}{2}i\epsilon \sin\beta) \pm \frac{1}{2}\sqrt{(1 - (\epsilon \sin\beta)^2 - \frac{1}{2}i\epsilon \sin\beta)^2 - 2i\epsilon \sin\beta)} \tag{2.78}$$

Grammeltvedt [33] shows that for the leapfrog-trapezoidal method, the computational mode is suppressed while the physical mode still has an amplification factor of about one.

Some comments on the discretization of the flux terms in Equation (2.69) are in order. The usual discretization of $(wv)_x$ is

$$(wv)_x^{fd} = \frac{1}{2\Delta x}(w_{i+1}v_{i+1} - v_{i-1}w_{i-1}) \tag{2.79}$$

Zalesak [22] suggests a discretization that improves the nonlinear stability properties of the scheme. He suggests that the product wv be differenced by parts:-

$$(wv)_x^{fd} = \frac{1}{2\Delta x}(w_i(v_{i+1} - v_{i-1}) + v_i(w_{i+1} - w_{i-1})) \tag{2.80}$$

which is equivalent to the straightforward central differencing of

$$(wv)_x = wv_x + vw_x \tag{2.81}$$

This type of differencing has been termed Zip differencing by Zalesak. The reason for the improved stability properties can be seen by examining the truncation error for the usual finite difference discretization

$$TE = \frac{1}{6}(\frac{\partial^3 wv}{\partial x^3})_i(\Delta x)^2 + \frac{1}{120}(\frac{\partial^5 wv}{\partial x^5})_i(\Delta x)^4 + O(\Delta x)^6 \tag{2.82}$$

and comparing it with that for the Zip differencing discretization

$$TE = \frac{1}{6}(w\frac{\partial^3 v}{\partial x^3} + v\frac{\partial^3 w}{\partial x^3})_i(\Delta x)^2 + \frac{1}{120}(w\frac{\partial^5 v}{\partial x^5} + v\frac{\partial^5 w}{\partial x^5})_i(\Delta x)^4 + O(\Delta x)^6 \tag{2.83}$$

The leading term in Equation (2.82) can be found to contain an even derivative in w since

$$\frac{\partial^3 wv}{\partial x^3} = w\frac{\partial^3 v}{\partial x^3} + 3\frac{\partial^2 v}{\partial x^2}\frac{\partial w}{\partial x} + 3\frac{\partial^2 w}{\partial x^2}\frac{\partial v}{\partial x} + w\frac{\partial^3 w}{\partial x^3} \tag{2.84}$$

This even derivative will contribute a destabilizing or dissipative effect depending on the sign of $\frac{\partial v}{\partial x}$ except in the trivial case when $\frac{\partial v}{\partial x} = 0$. The truncation error for the Zip differencing discretization contains no even derivatives and so will give rise to errors of only dispersive nature.

The problem with Zip differencing is that it is quite difficult to implement in finite volume form since it requires the evaluation of metrics (or areas) at the cell centers. If we require the metric discretizations to allow uniform flow modelled on an irregular grid to stay uniform to within roundoff, it is not as straightforward as it might appear at first glance. In any case, the flux discretization used in FVFCT and expressed in Equation (2.69) is an average of the straightforward (Equation (2.79)) and Zip (Equation (2.80)) discretizations. While it does still have even derivative terms in its truncation error, it should have reduced inaccuracy associated with the even derivative in the truncation error than the straightforward discretization and the metric discretization complications are avoided.

2.7 Low Order Scheme

The main requirement of the low order scheme is that it should be monotonicity-preserving. A strongly dissipative term is included in the expression for the fluxes in accordance with the original Boris-Book limiter. A caution is in order here. If the dissipation flux term is too large, instability results. This can be verified by a simple Fourier analysis of the discretized diffusion equation. It is shown in reference [28] that for a discretized diffusion equation of the form

$$w_i^{n+1} = w_i^n + r(w_{i+1}^n - 2w_i^n + w_{i-1}^n) \tag{2.85}$$

The limiting value of r is given by

$$r_{\max} = \frac{1}{2} \tag{2.86}$$

For two and three dimensions the stability requirement is even more restrictive: $r^{2D}_{\max} = \frac{1}{4}$ and $r^{3D}_{\max} = \frac{1}{6}$.

It was felt that another criterion should be that the low order scheme should be capable of generating a valid solution of the Euler equations without the assistance of a high order scheme and FCT. This criterion was also checked for the high order scheme and served as a good validation of the fluxes produced by both schemes. Several schemes were tried for the low order method including the donor-cell method [35] (a conservative form of the first order upwind method), the Rusanov method [34],[24] and an Euler method with an added 2nd order dissipation term. The finite difference equation for the donor-cell method is

$$\mathbf{w}^{n+1}_{i,j,k} = \mathbf{w}^{n}_{i,j,k} - \frac{1}{V_{i,j,k}}(\mathbf{E}^{L}_{i+\frac{1}{2},j,k} - \mathbf{E}^{L}_{i-\frac{1}{2},j,k} + \mathbf{F}^{L}_{i,j+\frac{1}{2},k} - \mathbf{F}^{L}_{i,j-\frac{1}{2},k} + \mathbf{G}^{L}_{i,j,k+\frac{1}{2}} - \mathbf{G}^{L}_{i,j,k-\frac{1}{2}}) \quad (2.87)$$

with the fluxes given by,

$$\mathbf{E}^{L}_{i+\frac{1}{2},j,k} = \frac{\Delta t}{2}(\vec{v}^{n}_{i+\frac{1}{2},j,k} \cdot \vec{S}_{i+\frac{1}{2},j,k}((1-\beta_{i+\frac{1}{2},j,k})\mathbf{w}^{n}_{i,j,k} + (1+\beta_{i+\frac{1}{2},j,k})\mathbf{w}^{n}_{i+1,j,k}) + Sources \quad (2.88)$$

$$\mathbf{F}^{L}_{i,j+\frac{1}{2},k} = \frac{\Delta t}{2}(\vec{v}^{n}_{i,j+\frac{1}{2},k} \cdot \vec{S}_{i,j+\frac{1}{2},k}((1-\beta_{i,j+\frac{1}{2},k})\mathbf{w}^{n}_{i,j,k} + (1+\beta_{i,j+\frac{1}{2},k})\mathbf{w}^{n}_{i,j+1,k}) + Sources \quad (2.89)$$

$$\mathbf{G}^{L}_{i,j,k+\frac{1}{2}} = \frac{\Delta t}{2}(\vec{v}^{n}_{i,j,k+\frac{1}{2}} \cdot \vec{S}_{i,j,k+\frac{1}{2}}((1-\beta_{i,j,k+\frac{1}{2}})\mathbf{w}^{n}_{i,j,k} + (1+\beta_{i,j,k+\frac{1}{2}})\mathbf{w}^{n}_{i,j,k+1}) + Sources \quad (2.90)$$

where

$$\beta_{i+\frac{1}{2},j,k} = sign((\vec{v} \cdot \vec{S})^{n}_{i+\frac{1}{2},j,k}) \quad (2.91)$$

$$\beta_{i,j+\frac{1}{2},k} = sign((\vec{v} \cdot \vec{S})^{n}_{i,j+\frac{1}{2},k}) \quad (2.92)$$

$$\beta_{i,j,k+\frac{1}{2}} = sign((\vec{v} \cdot \vec{S})^{n}_{i,j,k+\frac{1}{2}}) \quad (2.93)$$

With the Rusanov method the fluxes become

$$\begin{aligned}\mathbf{E}^{L}_{i+\frac{1}{2},j,k} \;=\; & (\frac{\Delta t}{2}((\vec{v} \cdot \vec{S})^{n}_{i+\frac{1}{2},j,k}(\mathbf{w}^{n}_{i,j,k} + \mathbf{w}^{n}_{i+1,j,k}) - \\ & \nu_2((\vec{v} \cdot \vec{S})^{n}_{i+\frac{1}{2},j,k} + \frac{(c_{i+1,j,k} + c_{i,j,k})}{2}|\vec{S}|)(\mathbf{w}^{n}_{i+1,j,k} - \mathbf{w}^{n}_{i,j,k})) + Sources \end{aligned} \quad (2.94)$$

etc. where $c_{i,j,k}$ is the speed of sound and $\nu_2 \approx 1$ is a dissipation coefficient chosen by the user. The idea of this scheme is to make the dissipation coefficient proportional to the local CFL number. The fluxes for the Euler method used included a conservative, zeroth order dissipation term:-

$$\mathbf{E}^L_{i+\frac{1}{2},j,k} = \Delta t((\vec{v}\cdot\vec{S})^n_{i+\frac{1}{2},j,k}(\frac{\mathbf{w}^n_{i,j,k}+\mathbf{w}^n_{i+1,j,k}}{2}) - \nu_2 V_{i+\frac{1}{2},j,k}(\mathbf{w}^n_{i+1,j,k}-\mathbf{w}^n_{i,j,k})) + Sources \quad (2.95)$$

etc. The Donor-cell method has been found to be incapable of producing an acceptable solution for the 2-D channel problem to be discussed in the next section. This could be a consequence of the flip-flopping of the dissipative term in regions where the vertical component of velocity changes sign.

The Rusanov and Euler methods on their own produce acceptable solutions to the 2-D channel problem (see Chapter (3) for results of the Rusanov method). The Rusanov method appears to produce better results without the aid of FCT because the scheme tends to apply reduced damping at the majority of cells and a larger damping only where it is really needed (e.g., in the vicinity of shocks). However, the Euler method, with its zeroth order damping term, produces a w^{td} profile free of nonphysical extrema more reliably. For the calculation of flowfields associated with threedimensional lobed mixer, the Euler scheme is used as the low order scheme for the FVFCT algorithm, while for the 2-D channel flow problem, the Rusanov scheme is used.

2.8 Boundary Conditions

2.8.1 Farfield Boundary Conditions

Characteristic-based boundary conditions were used at the inflow and outflow boundaries for most of the calculations carried out in this research. For subsonic flow, the boundary conditions at inflow are found by specifying the four characteristic variables, entropy, s, the tangential velocity components, v_y and v_z and the Riemann invariant corresponding to downstream running acoustic waves, r^+. The fifth characteristic variable r^- is extrapolated from the interior of the computational

domain. This then produces a closed system at the boundary which can then be solved to give the following set of equations from which the state vector can be deduced.

$$v_{x_b} = \frac{1}{2}(v_{x_{-\infty}} + v_{x_I} + \frac{2}{\gamma - 1}(1 - c_I)) \tag{2.96}$$

$$c_b = \frac{\gamma - 1}{4}(v_{x_{-\infty}} + v_{x_I} + \frac{2}{\gamma - 1}(1 + c_I)) \tag{2.97}$$

$$\rho_b = c_b^{\frac{2}{\gamma-1}} \tag{2.98}$$

$$v_{y_b} = v_{y_{-\infty}} \tag{2.99}$$

$$v_{z_b} = v_{z_{-\infty}} \tag{2.100}$$

$$P_b = \frac{1}{\gamma}(\frac{\gamma - 1}{4}(v_{x_{-\infty}} + v_{x_I}) + \frac{1 + c_I}{2})^{\frac{2\gamma}{\gamma-1}} \tag{2.101}$$

At exit, four characteristic variables (s, v_y, v_z, r^+) are extrapolated from the interior while the back pressure is specified. This results in the following set of equations for the boundary state vector.

$$P_b = P_b \tag{2.102}$$

$$\rho_b = \rho_I(\frac{P_b}{P_I})^{\gamma} \tag{2.103}$$

$$v_{y_b} = v_{y_I} \tag{2.104}$$

$$v_{z_b} = v_{z_I} \tag{2.105}$$

$$v_{x_b} = v_{x_I} + \frac{2}{\gamma - 1}(c_I - \sqrt{\frac{\gamma P_b}{\rho_b}}) \tag{2.106}$$

However, for the two-dimensional shear layer calculations to be presented in the next chapter, a different set of boundary conditions are imposed. These boundary conditions are intended to allow feedback between the fluid just entering the computational domain, and the disturbances created downstream by the Kelvin-Helmholtz rollup [26]. This issue will be discussed further in the next chapter. In these cases, the inflow density and velocity are specified and a zero slope condition on the pressure at the inflow boundary is used to derive the energy. For outflow, the density and

velocity are extrapolated from the interior while the pressure is found by assuming that pressure relaxes to some ambient value P_{amb} at $x = \infty$. Interpolation can then be performed between the boundary cell and $x = \infty$ in the variable $\frac{1}{x-x_s}$ where x_s is the x-location of the tip of the splitter plate. This results in the following equation for P.

$$P_g = P_I + \frac{x_g - x_I}{x_g - x_s}(P_{amb} - P_I) \tag{2.107}$$

where subscripts g, s and I denote the guard cell, the cell at the tip of the splitter plate and the cell adjacent to the outflow boundary, respectively. (The guard cell is a cell just outside the numerical domain that is used as a dummy for calculating values at the cell faces at each boundary.)

2.8.2 Solid Body Boundary Conditions

Noting that the normal velocity at solid surfaces vanishes, and dropping terms of higher order terms, the boundary conditions at the wall are derived from solving the component of the momentum equation in the direction normal to the streamsurface on the wall, assuming zero normal velocity and dropping terms of order higher than first order [36]. This is accomplished by forming the inner product of the momentum equation with $\hat{n}$ followed by the imposition of the above-mentioned boundary conditions on velocity. For steady flow, this leads to the following equation.

$$\rho\vec{v}\cdot(\vec{v}\cdot\nabla)\hat{n} = \hat{n}\cdot\nabla P \tag{2.108}$$

Application of a generalized transformation yields the following equation (for a body-aligned grid).

$$\begin{aligned} P_\eta &= \frac{1}{\eta_x^2+\eta_y^2+\eta_z^2}(-P_\xi(\xi_x\eta_x+\xi_y\eta_y+\xi_z\eta_z) - P_\varsigma(\varsigma_x\eta_x+\varsigma_y\eta_y+\varsigma_z\eta_z) + \\ &\quad \frac{\rho}{\sqrt{\eta_x^2+\eta_y^2+\eta_z^2}}(C_{xx}v_x^2 + C_{yy}v_y^2 + C_{zz}v_z^2 + C_{xy}v_xv_y + C_{xz}v_xv_z + C_{yz}v_yv_z)) \end{aligned} \tag{2.109}$$

where

$$C_{xx} = \xi_x\frac{\partial n_x}{\partial\xi} + \eta_x\frac{\partial n_x}{\partial\eta} + \varsigma_x\frac{\partial n_x}{\partial\varsigma} \tag{2.110}$$

$$C_{yy} = \xi_y \frac{\partial n_y}{\partial \xi} + \eta_y \frac{\partial n_y}{\partial \eta} + \varsigma_y \frac{\partial n_y}{\partial \varsigma} \tag{2.111}$$

$$C_{zz} = \xi_z \frac{\partial n_z}{\partial \xi} + \eta_z \frac{\partial n_z}{\partial \eta} + \varsigma_z \frac{\partial n_z}{\partial \varsigma} \tag{2.112}$$

$$C_{xy} = \xi_y \frac{\partial n_x}{\partial \xi} + \eta_y \frac{\partial n_x}{\partial \eta} + \varsigma_y \frac{\partial n_x}{\partial \varsigma} + \xi_x \frac{\partial n_y}{\partial \xi} + \eta_x \frac{\partial n_y}{\partial \eta} + \varsigma_x \frac{\partial n_y}{\partial \varsigma} \tag{2.113}$$

$$C_{xz} = \xi_z \frac{\partial n_x}{\partial \xi} + \eta_z \frac{\partial n_x}{\partial \eta} + \varsigma_z \frac{\partial n_x}{\partial \varsigma} + \xi_x \frac{\partial n_z}{\partial \xi} + \eta_x \frac{\partial n_z}{\partial \eta} + \varsigma_x \frac{\partial n_z}{\partial \varsigma} \tag{2.114}$$

$$C_{yz} = \xi_z \frac{\partial n_y}{\partial \xi} + \eta_z \frac{\partial n_y}{\partial \eta} + \varsigma_z \frac{\partial n_y}{\partial \varsigma} + \xi_y \frac{\partial n_z}{\partial \xi} + \eta_y \frac{\partial n_z}{\partial \eta} + \varsigma_y \frac{\partial n_z}{\partial \varsigma} \tag{2.115}$$

Note that the coefficients $C_{xx}, C_{yy}, C_{zz}, C_{xy}, C_{xz}, C_{yz}$ need only be calculated once in a preprocessing stage of the calculation. It is worth noting that these could safely be set to zero in situations where the radius of curvature is small (such as the calculation of the flow over Ni's bump (see Chapter 3)). However, in general this not so (e.g. the three-dimensional lobed mixer calculations (Chapter 4)) and they must be included in the calculations.

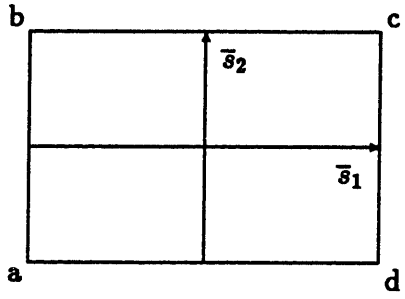

Figure 2.1: Typical cell face showing vectors $\vec{s_1}, \vec{s_2}$ used to find $\vec{S}$

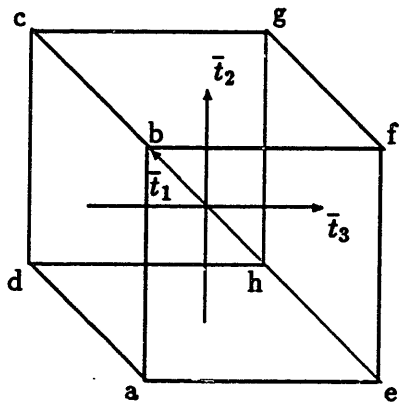

Figure 2.2: Typical cell showing vectors $\vec{t_1}, \vec{t_2}, \vec{t_3}$ used to find V

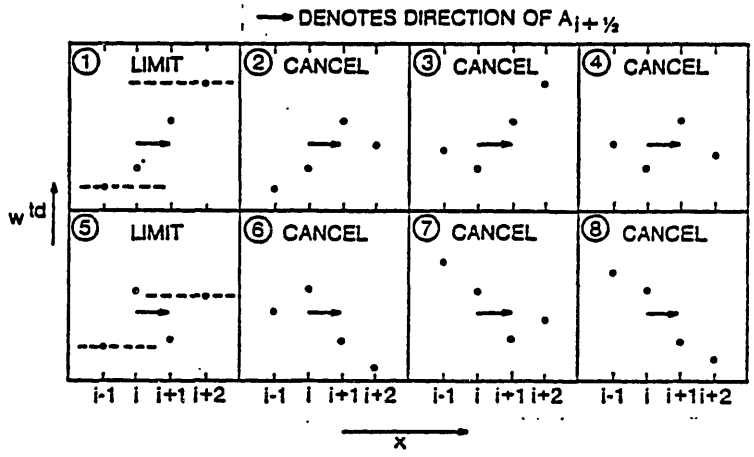

Figure 2.3: The eight possible configurations of the w^{td} in the neighbourhood of a positive antidiffusive flux $A_{i+1/2}$. (Taken from Zalesak)

Chapter 3

Development of the Numerical Algorithm for the Implementation of FCT

This chapter describes the development of both the timestep-splitting Euler solver, LCPFCT and the fully multidimensional FCT Euler solver to which we have given the acronym FVFCT. Features of the low order and high order schemes discussed in Chapter 2 will be further elucidated here.

Before applying the numerical scheme to the computational study of three-dimensional flowfields associated with the lobed mixer, the numerical scheme (and the computer code that implements the scheme) is used to compute flow in situations where reliable and accurate results exist so that appropriate comparisons can be made to ensure the correctness and accuracy of the scheme. In general, a good measure of the quality of a numerical scheme can be estimated by its ability to correctly predict

(1) shock location and strength

(2) preservation of entropy or stagnation pressure for an inviscid, isentropic situation

(3) circulation variation in accordance with Kelvin's Theorem

(4) vorticity distribution (i.e. vortex sheet location and strength as well as its subsequent evolution)

Thus a way to accomplish this assessment would be to use the numerical scheme to compute

(i) the two-dimensional flow through a channel with a circular arc for flowfields ranging from subsonic through transonic to supersonic regimes

(ii) the Kelvin-Helmholtz instability in a two-dimensional shear layer

Simulation (i) is commonly referred to as "Ni's Bump" [43,15,16] and is a good case for assessing the ability of the scheme to address compressibility effects adequately. On the other hand, simulation (ii) [26,27] above would give a measure of how well the scheme can describe the evolution of a shear layer. These features are of interest and importance in the research issues alluded to in Chapter 1. To be completely thorough in this effort, we should also assess the ability of the numerical scheme to give an adequate description of a contact discontinuity not in alignment with a grid line. This is an issue since as the mixing layer evolves downstream of lobed mixers, the vortex sheet will in general not lie along the grid lines. Such an assessment would give a more representative indication of the performance of the algorithm when it is used to calculate a three-dimensional flow dominated by vortical structures.

The calculations and comparisons proposed above provide means for assessing the quality of the numerical scheme in its ability to describe flow features (e.g. vortex sheets, shocks, expansions, flow along curved surfaces) that are expected to be present in the lobed mixer flowfield (with the exception of three-dimensionality) at a computationally low expense.

3.1 Flow in a Channel over a Circular Arc Bump

Results from the calculations of subsonic, transonic and supersonic flow over a circular arc bump are presented in this section. Three numerical schemes are used to generate solutions for each of these test cases:

(i) low order Rusanov method;

(ii) high order Leapfrog-Trapezoidal method;

(iii) the FCT hybrid of these two.

Figures 3.1-3.3 show the 64x16 node grid used for the supersonic, subsonic and transonic calculations, respectively. For the supersonic calculation, the circular arc has a thickness-to-chord ratio τ of 0.04. Note that this is equivalent to a circular arc airfoil of 0.08 thickness-to-chord ratio at zero angle of incidence. For both the subsonic and transonic calculations, a thickness-to-chord ratio of 0.1 was used. These are the standard thickness-to-chord ratios used for these test cases [43,15,16]. Channel height is one chord for all cases. The grids are generated using an elliptic grid generation scheme with a stretching parameter that clusters the $\eta = const$ lines to the lower wall. Another characteristic of the grids is that nodes are separated by constant distance Δs (or constant angle $\Delta\theta$) around the circular arc boundary and by constant distance Δx on the flat portions of the lower wall. Neumann boundary conditions are imposed at the left, right and top boundaries while Dirichlet boundary conditions are imposed at the lower boundary for the generation of each grid.

On a final note, we choose not to use LCPFCT for the solution of this test case. This is because a boundary-conforming grid is adopted for these calculations (for the reasons given in Chapter two). Therefore, the use of directional timestep-splitting would introduce unacceptable grid-dependent errors (as noted in Section 2.3).

3.1.1 Supersonic Circular Bump

Figures 3.4-3.6 show the results of the supersonic test case as calculated by the high order leapfrog-trapezoidal scheme. As can be seen in Figure 3.4, an oblique shock forms at the leading edge of the circular arc bump which curves and weakens slightly due to the Prandtl-Meyer expansion fan emanating from the circular arc bump. The shock loses its sharpness as we move away from the lower wall due to discretization error (this loss of sharpness would not be so severe if the shock lay along one of the grid lines). A short Mach stem is barely in evidence as the shock is reflected from the upper wall. The reflected shock curves and weakens even more as it is intersected by a larger portion of the expansion fan. Just downstream of the trailing edge, the reflected shock encounters

the shock emanating from the trailing edge, before it undergoes another reflection (from the lower wall this time) and then coalesces with the trailing edge shock. Details of the shock interaction at trailing edge are somewhat obscured by the high levels of numerical damping added to ensure stability of the scheme in this region of high gradients.

Nonetheless, much information can be extracted from the high order solution. The angle of the oblique shock formed at the leading edge is about

$$\beta_{high} = 55.8 \pm 1.3 \tag{3.1}$$

by measurement from the leading edge to the impingement point on the upper wall. Note that this measurement of the shock angle implicitly assumes that the shock is straight. This will lead to an estimate of the shock angle at the arc leading edge that is lower than in actuality. (Due to the smearing out of this shock, maximum and minimum measurements of the shock angle were made.) A theoretical prediction for the shock angle just downstream of the leading edge (before it starts to curve toward the expansion fan) can be derived form the Rankine-Hugoniot shock relations. The angle of deflection is

$$\theta = \arctan(\frac{\tau}{\tau^2 - \frac{1}{4}}) = 9.14\,\text{deg} \tag{3.2}$$

where τ is the thickness-to-chord ratio of the circular arc. The Rankine-Hugoniot relations (for inviscid, adiabatic flow) predict that the shock angle is given by the following expression.

$$\tan\theta = 2\cot\beta\frac{M_1^2\sin^2\beta - 1}{M_1^2(\gamma + \cos 2\beta) + 2} \tag{3.3}$$

By looking up shock tables or solving this equation implicitly by an iterative method the shock angle is found to be

$$\beta_{theoretical} = 64.05\,\text{deg} \tag{3.4}$$

However, the Rankine-Hugoniot relations cannot be used in a straightforward manner to give the impingement point of the shock on the upper wall which is essentially what Equation (3.1)

represents. Taking into account the shock curvature (which causes the measured angle to be less than the theoretical shock angle) and the smearing out of the shock (which makes it difficult to measure the impingement point accurately), it can be said that the numerical scheme gives a result that is consistent in spite of the approximate method used to estimate the shock angle. The Rankine-Hugoniot relations also provide a means for calculating the Mach number behind the shock M_2.

$$M_2 = \frac{1}{\sin\beta}\sqrt{\frac{1+\frac{\gamma-1}{2}M_1^2\sin^2\beta}{\gamma M_1^2\sin^2\beta - \frac{\gamma-1}{2}}} = 0.987 \tag{3.5}$$

From Figure 3.5 we see that the minimum Mach number behind the leading edge shock is

$$M_{2_{high}} = 1.08 \tag{3.6}$$

The discrepancy is mainly due to numerical damping which has smeared out the shock.

Figures 3.7- 3.9 show the results of the supersonic test case as calculated by the low order scheme. In Figure 3.8 we see that the shock that should appear at the leading edge of the circular arc bump has been smeared out and extends 5 or 6 cells upstream of the leading edge at the wall. At the upper wall it has been smeared out even farther as can be seen in Figure 3.7. The first reflected shock is not in evidence. The high levels of numerical damping have reduced the usefulness of the solution. Although the numerical dissipation introduced into this scheme to preserve monotonicity could be reduced to allow the numerical solution to resolve more of the features of the flow, the low order results presented here serve to demonstrate the ineffectiveness of the low order scheme when used to generate a solution to this type of a problem on its own. However, they also show that the low order scheme has the ability to deliver fluxes that preserve monotonicity in the w^{td} distribution.

Figures 3.10- 3.14 show the results of the supersonic test case as calculated by the FCT hybrid scheme. The FCT scheme generates a leading edge shock that is only one cell at the lower wall (Figure 3.11) and two cells wide as it approaches the top wall. The Mach stem is also one cell wide. The reflected shock is two or three cells wide and in Figure 3.10 the details of the shock

interaction downstream of the bump trailing edge are much more discernable than the high order solution. The leading edge shock angle is measured to be

$$\beta_{fct} = 55.9 \pm 1.3 \tag{3.7}$$

and the Mach number behind the shock is found from Figure 3.11 to be

$$M_{2_{fct}} = 1.07 \tag{3.8}$$

For FCT, the discrepancy between Equation 3.8 and Equation 3.5 is mainly due to the phenomenon of clipping. This clipping phenomenon can be particularly damaging in the region of a peaked maximum or minimum which is the case here. The source of clipping for an analytical solution with a peaked profile (as opposed to a step profile) stems from the inability of the flux limiter to allow the antidiffusive fluxes to regenerate a local extremum from the "transported-and-diffused" profile. Clipping will be discussed in more detail in Chapter(4). Furthermore it should be noted that the prediction given in Equation 3.5 is for the point immediately behind the shock while that given in Equation 3.8 is at the cell centre adjacent to the shock. This also contributes to the discrepancy.

There are, however, some problems with the FCT Hybrid solution. There is some unphysical upstream propagation of information in the region of the shocks (see Figures 3.13- 3.14). This can be explained by the following reasoning. Ideally, flux limiting should be applied after both the predictor and corrector steps. This, however, would make the scheme excessively expensive in terms of CPU time. Therefore the limiter is only applied after the corrector step. The predictor step thus causes a nonphysical maximum to be generated in the vicinity of a discontinuity that has an origin in Gibbs phenomenon. The corrector step in turn allows the ripple to propagate to the next cell by which time it has become a local minimum. The flux limiter is then applied. The maximum is clipped as it should be. But the local minimum that is two cells away from the discontinuity survives since it lies within the bounds of the maximum and minimum defined by the

"transported-and-diffused" solution in the vicinity of the discontinuity. This is the source of the small oscillation observed upstream of the shock in Figure 3.14. It should also be pointed out that this FCT solution is not a steady-state solution due to the low levels of damping (zero second order damping and very low fourth order damping). Unless numerical dissipation is added, convergence is difficult to achieve with FCT schemes due to the inherent unsteadiness associated with the limiting mechanism. It is this unsteady nature of the solution that is responsible for the presence of small residual oscillations in the neighbourhood of the outflow boundary. Furthermore, oscillations are present in the plot of normalized total pressure change (Figure 3.12).

The above-mentioned unsteadiness is one of the reasons for these oscillations. Another is the fact that flux-limiting is performed on the conserved quantities only (i.e., mass, momentum and total energy). Hence, FCT can provide no guarantee that no non-physical extrema will arise in derived quantities such as static and total pressure. Indeed overshoots and undershoots in derived quantities are possible since in the region of a shock, the numerical jump in momentum may spatially lead the jump in energy. A way around this problem is to use flux-synchronization in which the antidiffusive fluxes at a face $(i+\frac{1}{2},j,k)$ are all limited by the same fraction $C'_{i+\frac{1}{2},j,k}$. $C'_{i+\frac{1}{2},j,k}$ can be determined from one or more of the conservation equations. One such possibility is

$$\begin{aligned} C'_{i+\frac{1}{2},j,k}(\rho) &= C'_{i+\frac{1}{2},j,k}(\rho v_x) = C'_{i+\frac{1}{2},j,k}(\rho v_y) = C'_{i+\frac{1}{2},j,k}(\rho v_z) = C'_{i+\frac{1}{2},j,k}(E_t) \\ &= min(C_{i+\frac{1}{2},j,k}(\rho), C_{i+\frac{1}{2},j,k}(E_t)) \end{aligned} \tag{3.9}$$

FCT researchers are currently concentrating their efforts in flux-synchronization [23] as the best means of improving FCT algorithms.

3.1.2 Transonic Circular Bump

The grid used for this calculation is shown in Figure 3.2. The inflow Mach number was 0.675. Figures 3.15- 3.19 show the results of the high order solution for this test case while figures 3.20- 3.24 show the results of the FCT hybrid solution for this test case. It can be seen from (for example)

Figure 3.20 that the flow is accelerated around the bump into a supersonic region terminated by a shock. The same numerical damping coefficients were used for both the FCT hybrid and the high order schemes. As a result the solutions are almost identical except for the details around the shock. Since the flow is inviscid, total pressure losses should be confined to the vicinity of the shock. Figure 3.19 and Figure 3.24 show that this is the case for the high order and the FCT hybrid scheme except for some resolution-based total pressure variation at the leading and trailing edges. Notice also that contours of constant total pressure loss closely follow the streamlines downstream of the shock.

Normal shock relations [45] provide a means for checking the validity of the solution at least in the vicinity of the shock. The strength of the shock is given by

$$\frac{\Delta P}{P_1} = \frac{P_2 - P_1}{P_1} = \frac{2\gamma}{\gamma + 1}(M_1^2 - 1) \tag{3.10}$$

and the Mach number behind the shock is given by

$$M_2 = \sqrt{\frac{1 + \frac{\gamma-1}{2}M_1^2}{\gamma M_1^2 - \frac{\gamma-1}{2}}} \tag{3.11}$$

Table 3.1 presents a comparison of the values of shock strength as predicted by Equation 3.10 (given the numerically found M_1) and those found in the solutions produced by the FCT and High Order schemes and as depicted in Figures 3.16, 3.18, 3.21, 3.23. It also presents similar comparisons for M_2. The High Order scheme predicts a stronger shock due to the undesirable clipping in the region of the shock caused by the flux limiter. If anything, the High Order scheme produces a superior solution.

Figures 3.25- 3.27 show the results of the low order solution for this test case. Of course, the low order method proves to be too diffusive to resolve the transonic shock and indeed the low order method does not allow the flow to become supersonic. As will be seen subsequently, the solution is quite similar to the subsonic case with $M_{inflow} = 0.5$.

Table 3.1: Comparison of normal shock relation and numerically predicted shock values

	High Order Solution	FCT Hybrid Solution
M_1	1.425	1.366
$M_{2_{theoretical}}$	0.729	0.755
$M_{2_{numerical}}$	0.745	0.718
P_1	0.303	0.324
P_2	0.655	0.655
$(\frac{\Delta P}{P_1})_{theoretical}$	1.204	1.021
$(\frac{\Delta P}{P_1})_{numerical}$	1.160	1.010

3.1.3 Subsonic Circular Bump

For this test case, we have taken M_{inflow} to be 0.5. There are no supersonic regions and so all changes in total pressure are numerical in origin. Changes in total pressure are a good indication of the quality of the solution. The symmetry of the solution can also be a good indication.

Figures 3.28- 3.30 show the results of the high order scheme. The solution is almost symmetric except for some asymmetry in, for example, the Mach number contour plot (Figure 3.28) downstream of the trailing edge. This is due to the generation of an entropy layer at the bump leading edge and trailing edge that is numerical in origin. Comparison with the Mach distribution in reference [43] is of limited use since homoenergetic ($H^0 = const$) flow is assumed in that calculation and this is not the case for the results presented herein. Levels of total pressure loss are very small as shown in Figure 3.30 except for those due to small resolution-related, nonphysical oscillations confined to the leading and trailing edges.

Figures 3.34- 3.38 show the results of the FCT hybrid scheme. It can be seen that the results are almost identical to the High Order results except in the vicinity of the leading and trailing edges and at the apex of the bump. These differences can be traced to the clipping effect of the

flux limiter near extrema mentioned in Section(3.1.1). For example, examination of the density distribution along the lower wall (Figure 3.37) reveals that a plateau has been created at the apex of the bump by the effect of the flux limiter. This clipping also introduces small dispersive errors which degrade the quality of the solution slightly. The satisfactory nature of the solution by the FCT hybrid scheme can be deduced from the computed results.

The asymmetry of the low order solution and the high levels of total pressure loss indicate the unsatisfactory nature of this solution. However the marginal credibility of the solution confirms that the low order fluxes can be expected to yield a "transported-and-diffused" solution for the FCT hybrid scheme that is free of nonphysical extrema. This is also confirmed by the satisfactory nature of the FCT hybrid scheme.

3.1.4 Summary of the Computed Results for Ni's Bump

The low order scheme is found to produce unsatisfactory results for all three (supersonic, transonic and subsonic) test cases. Shocks are severely smeared out for the supersonic case. Flow details are obscured almost beyond recognition for all three cases. Large decreases in total pressure are observed for the subsonic case all of which is numerical in origin. However, all the solutions generated appear to be free of nonphysical extrema. It is concluded, therefore, that the low order method will produce satisfactory "transported-and-diffused" profiles (w^{td}) for the Flux-Corrected Transport algorithm.

The FCT hybrid and high order schemes are both found to produce satisfactory results for all three cases. Although some clipping is evident in the solutions generated by the FCT scheme, it produces sharper shocks (one cell wide at leading edge for the supersonic case) and delineates the details of the complex shock structure downstream of the trailing edge more clearly than the high order scheme. The transonic and subsonic solutions generated by the FCT hybrid and high order schemes are almost identical.

3.2 Planar Shear Layer Calculations

We have shown that the code is capable of resolving flow features associated with Ni's bump. As we are also interested in using the numerical scheme to investigate the fluid mechanics associated with the evolution of shear layers, it is logical to next use the code to examine the phenomenon of the Kelvin-Helmholtz instability found in shear layers. We anticipate encountering this in our subsequent investigation of the three-dimensional flow produced by the lobed mixer. Theoretical analyses of the Kelvin-Helmholtz instability in compressible flowfields abound in the literature. Landau [47] looked at the stability of the compressible shear layer while Blumen *et al* [37,38] present a more detailed analysis in which the transverse velocity variation is represented by a hyperbolic tangent profile. In addition, the literature contains the results of several numerical (from both the Lagrangian [42] and Eulerian [26] perspectives) and experimental [39,40,41] investigations of planar shear layers. These numerical, theoretical and experimental results provide a source of information that can be used for assessing the quality of the planar shear layer results computed by the present numerical scheme.

3.2.1 Timestep-Splitting Calculations

The timestep-splitting LCPFCT-based algorithm is used for the computation of the evolution of a planar shear layer with inflow Mach numbers of $M_{upper} = 0.058$ and $M_{lower} = 0.289$. The grid used for this calculation is shown in Figure 3.39. It is similar to the grid used in Grinstein's [26] calculation which also uses the same inflow Mach numbers. Note that the x- and y-axes are numbered dimensionally (in centimetres) so that results presented herein can be compared directly with the results presented in reference [26]. A section of the splitter plate is included in the computational domain with the trailing edge at 2cm from the inflow boundary and a zero slope condition on the pressure is imposed as explained in Section(2.8.2). These two factors allow the instability, once initiated to be self-sustaining.

The results are shown in Figures 3.40 and 3.41. The passive scalar, ψ, shown in Figure 3.40 represents the mixture-fraction defined as

$$\psi = \frac{N_{lower}}{N_{lower} + N_{upper}} \tag{3.12}$$

where N_{lower} and N_{upper} are the number densities (e.g. $moles/cm^2$) of the material from the lower and upper streams, respectively. Since ψ is a passive scalar that convects with the flow it satisfies

$$\frac{D\psi}{Dt} = \frac{\partial \psi}{\partial t} + \vec{v} \cdot \nabla \psi = 0 \tag{3.13}$$

The shear layer has to be forced with disturbance of an appropriate frequency for the instability to be initiated and sustained. However for the case being computed here, none was required; this is the result of the fact that the disturbance that triggers the Kelvin-Helmholtz instability arises through the following mechanism. The initial condition for the calculation imposes a jump in velocity that occurs over two cells on either side of the middle of the channel. This is the closest possible discrete approximation to a discontinuity. Subsequent to the initiation of the computation, the fluid leaving the trailing edge of the splitter plate suddenly finds itself adjacent to a stream moving at a different speed so that it is subjected to a shearing stress produced by the presence of (albeit small) numerical dissipation (present in the LCPFCT scheme even after the antidiffusion step). This causes the fluid in the faster stream to slow down and the fluid in the slower stream to speed up. For cells far downstream of the tip of the splitter plate, no variation develops in the streamwise direction because the change in convective velocity at the right face is matched by an equal change at the left face. However, at the cell immediately upstream of the tip, the convective velocity does not change because it is still adjacent to the splitter plate wall, while one cell downstream, the convective velocity has changed. Therefore the convective velocity at the common face is not matched by an equal velocity at the opposite face for both cells. This imbalance in cell face convective velocities causes a deficit in the slower stream - and a surplus in the faster stream - of conserved quantities (mass,momentum,energy) in those cells immediately upstream of

the trailing edge. Since no Kutta condition is enforced, this allows the trailing edge of the splitter plate to become slightly loaded. A small vertical component of velocity at the trailing edge results, so that the velocity is not tangential at the trailing edge. It is this disturbance that is responsible for the initiation of shear layer instability. This instability is self-sustaining since the small loading at the trailing edge is allowed to fluctuate by virtue of the imposed inflow boundary condition on pressure.

For an inviscid, incompressible, planar flowfield, vorticity satisfies the convective equation.

$$\frac{D\omega}{Dt} = \frac{\partial \omega}{\partial t} + \vec{v} \cdot \nabla \omega = 0 \tag{3.14}$$

Therefore, for incompressible flow, lines of constant vorticity should coincide with lines of constant ψ. A glance at the results presented in Figures 3.40-3.41 show that this not the case. However, especially in the rolled-up structures that are formed from the initially vortex sheet, maxima and minima in vorticity are always located very close to corresponding maxima and minima in ψ. The local deviation is explained by the fact that vorticity is not one of the conserved variables and is therefore not subjected to flux-correction whereas ψ is and so nonphysical maxima and minima are more likely to arise in ω than in ψ.

Blumen *et al* provide a means for making a theoretical prediction of the axial exponential growth rate for the linear stages of the instability of a compressible, inviscid, planar shear layer. For a convective Mach number, $M_c = 0.1155$, where

$$M_c = \frac{M_{lower} - M_{upper}}{2} \tag{3.15}$$

(for equal sound speeds), they predict that the temporal growth rate corresponding to the most unstable wavelength, $\alpha = 0.432$, is

$$\alpha c_i = 0.186 \tag{3.16}$$

where c_i is the imaginary part of the complex phase velocity. Hence the theoretical prediction for

the temporal growth rate is

$$\eta = \hat{\eta} e^{c_i \alpha t^*} = \hat{\eta} e^{0.186 t^*} \tag{3.17}$$

where t^* is a nondimensional time given by $t^* = Vt/L$ and L and V are a length scale and a velocity scale "characteristic of the transverse variation of the basic current" $V(y)$. Hence L for this problem is the cell height at the vortex sheet and V is the velocity difference between the upper and lower streams. This can be transformed to an expression for the axial growth rate if we assume that the structures are convected with the mean velocity $\bar{V}$ such that $x = \bar{V}t$ to give

$$\begin{aligned} \log \eta - \log \hat{\eta} &= \frac{\alpha c_i V}{\bar{V} L} x \\ &= 308.5x \end{aligned} \tag{3.18}$$

An approximate estimate of the growth rate for the early linear stages of the instability was made, wherby individual vortices were tracked and the associated deflections η were measured from the ψ contour plot. From a graph of $\log \eta$ versus axial distance , x, an average slope (corresponding to their axial exponential growth rates) can be estimated from the evolution of three vortical structures. Its estimated value is

$$\bar{m} = (\frac{\alpha c_i V}{\bar{V} L})_{numerical} = \frac{143.9 + 194.9 + 169.3}{3} = 169.4 \tag{3.19}$$

It can be seen that this result is a factor of 2 smaller than the growth rate predicted by Blumen in Equation 3.18. Although this may seem like a large deviation, consideration should be made of factors that contribute to the discrepancy. These include the fact that Blumen's most amplified wavelength is not the most amplified wavelength observed numerically and the fact that the residual dissipation left by the LCPFCT algorithm would be expected to reduce the growth rate.

Comparison of Figures 3.40- 3.41 with results in the literature, particularly [26], reveals that the results concur qualitatively. Quantitatively, the details of the flow structures differ from those found in [26] because of differences in numerical algorithm, grid and initial conditions. The features of the flow can also depend on the details of initiation of the instability.

Figure 3.42 shows the results of a supersonic planar shear layer calculation performed by LCPFCT on a uniform 400x80 grid. The inflow Mach numbers are $M_{lower} = 2.0$ and $M_{upper} = 1.2$. The Kelvin-Helmholtz instability is still observed to occur although the growth rate is much smaller, as predicted by the compressible stability analyses in references [47,37,38]

3.2.2 Finite Volume Calculations

The grid used for this calculation is the same as that used in subsonic calculation in Section(3.2.1). Likewise, the inflow Mach numbers are taken to be the same. The limiter used was a combination of Zalesak's multidimensional limiter and the Boris-Book limiter as defined in Equation 2.36. The Boris-Book limiter corrects the antidiffusive fluxes in each coordinate direction prior to their being passed to the Zalesak limiter. As can be seen from the results shown in Figures 3.43- 3.44, no instability evolved. This is because of the nondissipative nature of the Leapfrog-Trapezoidal method used as the high order scheme. The leapfrog-trapezoidal method returns antidiffusive fluxes that regenerate the original step profile from the "transported-and-diffused" solution after flux-correction.

3.2.3 Summary of Two-dimensional Shear Layer Calculations

The use of timestep-splitting with LCPFCT produces plausible results without forcing for the subsonic and supersonic two-dimensional shear layers. Qualitative agreement with results quoted in the literature is found. The initiation of the instability without forcing was traced to a mechanism dependent on residual diffusion from the diffusion/antidiffusion process in the numerical scheme.

With no forcing, the solution generated by FVFCT exhibits no instability. This is because the residual diffusion mechanism in the diffusion/antidiffusion process found in LCPFCT is not present in FVFCT.

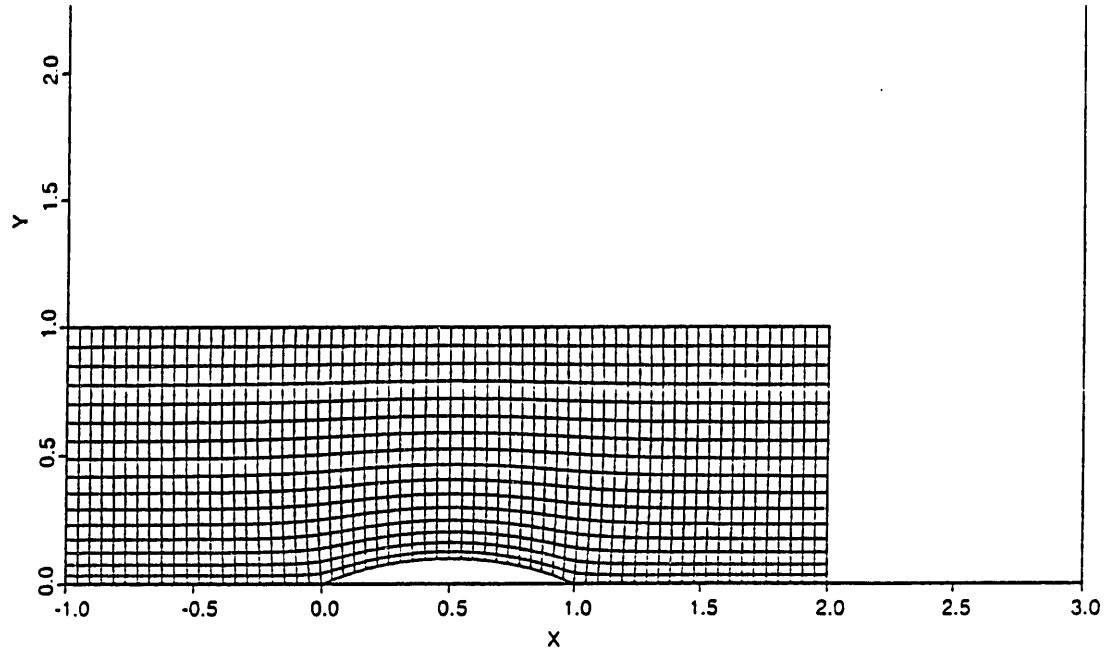

Figure 3.1: Grid with 10% thickness circular arc bump used for subsonic calculation

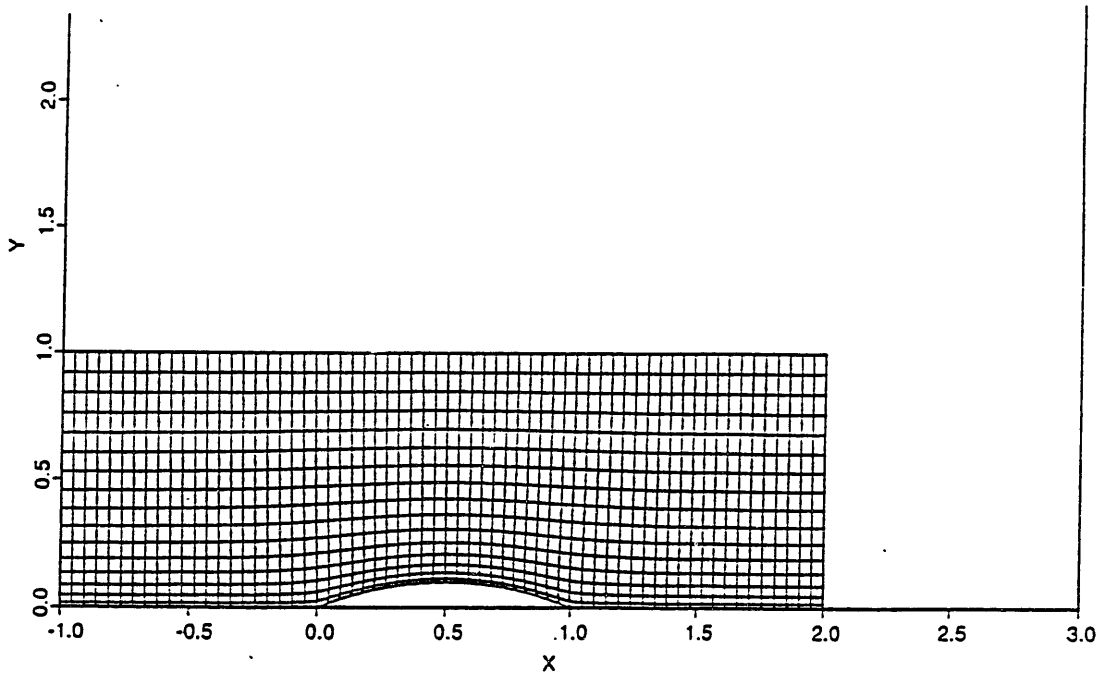

Figure 3.2: Grid with 10% thickness circular arc bump used for transonic calculation

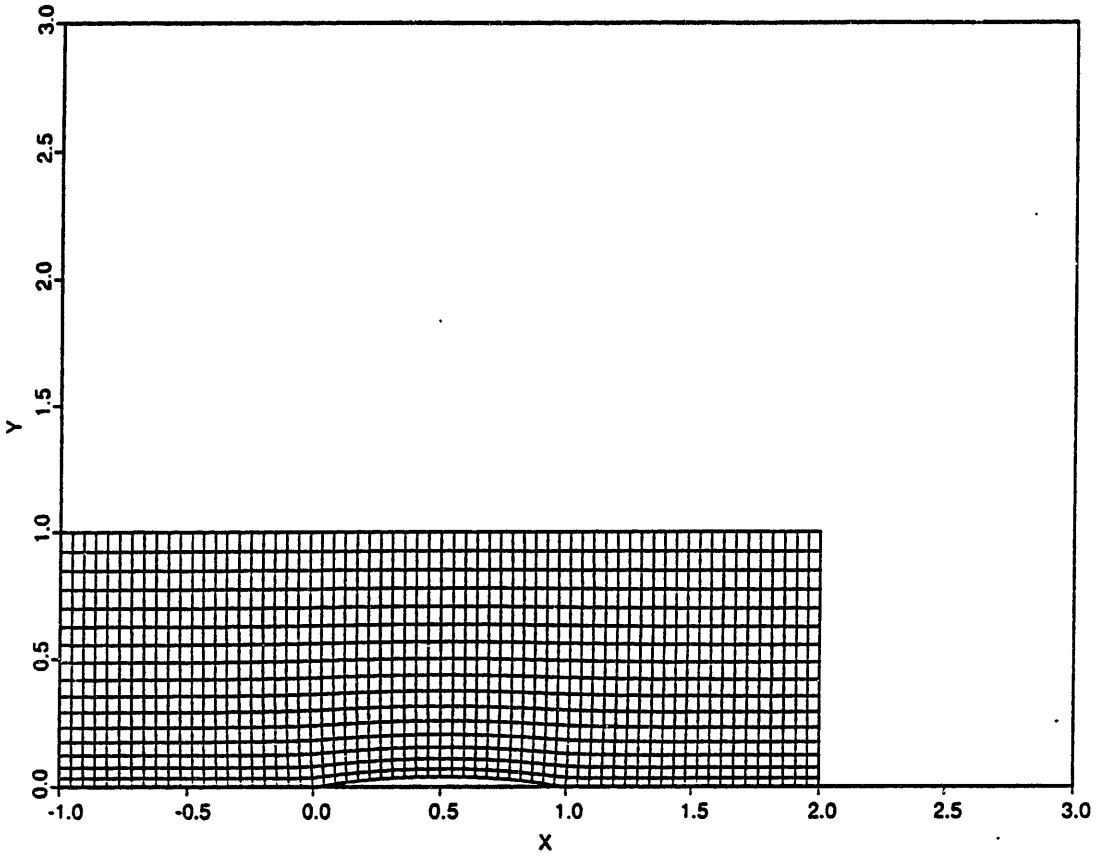

Figure 3.3: Grid with 4% thickness circular arc channel used for supersonic calculation

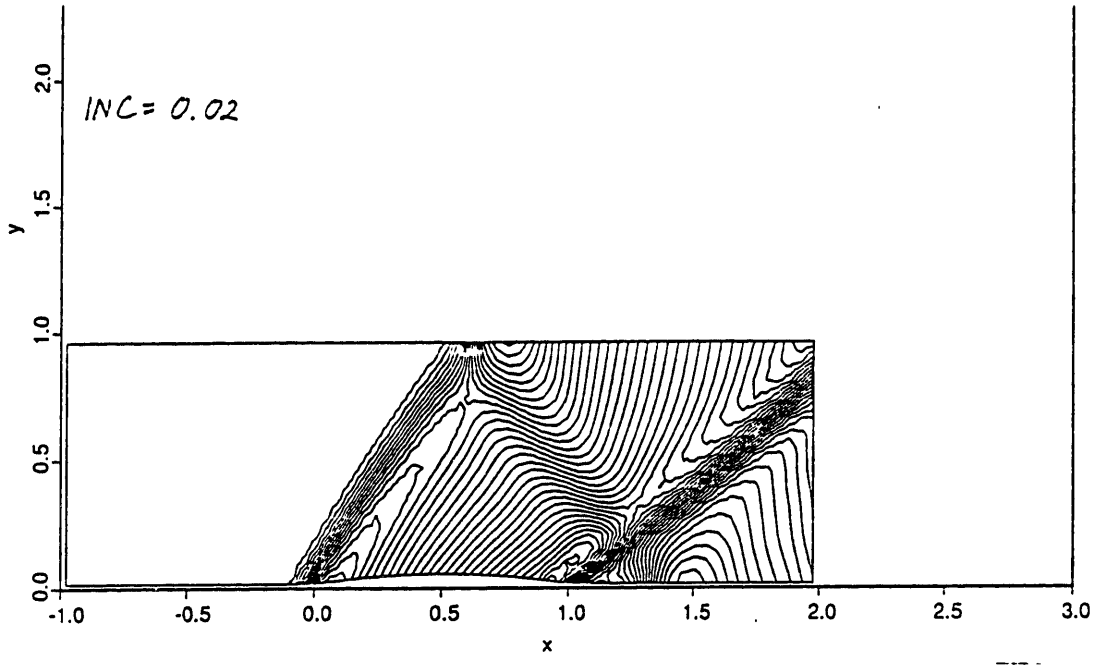

Figure 3.4: Isomach contours for supersonic calculation by High Order Scheme

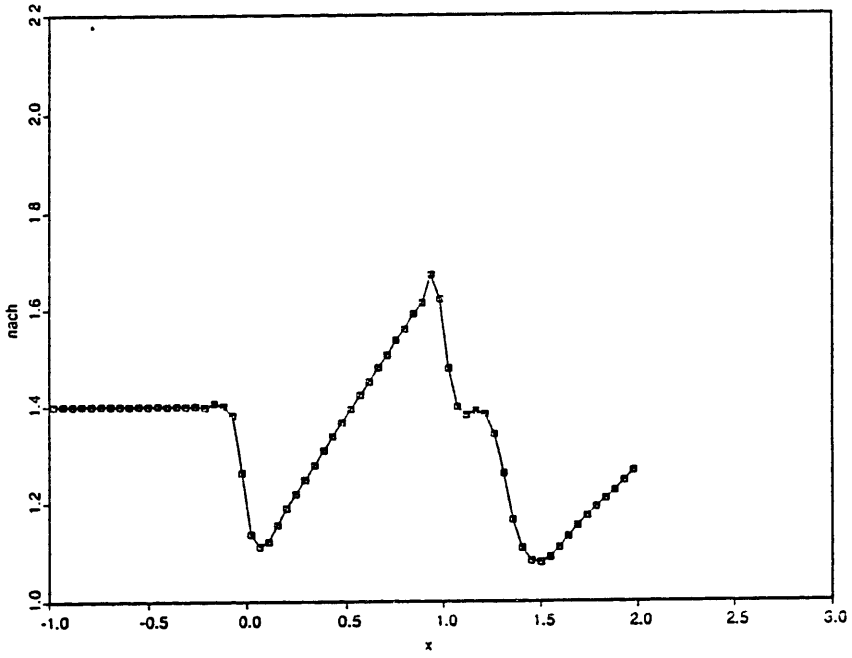

Figure 3.5: Mach Number Distribution along the lower wall as calculated by the High Order Scheme for supersonic inflow

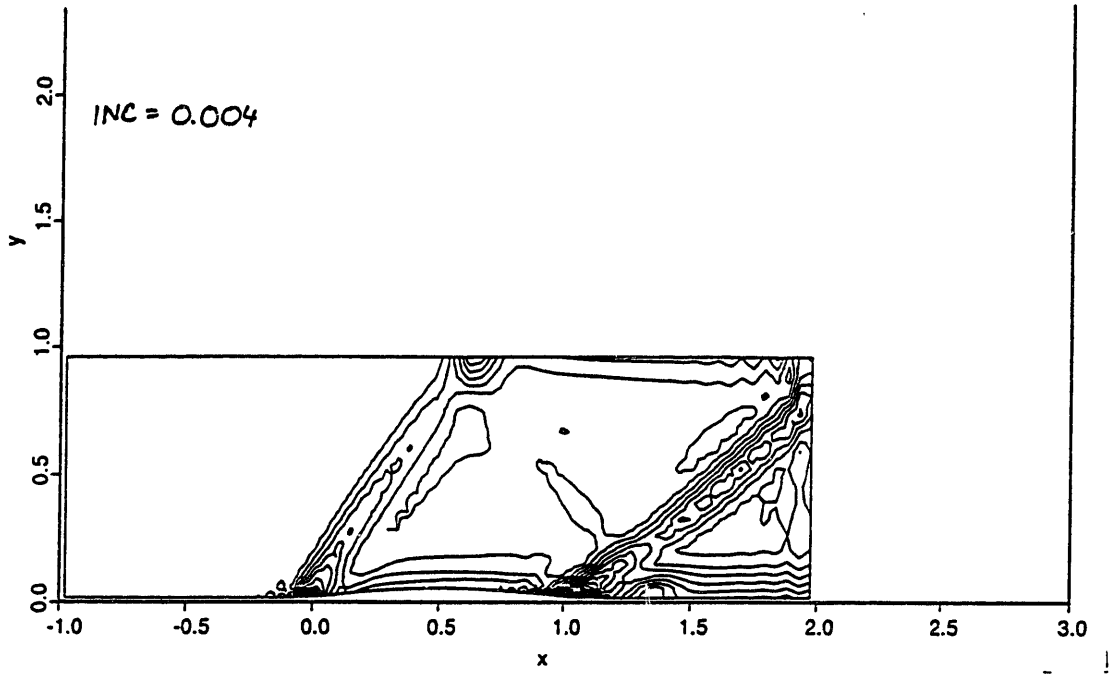

Figure 3.6: Total pressure contours for supersonic calculation by High Order Scheme

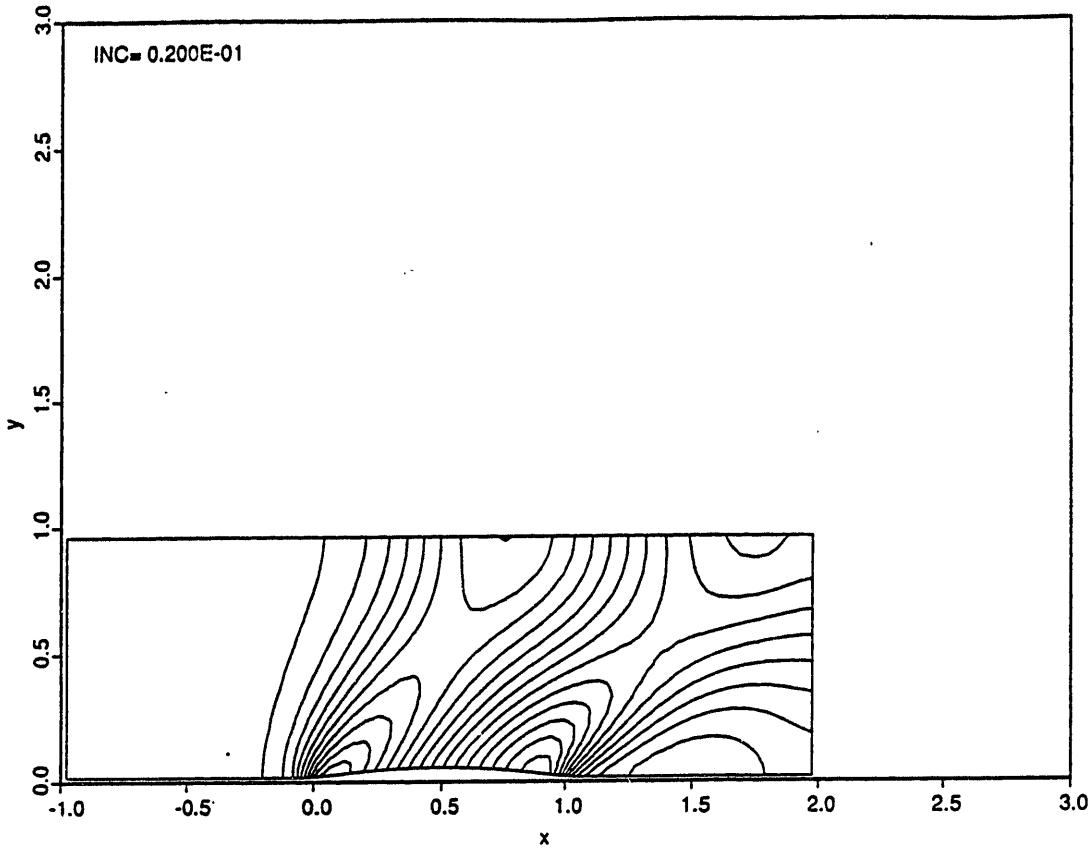

Figure 3.7: Isomach contours for supersonic calculation by Low Order Scheme

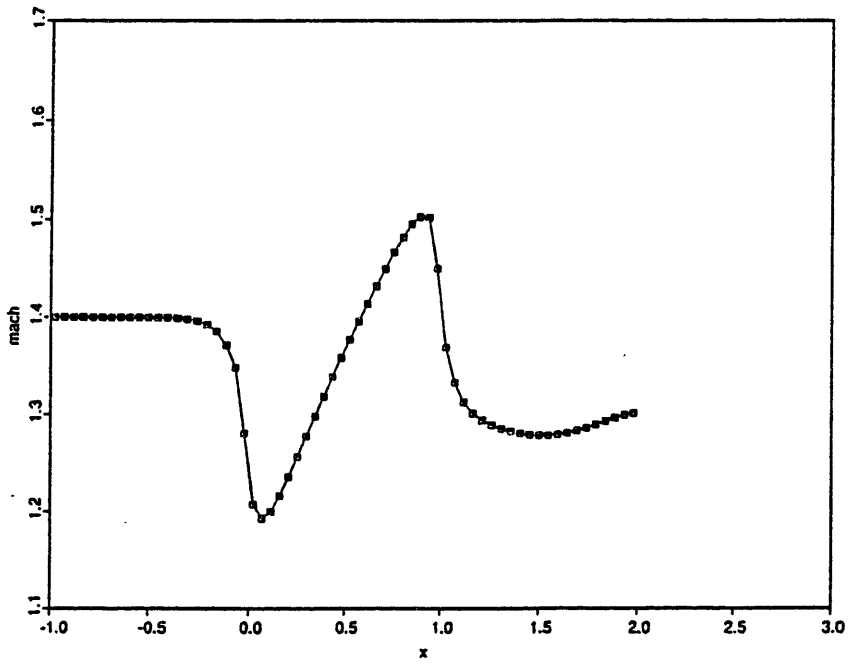

Figure 3.8: Mach Number Distribution along the lower wall as calculated by the Low Order Scheme for supersonic inflow

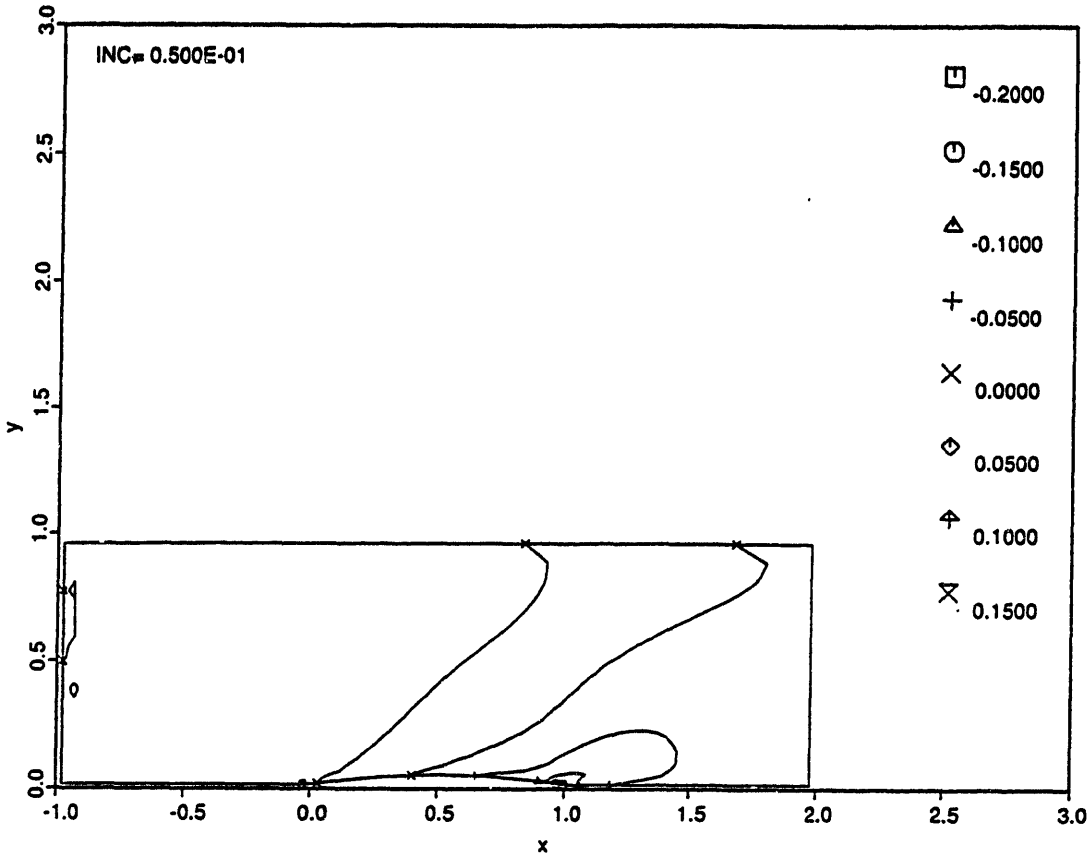

Figure 3.9: Total pressure contours for supersonic calculation by Low Order Scheme

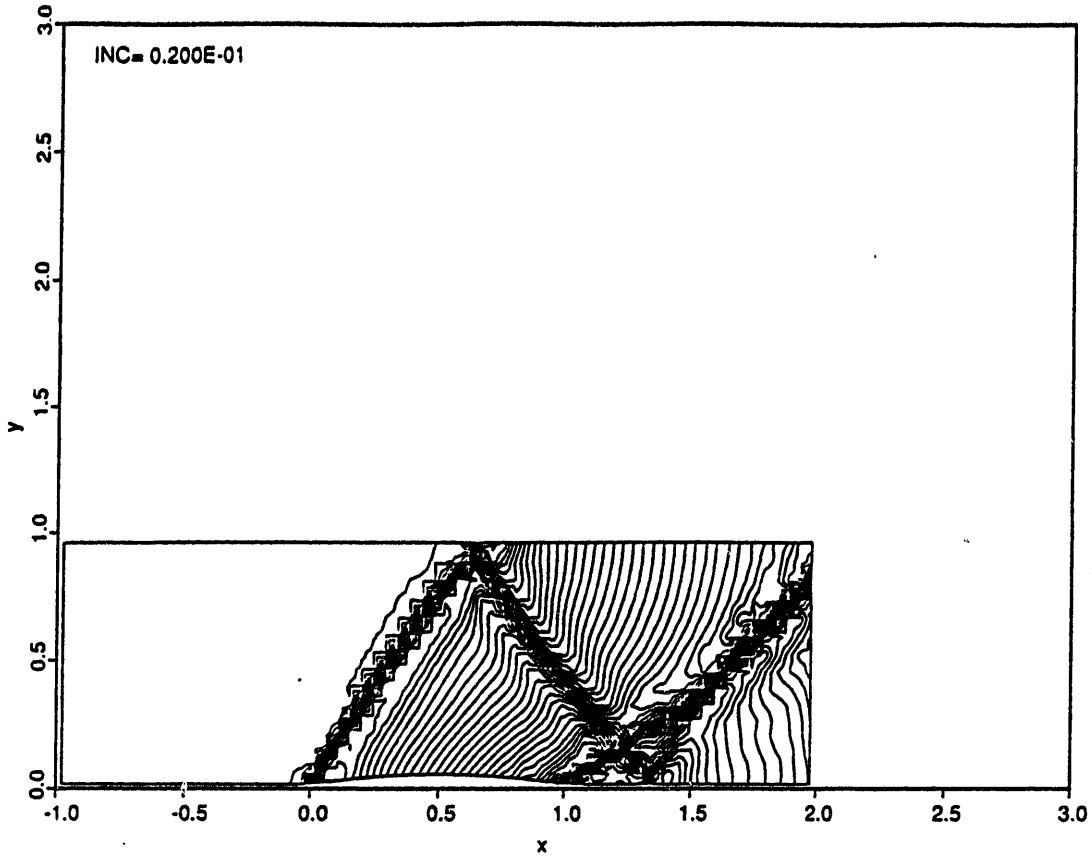

Figure 3.10: Isomach contours for supersonic calculation by FCT Scheme

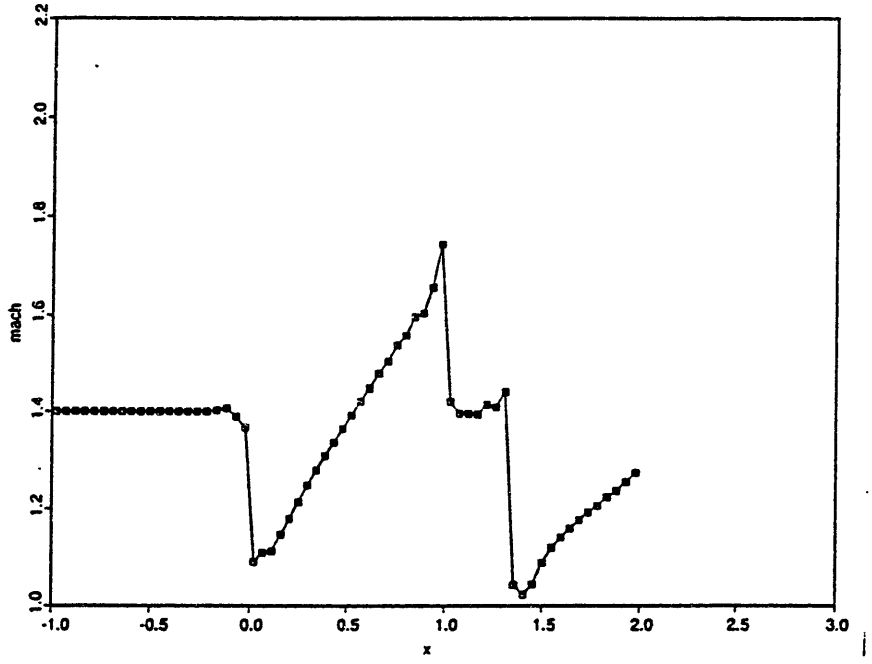

Figure 3.11: Mach Number Distribution along the lower wall as calculated by the FCT Scheme for supersonic inflow

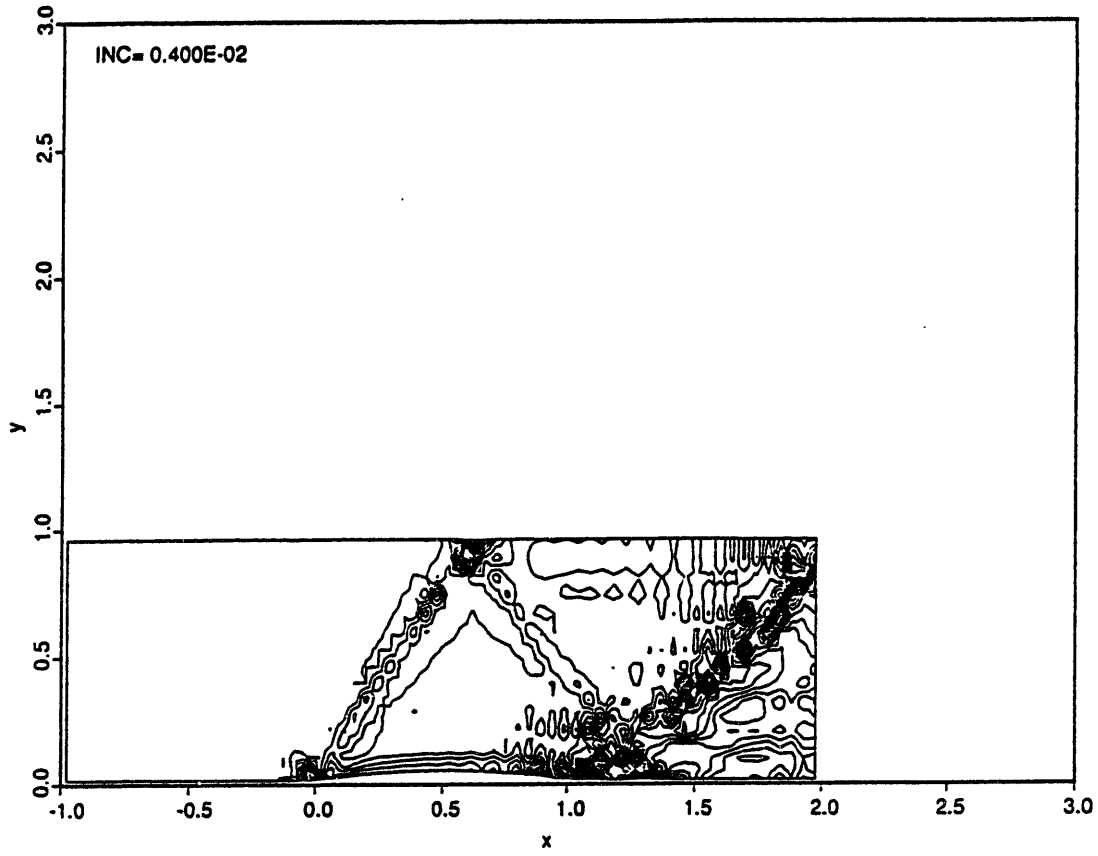

Figure 3.12: Total pressure contours for supersonic calculation by FCT Scheme

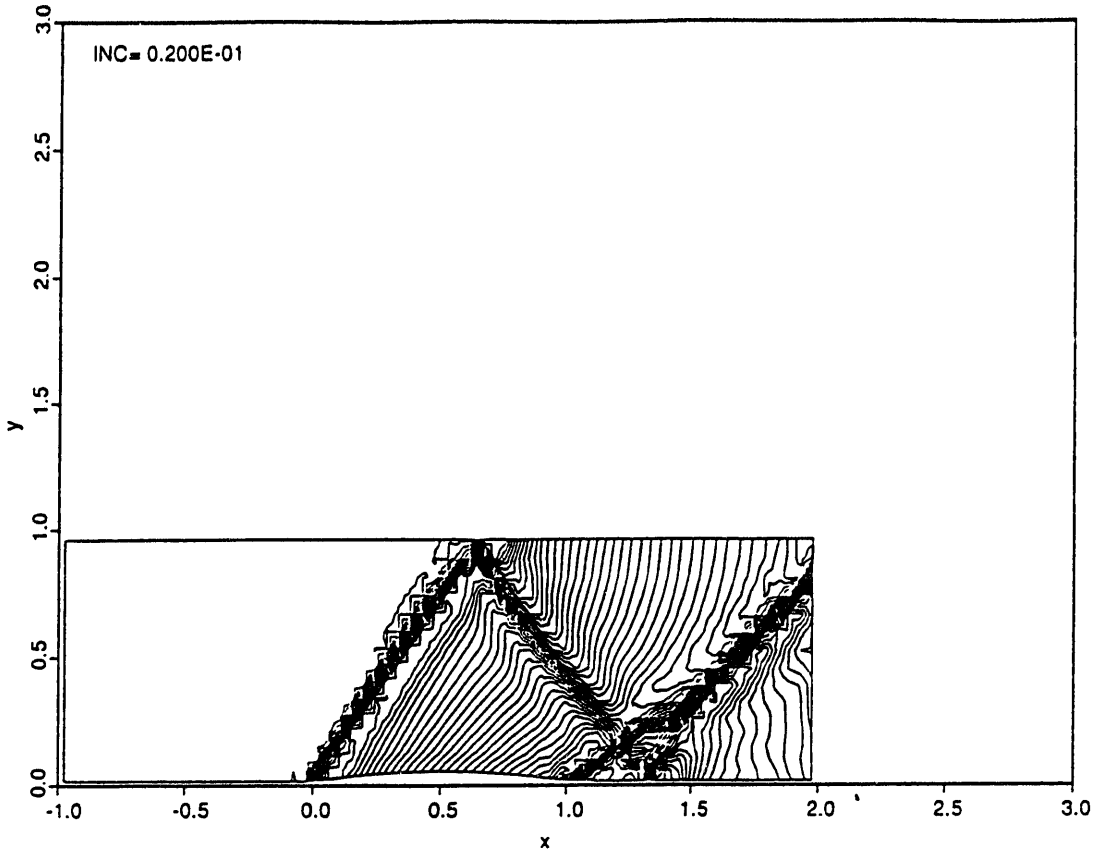

Figure 3.13: Density contours for supersonic calculation by FCT Scheme

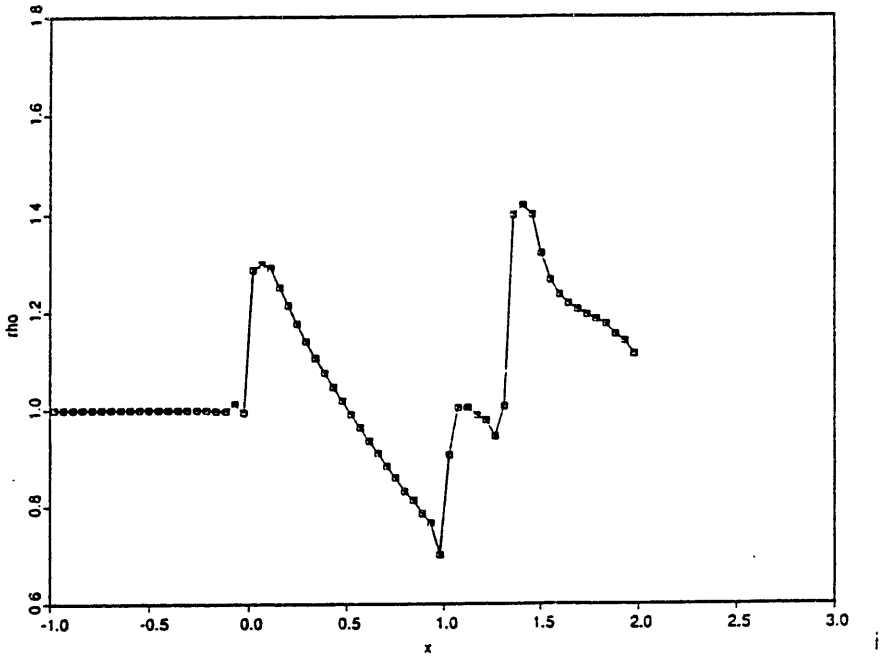

Figure 3.14: Density Distribution along the lower wall as calculated by the FCT Scheme for supersonic inflow

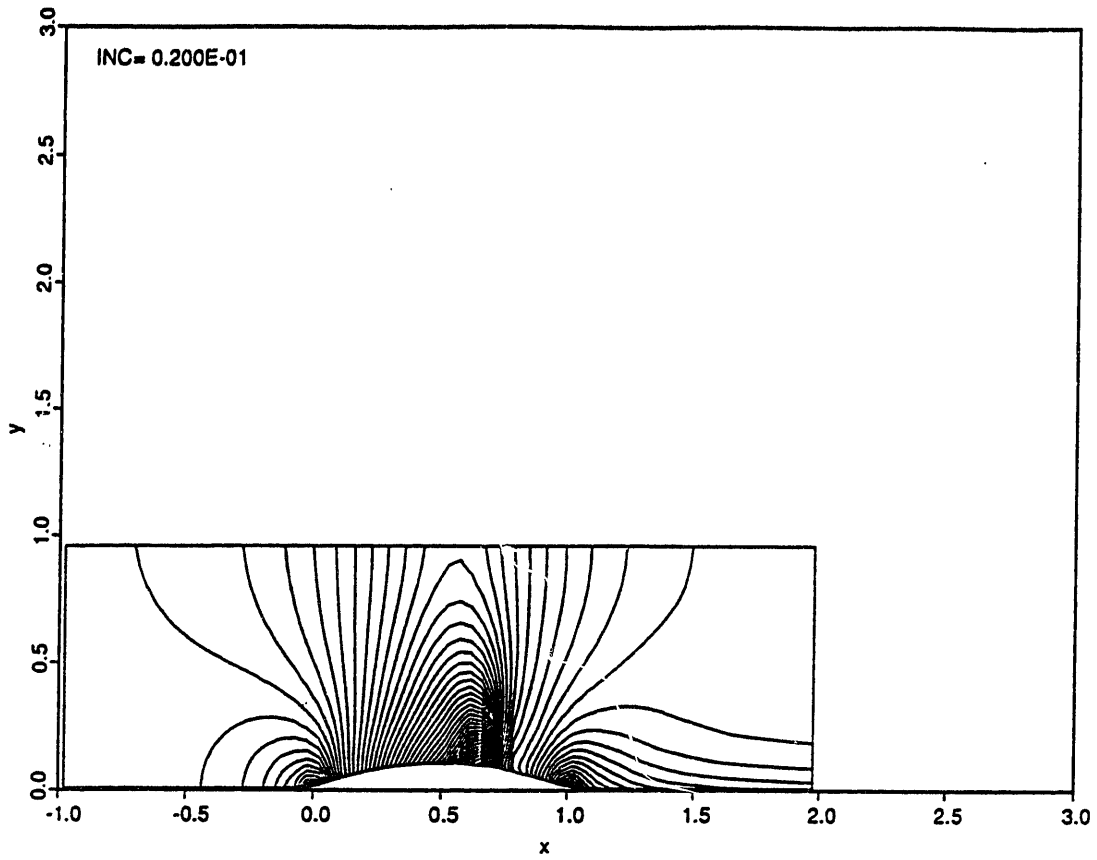

Figure 3.15: Isomach contours for transonic calculation by High Order Scheme

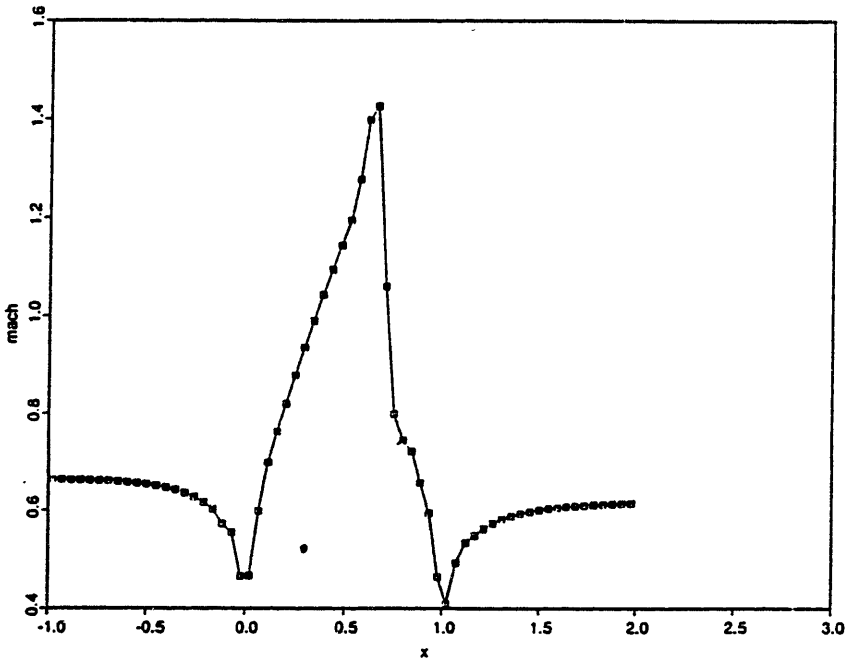

Figure 3.16: Mach Number Distribution along the lower wall as calculated by the High Order Scheme for transonic inflow

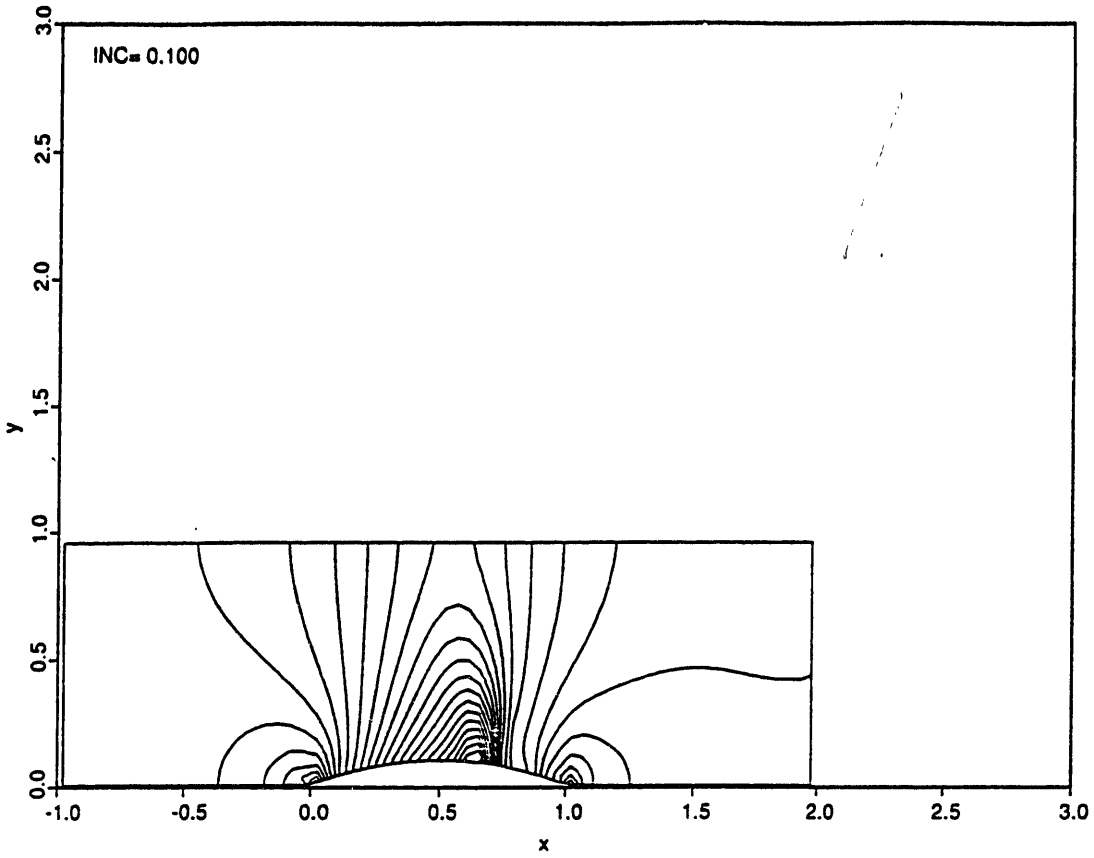

Figure 3.17: c_p contours for transonic calculation by High Order Scheme

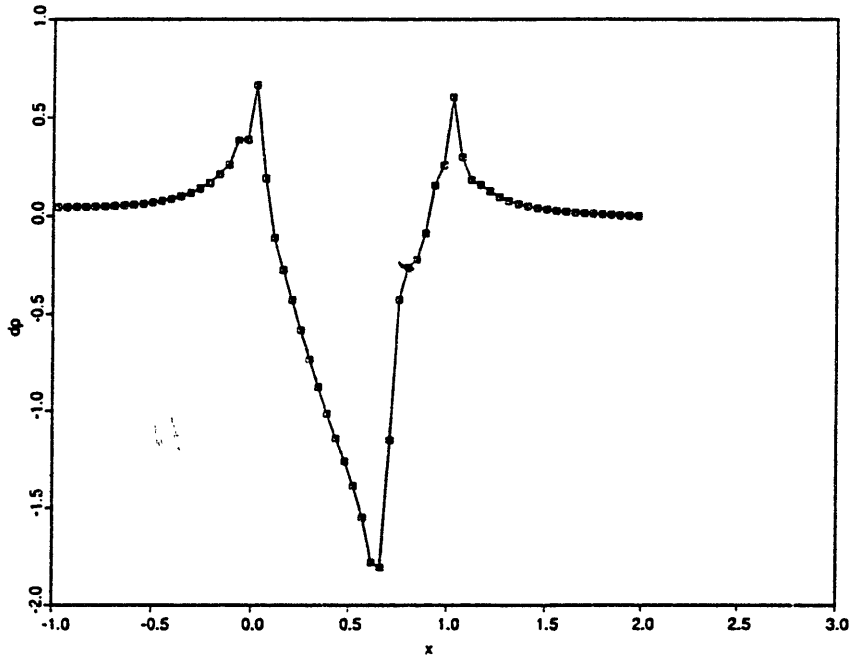

Figure 3.18: c_p distribution along the lower wall as calculated by the High Order Scheme for transonic inflow

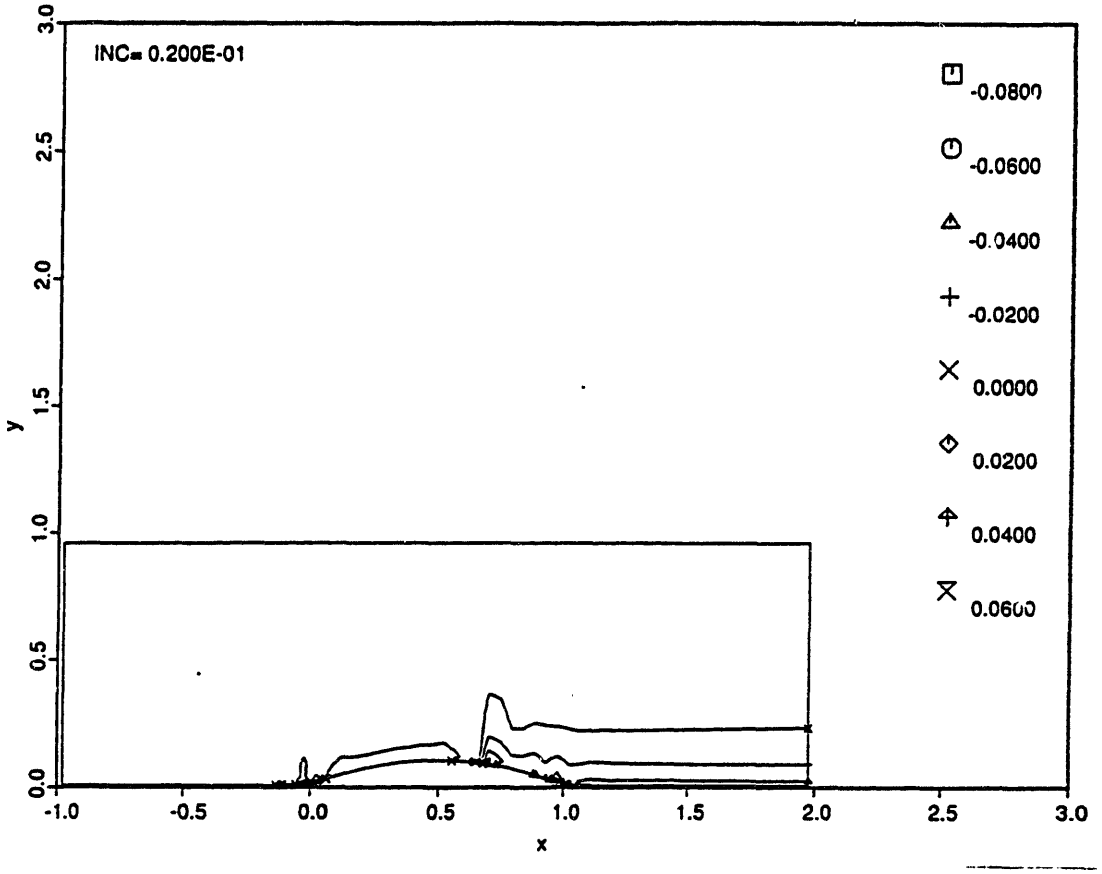

Figure 3.19: Total pressure contours for transonic calculation by High Order Scheme

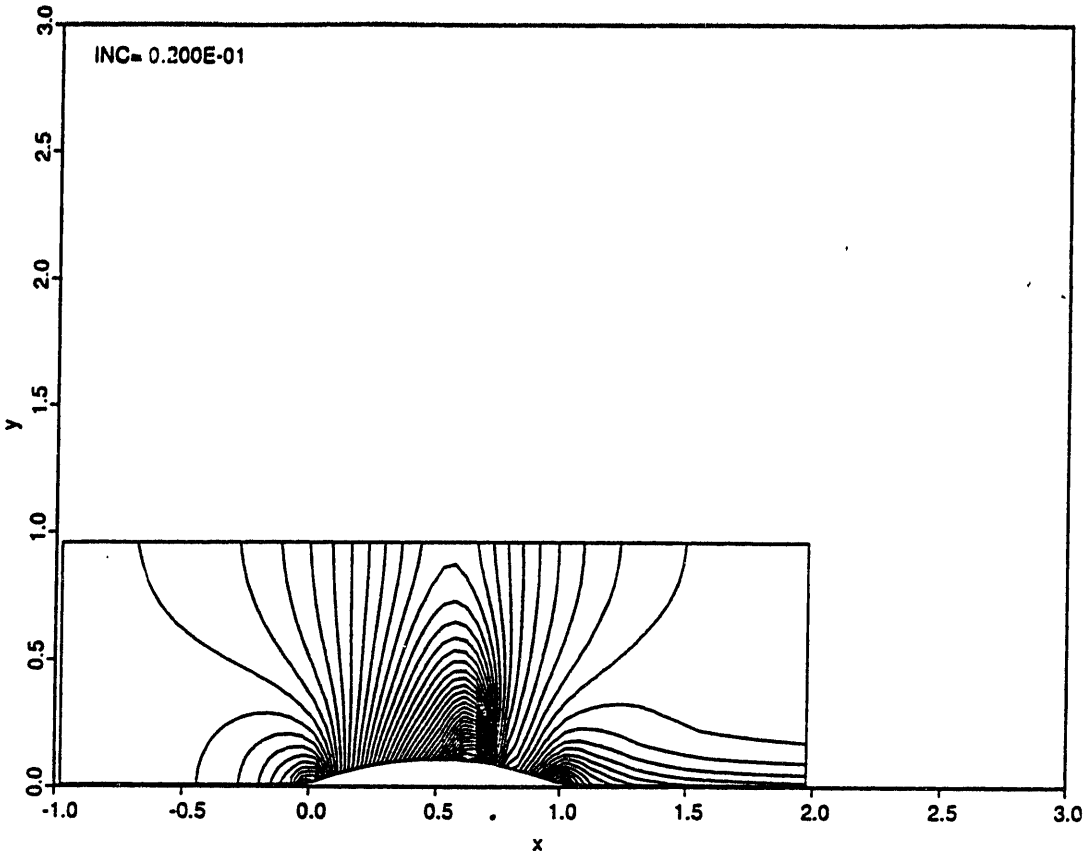

Figure 3.20: Isomach contours for transonic calculation by FCT Scheme

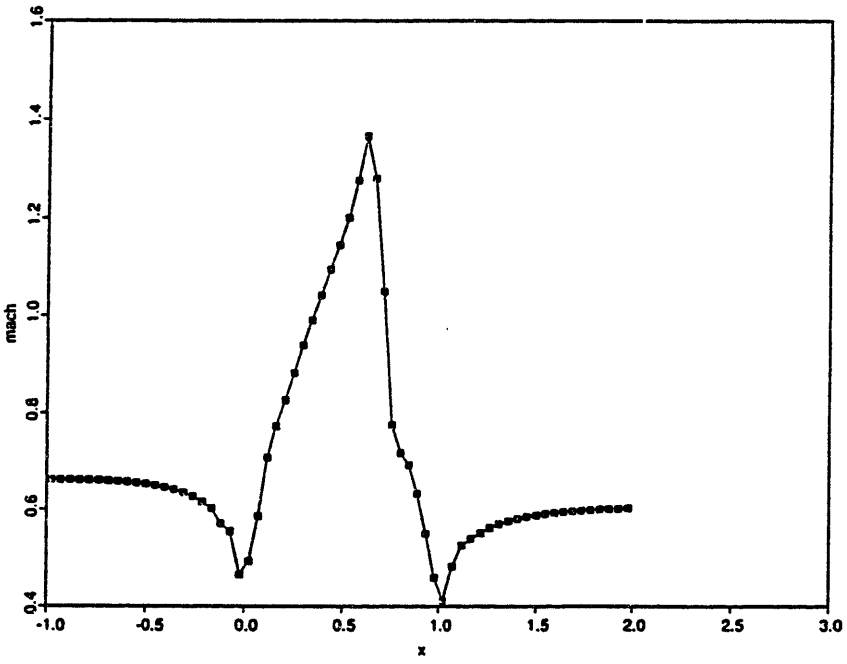

Figure 3.21: Mach Number Distribution along the lower wall as calculated by the FCT Scheme for transonic inflow

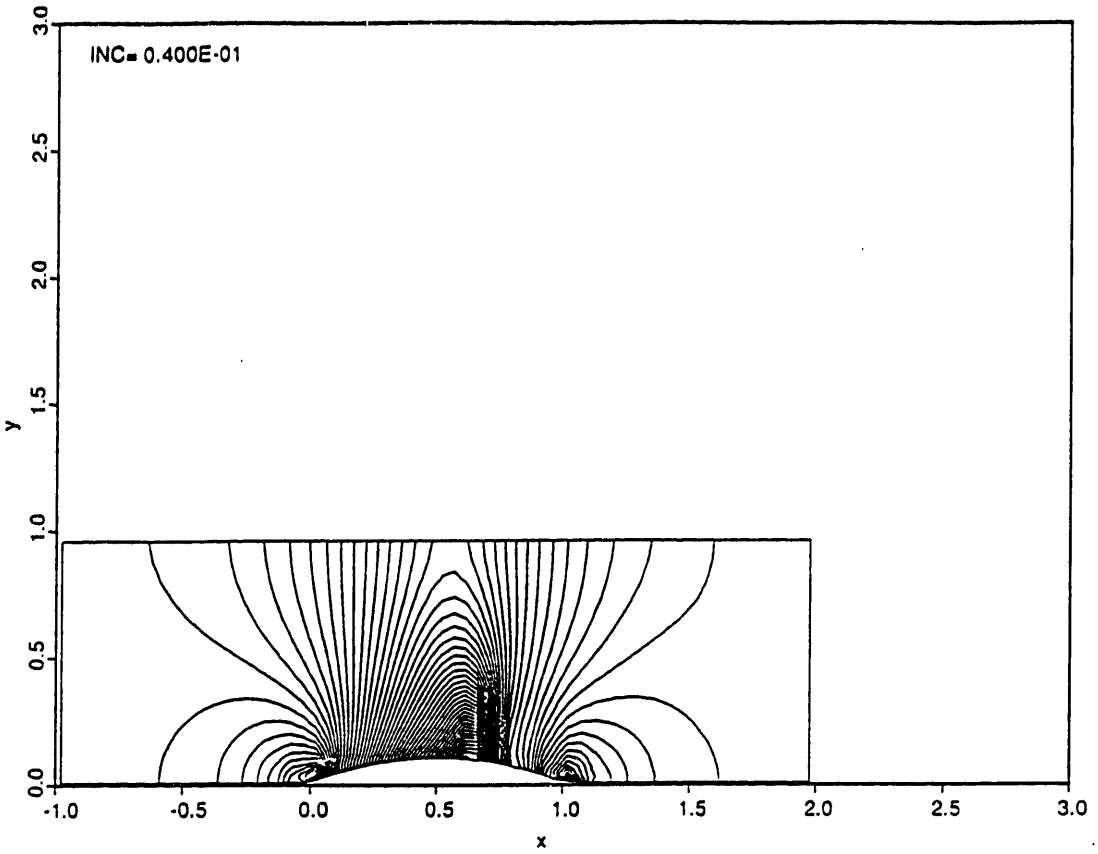

Figure 3.22: c_p contours for transonic calculation by FCT Scheme

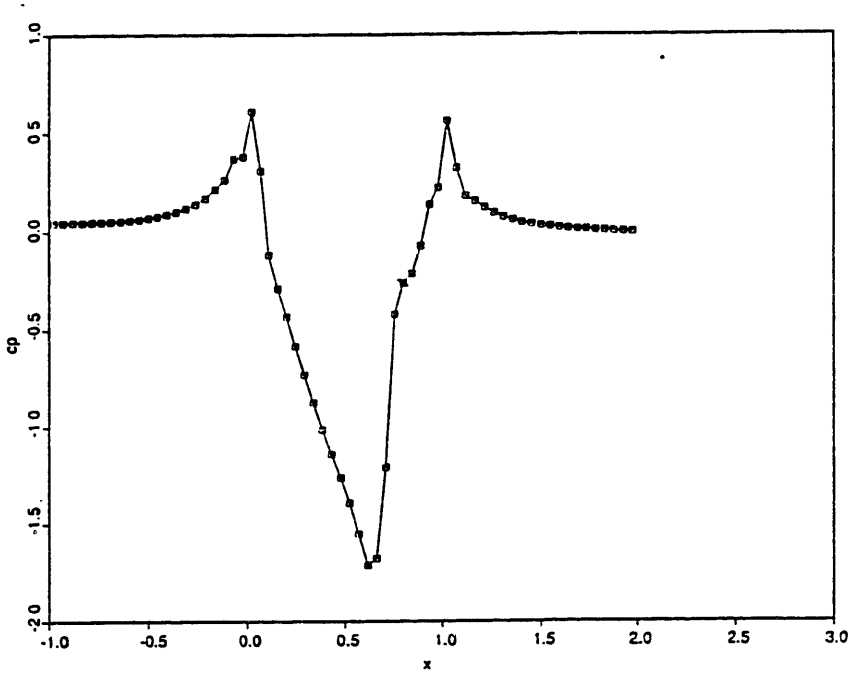

Figure 3.23: c_p distribution along the lower wall as calculated by the FCT Scheme for transonic inflow

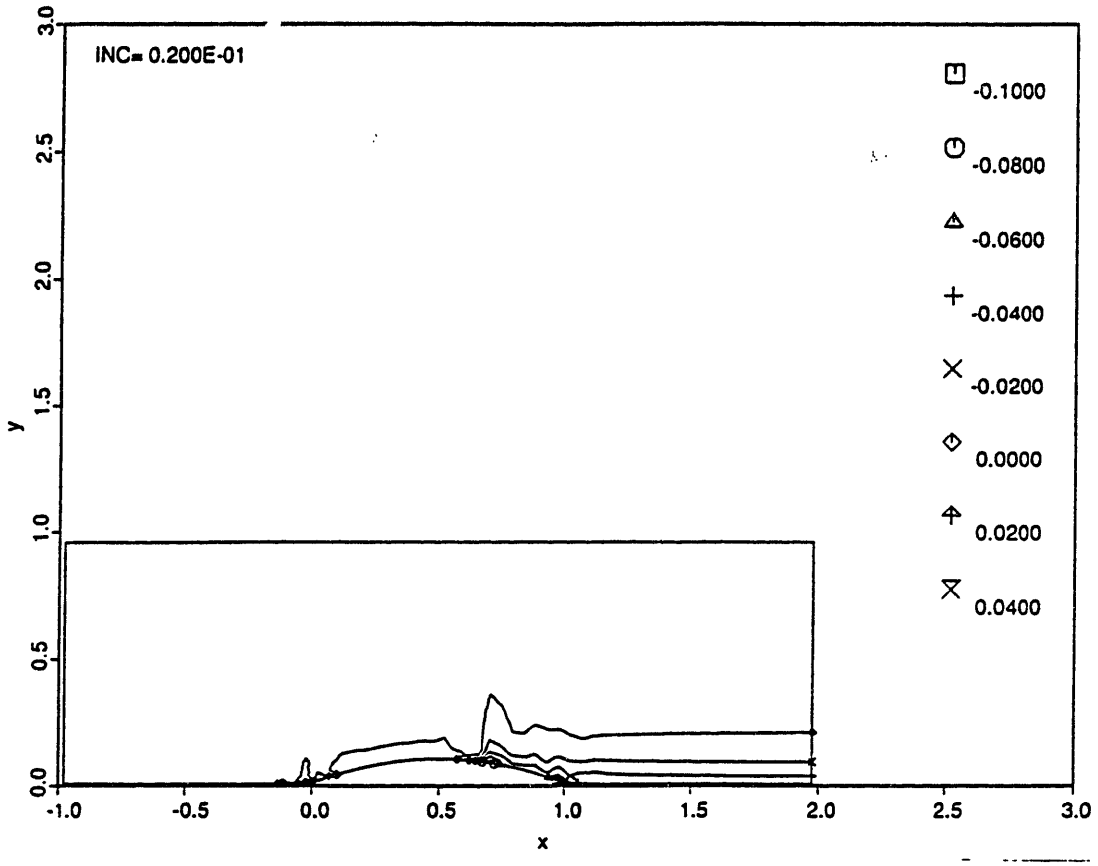

Figure 3.24: Total pressure contours for transonic calculation by FCT Scheme

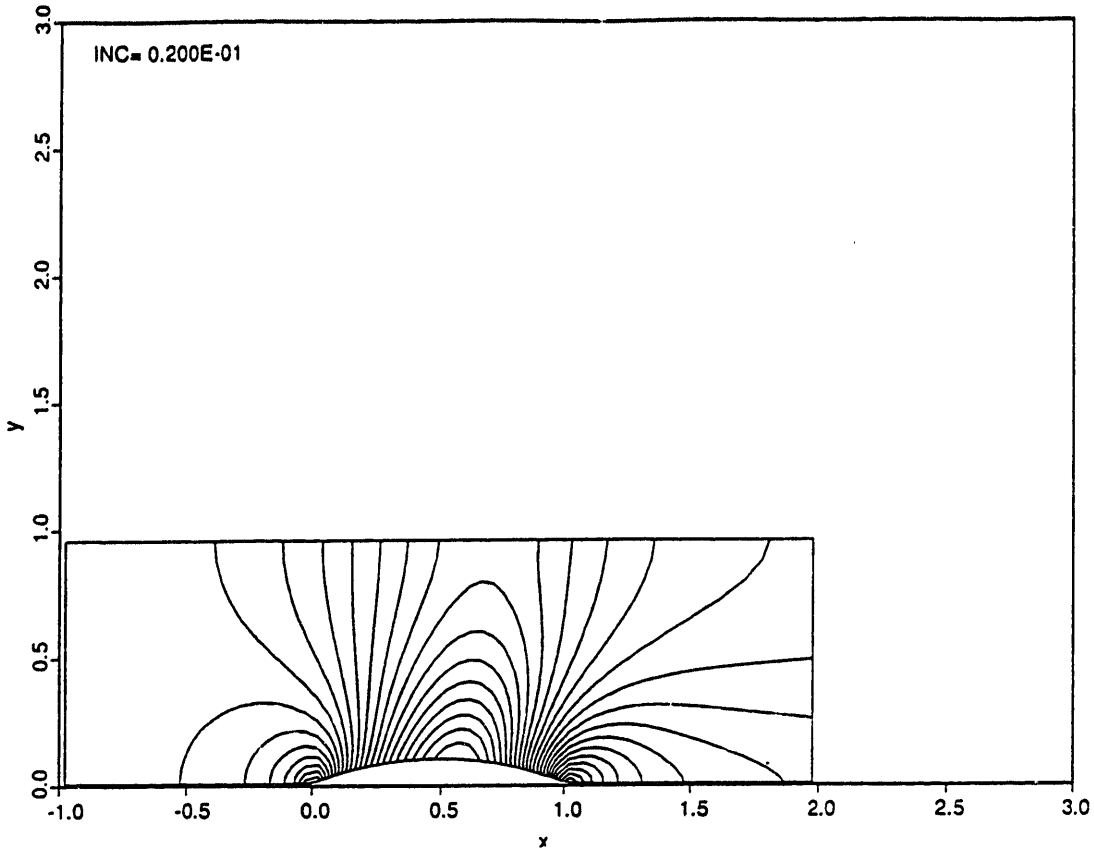

Figure 3.25: Isomach contours for transonic calculation by Low Order Scheme

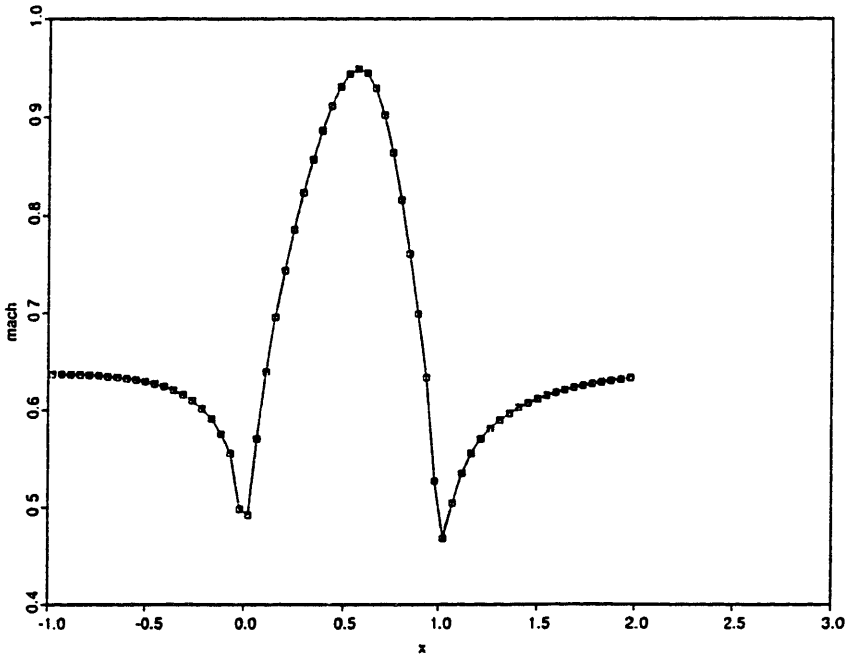

Figure 3.26: Mach Number Distribution along the lower wall as calculated by the Low Order Scheme for transonic inflow

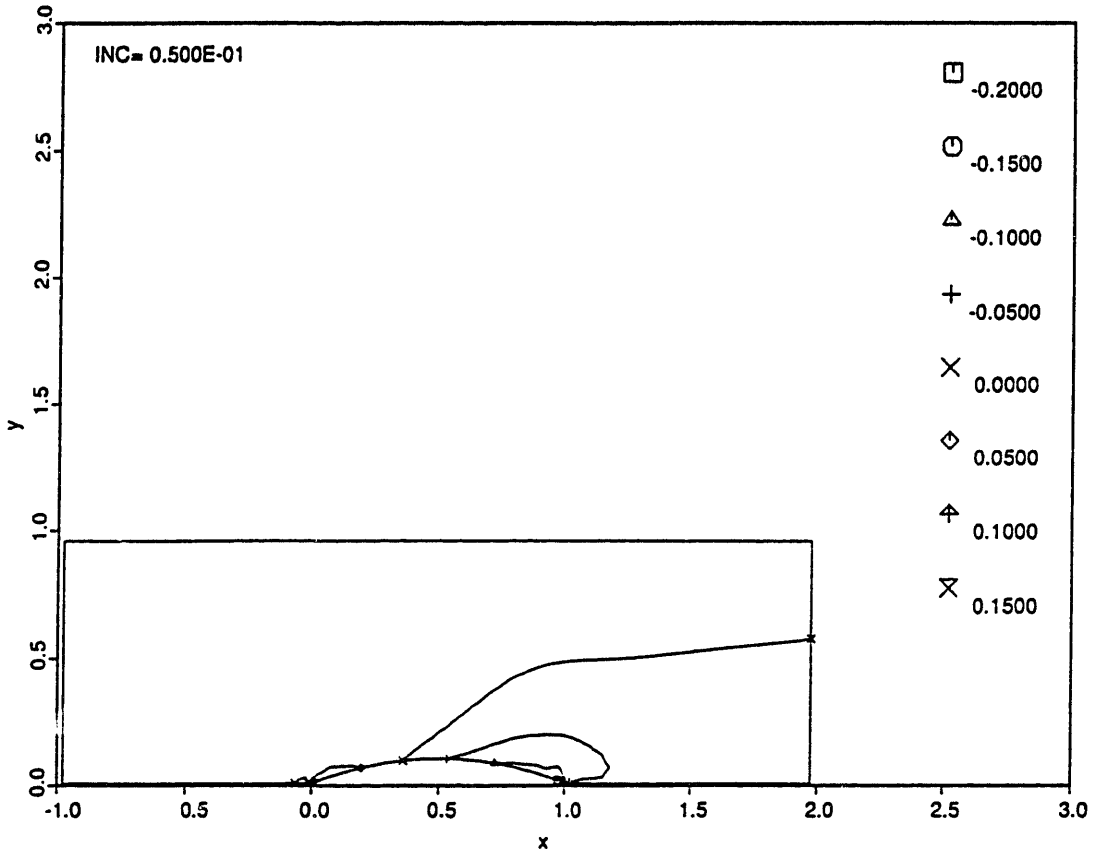

Figure 3.27: Total pressure contours for transonic calculation by Low Order Scheme

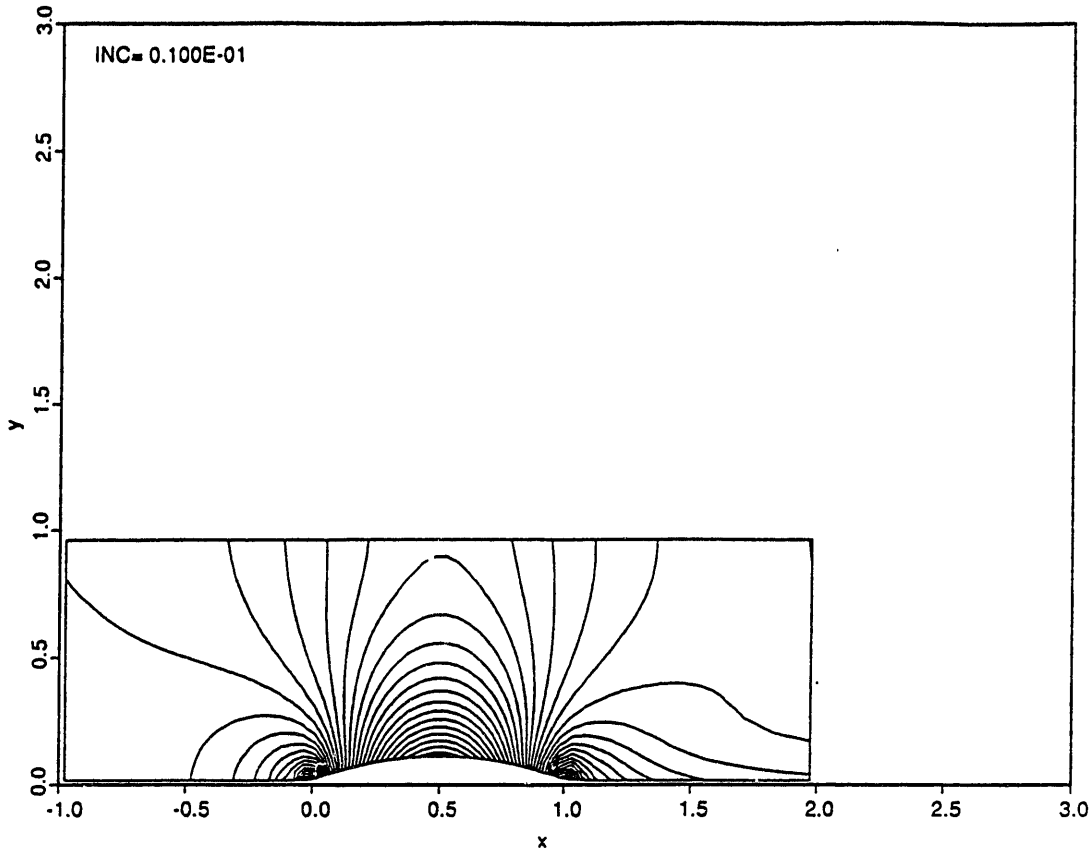

Figure 3.28: Isomach contours for subsonic calculation by High Order Scheme

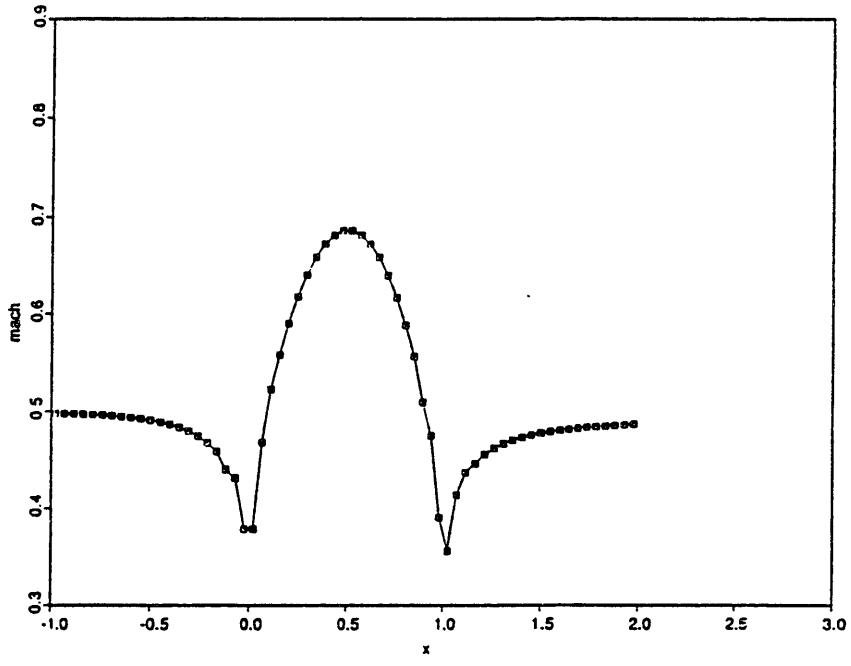

Figure 3.29: Mach Number Distribution along the lower wall as calculated by the High Order Scheme for subsonic inflow

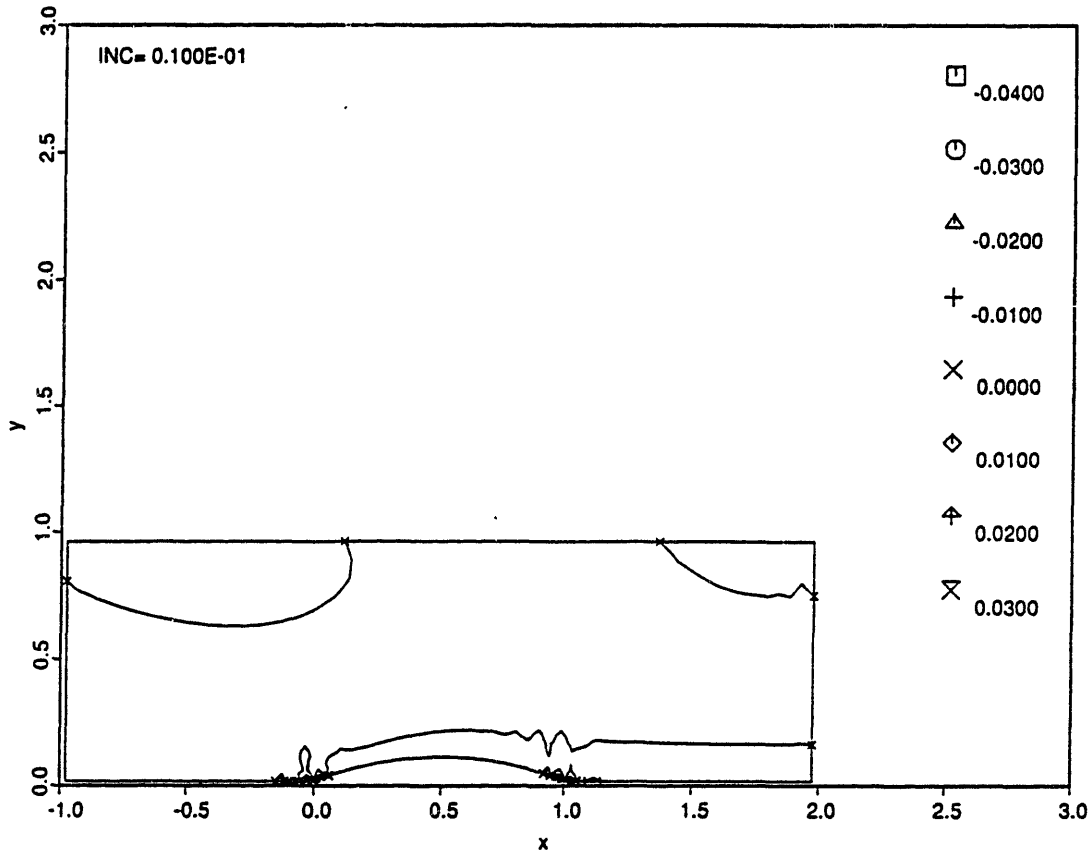

Figure 3.30: Total pressure contours for subsonic calculation by High Order Scheme

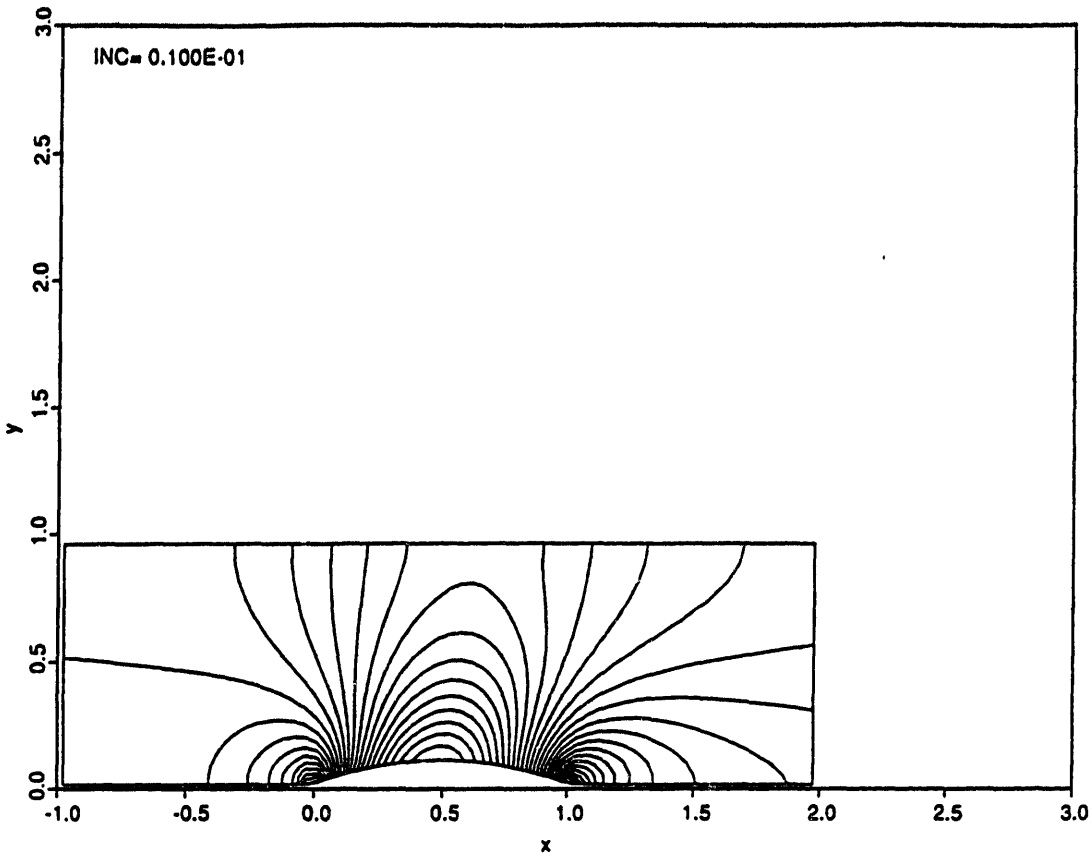

Figure 3.31: Isomach contours for subsonic calculation by Low Order Scheme

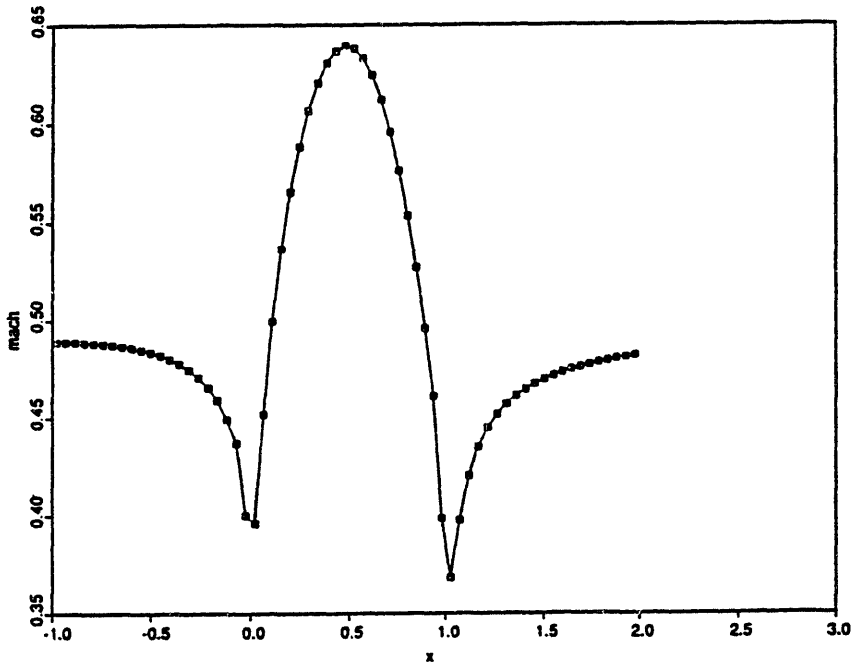

Figure 3.32: Mach Number Distribution along the lower wall as calculated by the Low Order Scheme for subsonic inflow

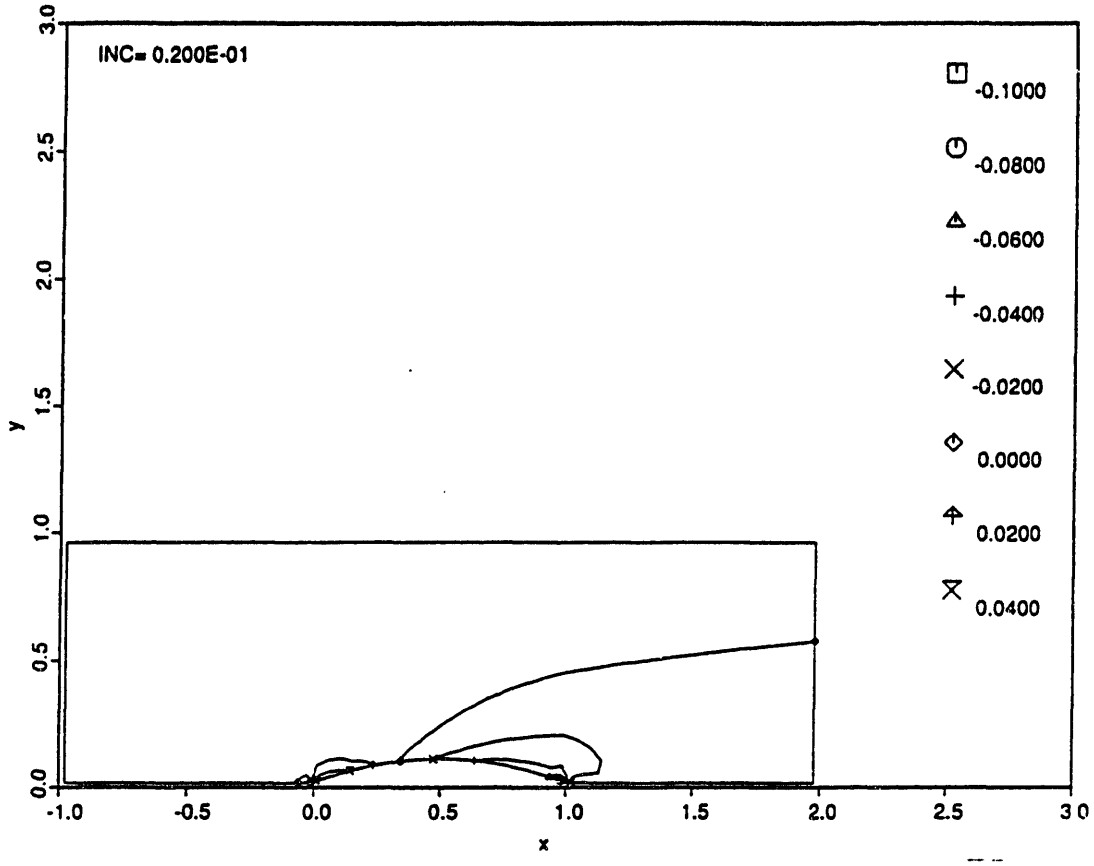

Figure 3.33: Total pressure contours for subsonic calculation by Low Order Scheme

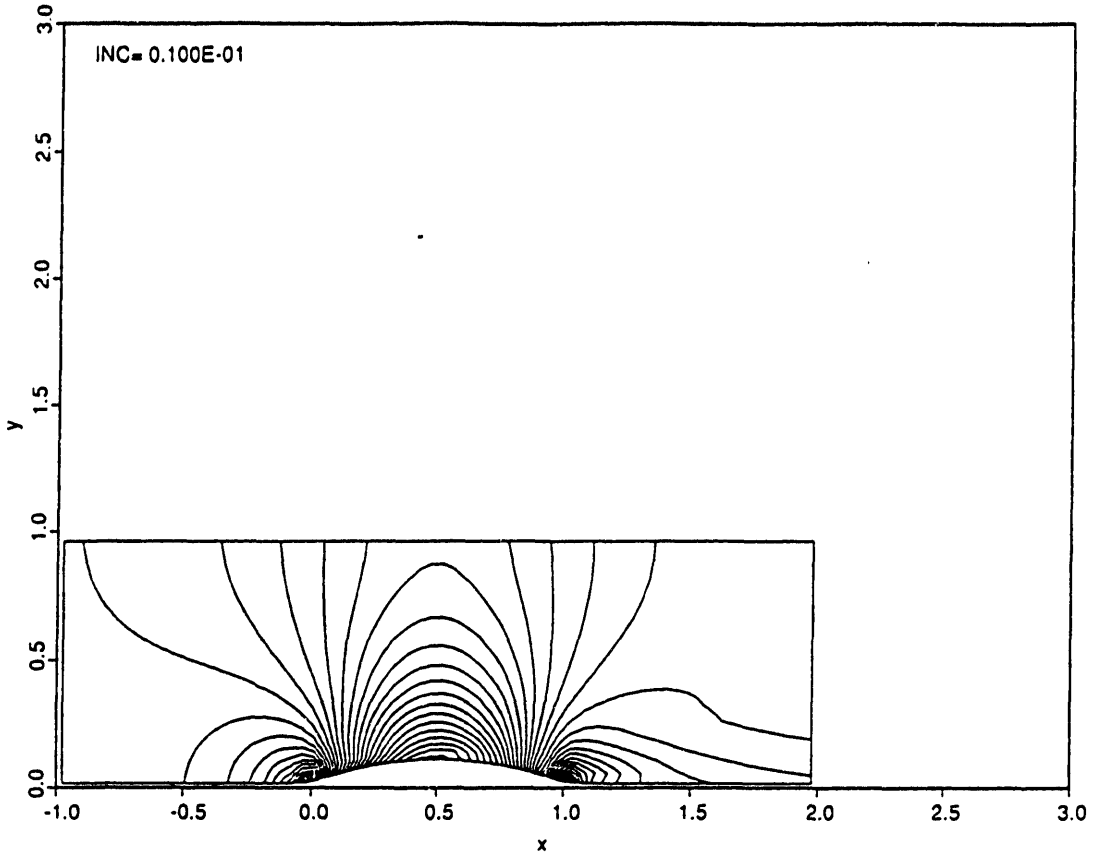

Figure 3.34: Isomach contours for subsonic calculation by FCT Scheme

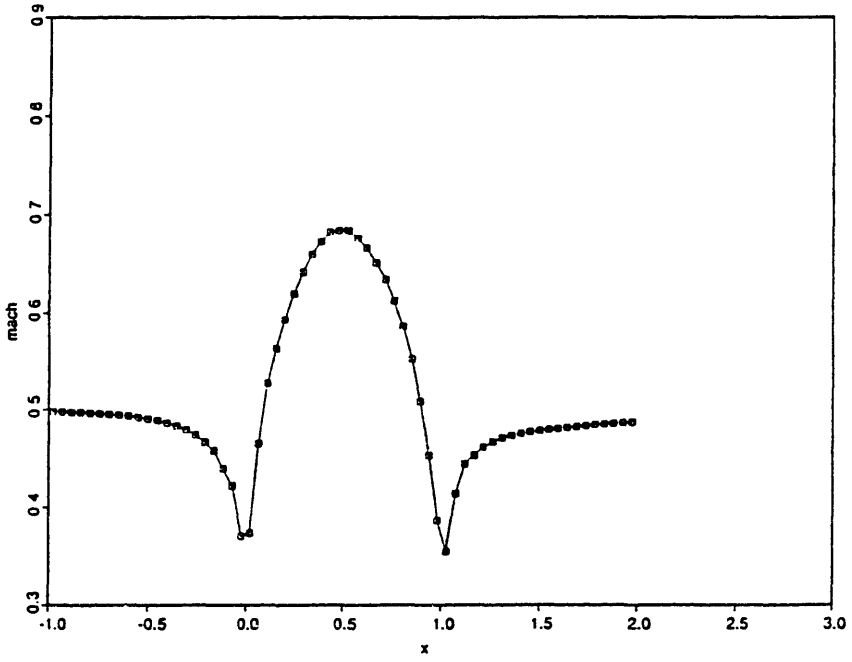

Figure 3.35: Mach Number Distribution along the lower wall as calculated by the FCT Scheme for subsonic inflow

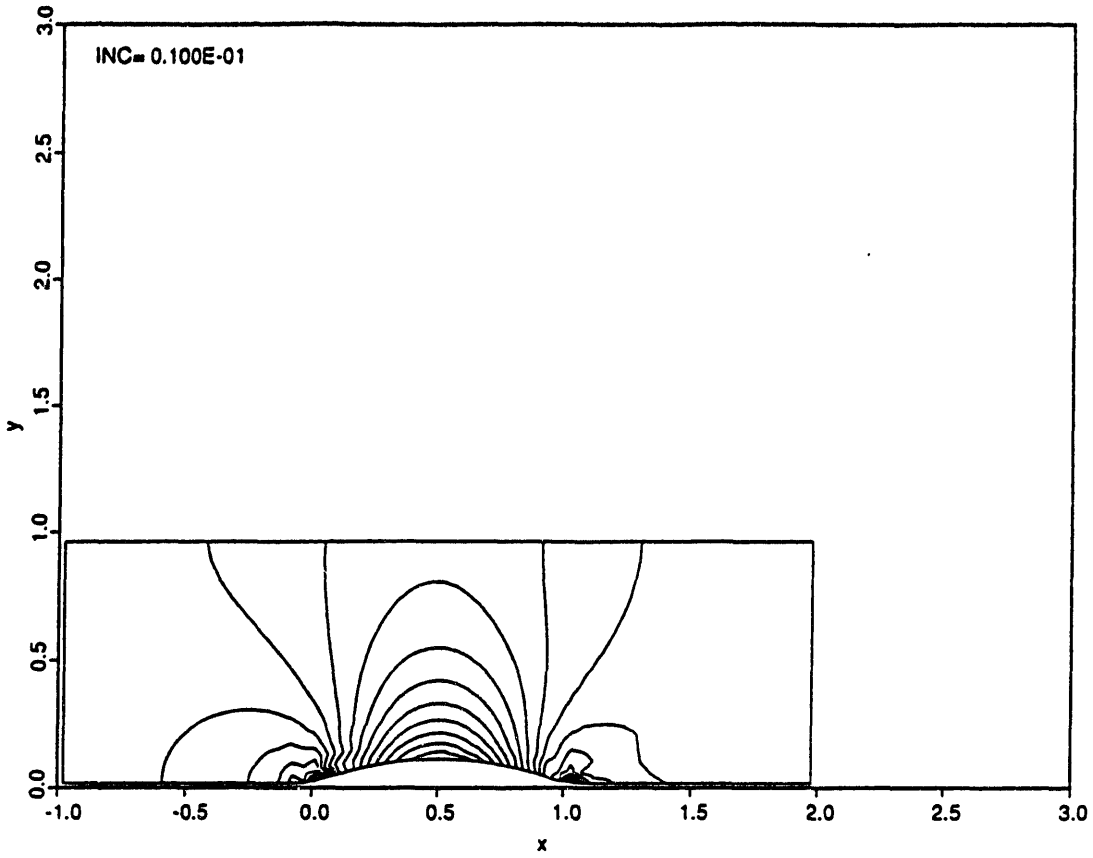

Figure 3.36: Density contours for subsonic calculation by FCT Scheme

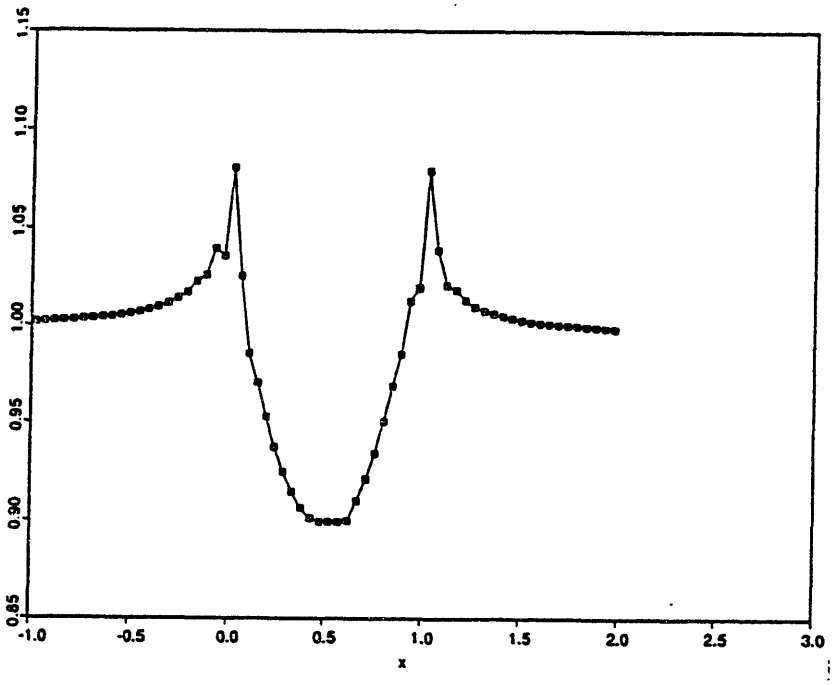

Figure 3.37: Density Distribution along the lower wall as calculated by the FCT Scheme for subsonic inflow

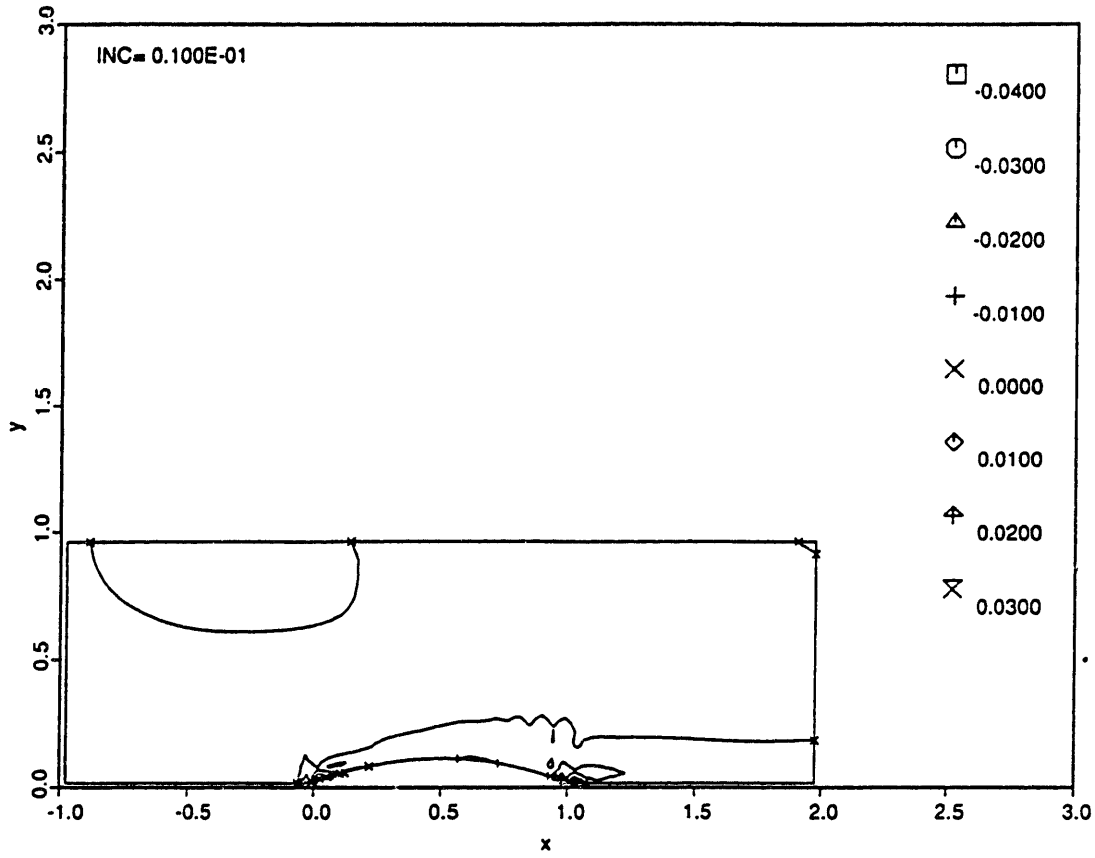

Figure 3.38: Total pressure contours for subsonic calculation by FCT Scheme

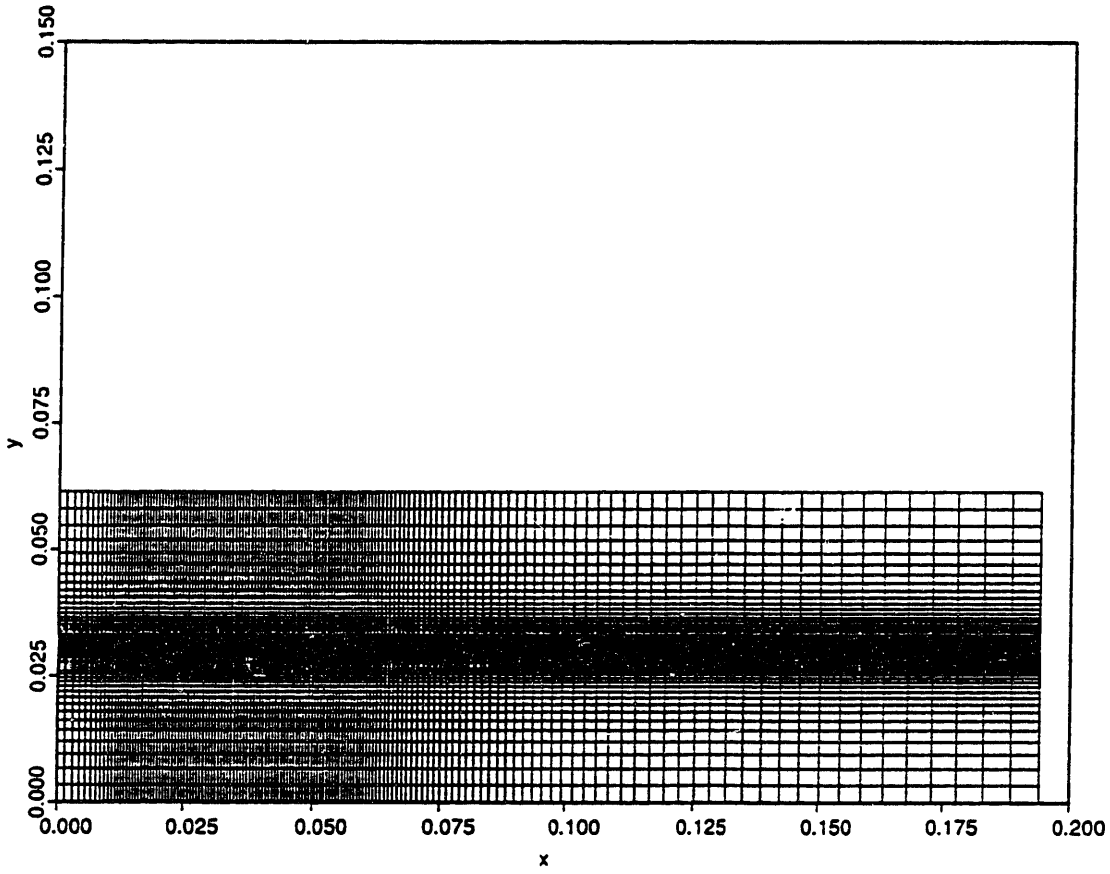

Figure 3.39: Grid used for subsonic planar shear layer calculations

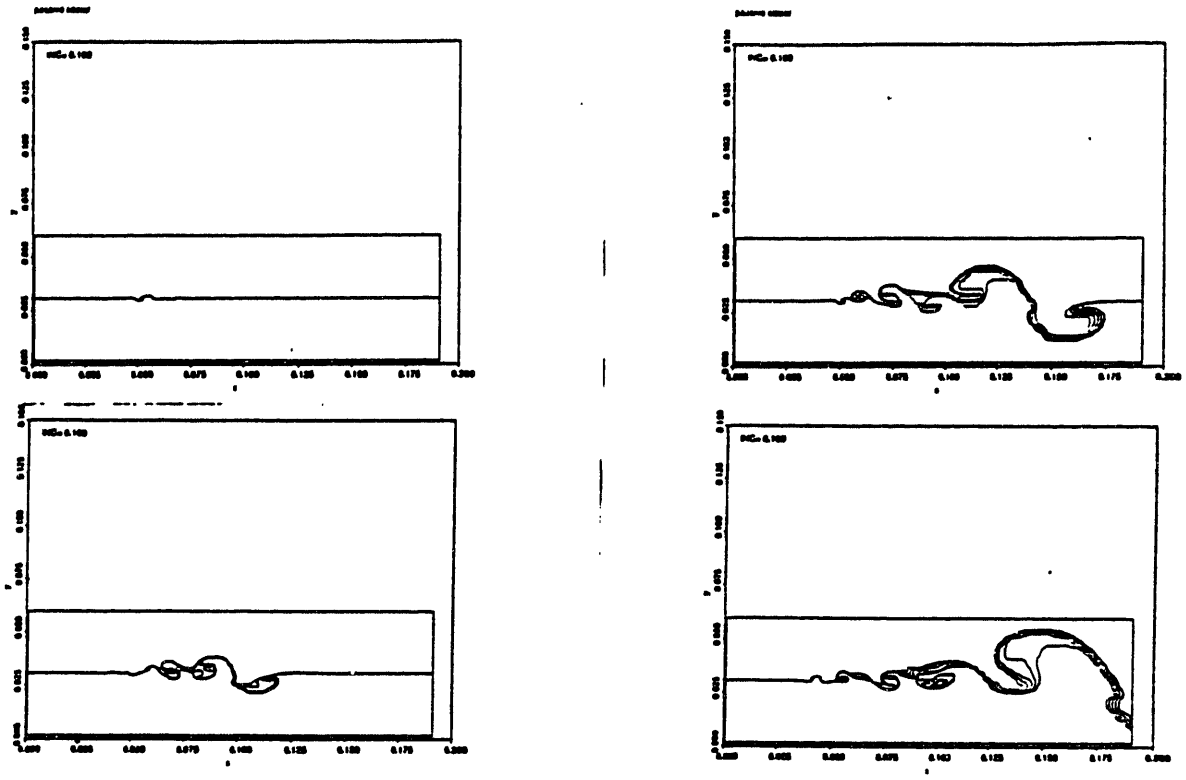

Figure 3.40: Passive scalar, $\psi = \frac{\bar{N}_{lower}}{N_{lower}+N_{upper}}$ at various stages in the evolution of the subsonic instability

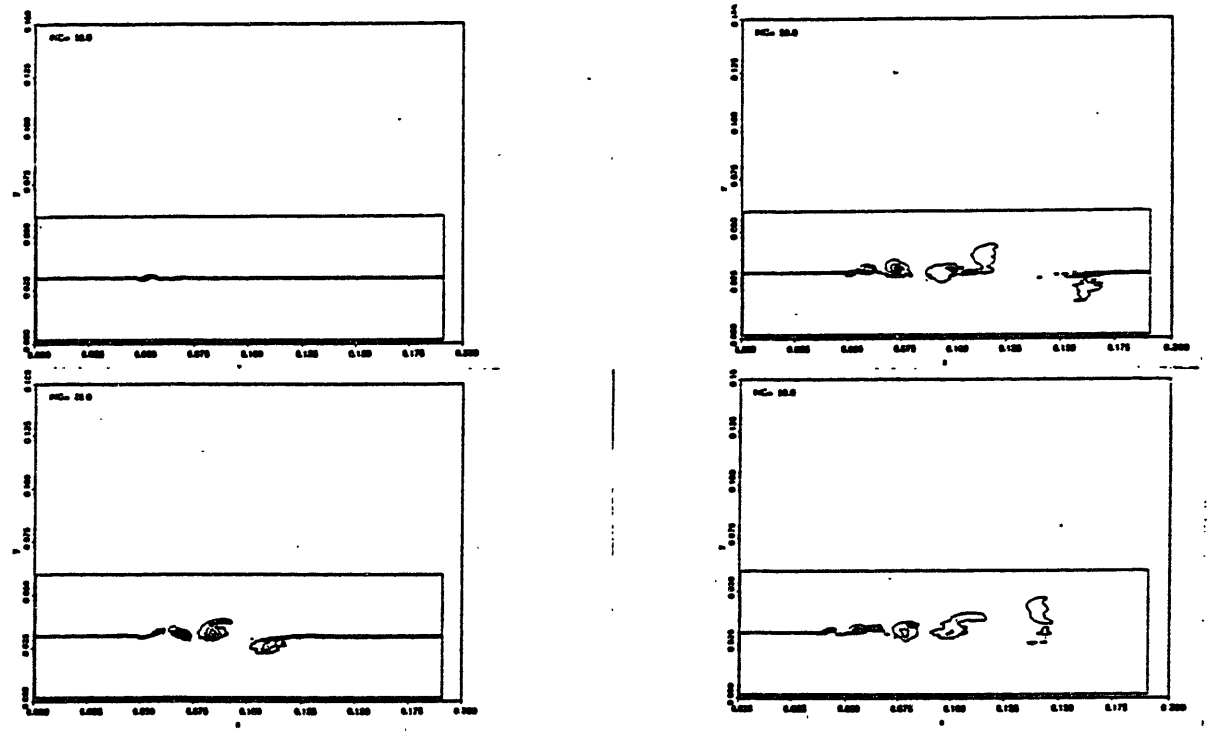

Figure 3.41: Vorticity at various stages in the evolution of the subsonic instability

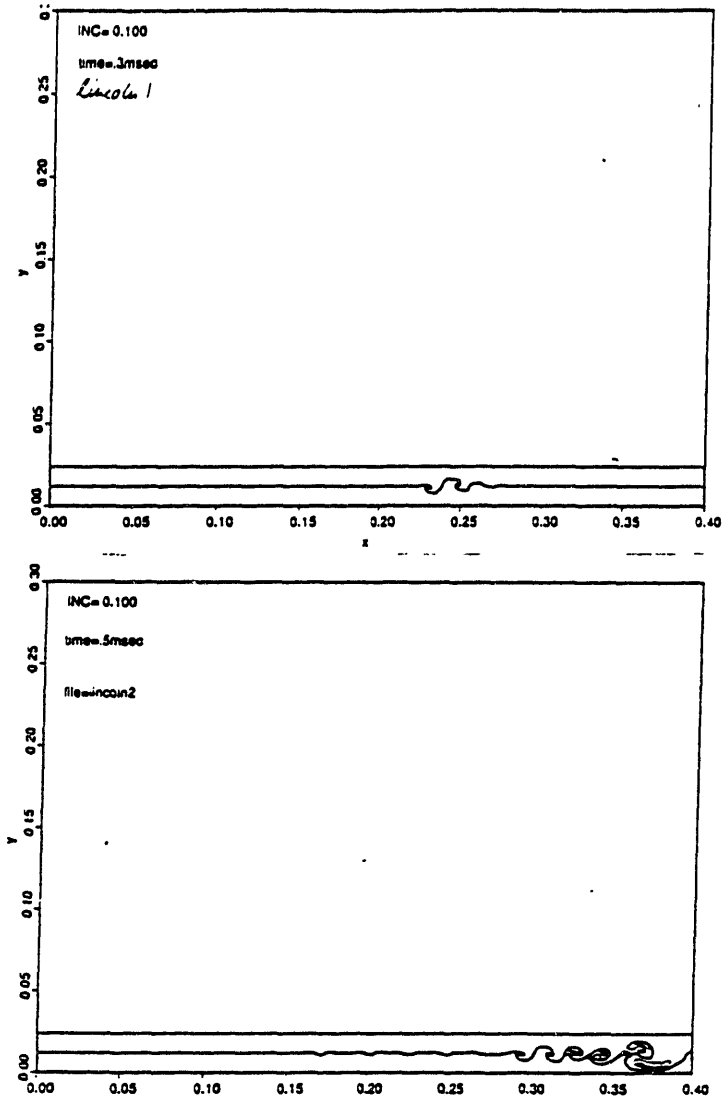

Figure 3.42: Passive scalar, $\psi = \frac{N_{lower}}{N_{lower}+N_{upper}}$ at various stages in the evolution of the supersonic instability

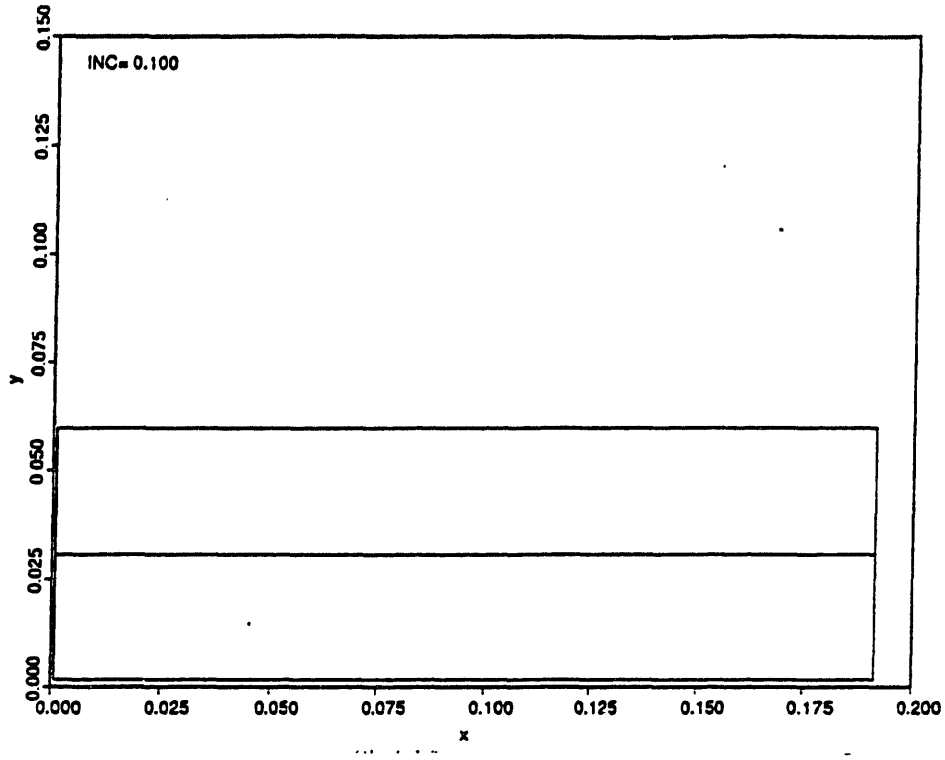

Figure 3.43: Passive scalar, $\psi = \frac{N_{lower}}{N_{lower}+N_{upper}}$ at various stages in the evolution of the instability as calculated by FVFCT

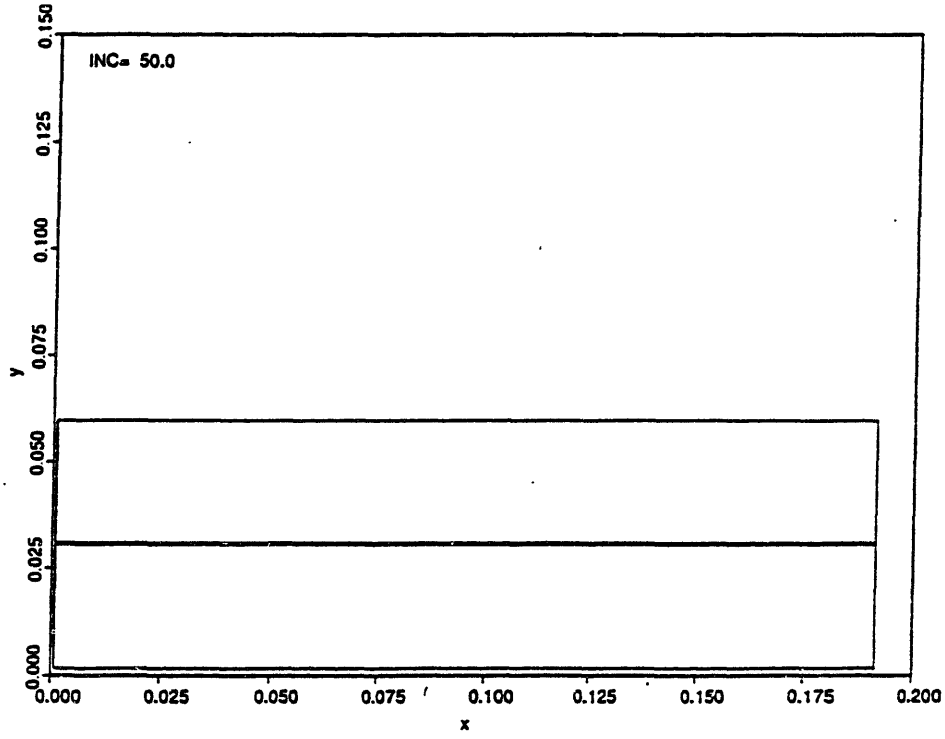

Figure 3.44: Vorticity at various stages in the evolution of the instability as calculated by FVFCT

Chapter 4

Lobed Mixer Calculations

Numerical solutions to the three-dimensional Euler equations for the flowfield in a lobed mixer and in the downstream mixing duct are presented in this chapter. In particular, the following computations are performed on the following configurations for the purpose of assessing the influence of compressibility and the effect of lobe penetration (as measured by the amplitude-to-wavelength ratio (a/λ) and the penetration angle α) on the evolution of the three- dimensional shear layer:

(1) Subsonic low penetration lobed mixer

(2) Supersonic low penetration lobed mixer

(3) Subsonic high penetration lobed mixer

(4) Supersonic low penetration lobed mixer

In all cases, the stagnation pressure is chosen to be uniform (i.e. the inflow velocities are chosen to be equal for the upper and lower streams). Consequently, the role of spanwise vorticity is not investigated here. However, a study of (i) vs. (ii) and (iii) v. (iv) would allow one to assess the effect of compressibility while a study of (i) vs. (iii) and (ii) vs. (iv) allows one to assess the effect of lobe penetration. Section 4.3 and 4.4 presents the results for a low penetration mixer with subsonic and supersonic Mach numbers at the inflow boundaries, respectively. The low penetration mixer, shown in Figure(4.2), has a penetration angle of 5.77^0 and an amplitude-to-wavelength ratio of $a/\lambda = 0.25$ at the lobe trailing edge. Similarly, section 4.5 an 4.6 present the results for a high penetration mixer with subsonic and supersonic Mach numbers at the inflow boundary, respectively. The high penetration mixer, shown in Figure(4.3), has a penetration angle of 22^0 and an amplitude-to-wavelength ratio of $a/\lambda = 0.5$ at the lobe trailing edge. Section 4.2 explains

the grid generation algorithm.

4.1 Further Details of the Numerical Scheme

The low order method used for the lobed mixer calculations is the Euler method with fluxes given by equation 2.95 and values of ν_2 between 0.0833 and 0.1666. The high order method used is the Leapfrog-Trapezoidal method with fourth order dissipation added in the computational region upstream of the trailing edge. The upstream fluxes are thus given by

$$\begin{aligned} \mathbf{E}^n_{i+\frac{1}{2},j,k} &= \frac{\Delta t}{4}((\vec{v}_{i+1,j,k} + \vec{v}_{i,j,k}) \cdot \vec{S}_{i+\frac{1}{2},j,k})(\mathbf{w}_{i+1,j,k} + \mathbf{w}_{i,j,k}) \\ &\quad \gamma_{upstream} V_{i+\frac{1}{2},j,k}(\mathbf{w}_{i+2,j,k} - 3\mathbf{w}_{i+1,j,k} + 3\mathbf{w}_{i,j,k} - \mathbf{w}_{i-1,j,k}) + Sources \end{aligned} \quad (4.1)$$

No artificial dissipation is used downstream of the trailing edge because this would result in excessive diffusion of the vortex sheet in the downstream flowfield.

The flux limiter used is the Zalesak multidimensional limiter with the one-dimensional Boris-Book limiter prelimiting the $\xi-$ and $\zeta-$fluxes. Several combinations were investigated and this proved to be the best for this problem. A vortex sheet is expected to be shed off the trailing edge of the lobed mixer, so that quantities such as $\rho v_y, \rho v_z$ will be convected in a direction perpendicular to large gradients in those quantities. In such a situation, the Zalesak limiter (acting alone) may fail to preserve monotonicity [21]. This is because the Zalesak limiter only checks for the creation and accentuation of extrema above or below the bounds set by w^{max} and w^{min}. When the gradient is large, the difference between w^{max} and w^{min} is large, so that the effectiveness of the limiter in detecting violations of monotonicity in directions other than that of the large gradient is reduced. This fact has been noted in Section 2.5. Hence extrema with respect to the perpendicular direction can be created and accentuated as long as they lie within the bounds set by w^{max} and w^{min}. Although the solution may remain stable, these errors are considered to be unacceptable.

Zalesak [21] suggests the use of the one-dimensional Boris-Book limiter to prelimit the antidif-

fusive fluxes so as to prevent the occurence of these dispersive ripples. This was investigated but it was found that when the Boris-Book limiter acted on the fluxes across the vortex sheet, severe clipping resulted leading to excessive diffusion of the vortex sheet. The clipping phenomenon can be seen from the results obtained with the use of two different limiters. These results (Figure 4.1) show the ρv_y profiles at the midspan (i.e. z=0.25) of the trailing edge and at five axial locations downstream of the trailing edge. Limiter 1 is the Zalesak limiter with the Boris-Book limiter prelimiting $\xi-$ and $\varsigma-$ antidiffusive fluxes. Limiter 2 is the Zalesak limiter with the Boris-Book limiter prelimiting the $\xi-$, $\eta-$ and $\varsigma-$ antidiffusive fluxes. The clipping phenomenon is evident for Limiter 2; this is not the case for Limiter 1. It can be seen that there is a discontinuity at the trailing edge with sharply-peaked profiles on either side for both solutions. The low order method will attenuate the peaked profiles; while the uncorrected antidiffusive fluxes would resurrect the profile, the Boris-Book limiter would step in to prevent this from happening since it would constitute an accentuation of the extrema in w^{td} by the definition used in its formulation. The clipping continues in the next timestep and so on until eventually we are left with the characteristic three point plateau as seen in Figure 4.1. In the use of the Zalesak limiter clipping can also occur when the peaked profile is transported across cell faces, though not nearly as severely since it has the ability to look back to the previous timestep in its search for the limiting values, w^{max} and w^{min}. At the trailing edge, the direction normal to the vortex sheet coincides with the η direction by design (although this does not remain true as the vortex sheet is convected downstream). Hence using the Boris-Book limiter to prelimit only the $\xi-$ and $\varsigma-$ antidiffusive fluxes causes no clipping and prevents dispersive ripples from arising - at least close the trailing edge. These investigations show that the limiter causes no problems at all in the rest of the mixing duct. An improved limiter would use a one-dimensional Zalesak limiter to prelimit the antidiffusive fluxes instead of the Boris-Book limiter since this could be done in all three computational directions without much clipping. The flexibility of the Zalesak limiter is such that there are measures that one can take to remove the clipping problem entirely

at least for the test case discussed in ref [21]. However, as mentioned earlier, for all the lobed mixer calculations performed, the flux limiter used is the Zalesak multidimensional limiter with the one-dimensional Boris-Book limiter prelimiting the $\xi-$ and $\varsigma-$fluxes.

4.2 Grid Generation Algorithm

To prevent the requirements for special treatment at the lobe surfaces and the associated inaccuracies (as discussed in Section (2.3)) we choose a body-aligned grid for all the calculations. For resolution purposes, clustering of grid lines to the lobe surface with minimal skewing of cells is also desirable. The use of Steger and Sorensen's [11] elliptic grid generation algorithm is found to satisfy both of these requirements. It allows the grid lines adjacent to the lobe boundary to be clustered to an almost constant distance Δs from the boundary and it forces $\xi = constant$ lines to intersect the boundary in a near normal fashion.

These two effects are achieved by adding to the elliptic governing equations the forcing terms as suggested by Thomson *et al* [31]. It is these forcing terms that impose the desired clustering. Thus the grids are generated through the solution of the following system of coupled Poisson's equations

$$\begin{aligned} \xi_{xx} + \xi_{yy} &= P(\xi,\eta) \\ \eta_{xx} + \eta_{yy} &= Q(\xi,\eta) \end{aligned} \tag{4.2}$$

with the forcing terms taken to be

$$\begin{aligned} P &= P_1 e^{-a(\eta-\eta_1)} \\ Q &= Q_1 e^{-b(\eta-\eta_1)} \end{aligned} \tag{4.3}$$

These choices are in accordance with the suggestions in reference [11]. Following the use of a generalized transformation as in reference [11], these equations become

$$\alpha x_{\xi\xi} - 2\beta x_{\xi\eta} + \gamma x_{\eta\eta} = -J^2(P x_\xi + Q x_\eta)$$

$$\alpha y_{\xi\xi} - 2\beta y_{\xi\eta} + \gamma y_{\eta\eta} = -J^2(Py_\xi + Qy_\eta) \tag{4.4}$$

where

$$\alpha = x_\eta^2 + y_\eta^2 \tag{4.5}$$

$$\beta = x_\xi x_\eta + y_\xi y_\eta \tag{4.6}$$

$$\gamma = x_\xi^2 + y_\xi^2 \tag{4.7}$$

P_1 and Q_1 are chosen such that they force the spacing between the grid lines $\eta = \eta_1$ and $\eta = \eta_2$ to satisfy the above-mentioned boundary clustering and orthogonality requirements. As explained in [11] the following choices achieve the desired clustering of grid lines and the orthogonality of $\xi-$ lines on the surface:

$$P_1 = J^{-1}(y_\eta R_1 - x_\eta R_2)_{\eta=\eta_1} \tag{4.8}$$

$$Q_1 = J^{-1}(-y_\xi R_1 + x_\xi R_2)_{\eta=\eta_1} \tag{4.9}$$

$$R_1 = -J^{-2}(\alpha x_{\xi\xi} - 2\beta x_{\xi\eta} + \gamma x_{\eta\eta})_{\eta=\eta_1} \tag{4.10}$$

$$R_2 = -J^{-2}(\alpha y_{\xi\xi} - 2\beta y_{\xi\eta} + \gamma y_{\eta\eta})_{\eta=\eta_1} \tag{4.11}$$

The details for evaluating R_1 and R_2 at the boundary are given in [11]. The relaxation scheme used for the evaluation of P_1 and Q_1 is

$$P_1^{n+1} = P_1^n + \omega_P(J^{-1}(y_\eta R_1 - x_\eta R_2)^{n+1} - P_1^n) \tag{4.12}$$

$$Q_1^{n+1} = Q_1^n + \omega_Q(J^{-1}(-y_\xi R_1 + x_\xi R_2)^{n+1} - Q_1^n) \tag{4.13}$$

where ω_P and ω_Q are chosen to vary linearly with the log of the relative error between two consecutive iterations. For example,

$$\omega_P = \omega_P^0 + (\omega_P^1 - \omega_P^0)\frac{log\epsilon - log\epsilon^0}{log\epsilon^1 - log\epsilon^0} \tag{4.14}$$

and

$$\omega_P^1 = 0.002 \tag{4.15}$$

$$\omega_P^0 = 0.04 \tag{4.16}$$

$$\epsilon^0 = 1 \tag{4.17}$$

$$\epsilon^1 = 10^{-5} \tag{4.18}$$

$$\epsilon = \frac{\sum_{i,j}((x_{i,j}^{n+1} - x_{i,j}^n)^2 + (y_{i,j}^{n+1} - y_{i,j}^n)^2)}{\sqrt{\sum_{i,j}(x_{i,j}^{n^2} + y_{i,j}^{n^2})}} \tag{4.19}$$

The selection of a and b in equation(4.3) is important since if too large a value is chosen, no clustering at all occurs while if too small a value is chosen, the SOR iteration scheme would not converge. The best values of a and b were found to be about 0.5 for a grid with $\eta_{max} = 17$ although the optimum choices of a and b depend on η_{max}.

This two-dimensional grid-generation algorithm is then applied at a specified set of axial locations where a mid-channel sinusoidal boundary (corresponding to the lobe surface upstream of the trailing edge) forms the lower boundary of the grid generation domain. The other boundaries are the upper wall, and the two symmetry boundaries. The result of this calculation gives the grid in the upper half of the channel. The grid for the lower half of the channel is found by finding the image under central symmetry of the upper half. This process produces a collection of 2-D grids which are then stacked to give the full 3-D grid. Figures 4.4-4.5 show the grids generated using this method for the low penetration (LPM) and high penetration (HPM) mixers. Note that $\Delta s = 0.02$ for the LPM grid and $\Delta s = 0.005$ for the HPM grid.

It should be pointed out here that all lobed mixers investigated here have sinusoidal profiles. It is found that there is a limiting value of amplitude-to-wavelength ratio ($(a/\lambda)_{max} \approx 0.85$) beyond which either the grid-generation algorithm will not converge or the desired clustering is not obtained. The distortion of the $\xi = constant$ lines close to the boundary with the largest slope causes the right-hand-side forcing term to become excessively large; this would imply a relatively large change in the right-hand-side term during each iteration which can be destabilizing. Practical lobed mixers, however, do not have sinusoidal profiles in general and, in fact, the best mixers tested [3]

have had vertical or past-vertical sections between crest and trough. The grid-generation algorithm used would appear to be incapable of generating acceptable grids for these cases. However, Malecki *et al* [8] recently reported an algorithm that was successful in generating a stacked 3-D grid for a lobed mixer with vertical midsections and this appears to be a promising method. They used a conformal mapping technique followed by an elliptic smoothing technique for each 2-D planar slice. Furthermore, their specification of computational variables $\xi = constant$ and $\eta = constant$ along the physical boundaries provide a scheme for which the internal grid lines do not have to undergo such destabilizing distortions as is found in conventional boundary specifications (in which $\eta = \eta_{max}$ corresponds to $y = y_{max}$ and $\eta = 1$ corresponds to the physical lobe boundary). These boundary specifications provide a possible means for the scheme used in this research to generate grids for lobed mixers with vertical or past-vertical midsections. However this has not been investigated in the present work. It is argued, however, the advanced mixer flowfield should definitely bear qualitative resemblance to the low penetration and high penetration lobed mixer flowfields investigated here. Furthermore, these mixer designs *are* adequate for assessing the compressibility and lobe penetration effects mentioned in the above paragraph.

4.3 Low Penetration Mixer: Subsonic Calculation

The geometry of the lobed mixer used for this calculation has been chosen to be similar to that of a mixer used in an experimental investigation undertaken at UTRC [3]. The mixer (shown in Figure 4.2) has a low penetration angle of $\alpha = 5.77\,\text{deg}$ (hence the name low penetration mixer - LPM) and a trailing edge amplitude-to-wavelength ratio of $a/\lambda = 0.25$. Since the trailing edge velocity distribution depends on these parameters, the mixer is chosen to possess these same numerical values so that the results could be compared with those from the experiments. However, the axial amplitude variations are slightly different for the two lobes and the resulting nonequal loading distributions will result in slightly different spanwise velocity profiles along the lobe surface

which will slightly alter the transverse velocity profiles due to the boundary tangency condition. However, the maximum difference in amplitude (which occurs near the leading edge) is only 2.4% of the trailing edge amplitude.

As a first calculation of flow over this mixer we choose $M_\infty = 0.5$, $\nu_2 = 0.125$ and $\gamma_4 = 0.0002$. The grid used for this calculation is shown in Figure 4.4; it has a resolution of 128x32x16. An estimate of the total temporal variation between timesteps was found from the root-mean-square state vector difference

$$\varepsilon = \sqrt{\frac{\sum_{i,j,k,l}(w^{n+1}_{i,j,k,l} - w^{n}_{i,j,k,l})^2)}{IJK}} \tag{4.20}$$

where subscript l represents the different components of the Euler equations (e.g. $w_{i,j,k,1} = \rho_{i,j,k}$). The history of the temporal variation as measured by ε is plotted in Figure 4.6 against iteration number. Four thousand iterations have been performed with timestep $\Delta t = 0.01$. The final value was $\varepsilon = 2.75 \times 10^{-5}$ and it was felt that this was sufficiently converged for the solution to be termed steady.

Figure 4.7 shows the transverse velocity distribution in the axial plane located at the first cell downstream of the lobe trailing edge. It can be seen that the transverse velocity reaches a maximum at a spanwise location of $z/\lambda = 0.5$ and on the inside surface of the mixer. This nondimensional maximum transverse velocity is $v_{y_{max}} = .0469$. This is close to the "ideal maximum" that would occur if the axial velocity retains its freestream value, i.e. $v_{y_{ideal}} = v_{x_\infty} \tan 5.77^0 = 0.05$. Indeed, examination of the velocity vector distribution in the spanwise plane (Figure 4.8) shows that the angle of the velocity vector adjacent to the lobe surface at the axial location just upstream of the trailing edge is 5.33 deg (where the spanwise velocity is assumed small). However, above the lobe the angle of the velocity vector is 3.06 deg which is significantly less than the wall angle of $\alpha = 5.77$ deg. This matter is clarified by an examination of Figure 4.9 which shows the secondary velocity vector distribution in the same axial plane as Figure 4.7. There is a large component of spanwise velocity at the cell above the lobe surface adjacent to the symmetry boundary, which

reduces the transverse velocity required for tangency to be satisfied. This large spanwise velocity close to the symmetry boundary also suggests that the solution may be improved by increasing resolution in this region. The general circulatory motion of the secondary flowfield generated by the lobed mixer is also apparent in Figure 4.9. The circulation around a path enclosing the region extending from the left symmetry boundary to the right symmetry boundary and from the lower wall to the upper wall is calculated to be $\Gamma = 0.045 = 0.090 U_\infty \lambda$.

Results derived from the UTRC experimental investigation are shown in Figures 4.10-4.11. It can be seen that qualitatively and insofar as normalized quantities (e.g. v/U_∞) are concerned, the two results agree quite well in spite of the slightly different axial amplitude variations and the different inflow Mach numbers. Figure 4.12 shows profiles of transverse velocity normalized by the freestream axial velocity for both experimental and numerical results at spanwise location $z = 0$ corresponding to the lobe crest and at the axial location just downstream of the lobe trailing edge. Qualitative agreement is good with the experimental velocity peaking at a lower value because of the existence of a boundary layer. The experimentally found circulation is $\Gamma = 0.08 U_\infty \lambda$.

Also plotted in Figure 4.12 is the profile found from a numerical calculation with $M_\infty = 0.1$. This profile lies very close to the $M_\infty = 0.5$ profile. The circulation for this case was found to be $\Gamma = 0.0091 = 0.091 U_\infty \lambda$. It appears that the small compressible effect introduced in the $M_\infty = 0.5$ case has little effect on the trailing edge secondary flow field. As $M_\infty \rightarrow 0$, the computation of steady flow can be computationally expensive. Consequently, we shall use the results of the $M_\infty = 0.5$ for investigative purposes.

The mechanism for the generation of the trailing edge streamwise vorticity can be explained in light of the results in Figure 4.13 and Figure 4.14. Figure 4.13 shows three-dimensional contour plots of pressure coefficient, transverse and spanwise velocities while Figure 4.14 shows the axial variation of surface pressure coefficient at selected spanwise locations. At the lobe leading edge, (i.e. where the lobe amplitude first starts to vary from zero) a high pressure zone appears at

the lobe crest that deflects the flow upwards to keep the velocity tangential to the lobe surface. A corresponding low pressure zone appears at the lobe trough. The resulting spanwise pressure gradient drives the flow from crest to trough which can be seen in the developing transverse and spanwise velocity fields in Figure 4.13.

The resulting circulation (Γ) profile versus at the trailing edge can be seen in Figure 4.15. Each value of Γ in this plot has been calculated in the following fashion. For the selected spanwise location, z, in the trailing edge axial plane, the line integral

$$\Gamma = \oint \vec{v} \cdot \vec{ds} \tag{4.21}$$

is evaluated along an elemental closed contour enclosing the trailing edge at z. The discrete approximation to Equation 4.21 is obtained by evaluating

$$\Gamma_{discrete} = (\sum_{i=1}^{4} v_i \Delta s_i)_{\text{upper cell}} + (\sum_{i=1}^{4} v_i \Delta s_i)_{\text{lower cell}} \tag{4.22}$$

(where the summation is performed for every side of the given cell) for the two cells on either side of the trailing edge at z. All the vorticity is concentrated at the lobed mixer surface and the flow is irrotational away from the lobe boundary. Since the lobed mixer lies within these two cells, the above calculation should yield an accurate estimate of the shed circulation distribution along the lobe trailing edge. In addition, the generated grid is such that the nodes adjacent to the trailing edge are all at an equal distance $\frac{1}{2}t$ from the trailing edge lobe surface. This feature of the grid permits one to evaluate the shed vorticity from

$$\omega_{shed} = \frac{1}{S} \oint \vec{v} \cdot \vec{ds} = \frac{1}{S}((\sum_{i=1}^{4} v_i \Delta s_i)_{\text{upper cell}} + (\sum_{i=1}^{4} v_i \Delta s_i)_{\text{lower cell}}) = \frac{1}{t}\gamma_{bound} \tag{4.23}$$

where S is the net area of the two cells. Since the grid has constant Δs along the trailing edge, the values of Γ shown are proportional to the spanwise gradient of *bound* circulation, γ_{bound}, given by

$$\gamma_{bound} = \partial \Gamma_{bound} / \partial s \tag{4.24}$$

It can be seen that the maximum value of γ occurs at $z = .25$ corresponding to midspan (halfway between crest and trough) and $\gamma = 0$ at crest and trough where the transverse velocity is maximum. Thus the streamwise vorticity is a result of the migration of fluid from crest to trough driven by the spanwise pressure gradients. These in turn are the result of the transverse penetration of the lobe surface into the flow.

The Kutta condition requires that the loading decrease to zero at trailing edge, and it can be seen from Figure 4.13 that this appears to be the case in spite of the fact that no explicit Kutta condition was imposed. The loading is mostly confined to a region extending from the leading edge to about 1.5λ downstream. The surface pressure coefficient distribution at lobe crest shown in Figure 4.14 shows that some loading extends almost to the trailing edge at this spanwise location. However, the loading region that extends past the $x = 1.5\lambda$ mark is very narrow being confined to a short spanwise distance from the spanwise symmetry boundary. This can be seen in Figure 4.16 which shows the loading on the projected lobe surface.

We shall now use the compressible Bernoulli equation to assess the consistency of the computed aerodynamic loading on the lobed mixer. Using isentropic relations and the energy equation, it can be shown that

$$c_{p_{upper}} - c_{p_{lower}} - \frac{P_{t_\infty}}{\frac{1}{2}\rho U_\infty^2}((1 + \frac{\gamma - 1}{2} M_{upper}^2)^{\frac{-\gamma}{\gamma-1}} - (1 + \frac{\gamma - 1}{2} M_{lower}^2)^{\frac{-\gamma}{\gamma-1}}) = 0 \qquad (4.25)$$

Thus the residual in Equation(4.25) can be used as a measure of the quality of the computed results. This is shown in Figure 4.17 for the case considered here. The maximum absolute value of the residual is found to be about 2% of the dynamic pressure. Since flow is subsonic throughout, all changes in total pressure must be numerical in origin. Figure 4.18 shows a three-dimensional contour plot of total pressure change (normalized by freestream total pressure, P_{t_∞}). The largest total pressure change around the lobe is about 0.2% of P_{t_∞} (or about 6% of the dynamic pressure) which is equal to about 2% of the freestream dynamic pressure. This is of the same order as the residual from Equation(4.25).

Next, we shall proceed to examine the evolution of the shed vortex sheet in the mixing duct downstream of the lobe trailing edge. Figure 4.19 shows contour plots of total pressure change ΔP_t (normalized by the freestream total pressure P_{t_∞}) at various axial locations from the lobe trailing edge to mixing duct exit. The maximum absolute value of ΔP_t (all of which is numerical in origin) is 0.9% of P_{t_∞}. This represents an acceptably low level of error. Figure 4.20 shows the secondary velocity vector fields at three axial locations in the mixing duct at lobe trailing edge, 8λ downstream and at mixing duct exit. An important attribute of the FCT scheme is that the computed solution is such that the secondary flowfield persists as it is convected downstream (this might not be the case if artificial viscosity were used). This can be deduced from results in Figure 4.20 and as well as those of Figure 4.21 which shows the variation of circulation with axial distance. In fact the circulation increases from the trailing edge by as much as 15% (which is in violation of Kelvin's circulation theorem). This discrepancy is a result of the fact that circulation is not one of the quantities that is explicitly conserved in the discretized Euler equations of FVFCT. Figure 4.20 also shows that as the streamwise vortex sheet proceeds downstream, it takes on a circular shape. In other words the root-mean-square radial component of velocity from an origin located at $(y, z) = (0, 0.25)$ is reduced while the root-mean-square circumferential component is increased and the structure increasingly resembles a vortex with a viscous core.

This perception is reinforced by evidence presented in Figure 4.22 which shows contour plots of passive scalar, (ψ), axial vorticity (ω_x), and pressure coefficient, (c_p) at axial locations separated by one wavelength from trailing edge to mixing duct exit. The evolution of the vortex sheet into a structure with a viscous core alluded to above is confirmed by the presence of a circular region of near constant vorticity at mixing duct exit. Note that this region of near constant vorticity has evolved as a result of a combination of the nonlinear dissipation of the FCT numerical scheme and the fact that local length scales have become too small to be resolved by the numerical grid. The static pressure plot shows evidence of the low pressure region characteristic of the centre of a

streamwise vortex structure. Note that nonphysical wiggles appear in the the pressure and axial vorticity fields. This is because FCT checks for monotonicity only in the conserved quantities $(\rho, \rho v_x, \rho v_y, \rho v_z, E_t)$. Nonphysical extrema can therefore arise in the nonconserved quantities as pointed out in Section 3.1.1. One means of controling this situation is through flux synchronization [23] whereby the antidiffusive fluxes for each fluid variable are all corrected by the same factor.

The passive scalar plot shows contours of $\psi = 0.3$ to $\psi = 0.7$ in increments of 0.1. It therefore is representative of the interface between fluid particles originating above the lobe and those originating below the lobe. It can be seen that large portions of fluid from the upper stream have been swept by the induced velocity of the streamwise vortex into the bottom half of the channel. Intuitively, this represents an improved situation in terms of mixedness. This is an example of the large scale motions that Marble [49] recognizes as playing an important part in speeding up the mixing process along with molecular diffusion. The passive scalar equation modelled includes no diffusion term so any measured mixing is purely numerical in origin. As Marble points out large scale motions improve mixing by extending the interface between the two fluids and thus providing a larger area through which diffusive mixing can occur. In the absence of diffusion, we can estimate mixing properties in terms of the mixing rate that would occur if we suddenly "switch on" diffusion and allow molecules to diffuse from regions of $\psi = 0$ to $\psi = 1$ and vice versa. The mixing rate would then be given by

$$\begin{aligned} \frac{\partial}{\partial t}\int \psi N dV &= \int \nabla \cdot (k_D \nabla \psi) dV \\ &= \int k_D \hat{n} \cdot \nabla \psi dS \end{aligned} \tag{4.26}$$

where k_D is the transport coefficient appropriate for the diffusion of molecules, N is the total number of molecules per unit volume and

$$k_D = \kappa N \tag{4.27}$$

is the coefficient of diffusion (see for example Batchelor [48]). We assume that the flow was theo-

retically inviscid and nondiffusive before diffusion is "switched on" and so the only change in $\nabla\psi$ comes about due to changes in streamtube area. In the absence of diffusion and severe changes in streamtube cross-sectional area, we can then estimate the term $\nabla\psi$ to be aproximately constant along the interface and hypothesize that the major contribution to changes in the mixing rate given in Equation (4.26) is due to changes in the interface area. Therefore we can approximately quantify the mixing rate by

$$\frac{\partial}{\partial t}\int \psi N dV \sim s_i = s_{\psi=0.5} \tag{4.28}$$

(We also assume that the interface lies along the $\psi = 0.5$ contour in each axial plane.) Figure 4.23 shows the line graph of s_i versus distance from the lobe trailing edge. It can be seen that s_i increases almost linearly with axial distance and reaches a value of $s_i = 2.56$ which is almost four times its value at the trailing edge.

A further check in the validity of the solution in the mixing duct is provided by a Trefftz plane analysis discussed in [7]. This analysis tracks the evolution of the vortex sheet from the initial conditions given by the circulation distribution at lobe trailing edge as depicted in Figure 4.15. The analysis uses the slender body approximation so that one can transform the steady three-dimensional problem into an unsteady two-dimensional problem. Axial velocity is assumed constant and therefore a simple linear relationship exists between time and axial distance. Viscous and diffusive effects are included in the analysis with $Re = \frac{\Gamma}{\nu} = 360$ and $\frac{\nu}{D} = 1$. The Trefftz plane analysis in [7] does not include the potential influence of the presence of the lobed mixer. A comparison of the two solutions is presented in Figure 4.24 and Figure 4.25 which show the ψ distribution at axial locations 4λ and 9λ downstream of the lobe trailing edge. It can be seen that rather good agreement is obtained between the two solutions once account is taken of the diffusive effects in the Trefftz plane analysis. The degree to which the potential effect affects the downstream evolution can be gauged by comparing pressure fields at lobe trailing edge. Figure 4.26 show the respective pressure distributions at trailing edge. Except for differences at the symmetry boundary

where slight deterioration in the quality of the FVFCT solution occurs due to lack of resolution and at midspan of the trailing edge where the FVFCT solution gives a slightly lower pressure, the pressure fields are very similar. From the evidence presented in Figures 4.24-4.26 it can be concluded then that the potential effect for the low penetration mixer does not significantly affect the downstream evolution.

4.4 Low Penetration Mixer: Supersonic Calculation

An inflow Mach number of $M_\infty = 2.0$ is used for this calculation. The same grid was used as the one used in the subsonic case (see Figure 4.4). The rationale for this decision is as follows. Although the convective velocities will be larger implying larger convective distances, the transverse velocities should scale with the convective velocity ($v_y \sim v_x \tan\alpha$). Compressibility effects notwithstanding, it was felt that the phenomena of interest should occur in approximately the same axial distances. This prediction proved to be correct. Parameters used in the numerical algorithm were $\nu_2 = .0833$, $\gamma_{4_{lobe}} = 0.0002$ and $\gamma_{4_{duct}} = 0$. The convergence history is shown in Figure 4.27 and it can be seen that the final value of ε was 2.6×10^{-4} after 2400 timesteps with $\Delta t = 0.005$. This can be taken to be sufficiently small for steady flow to be assumed. However, unlike the subsonic case, ε appears to have reached its lowest value at this point and no further reduction seems likely to occur. One explanation for this is the lack of fourth order dissipation in the mixing duct. Although there is fourth order dissipation in the region upstream of the lobe trailing edge, pressure waves associated with small background residual oscillations can not travel upstream since flow is supersonic, in contrast to the subsonic case. Hence for the supersonic case, the nonlinear dissipation associated with FCT is the only mechanism for damping out background oscillations in the mixing duct.

Compressiblity effects for this case would be expected to influence the flow in the lobe region through the effects of shocks and expansions. However, since the angle of the lobe is small, shocks will be weak. Also, the transition from flat plate to sinusoidal profile with linear amplitude variation

is gentle with a large radius of curvature. Therefore isentropic compression waves will be formed until the compression waves coalesce. The limiting case is the 2-D case which, using Prandtl-Meyer relations, gives

$$M_2 = M(\nu_2) = M(\nu_2 - 5.77^0) = M(20.62^0) = 1.796 \tag{4.29}$$

The Mach angles are therefore

$$\mu_1 = sin^{-1}(\frac{1}{2}) = 30^0 \qquad \mu_2 = sin^{-1}(\frac{1}{1.796}) = 39.6^0 \tag{4.30}$$

and the compression waves will coalesce at an approximate axial distance

$$X_c = \frac{\tan \mu_2}{\tan \mu_2 - \tan \mu_1} = 3.31 \tag{4.31}$$

On the other hand the Mach number and angle in the expansion wave can be calculated from Prandtl-Meyer relations (assuming 2-D flow). They are

$$M_2 = M(\nu_2) = M(\nu_1 + 5.77^0) = M(32.16^0) = 2.216$$

$$\mu_2 = sin^{-1}(\frac{1}{1.796}) = 35.17^0$$

and this rough estimate tells us that the expansion waves emanating from the trough leading edge would reach the symmetry boundary at

$$X_e = \frac{0.5}{tan\mu_2} = 0.71 \tag{4.32}$$

for a 2-D case. Therefore, from this approximate 2-D analysis, it is expected that expansion waves will weaken the compression waves long before they have a chance to coalesce into a shock. The three-dimensional supersonic flowfield in the region of the lobe is depicted in Figure 4.28 which shows three-dimensional plots of c_p, v_y and v_z. As expected no strong shocks are evident. Other aspects of the flowfield are very similar to the subsonic case (Figure 4.13) with spanwise pressure gradients again driving fluid from crest to trough. Figure 4.29 shows contours of total pressure change from inflow to lobe trailing edge. The largest absolute value is 2.3% of the freestream total

pressure. It would appear that most of this variation is numerical in origin since the supersonic compression and expansion take place isentropically.

Significant differences are observed, however, in the loading distributions, Figure 4.30 and Figure 4.31 showing the line and contour plots, respectively, of the loading distribution. The loading at crest reaches a maximum about two cells downstream of the leading edge and, unlike the subsonic case, then decreases to a (small) negative value before rising above zero again. Also, the loading does not drop smoothly to zero at trailing edge (since information can not travel upstream) but rather the pressures are equalized by the formation of a weak shock and expansion fan. This is shown in Figure 4.32. The solution in this region is contaminated by small oscillations that are large compared to variations in physical quantities. They are a result of the sudden imposition of a steep gradient normal to the supersonic flow and also partly due to the previously-mentioned insufficiency of resolution adjacent to the symmetry boundary.

Figure 4.33 shows the transverse velocity distribution (normalized by inflow velocity) at trailing edge. Comparison with Figure 4.7 shows that the two are almost equivalent with all the contours matching except for the curved zero level contour at $y = 1$ and $y = -1$ associated with compression waves emanating from the lobe leading edge and their reflections from the symmetry boundary. The transverse profiles of normalized transverse velocity at lobe crest for subsonic and supersonic cases are shown in Figure 4.34 confirm that the features are essentially the same except for small differences associated with the above-mentioned compression characteristics. The normalized transverse velocity reaches the same maximum of $v/U = .094$ at the surface of the trough close to the ideal maximum of $(v/U)_{ideal} = \tan(5.77) = .1$.

The circulation profile at trailing edge is shown in Figure 4.35. Qualitatively, the profile is very similar to that found in the subsonic case (see Figure 4.15). The total circulation is $\Gamma^* = 0.189$ and nondimensional circulation is

$$\Gamma^* = \Gamma/U\lambda = 0.0945 \tag{4.33}$$

This value is not very different from that of the subsonic case.

The evolution of the vortex sheet in the mixing duct is also qualitatively very similar to the subsonic case. The largest absolute value of total pressure change in the mixing duct (see Figure 4.36) is about 5% of the freestream total pressure. Figure 4.37 confirms that the secondary flow field once again persists as it is convected downstream in the mixing duct. Also, the increase in circulation with axial distance is much smaller as shown in Figure 4.38. Circulation peaks at about 0.198 or 5% greater than the trailing edge value.

The vortex structure again evolves to one similar to a vortex with a viscous core as it moves downstream (see Figure 4.37 and Figure 4.39). No strong shocks are evident in the mixing layer. The contour plot of ψ show that fluid originating from the upper stream is swept (if anything, more rapidly) into the lower half of the channel. Comparison of the interface length, s_i, for the subsonic and supersonic cases (Figure 4.40) reveals that the supersonic case exhibits very slightly improved mixing properties. The interface length at 15λ from the lobe trailing edge is $s_i = 2.75$, an increase of 7% over the subsonic case. (Note that this is also the factor by which the respective circulations differ.)

4.5 High Penetration Mixer: Subsonic Calculation

An inflow Mach number of $M_\infty = 0.5$ was used for this calculation. The grid used is shown in Figure 4.5. Parameters used in the numerical algorithm were $\nu_2 = .125$, $\gamma_{4_{lobe}} = 0.0004$ and $\gamma_{4_{duct}} = 0$. The convergence history is shown in Figure 4.41 and it can be seen that the final value of ε was 2.3×10^{-4} after 8400 timesteps with $\Delta t = 2.5 \times 10^{-3}$. This is taken to be sufficiently small for steady flow to be assumed.

Figure 4.42 shows a three-dimensional plot of $\Delta P_t / P_{t_\infty}$ in the region of the lobe. The maximum absolute value of $\Delta P_t / P_{t_\infty}$ is found to be about 3%. Although this is an order of magnitude larger than that found in the low penetration case, it still represents a marginally acceptable numerical

error in the region of the lobed mixer. The three-dimensional flowfield in the region of the lobe is depicted in Figure 4.44 which shows three-dimensional plots of c_p, v_y and v_z. Although gradients are much larger than the low penetration case, the qualitative features of the flowfield are similar. The pressure field at the leading edge is characterized by much larger variation of c_p ($\sim +25\%$ at lobe crest and $\sim -25\%$ at lobe trough) than the low penetration case. Transverse velocity (v_y) quickly attains a maximum at $z/\lambda = 0$ and on the inner surface of the mixer. Figure 4.43 shows the transverse velocity (v_y) profile at this spanwise location with the experimental results. The experimental results are for a mixer that has the same penetration angle, but nondimensional values of amplitude (a/λ), mixer length (L_m/λ) and wall distance (H/λ) that are increased by a factor of 2. Hence, the geometrical set up used for the numerical calculations presented here double the wavelength of the UTRC configuration , In spite of this difference, the profiles are quite similar, with the numerical solution giving a maximum transverse velocity $v_y/U_\infty = .347$ that closely approaches the ideal value of $(v_y/U_\infty)_{\text{ideal}} = tan\alpha = 0.4$. These results suggest that the transverse profile of v_y at the symmetry boundary is not strongly dependent on λ. Magnitudes of v_z are smaller relative to the maximum value of transverse velocity $v_{z_{max}}/v_{y_{max}} = .360$ than for the low penetration case $v_{z_{max}}/v_{y_{max}} = .746$. The reason for this decrease is that the spanwise velocities (i.e. velocities tangential to the surface but normal to the streamwise direction) created by the spanwise pressure gradients have a reduced relative component of v_z than for the low penetration case and a larger relative component of v_y. This is because the lobe is closer to vertical at midspan.

The loading shown in Figure 4.45 and Figure 4.46 indicates that again, the loading is mostly confined to a region just downstream of the lobe trailing edge (except for a narrow region adjacent to the symmetry boundary that extends to close to the trailing edge). Indeed, because the axial length of the lobe is less, the Kutta condition forces the region of high loading to be confined to a region of smaller extent (from $x = 0$ to $x = 0.5$) than the low penetration mixer(from $x \approx 0$ to $x \approx 1.0$). This reduces the effective area over which the spanwise pressure gradient is significant

but this is matched by a corresponding increase in the magnitude of the loading.

The residual from Equation(4.25) is shown in Figure 4.47. The magnitude of this residual is an indication of the numerical production of entropy. The maximum value of ϵ is about 25% of a dynamic pressure corresponding to about $0.037P_{t\infty}$ which is of the same order as the maximum variation in total pressure, as expected. Although larger than the corresponding values for the low penetration mixer cases, these are still marginally acceptable.

The circulation distribution along the lobe trailing edge is shown in Figure4.48. Qualitatively, the profile is similar to that found in the low penetration case. The total circulation is computed to be $\Gamma = 0.268$ and the nondimensional circulation is

$$\Gamma^* = 0.536 \tag{4.34}$$

It can be seen from Figure 4.49, which shows the axial variation in circulation, that the secondary flowfield persists as it is convected downstream, as anticipated. These results also show that the axial variation in circulation can be as large as 10%. Total pressure variation in the mixing duct (Figure 4.50) is characterized by a maximum absolute value of about 7% of the freestream total pressure (or 47% of the freestream dynamic pressure). Again this is all of numerical origin for subsonic flow. As expected, this is larger than the corresponding value from the lobe region since the presence of the vortex sheet necessitates more flux correction with its associated detrimental effect on the monotonicity of nonconserved quanitities. Close examination of the c_p, ω_x and ψ contours in Figure 4.51 reveals that small scale oscillations are present even in the ψ contours. Associated with the above-mentioned variation in total pressure and circulation, the solution for the high penetration case is expected to have a higher degree of numerical contamination than the low penetration case. The main source of numerical error is believed to be associated with the quality of the numerical grid (Figure 4.5) used for the numerical solution. The closely packed grid lines around the lobe surface and the downstream surface emanating from the trailing edge were designed to optimize resolution in regions where gradients are expected to be highest. However, as pointed

out in Section 2.3, zeroth order dissipation fluxes are reduced with respect to convective fluxes in fine regions of the grid. Hence, the effectiveness of FCT appears to be reduced in these regions with the flux limiter no longer ensuring monotonicity. Furthermore, the resulting distortedness of the grid can also be a source of error. Dannenhoffer [50] separated these grid-related errors and categorized them in terms of stretchedness, skewness, curvedness and degree of convergence. Most of the error terms vanish as the temporal variation tends to zero. The temporal variation presented here has converged to a value of $\varepsilon = 2.3 \times 10^{-4}$ which is larger than the corresponding value for the low penetration subsonic case ($\varepsilon = 2.3 \times 10^{-5}$). Hence the grid-related errors associated with the temporal variation will be larger for the high penetration subsonic case than for the low penetration subsonic case. The errors associated with grid stretching appear to have strong influence on the solution presented here, particularly as the outflow boundary is approached. When a grid of good quality is used for the implementation of this numerical calculation, an improved numerical solution can be anticipated.

In spite of the presence of these numerical oscillations, the results nevertheless yield a reasonable description of the evolution of the vortex sheet in the mixing duct. Figure 4.51 and Figure 4.52 show that roll-up initially occurs near the extremities of the streamwise vortex structure where two clumps of vorticity are visible. This feature has also been seen in a separate Trefftz plane analysis [7] using the circulation distribution shown in Figure 4.48 as the initial condition. The streamwise vortex structure eventually evolves into a circular shape close to the exit of the computational domain. The rate of increase of s_i shown in Figure 4.53 is improved over the low penetration subsonic case from 0.120 to 0.784. This gives a ratio of 6.53, close to the ratio of normalized trailing edge circulations, $\frac{.536}{.090} = 5.96$.

4.6 High Penetration Mixer: Supersonic Calculation

An inflow Mach number of $M_\infty = 2.0$ was used for this calculation. The same grid (Figure 4.5) was used as for the subsonic calculation presented in the previous section. Parameters used in the numerical algorithm are $\nu_2 = .0833$, $\gamma_{4_{lobe}} = 0.0002$ and $\gamma_{4_{duct}} = 0$. The temporal variation of ε is shown in Figure 4.54. It is apparent that convergence was not achieved for this case. For completeness, a value of ε was 1.1×10^{-2} is obtained after 4800 timesteps for $\Delta t = 1.25 \times 10^{-3}$. An examination of the solution after 4800 iterations shows that it is the flow variables in the neighbourhood of the duct exit that contribute the major portion to this large temporal variation. This temporal variation is a result of numerical oscillations of the same nature as those found in the subsonic case. When flow is supersonic, pressure waves associated with background residual oscillations cannot travel upstream into the lobe region (where fourth order dissipation exists). Since there is no artificial dissipation in the mixing duct except for the nonlinear dissipation associated with FCT, these residual oscillations are not damped out as efficiently as for the subsonic case. As for the subsonic case, the worst oscillations occur close to the outflow boundary where the grid stretching and cell aspect ratios are largest. However in the supersonic case, these oscillations become so severe that flow becomes subsonic in certain parts of the outflow axial plane thereby complicating the imposition of outflow boundary conditions in the boundary condition procedure. However, as flow is supersonic everywhere except close to the outflow boundary, one might expect that these numerical oscillations do not contaminate the solution in the neighbourhood of the lobed mixer.

In view of this, it is proposed that the solution there can reasonably be used for investigating the flow at these conditions. Figure 4.55 shows $\Delta P_t/P_{t_\infty}$ variation upstream of the lobe trailing edge and the maximum absolute value of $\Delta P_t/P_{t_\infty}$ is found to be about 30%. (This positive change violates the 2nd Law of Thermodynamics. Negative changes,however, have a physical basis in the presence of shocks which we expect for this supersonic flowfield.) However, this positive change in

$\Delta P_t/P_{t_\infty}$ is local (a result of the fact that P_t is not a conserved quantity, as mentioned previously) and so the solution is only contaminated locally. Bearing this in mind, we can proceed to analyze other aspects of the flowfield in the lobe region. Figure 4.56 is a contour plot of density at a spanwise location corresponding to lobe crest ($z = 0$). Close to the leading edge, a shock is clearly in evidence in the upper stream and an expansion occurs in the lower stream. The existence of this shock is more clearly elucidated in Figure 4.57, which shows transverse profiles of density at lobe crest ($z = 0$) at axial locations from the leading to trailing edges. The sharpest discontinuity in these profiles corresponds to density differences across the lobe boundary while a discontinuity (smeared out over two cells) can be seen propagating from lobe boundary upwards until it impinges on the upper wall at $x/\lambda = 1.25$. A high density, high pressure region appears in the expansion fan below the lobe. Examination of Figure 4.58 shows that this high pressure region is a result of the conical shock that emanates from the crest on the far side of the channel impinging on the symmetry boundary. Interaction of compression and expansion waves occurs at the lobe surface as we move away from the leading edge region. This is reflected in the loading distribution shown in Figure 4.59 and Figure 4.60. The shock at leading edge and crest can also be deduced from this figure.

The circulation distribution at lobe trailing edge is shown in Figure 4.61. The profile is similar to that found in the subsonic case, both peaking at almost identical normalized values (1.97×10^{-2} for the subsonic case and 2.06×10^{-2} for the supersonic case. The total circulation is computed to be $\Gamma = 1.108$ so that its nondimensional value is

$$\Gamma^* = 0.554 \tag{4.35}$$

which again is not very different from that of the subsonic case.

Figure 4.62 shows that the circulation remains almost constant up to a point about three wavelengths downstream of the lobe trailing edge at which point quite large oscillations in circulation of about 10% of the trailing edge circulation can be seen. These results indicate that the solution in

the flow domain within 3λ of the trailing edge can reasonably be used for analysis. Total pressure variation in the mixing duct (Figure 4.63) is characterized by a maximum absolute value of about 72% of the freestream total pressure. Some of this variation is due to the shock system in the lobe region but there is also negative total pressure variation that is numerical in origin. Figure 4.65 and Figure 4.64 show that, like the subsonic case, two distinct streamwise vortices are again formed in the mixing duct. Figure 4.66 shows that s_i varies with axial distance in a similar fashion to the subsonic case in the region of interest.

4.7 Summary

Table 4.1 shows the results of the calculations discussed in the previous four sections and a comparison with the results of the UTRC experimental investigation [3]. They can be summarized as follows

(1) Good qualitative agreement is found between computed results and experimentally-measured results for the low penetration mixer in terms of trailing edge circulation, v_y distribution, and the secondary velocity vector field

(2) The effect of compressibility on the generation of streamwise vorticity and on the large scale motions in the mixing layer is found to be small for the lobe geometries investigated. This can be seen by comparing rows 1 and 2 for the low penetration mixer and rows 3 and 4 for the high penetration mixer. When the inflow Mach number M_∞ increases from 0.5 to 2.0, the computed results show that the trailing edge circulation Γ_{te} and the growth in interface area $\partial s_i/\partial x$ remains essentially unchanged in the case of the low penetration and high penetration mixers.

(3) Comparison of the circulation and interface length variation results for constant M_∞ reveals a close correlation between Γ and $\partial s_i/\partial x$. This can be seen by comparing the

values in Table 4.1

(4) The dependence of Γ_{te} on the penetration angle α and the trailing edge amplitude a/λ can be seen to agree with the inviscid scaling law derived in [3]. The scaling law is derived in an approximate analysis [3] that gives the following expression for the circulation introduced by a lobed mixer

$$\Gamma = C_1 U_{ref} a \tan \alpha \tag{4.36}$$

Values of C_1 found in [3] and in the present work are listed in the eighth and ninth columns in Table 4.1. Agreement between the numerical and experimental values is good.

Table 4.1: Table of Lobed Mixer Results

Mixer	a/λ	α	M_∞	Γ	Γ^*	$\frac{\partial s_i}{\partial x}$	C_1	$C_{1_{exp}}$
LPM	0.25	5.77	0.5	0.045	0.090	0.120	3.60	-
LPM	0.25	5.77	2.0	0.189	0.095	0.128	3.78	-
HPM	0.5	22	0.5	0.268	0.536	0.784	2.68	-
HPM	0.5	22	2.0	1.108	0.554	0.784	2.77	-
LPM(UTRC)	0.25	5.77	0.1	0.008	0.080	-	-	3.3
HPM(UTRC)	1.0	22	0.1	0.098	0.980	-	-	2.4

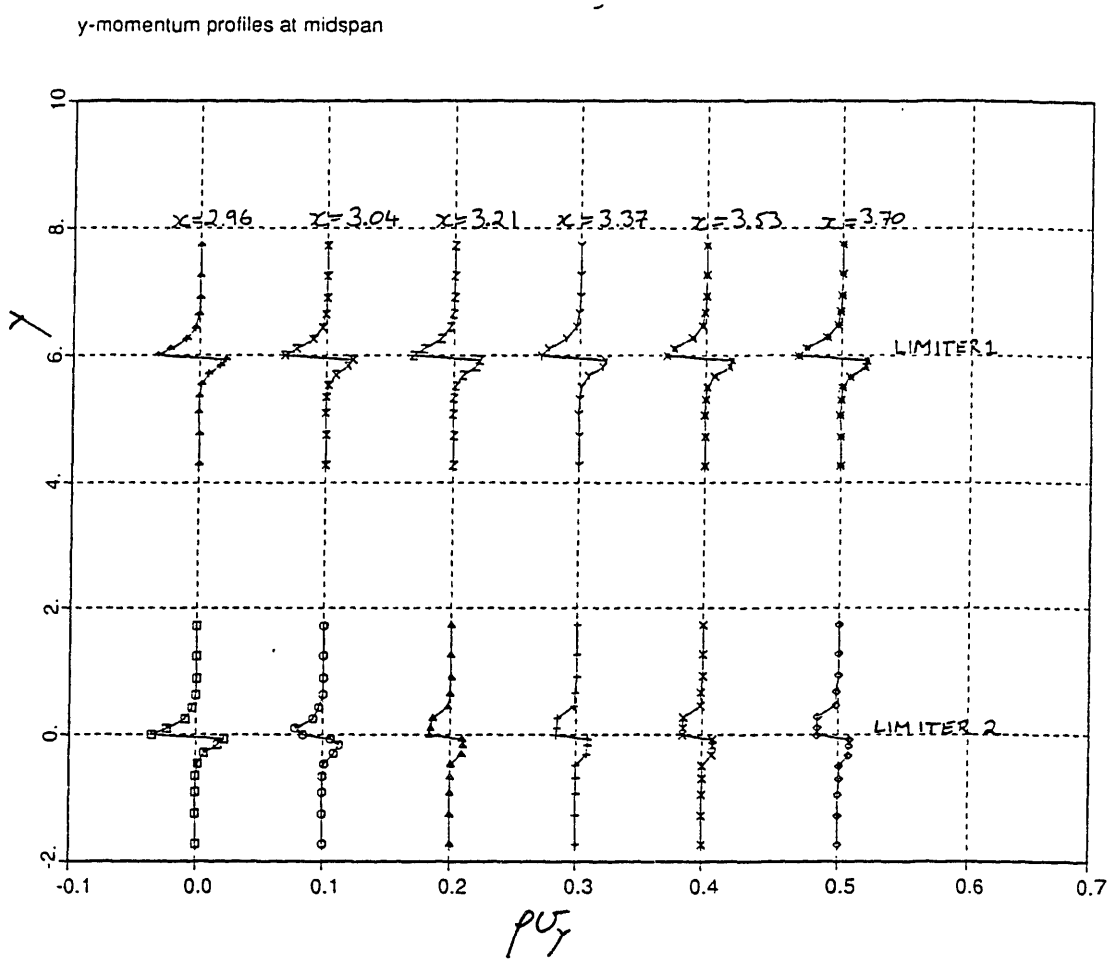

Figure 4.1: ρv_y profiles at midspan of lobe trailing edge and various axial locations downstream for coarse grid calculations. Limiter 1 is the Zalesak limiter with Boris-Book limiter prelimiting the $\xi-$ and $\varsigma-$ fluxes. Limiter 2 is the Zalesak limiter with Boris-Book limiter prelimiting the $\xi-$, $\eta-$ and $\varsigma-$ fluxes.

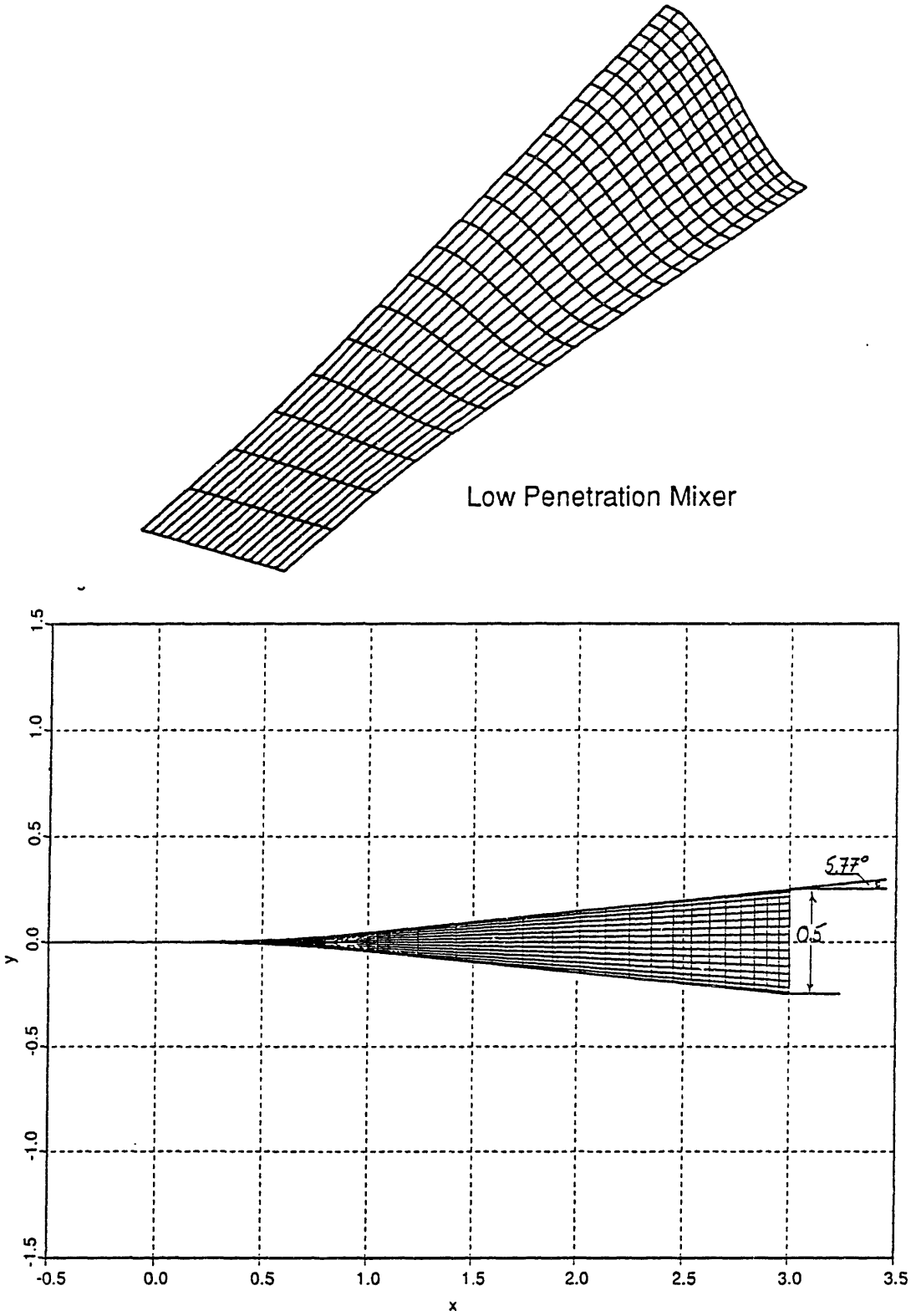

Figure 4.2: Low penetration mixer: (a) isometric view; (b) front elevation

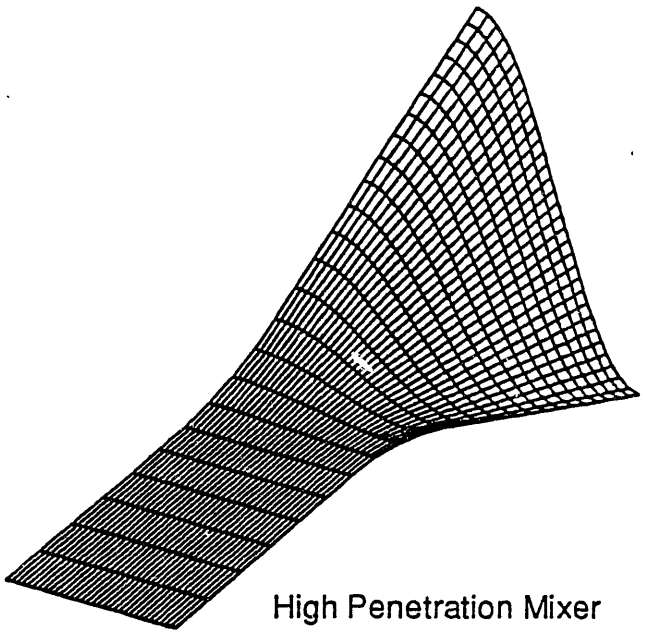

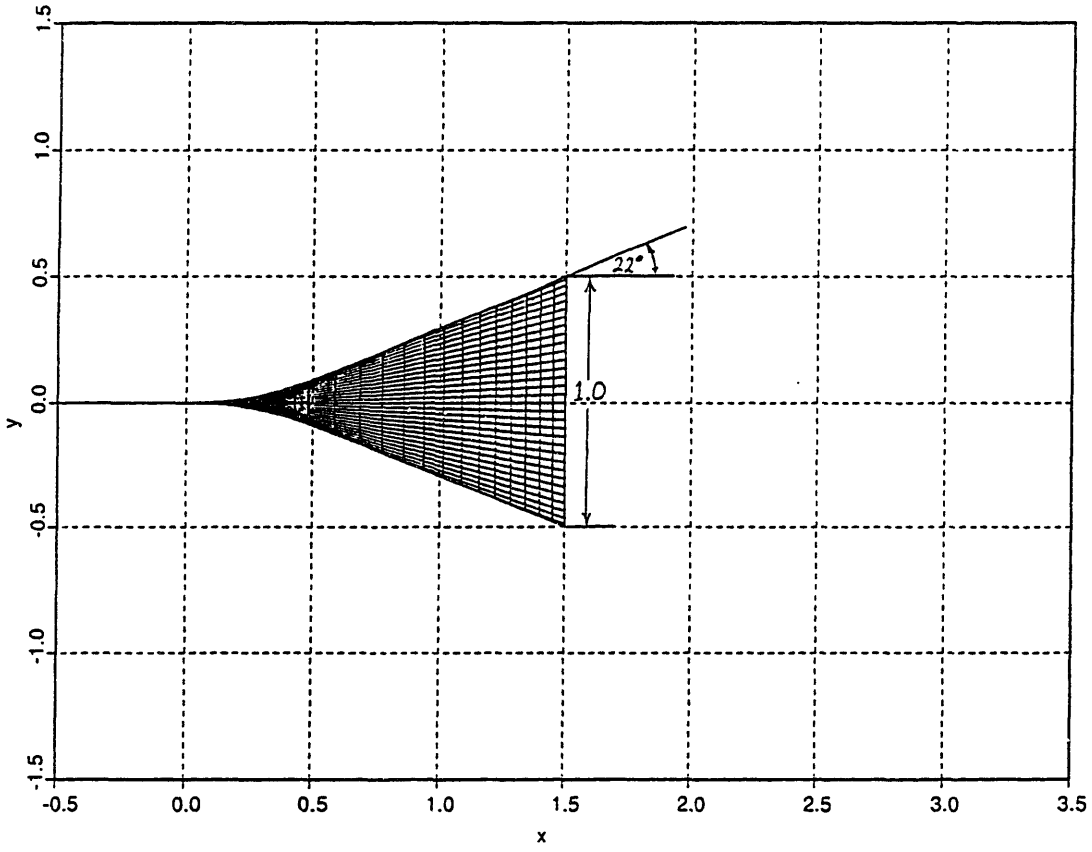

Figure 4.3: High penetration mixer: (a) isometric view; (b) front elevation

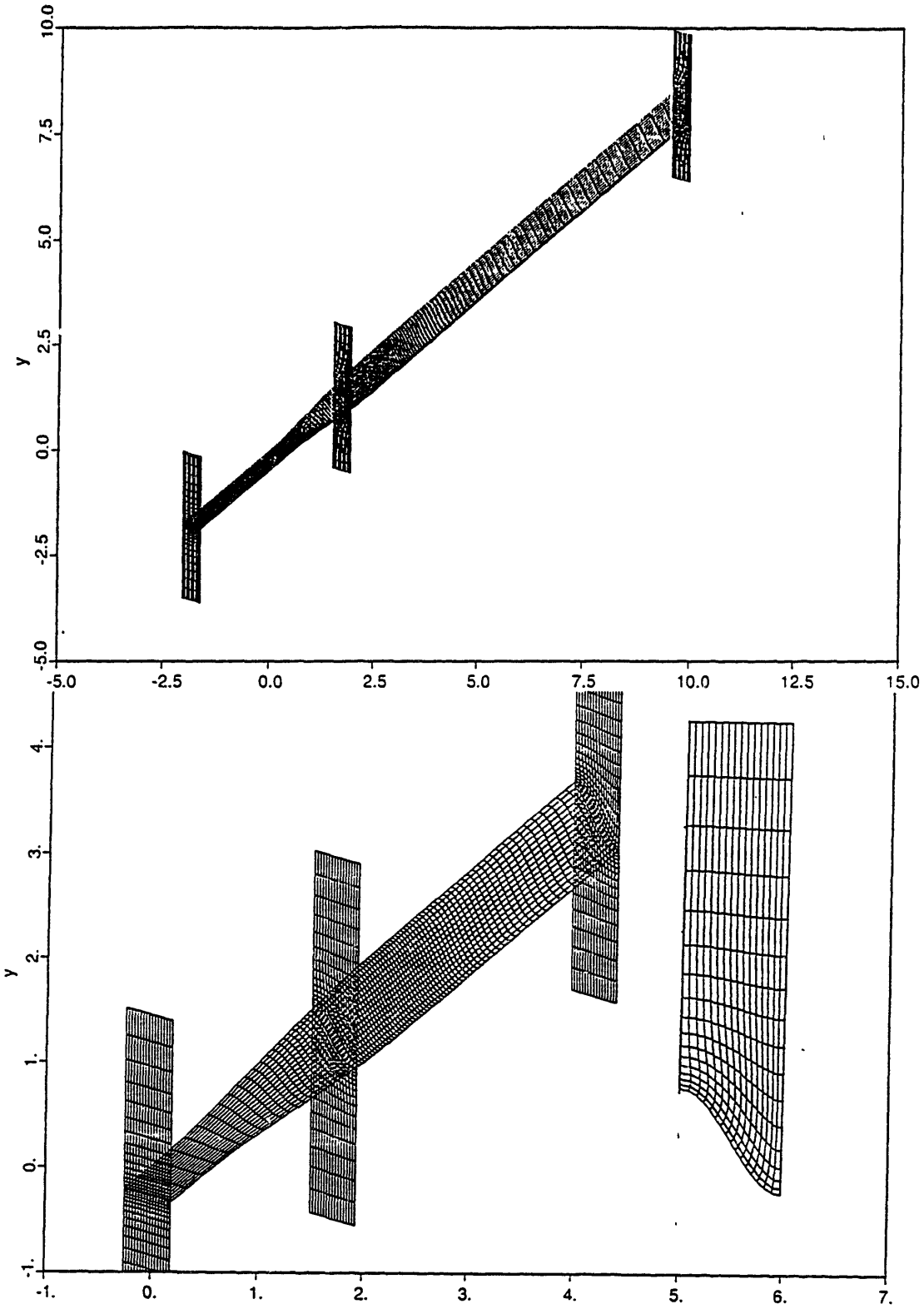

Figure 4.4: Numerical grid generated for the low penetration mixer: (a) isometric view of inflow, outflow, trailing edge and mid channel computational planes; (b) magnified isometric view showing $\xi = 10$, $\xi = 33$, $\xi = 97$ and $\eta = 17$ planes; (c) trailing edge plane.

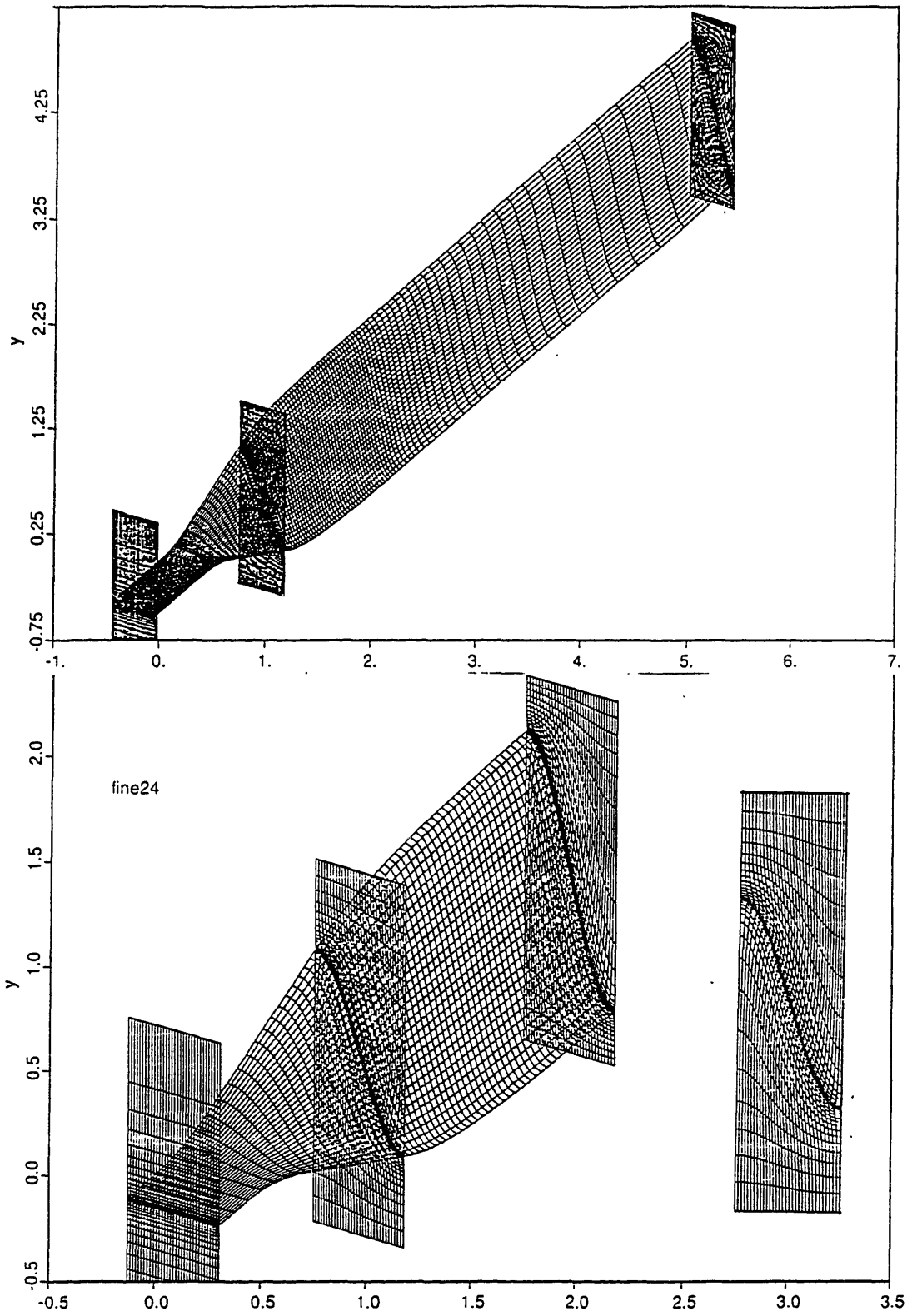

Figure 4.5: Numerical grid generated for the high penetration mixer: (a) isometric view of inflow, outflow, trailing edge and mid channel computational planes; (b) magnified isometric view showing $\xi = 9$, $\xi = 25$, $\xi = 65$ and $\eta = 17$ planes; (c) trailing edge plane.

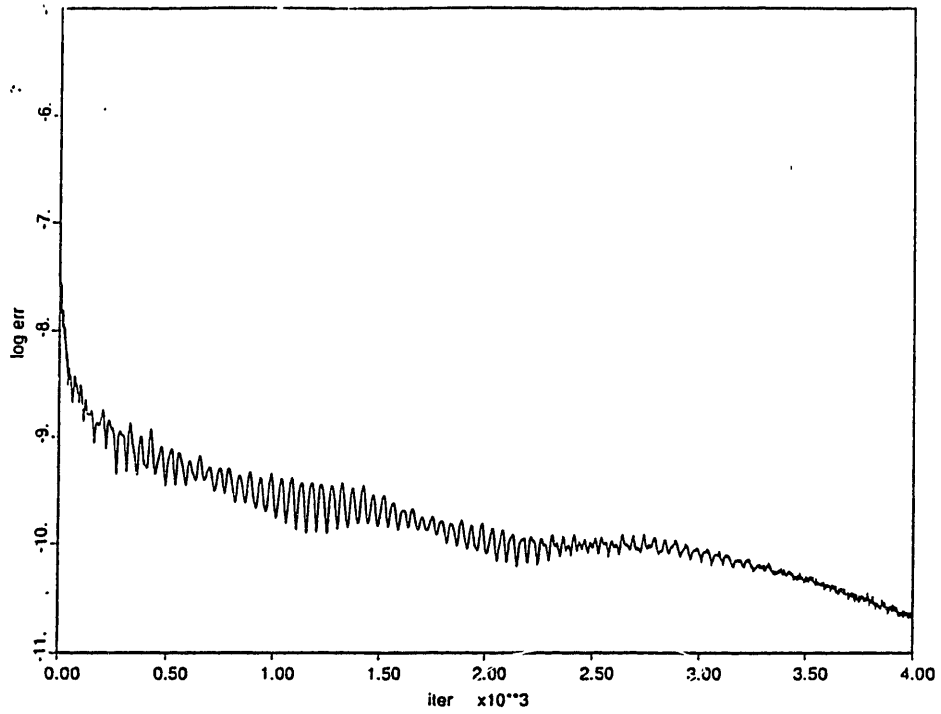

Figure 4.6: Convergence history for subsonic low penetration mixer case

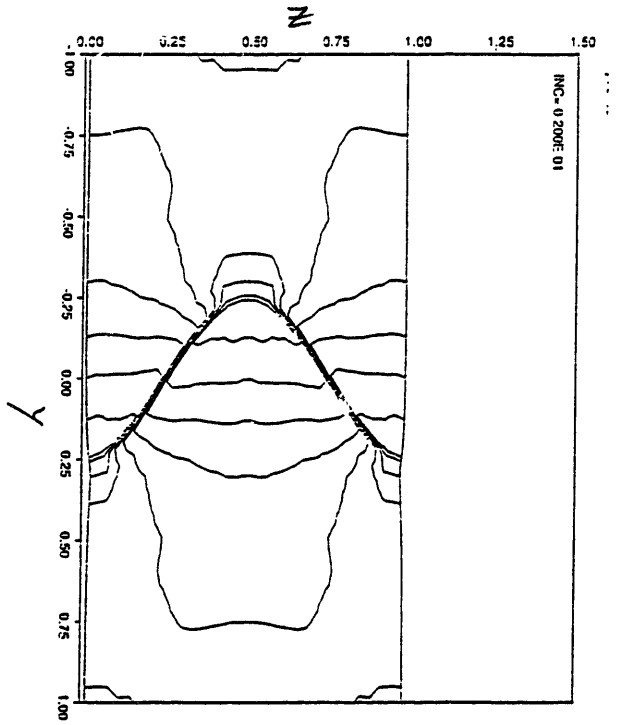

Figure 4.7: Contour plot of transverse velocity normalized by U_∞ at an axial location 0.02λ downstream of the lobe trailing edge. Nine contours in increments of .02 between -.08 and +.08 are plotted.

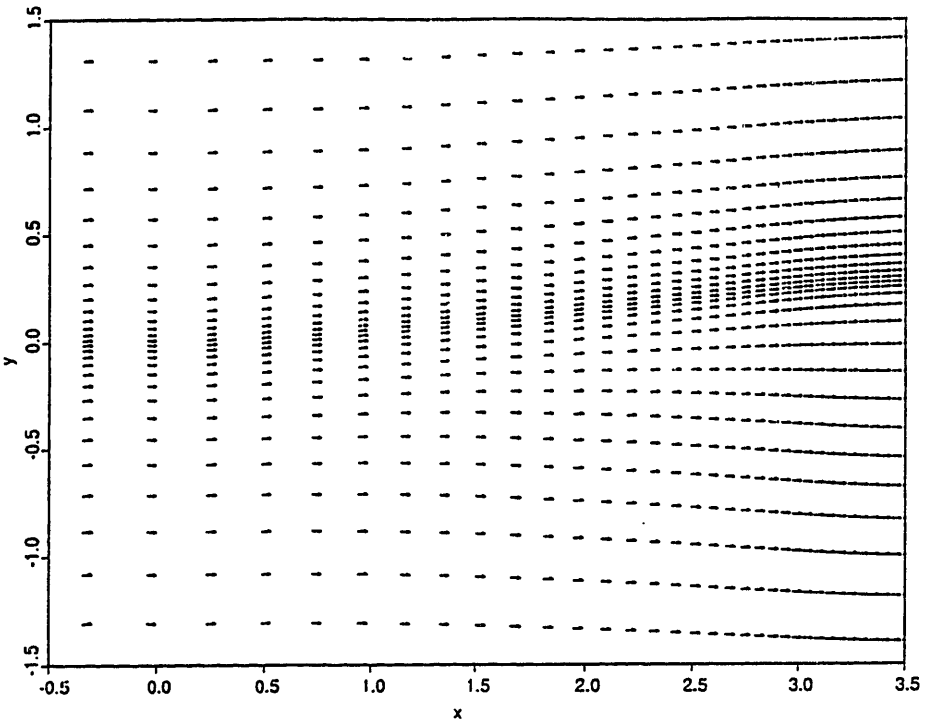

Figure 4.8: Velocity vector field formed by v_x and v_y components at the spanwise location corresponding to the lobe crest $z = 0$

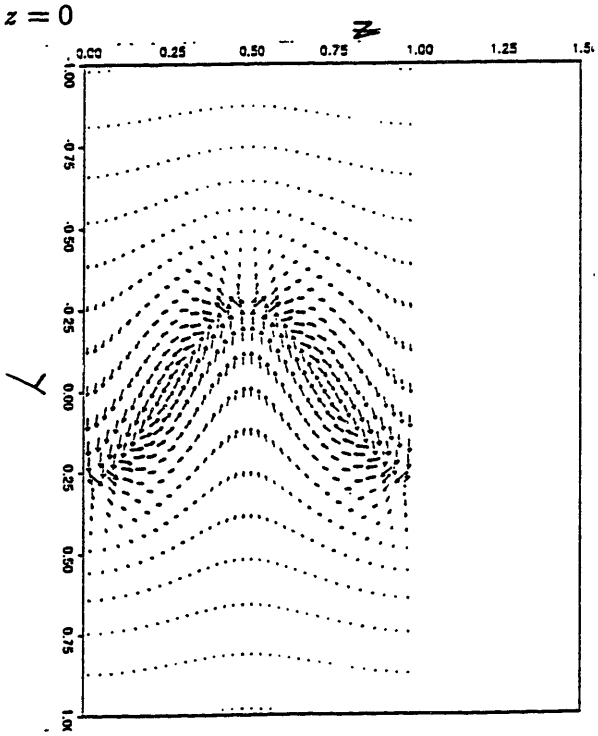

Figure 4.9: Secondary velocity vector field at an axial location 0.02λ downstream of the lobe trailing edge

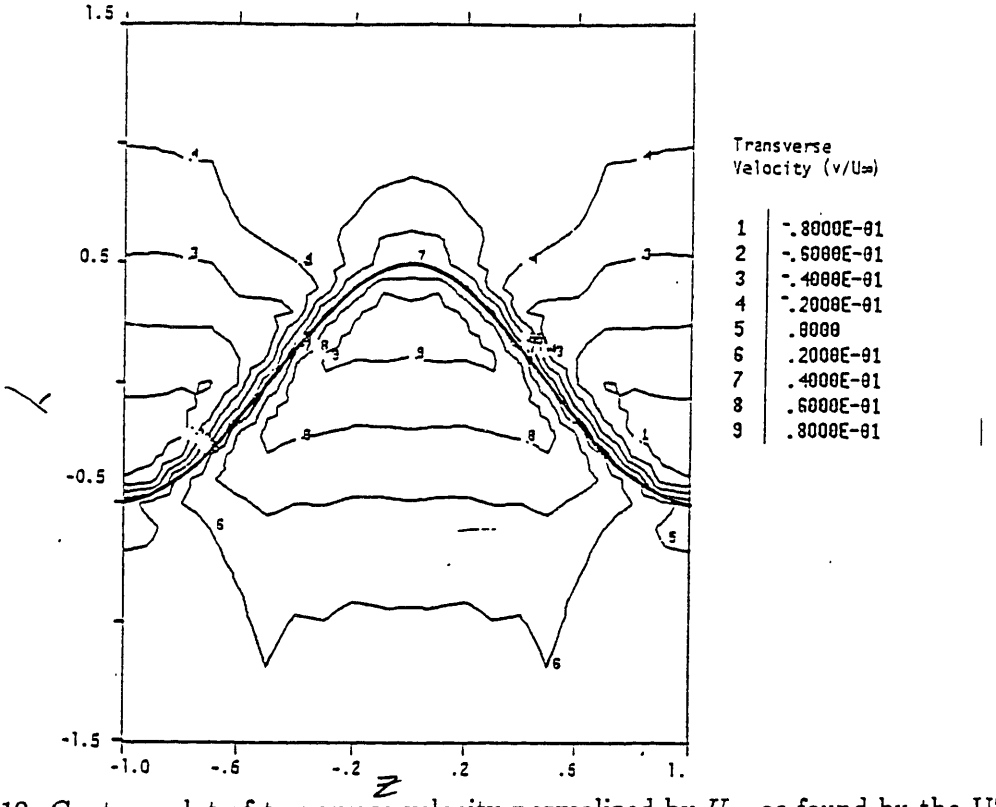

Figure 4.10: Contour plot of transverse velocity normalized by U_∞ as found by the UTRC experimental investigation

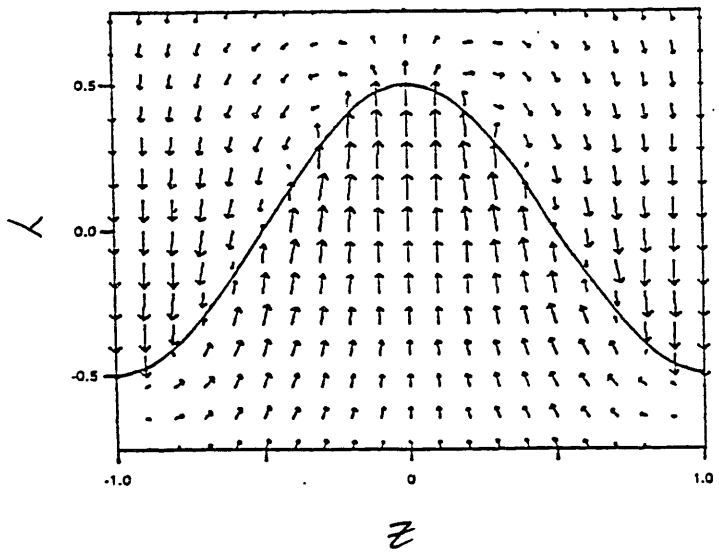

Figure 4.11: Secondary velocity vector field as found by the UTRC experimental investigation

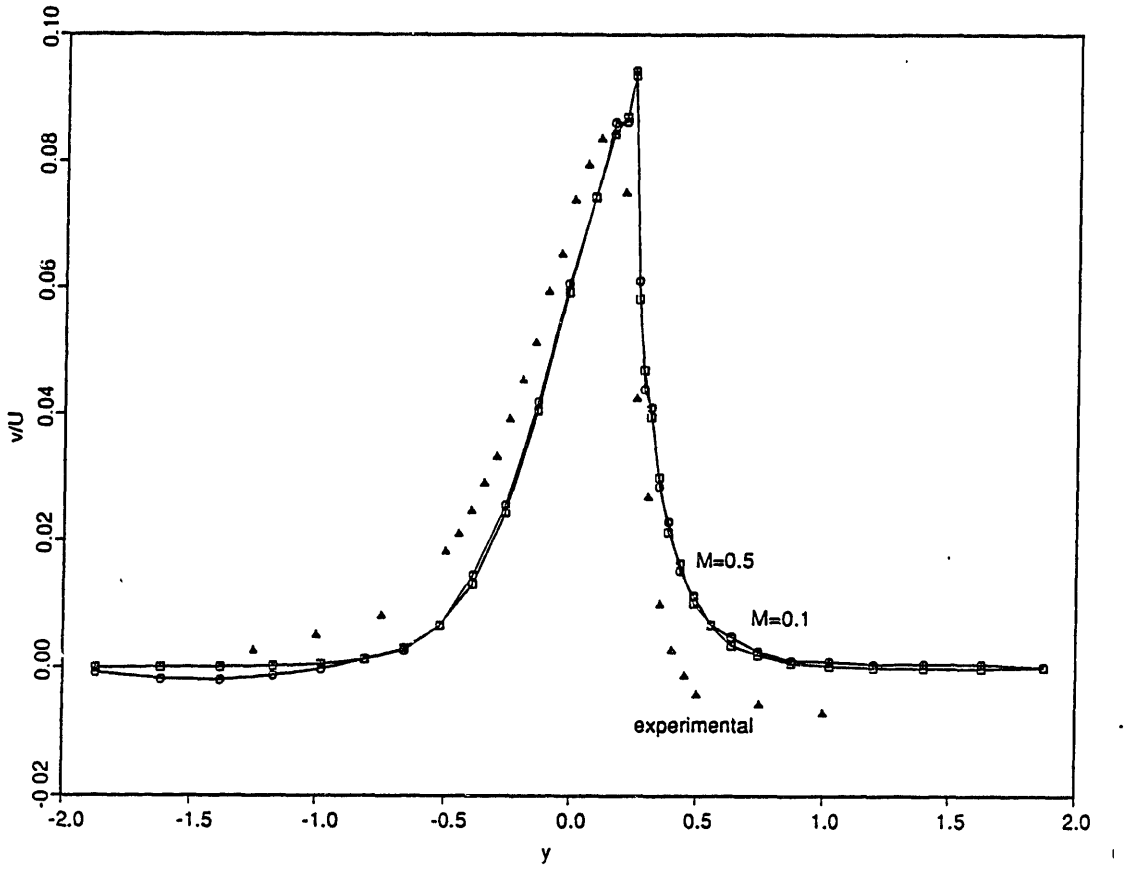

Figure 4.12: Transverse velocity profiles versus transverse distance, y at lobe crest ($z = 0$) and at an axial location just downstream of the lobe trailing edge as found by numerical investigations ($M_\infty = 0.5$ and $M_\infty = 0.1$) and the UTRC experimental investigation

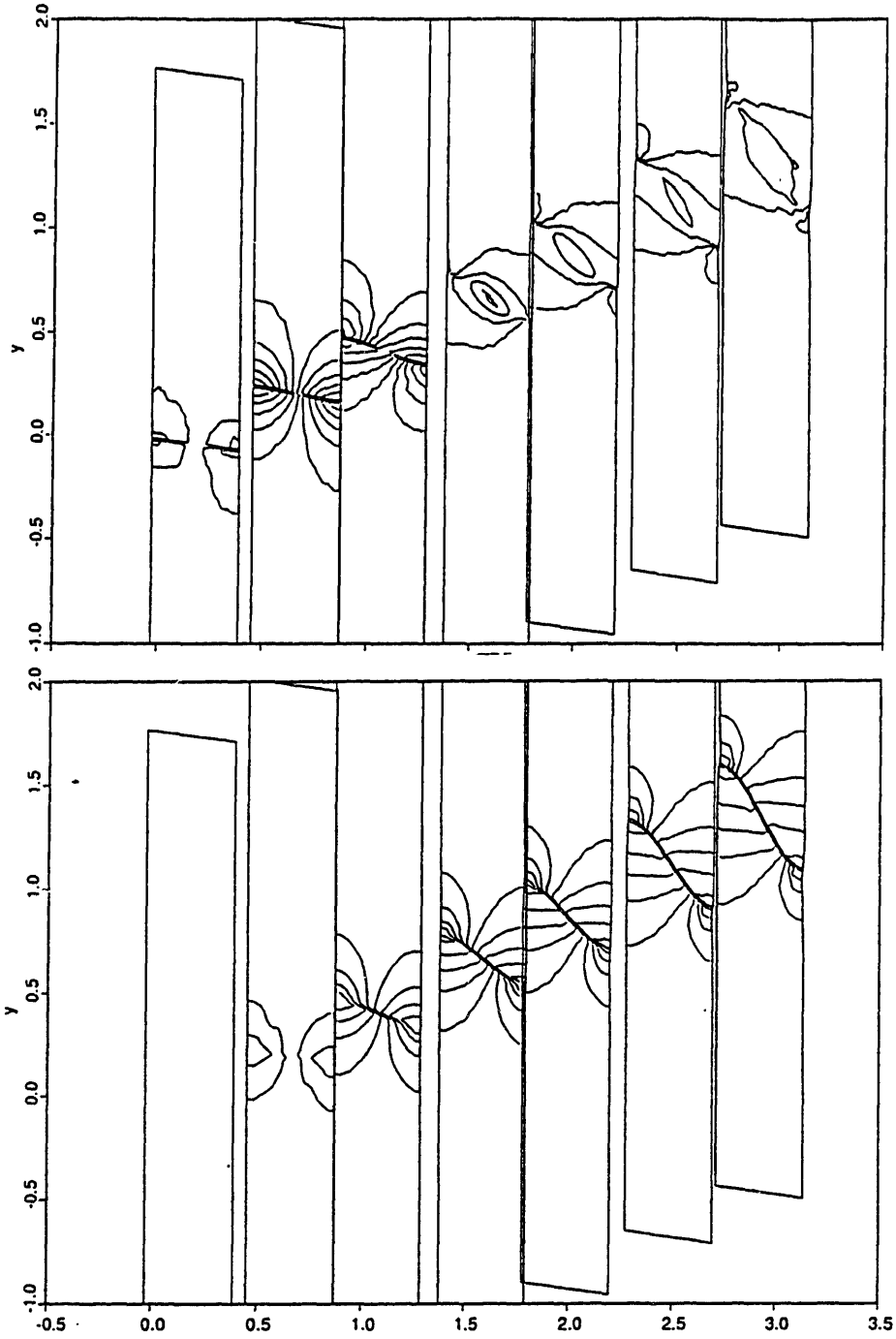

Figure 4.13: Three-dimensional contour plots of c_p, v_y and v_z. The first and last axial slices are located at the leading and trailing edges, respectively. The exact axial locations are $x/\lambda = -.05, 0.49, 0.94, 1.50, 1.95, 2.49, 2.97$. Contours are as follows:

c_p: 10 contours from -.0225 to +.0225 in increments of .005;

v_y: 8 contours from -.035 to +.035 in increments of .01

v_z: 10 contours from -.045 to +.045 in increments of .01

(continued overleaf)

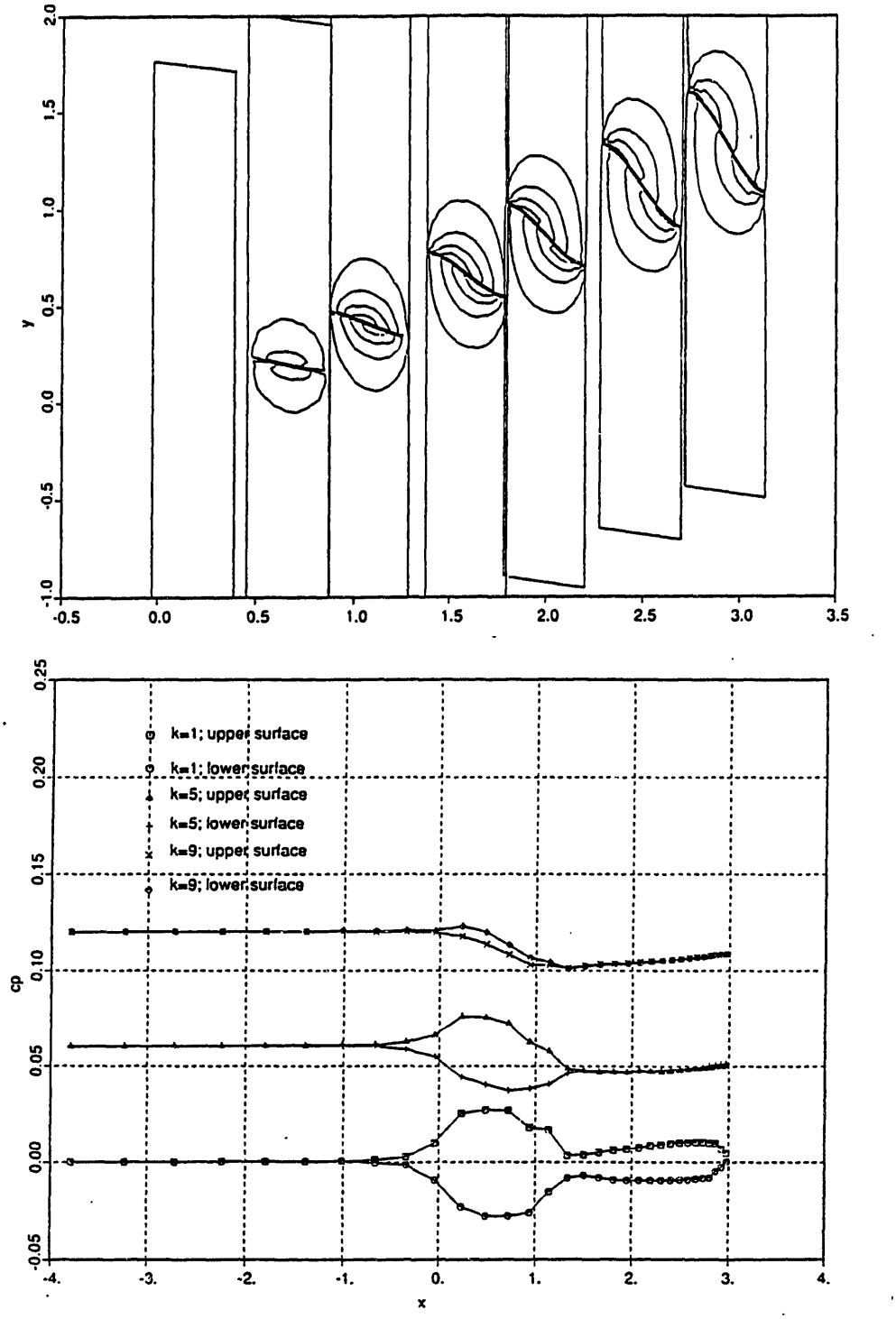

Figure 4.14: Axial variation of $c_{p_{upper}}$ and $c_{p_{lower}}$ for crest, quarterspan and midspan spanwise locations. These correspond to $\varsigma = 1, 5, 9$, respectively.

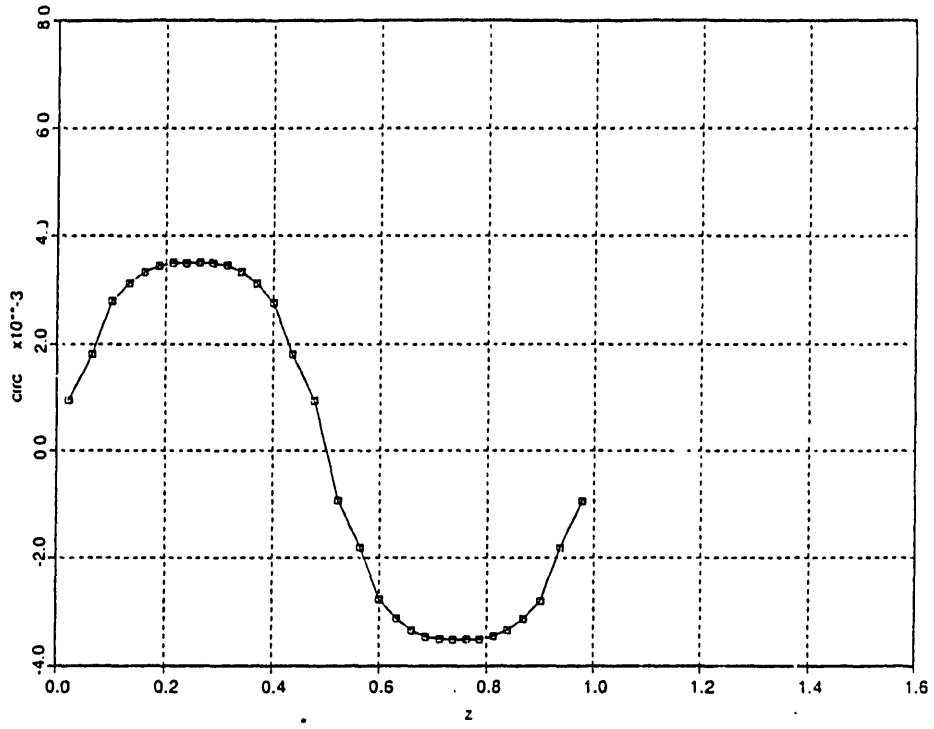

Figure 4.15: Circulation versus spanwise distance at lobe trailing edge.

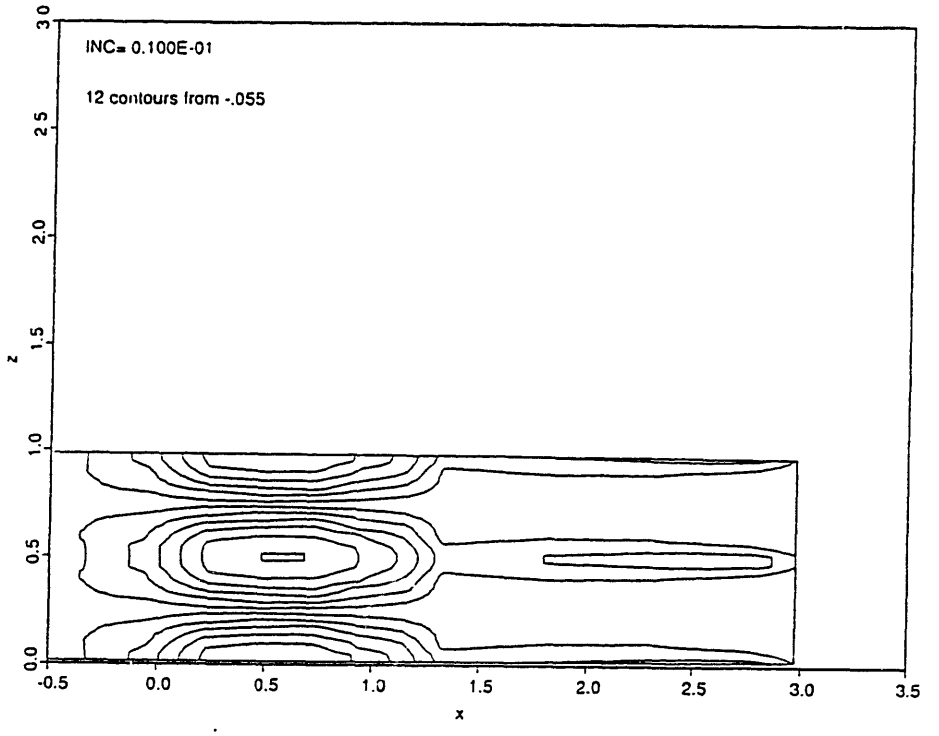

Figure 4.16: Loading $c_{p_{upper}} - c_{p_{lower}}$ on lobe surface projected onto a $y = constant$ surface

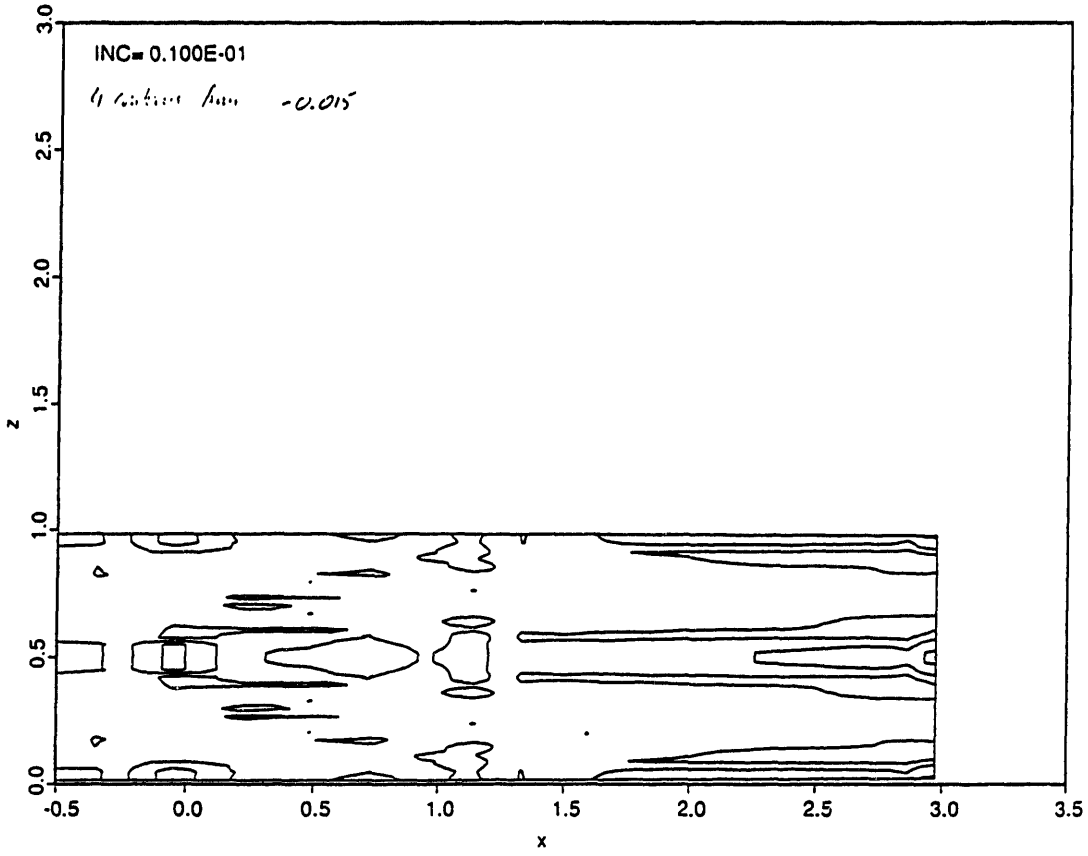

Figure 4.17: Residual from Equation 3.26 on lobe surface projected onto a y = constant surface. Four contours from -.015 to +.015 in increments of .01 are plotted.

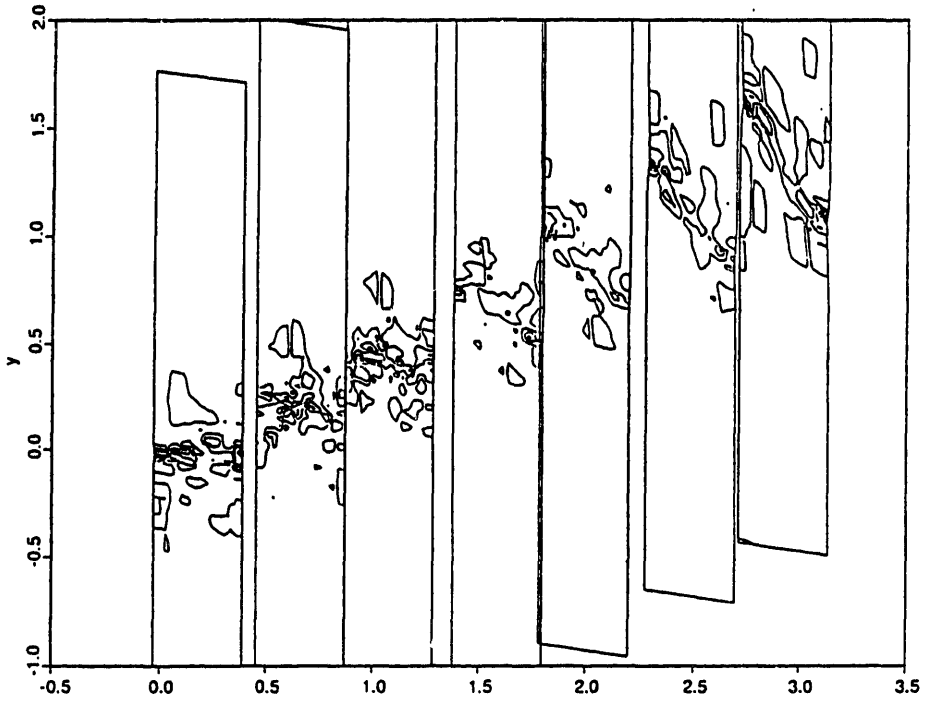

Figure 4.18: Threedimensional contour plot of total pressure change in flowfield around mixer. The first and last axial slices are located at the leading and trailing edges, respectively. The exact axial locations are $x/\lambda = -.05, 0.49, 0.94, 1.50, 1.95, 2.49, 2.97$. Eight contours from -1.75×10^{-3} to $+1.75 \times 10^{-3}$ in increments of 5×10^{-4} are plotted

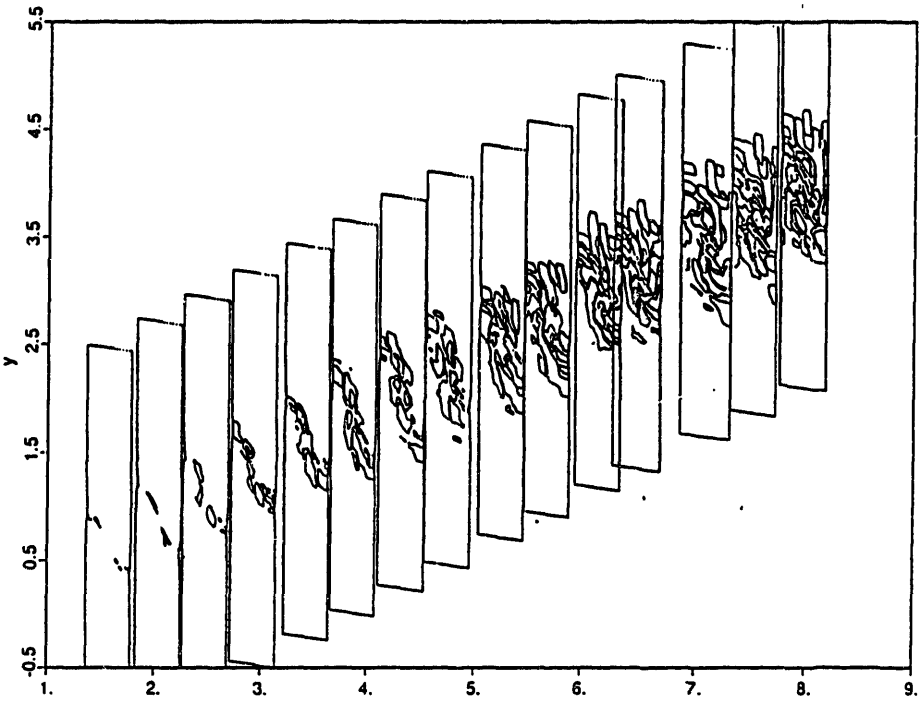

Figure 4.19: Contour plots of $\Delta P_t/P_\infty$ at various axial locations from lobe trailing edge to mixing duct exit. The axial locations are x/λ =2.97, 4.01, 4.97, 5.96, 7.06, 8.03, 9.02, 9.97, 11.06, 12.01, 13.06, 13.83, 15.11, 16.04, 17.05, 18.13, 18.71. Nine contours from -9×10^{-3} to 7×10^{-3} are plotted in increments of 2×10^{-3}

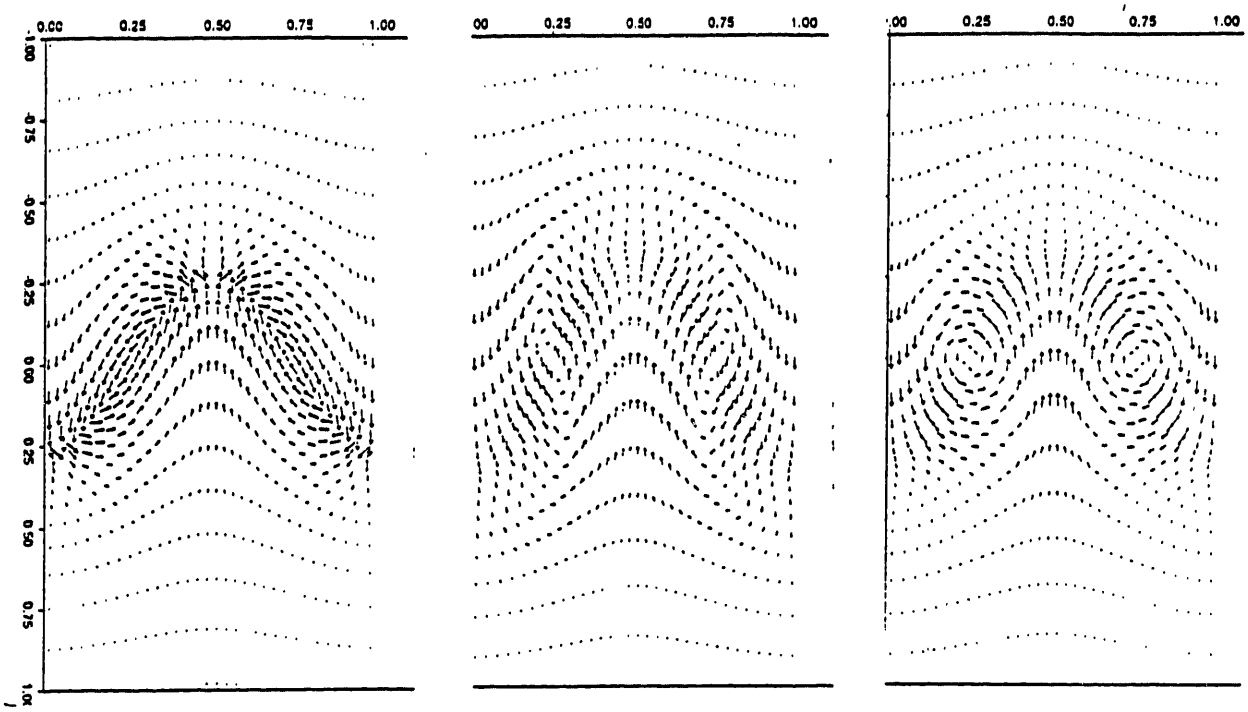

Figure 4.20: Secondary velocity vector field at axial locations $x/\lambda = 3.02, 11.06, 18.71$

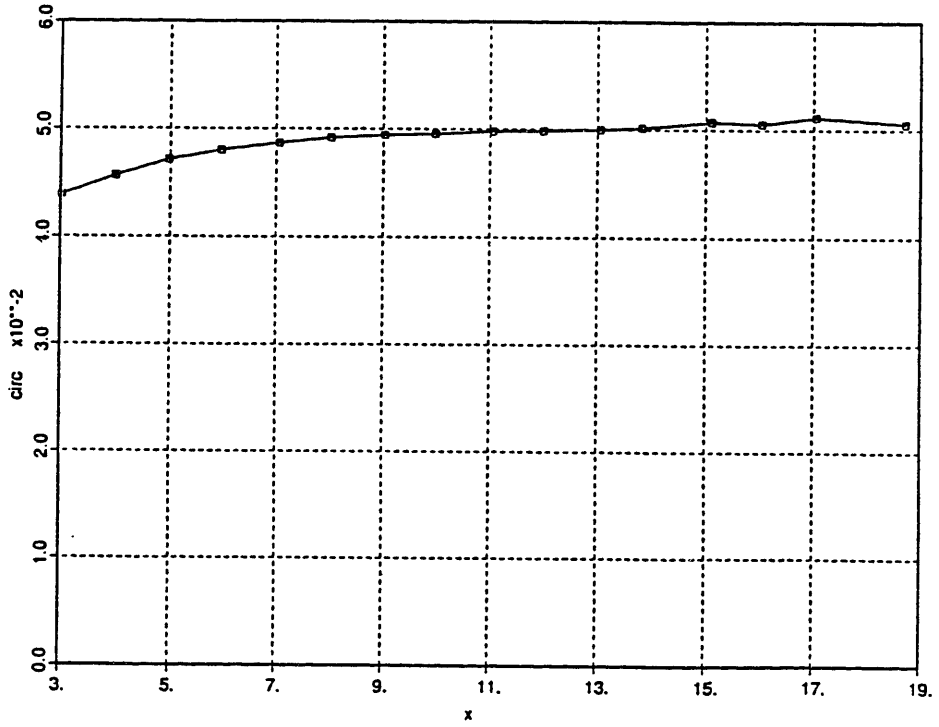

Figure 4.21: Circulation variation with axial distance

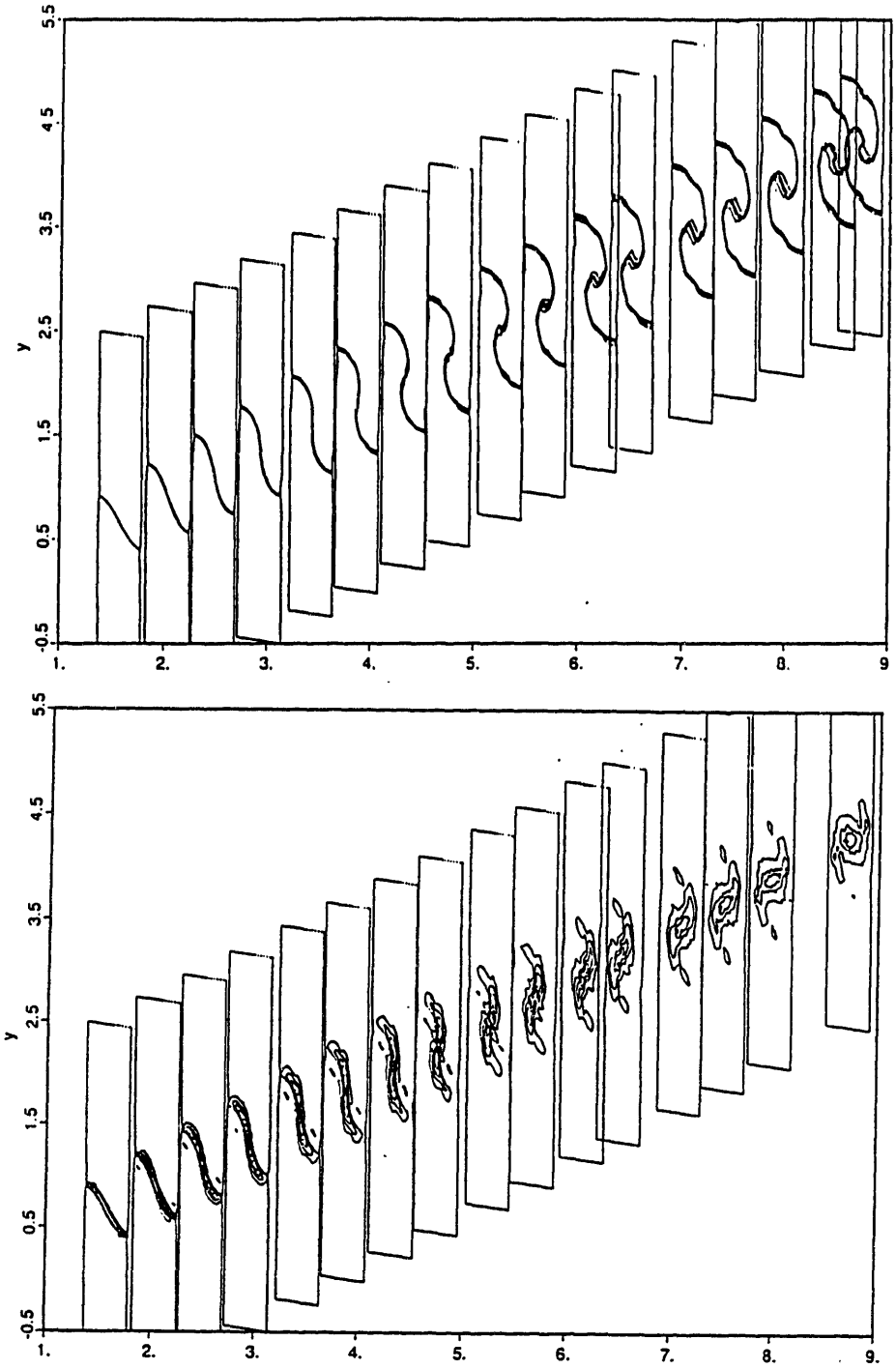

Figure 4.22: Contour plots of ψ, ω_x and c_p, at various axial locations from lobe trailing edge to mixing duct exit. The axial locations are x/λ =2.97, 4.01, 4.97, 5.96, 7.06, 8.03, 9.02, 9.97, 11.06, 12.01, 13.06, 13.83, 15.11, 16.04, 17.05, 18.13, 18.71. Contours are as follows:

ψ: 5 contours from 0.3 to 0.7 in increments of .1;

ω_x: 9 contours from 0.1 to 1.5 in increments of .02

c_p: 5 contours from -.0125 to +.0075 in increments of .005

(continued overleaf)

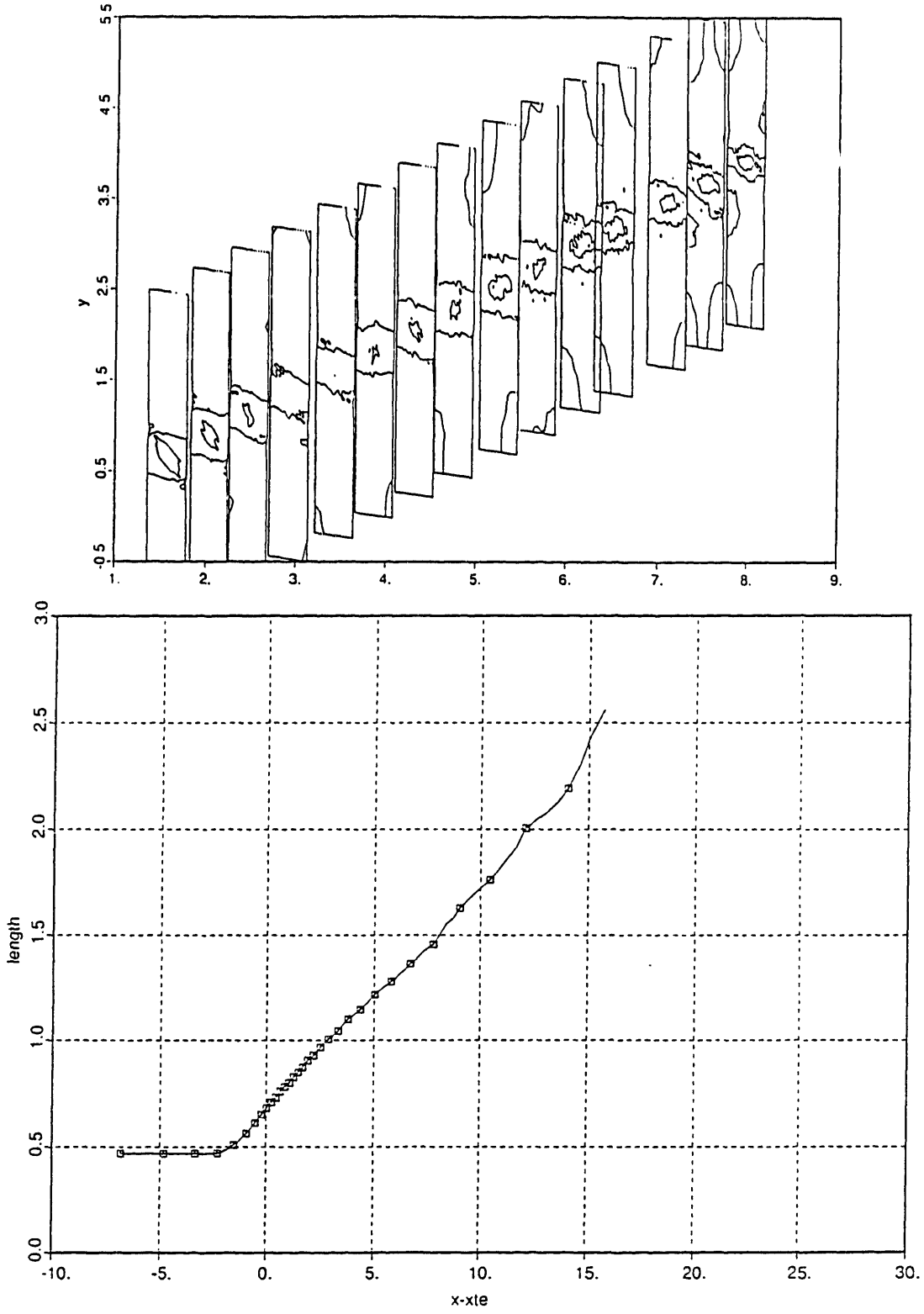

Figure 4.23: Length of $\psi = 0.5$ contour versus axial distance for subsonic low penetration calculation

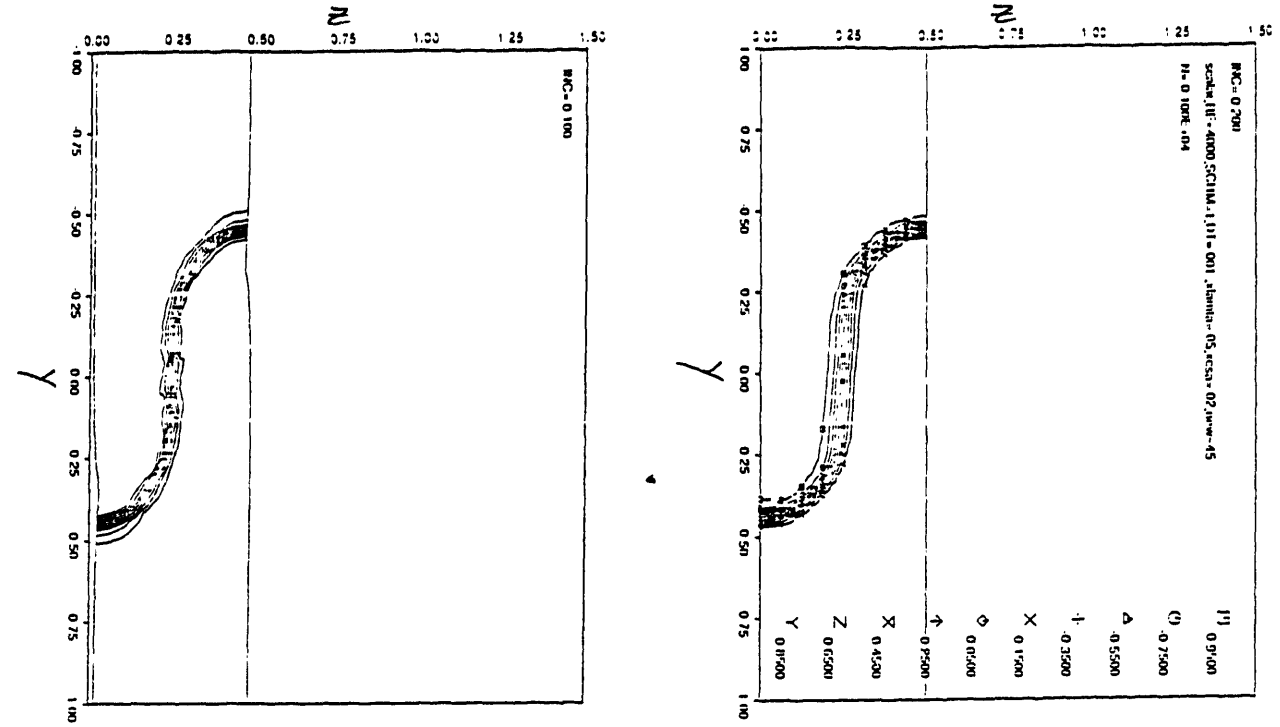

Figure 4.24: Comparison of ψ contour plots at an axial location 4λ downstream of the lobe trailing edge as calculated by 3-D FCT method (left) and Trefftz plane method

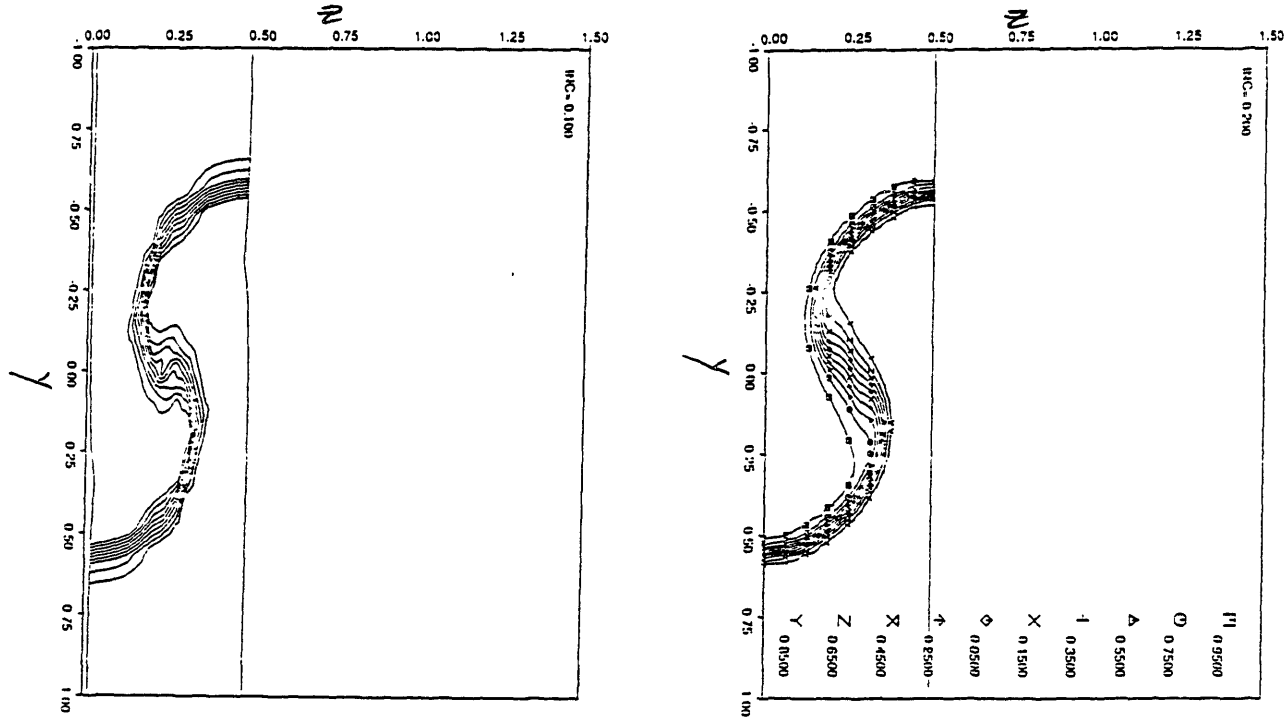

Figure 4.25: Comparison of ψ contour plots at an axial location 9λ downstream of the lobe trailing edge as calculated by 3-D FCT method (left) and Trefftz plane method

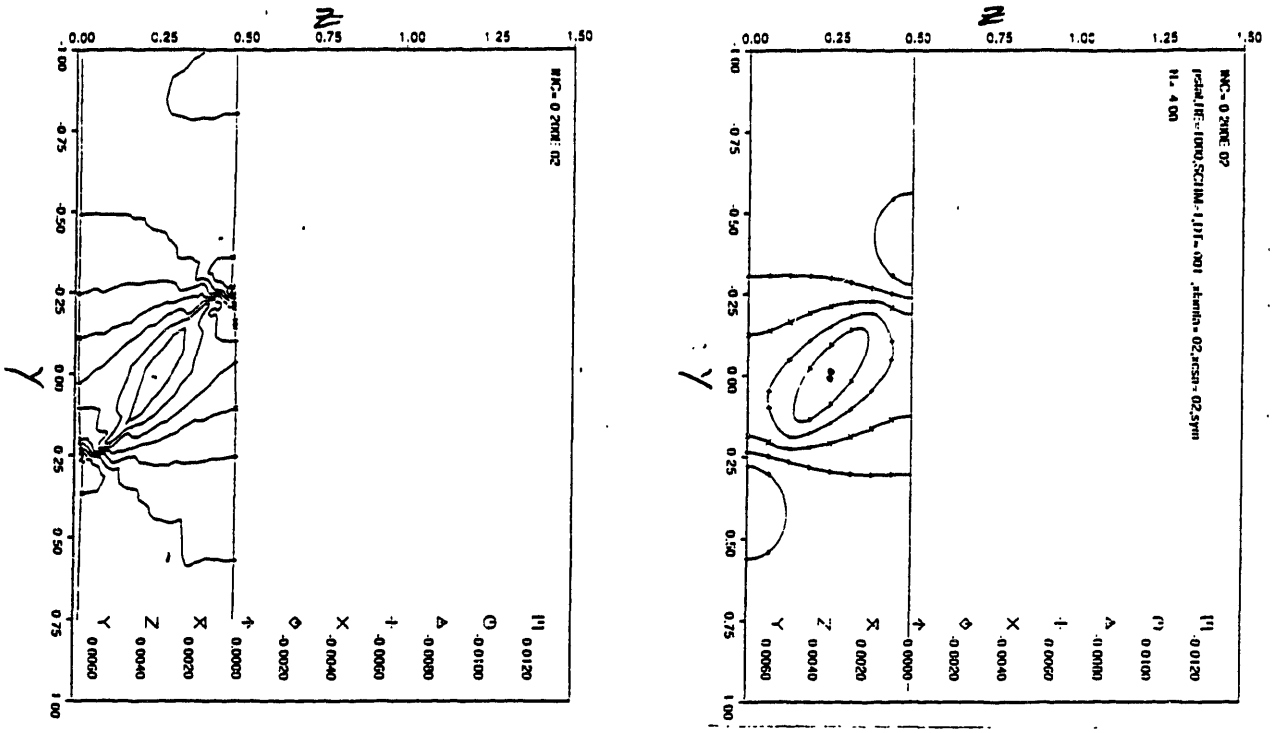

Figure 4.26: Comparison of c_p contour plots at the lobe trailing edge as calculated by 3-D FCT method (left) and Trefftz plane method

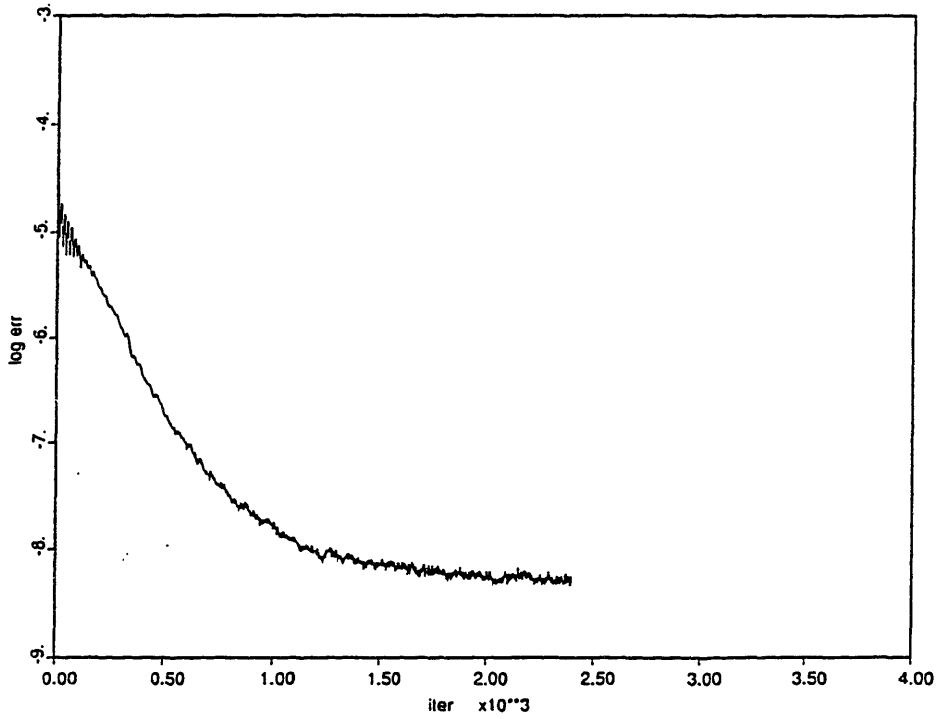

Figure 4.27: Convergence history for supersonic low penetration mixer case

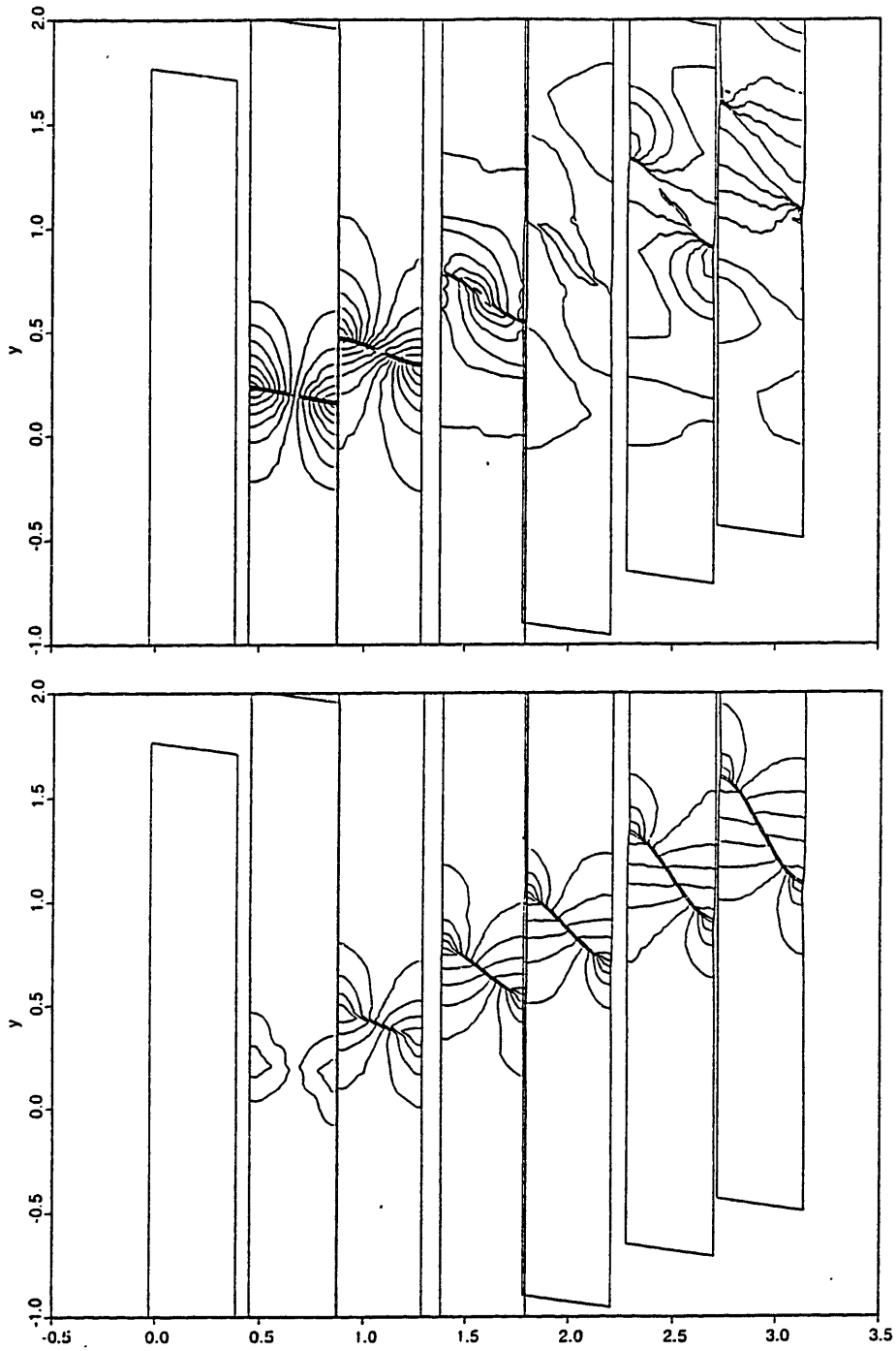

Figure 4.28: Three-dimensional contour plots of c_p, v_y and v_z for supersonic low penetation case. The first and last axial slices are located at the leading and trailing edges, respectively. The exact axial locations are $x/\lambda = -.05, 0.49, 0.94, 1.50, 1.95, 2.49, 2.97$. Contours are as follows:

c_p: 14 contours from -.0325 to +.0325 in increments of .005;

v_y: 10 contours from -.18 to +.18 in increments of .4

v_z: 10 contours from -.18 to +.18 in increments of .4

(continued overleaf)

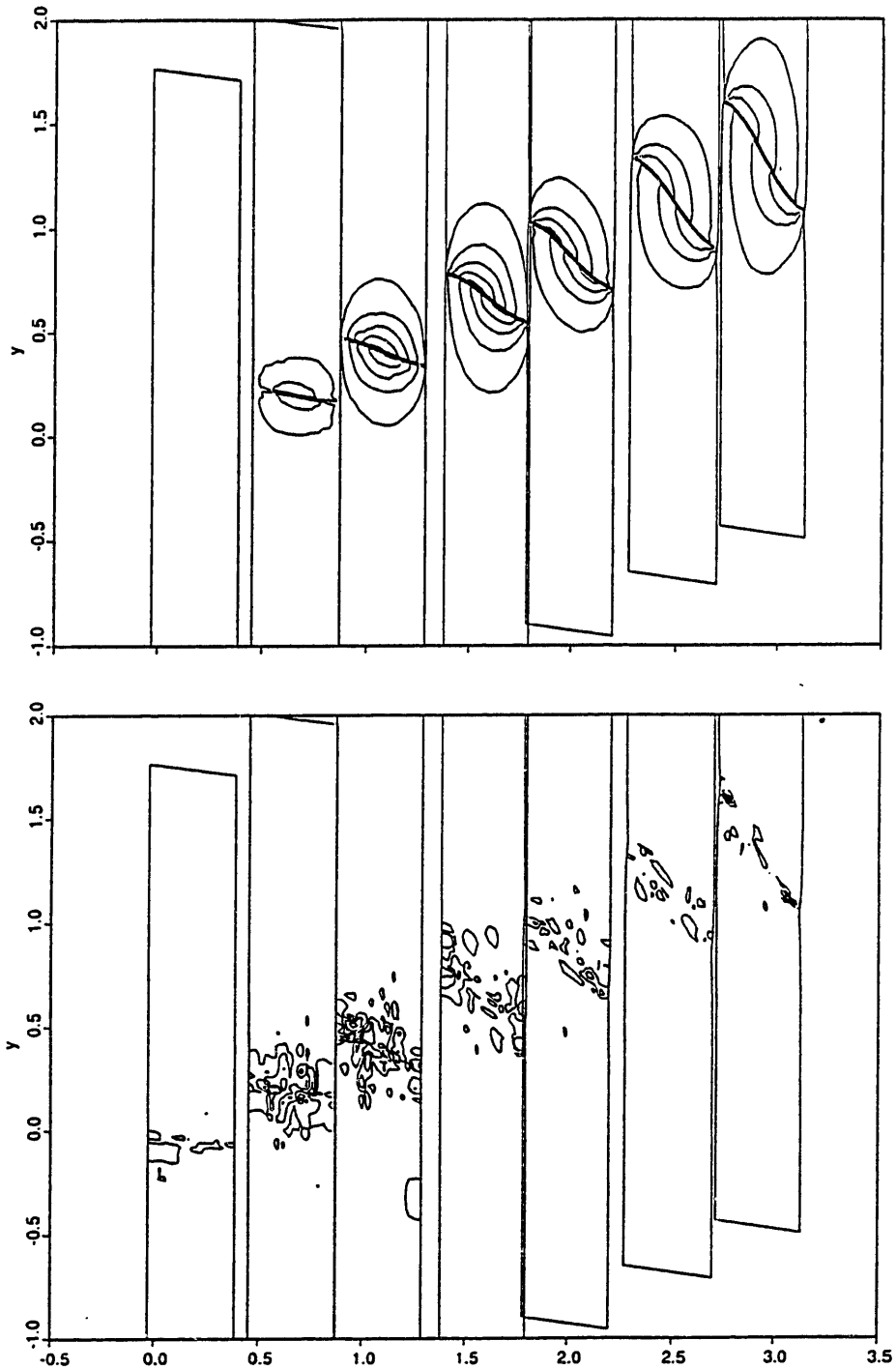

Figure 4.29: Threedimensional contour plot of total pressure change in flowfield around mixer. The first and last axial slices are located at the leading and trailing edges, respectively. The exact axial locations are $x/\lambda = -.05, 0.49, 0.94, 1.50, 1.95, 2.49, 2.97$. 12 contours from -2.75×10^{-2} to $+2.75 \times 10^{-2}$ in increments of 5×10^{-3} are plotted

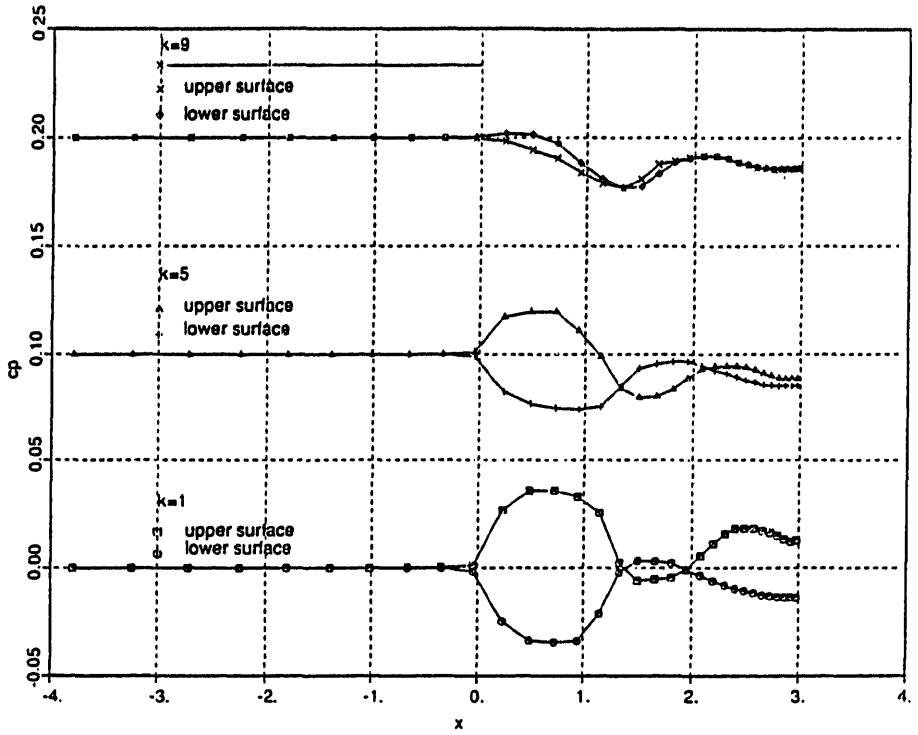

Figure 4.30: Axial variation of $c_{p_{upper}}$ and $c_{p_{lower}}$ for crest, quarterspan and midspan spanwise locations for supersonic calculation. These correspond to $\varsigma = 1, 5, 9$, respectively.

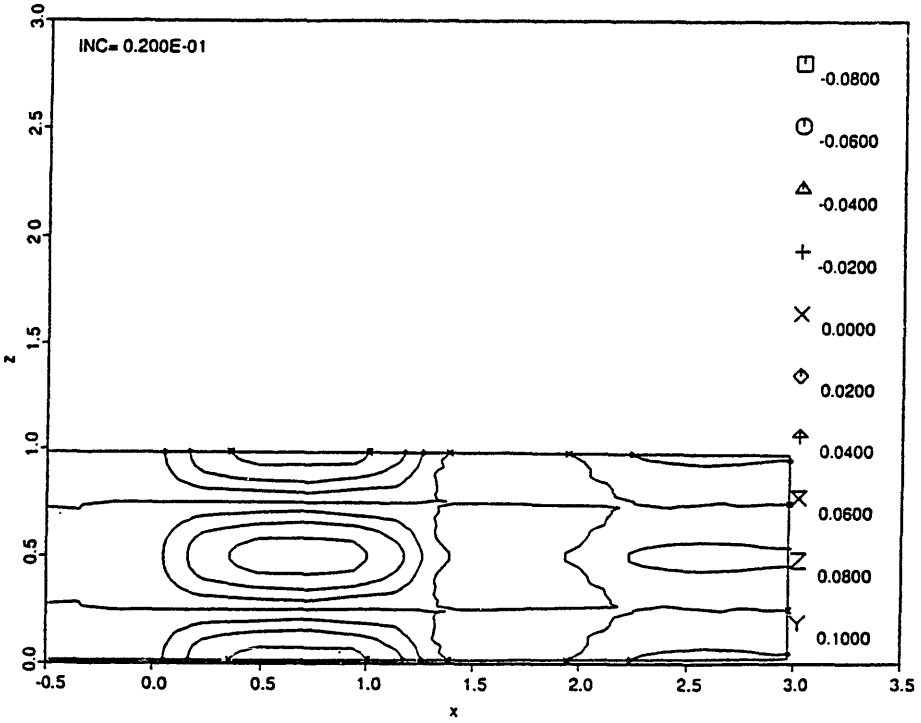

Figure 4.31: Loading $c_{p_{upper}} - c_{p_{lower}}$ on lobe surface projected onto a $y = consant$ surface for supersonic case.

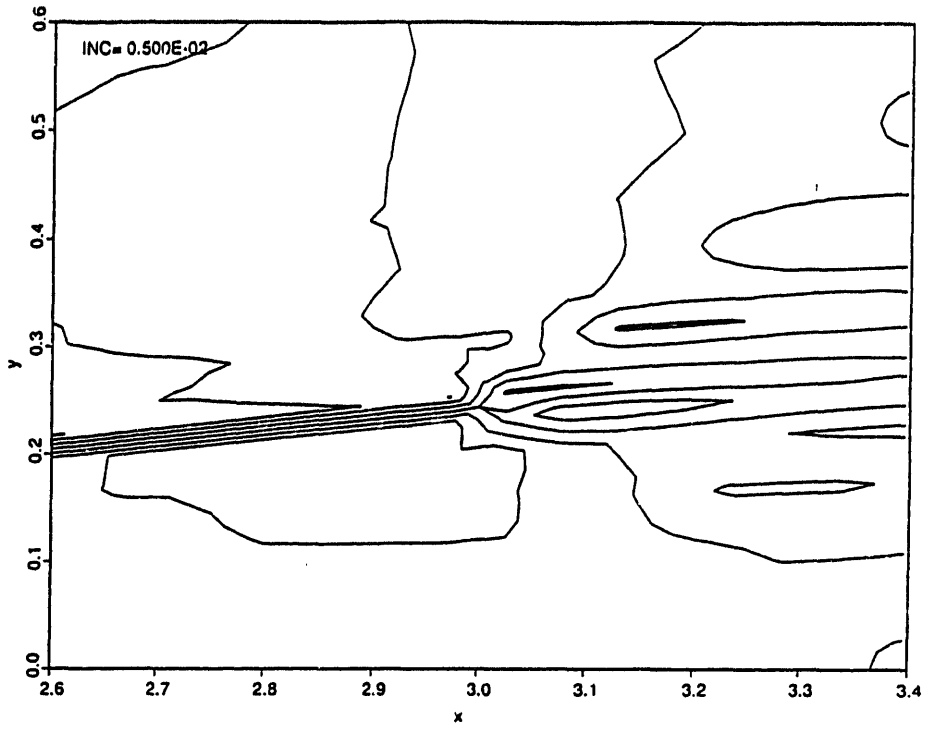

Figure 4.32: Contour plot of c_p at spanwise location adjacent to the symmetry boundary ($\zeta = 1$)

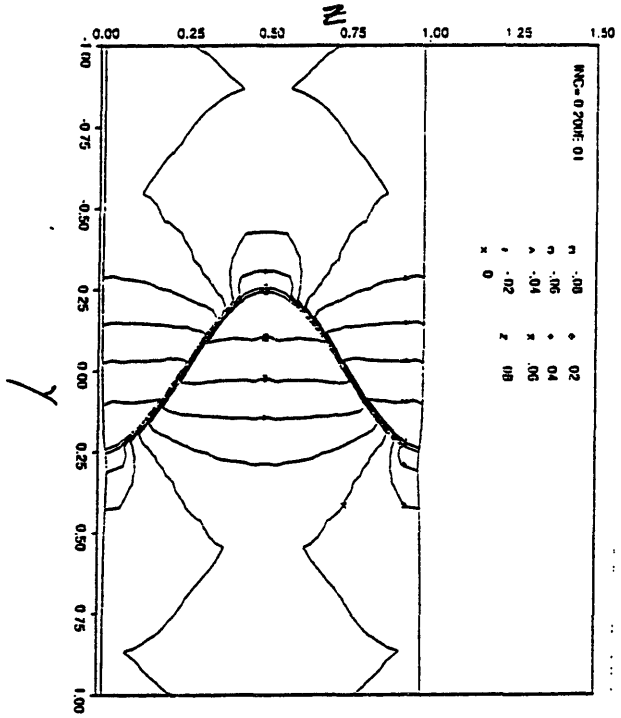

Figure 4.33: Contour plot of transverse velocity normalized by U_∞ at an axial location 0.02λ downstream of the lobe trailing edge for supersonic case. Nine contours in increments of .02 between -.08 and +.08 are plotted.

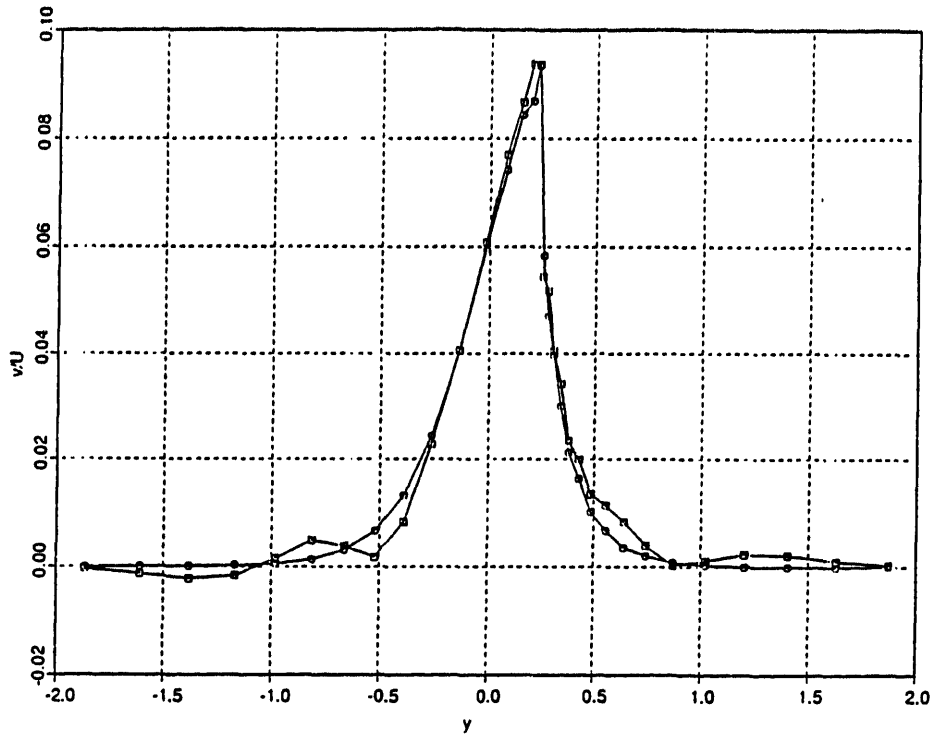

Figure 4.34: Transverse velocity profiles at lobe crest ($z = 0$) and at an axial location just downstream of the lobe trailing edge as found by numerical investigations $M_\infty = 0.5$ and $M_\infty 2.0$

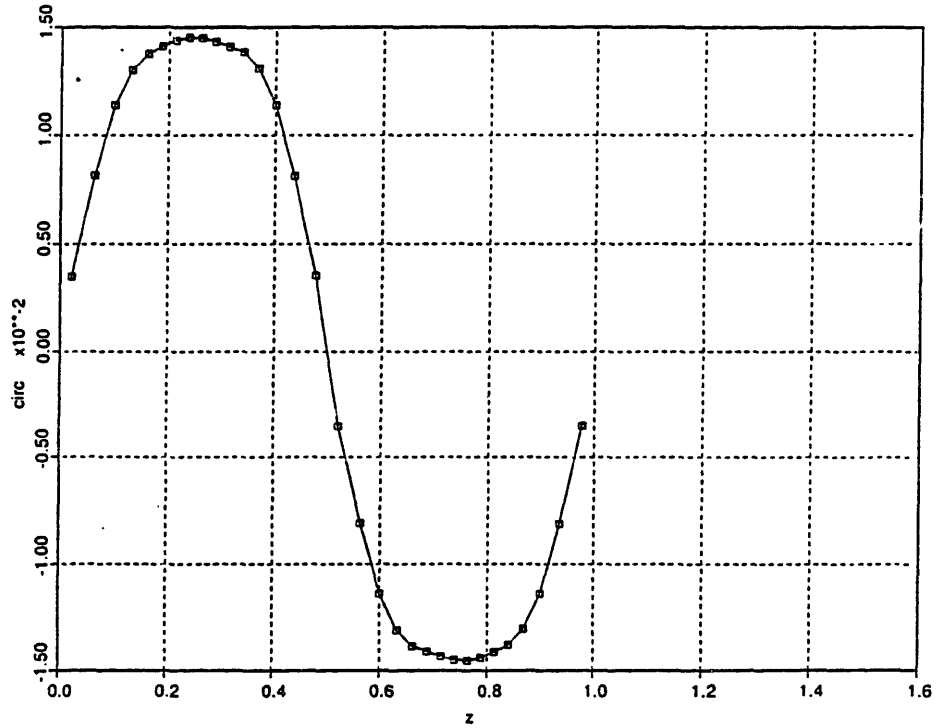

Figure 4.35: Circulation versus spanwise distance at lobe trailing edge for supersonic low penetration calculation.

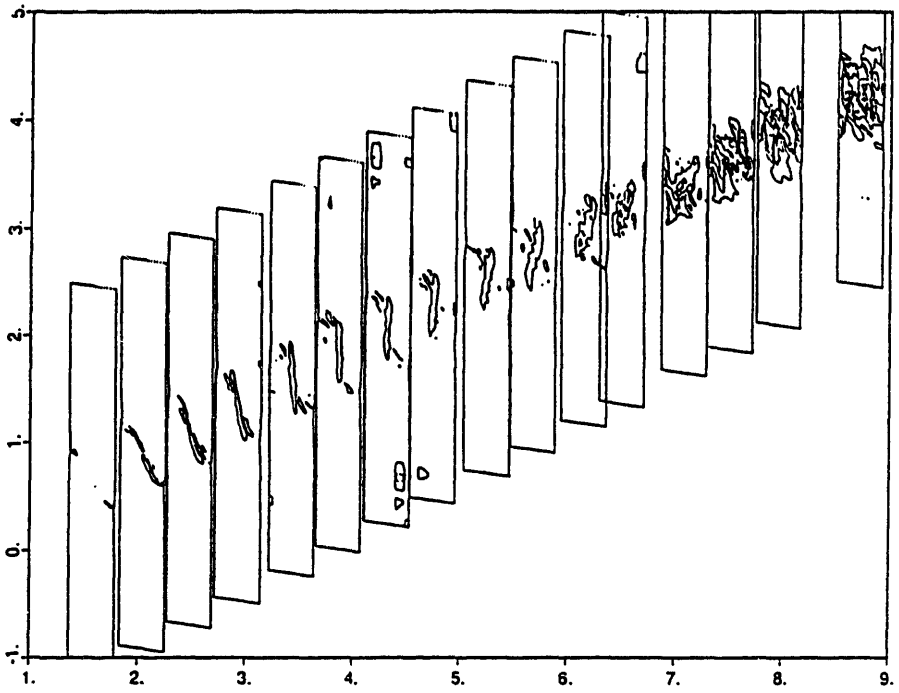

Figure 4.36: Contour plots of $\Delta P_t/P_\infty$ at various axial locations from lobe trailing edge to mixing duct exit. The axial locations are x/λ =2.97, 4.01, 4.97, 5.96, 7.06, 8.03, 9.02, 9.97, 11.06, 12.01, 13.06, 13.83, 15.11, 16.04, 17.05, 18.13, 18.71. Nine contours from -5.5×10^{-2} to 2.5×10^{-2} are plotted in increments of 1×10^{-2}

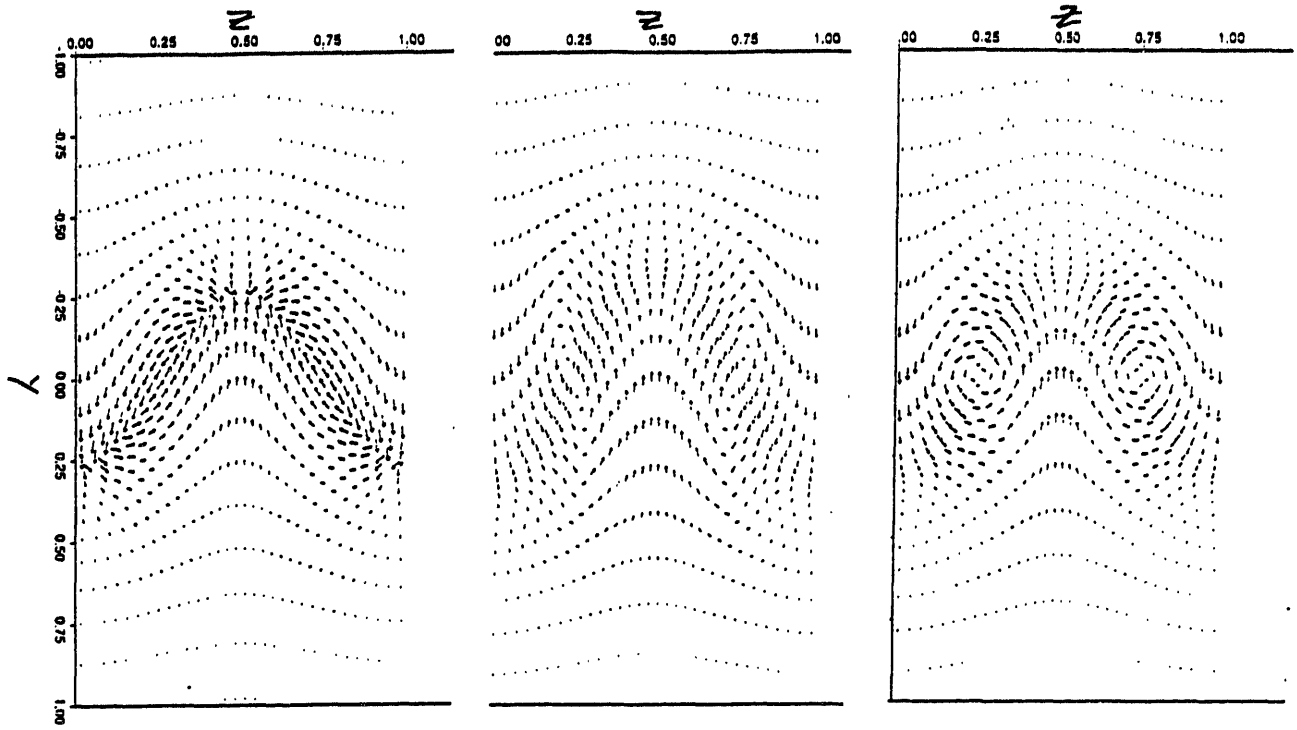

Figure 4.37: Secondary velocity vector field at axial locations $x/\lambda = 3.02, 11.06, 18.71$

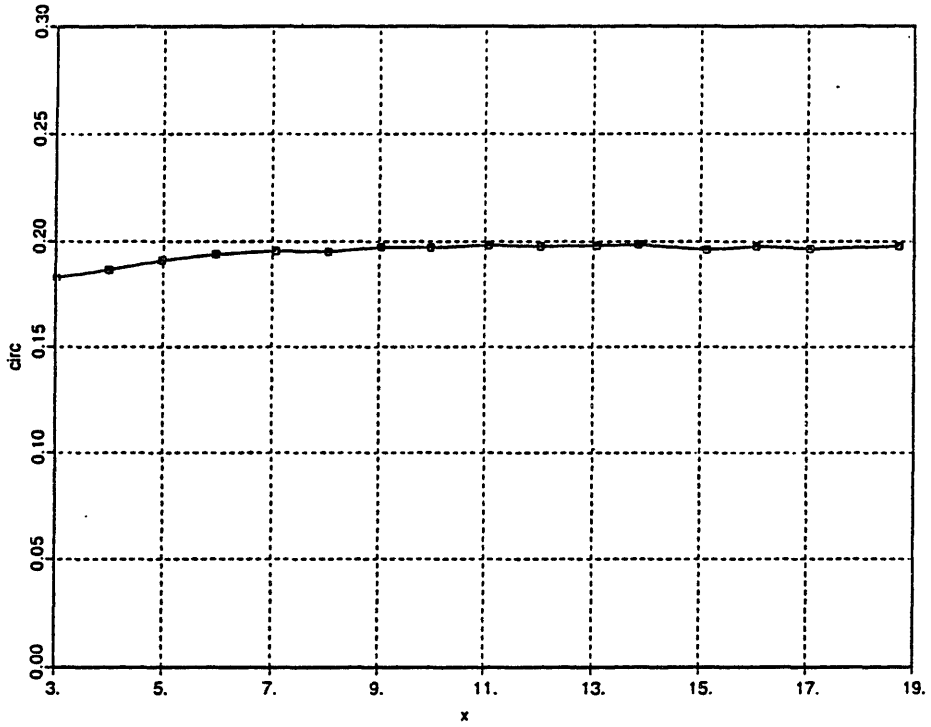

Figure 4.38: Circulation variation with axial distance for supersonic low penetration calculation

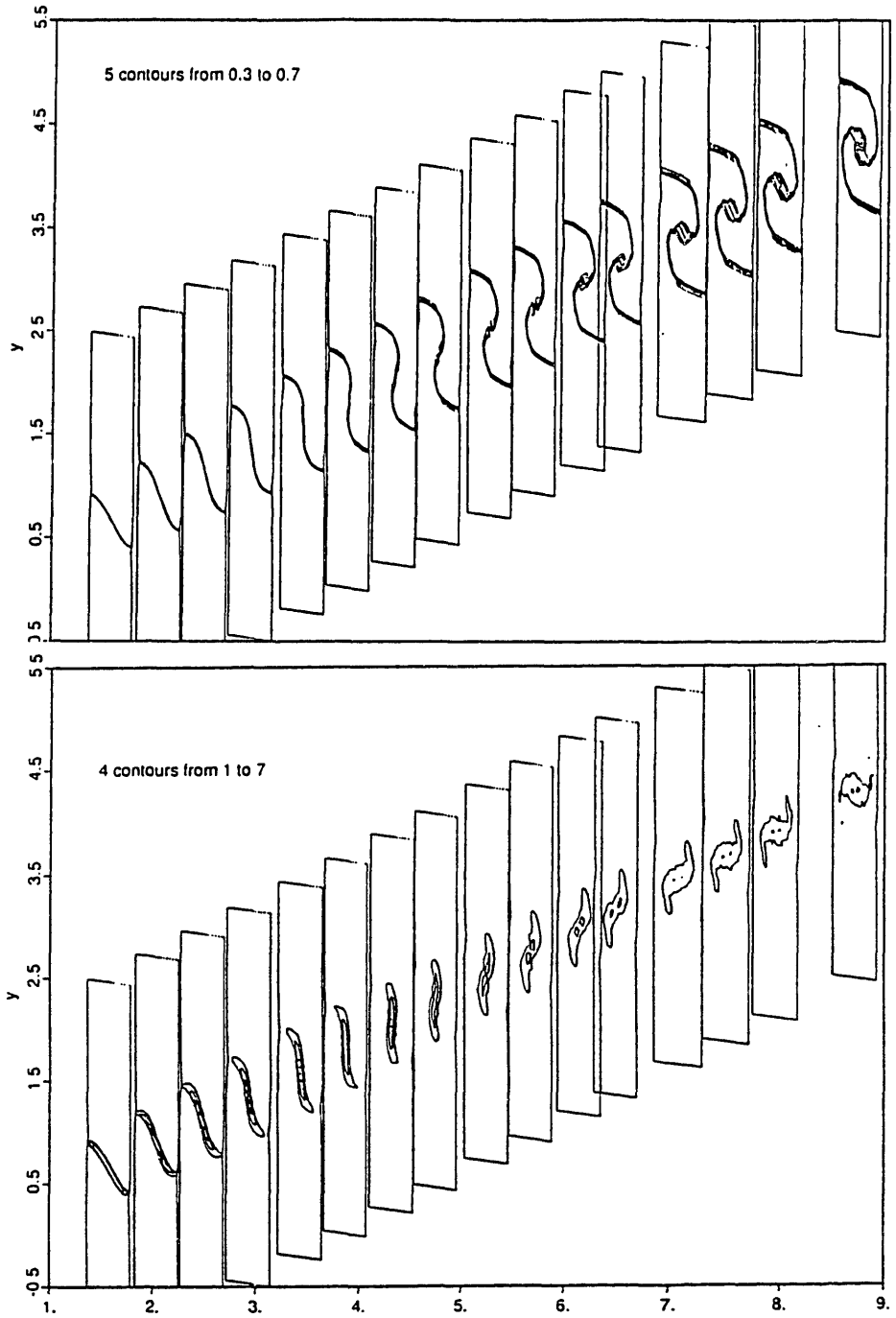

Figure 4.39: Contour plots of ψ, ω_x and c_p, at various axial locations from lobe trailing edge to mixing duct exit. The axial locations are x/λ =2.97, 4.01, 4.97, 5.96, 7.06, 8.03, 9.02, 9.97, 11.06, 12.01, 13.06, 13.83, 15.11, 16.04, 17.05, 18.13, 18.71. Contours are as follows:

ψ: 5 contours from 0.3 to 0.7 in increments of .1;

ω_x: 4 contours from 1.0 to 7.0 in increments of 2.0

c_p: 6 contours from -.0125 to +.0125 in increments of .005

(continued overleaf)

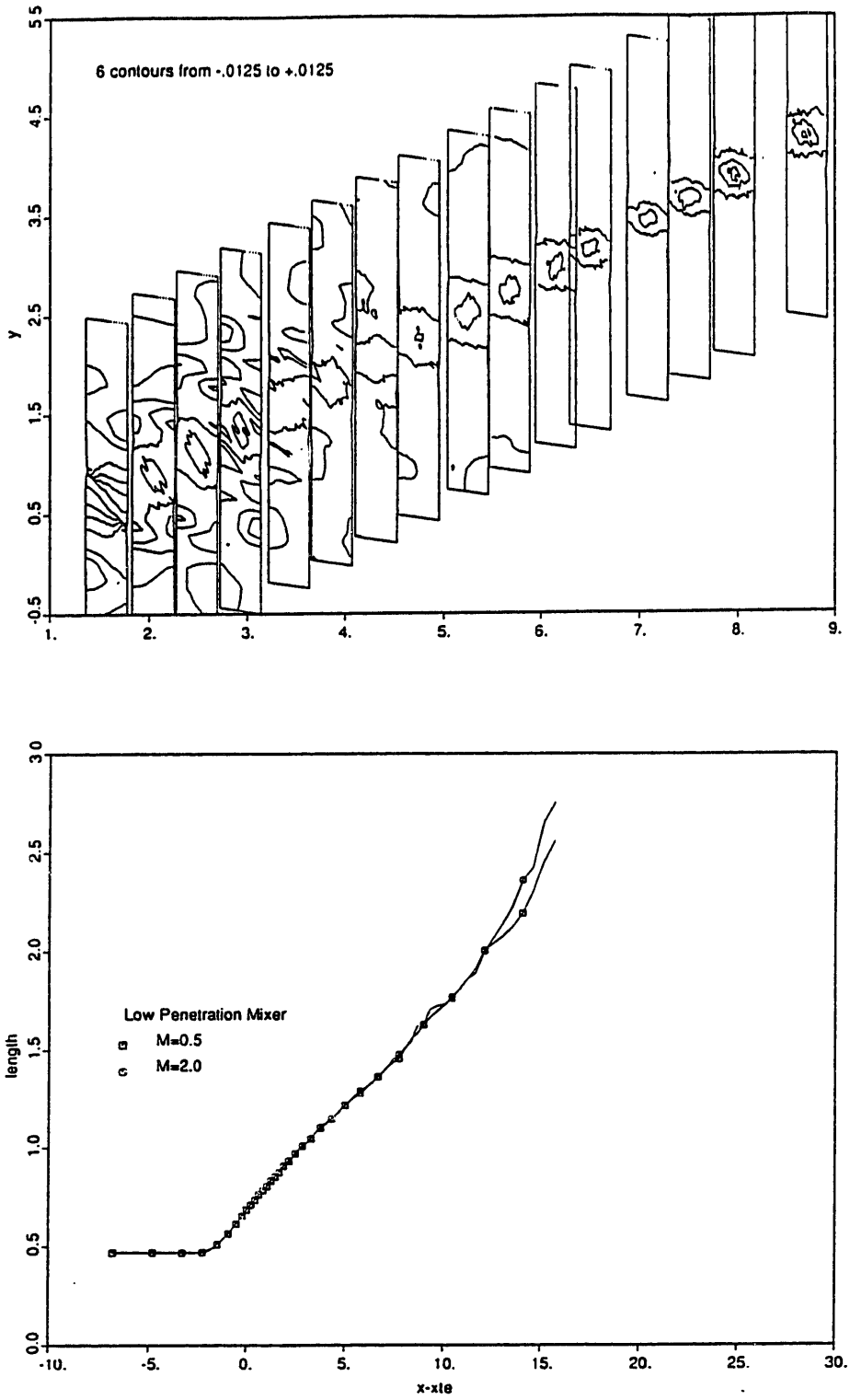

Figure 4.40: Length of $\psi = 0.5$ contour versus axial distance for subsonic versus supersonic low penetraion calculation

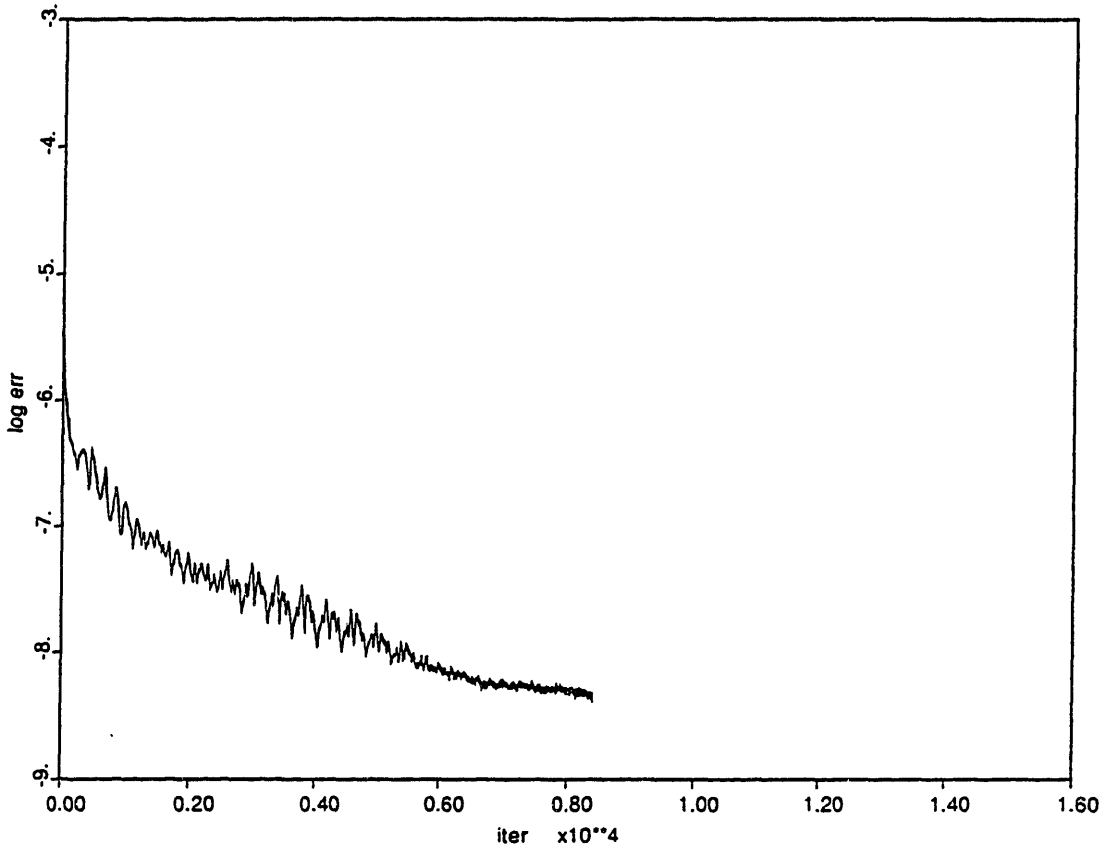

Figure 4.41: Convergence history for subsonic high penetration mixer case

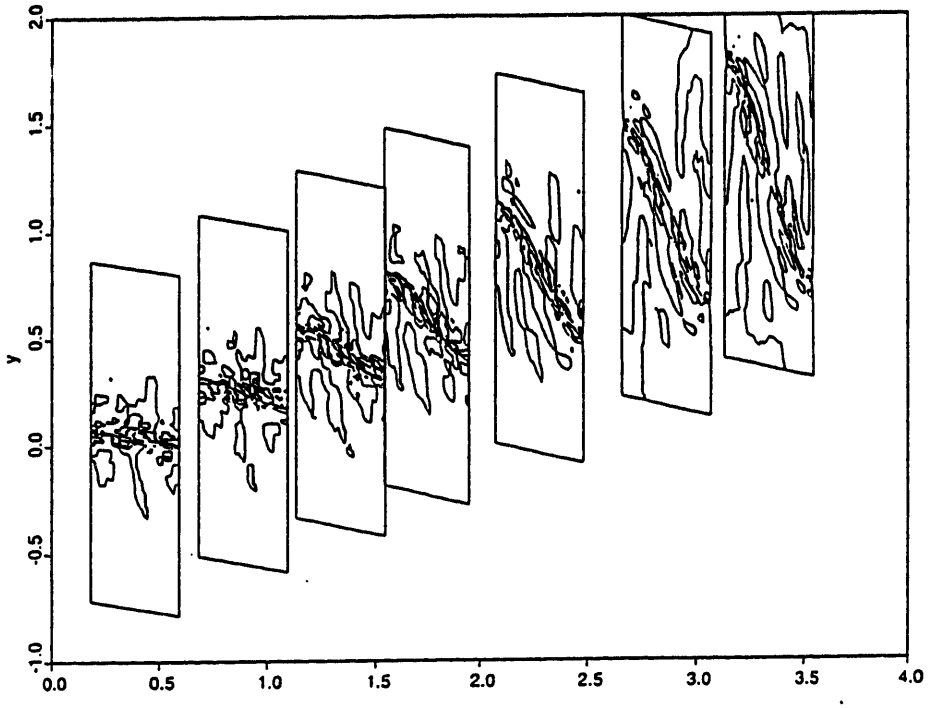

Figure 4.42: Threedimensional contour plot of total pressure change in flowfield around mixer. The first and last axial slices are located at the leading and trailing edges, respectively. The exact axial locations are $x/\lambda = .08, 0.32, 0.53, 0.724, 0.98, 1.25, 1.48$. Eight contours from -3.5×10^{-2} to $+3.5 \times 10^{-2}$ in increments of 1×10^{-2} are plotted

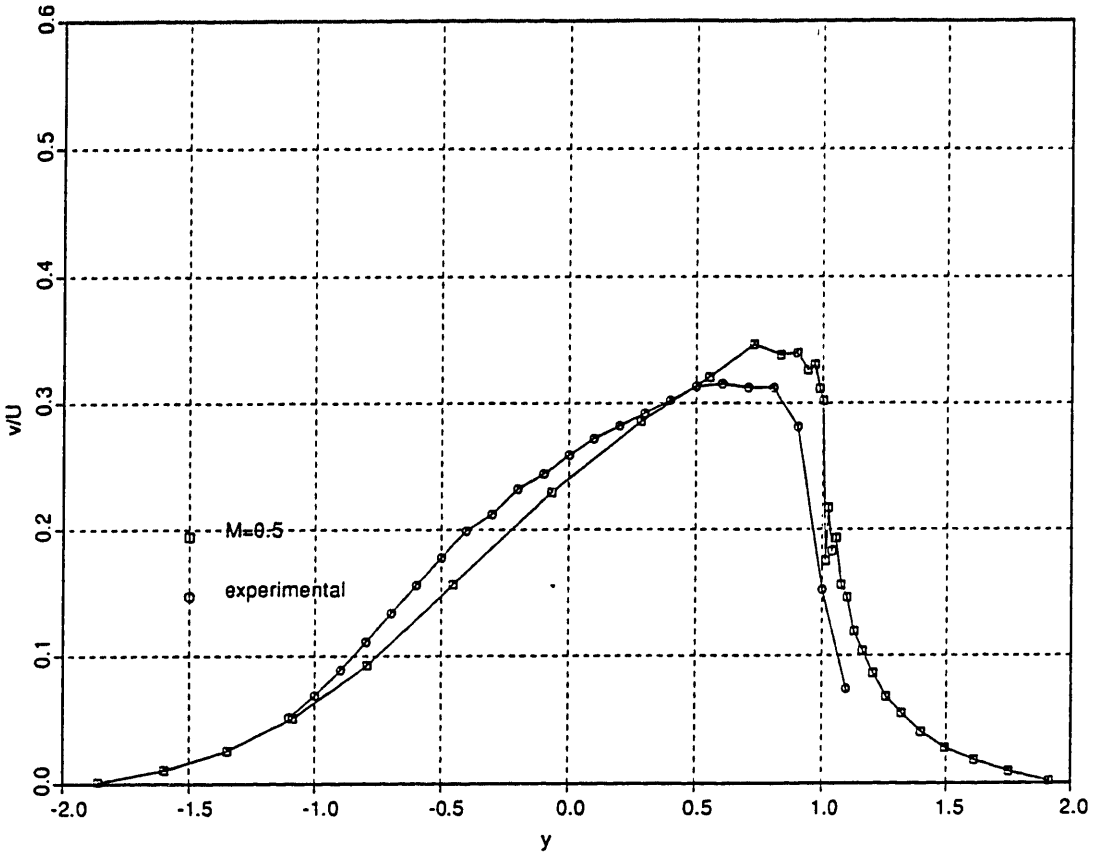

Figure 4.43: Transverse velocity profiles versus transverse distance, y at lobe crest ($z = 0$) and at an axial location just downstream of the lobe trailing edge as found by numerical investigations ($M_\infty = 0.5$) and the UTRC experimental investigation

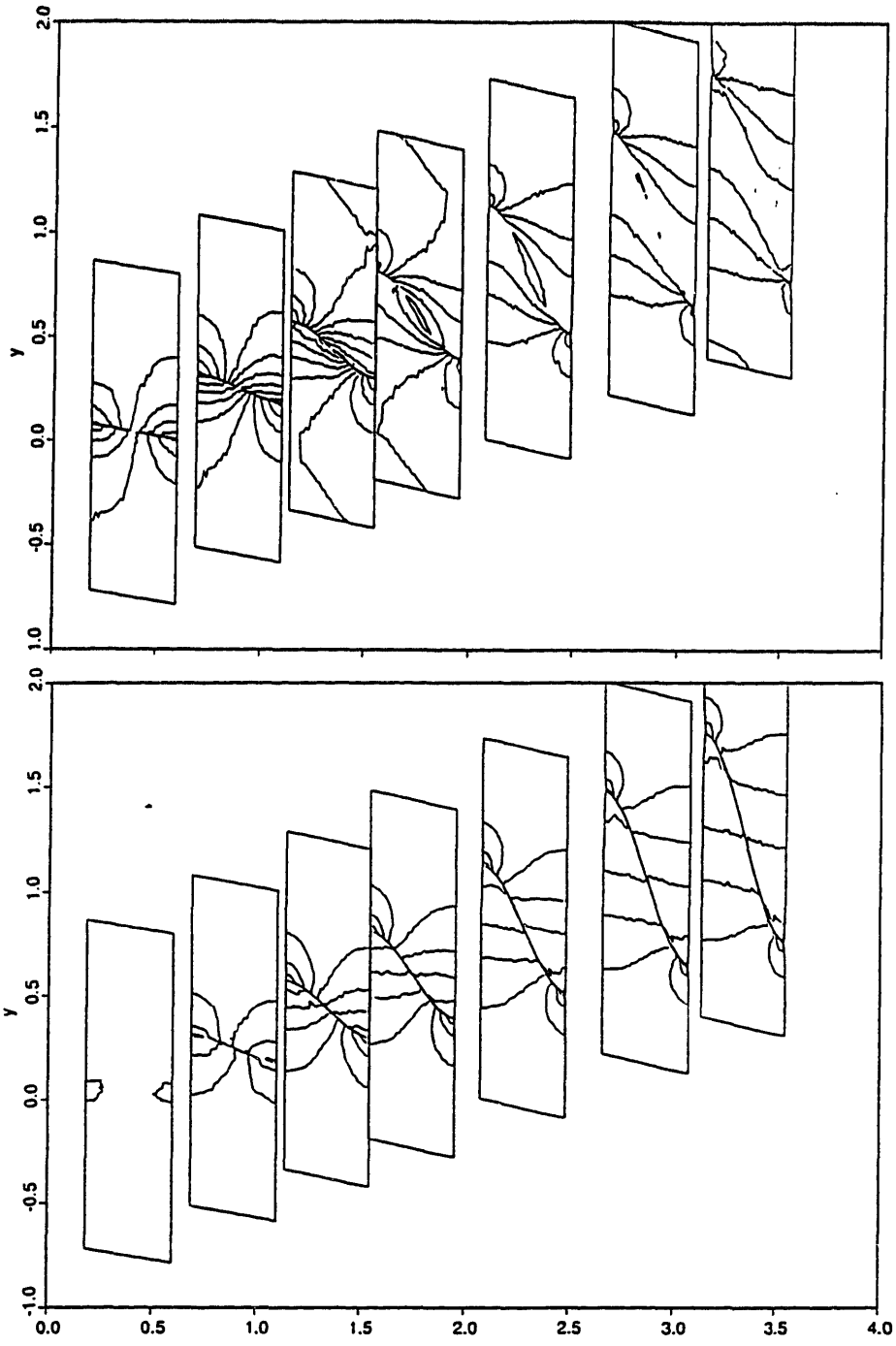

Figure 4.44: Three-dimensional contour plots of c_p, v_y and v_z. The first and last axial slices are located at the leading and trailing edges, respectively. The exact axial locations are $x/\lambda = .08, 0.32, 0.53, 0.724, 0.98, 1.25, 1.48..$ Contours are as follows:

c_p: 12 contours from -.275 to +.275 in increments of .05;

v_y: 8 contours from -.175 to +.175 in increments of .05

v_z: 6 contours from -.125 to +.125 in increments of .05

(continued overleaf)

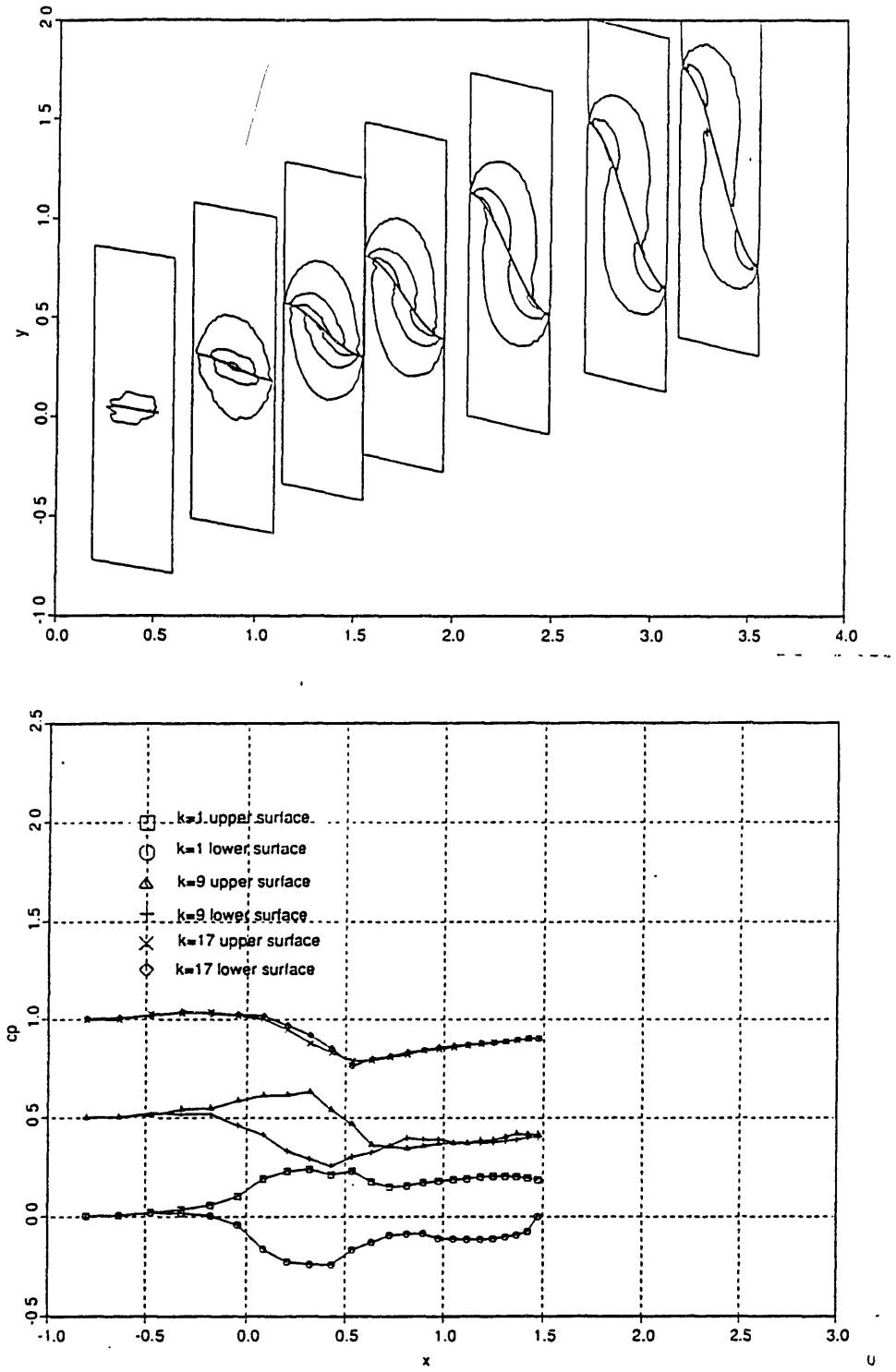

Figure 4.45: Axial variation of $c_{p_{upper}}$ and $c_{p_{lower}}$ for crest, quarterspan and midspan spanwise locations. These correspond to $\varsigma = 1, 9, 17$, respectively.

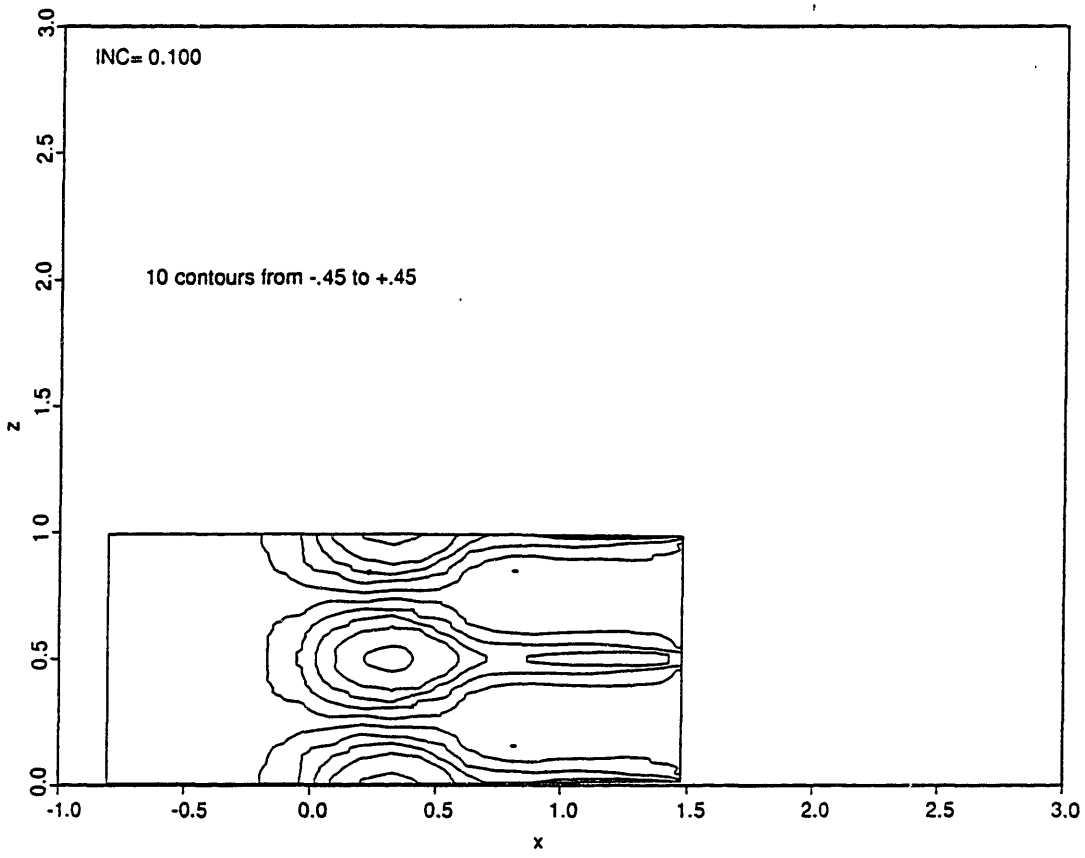

Figure 4.46: Loading $c_{p_{upper}} - c_{p_{lower}}$ on lobe surface projected onto a $y = consant$ surface

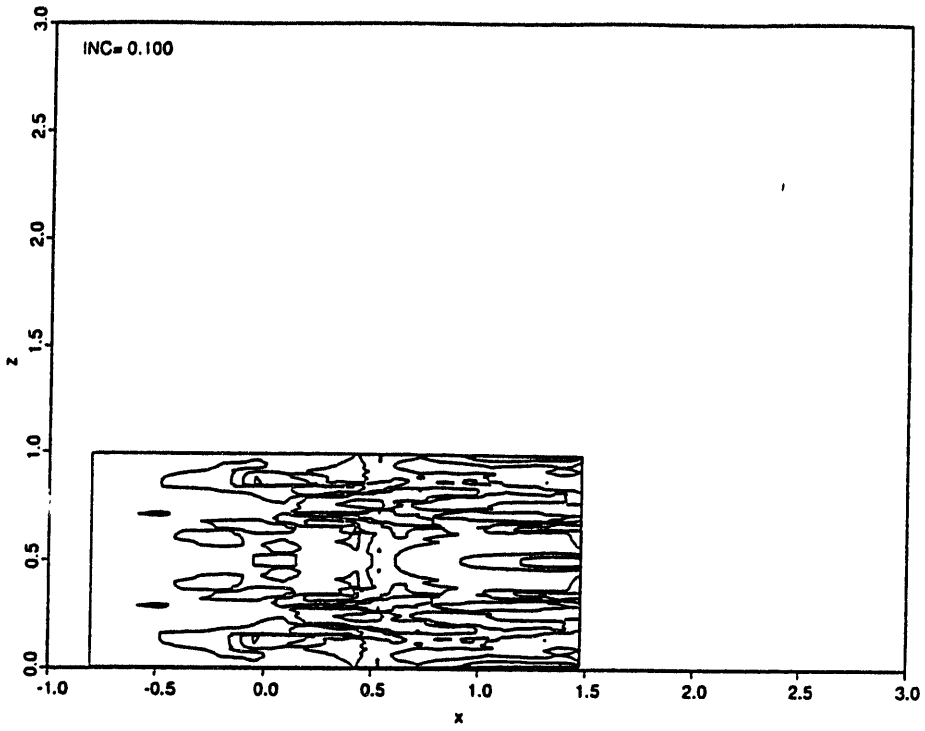

Figure 4.47: Residual from Equation 3.26 on lobe surface projected onto a y = consant surface. Six contours from -.25 to +.25 in increments of .1 are plotted.

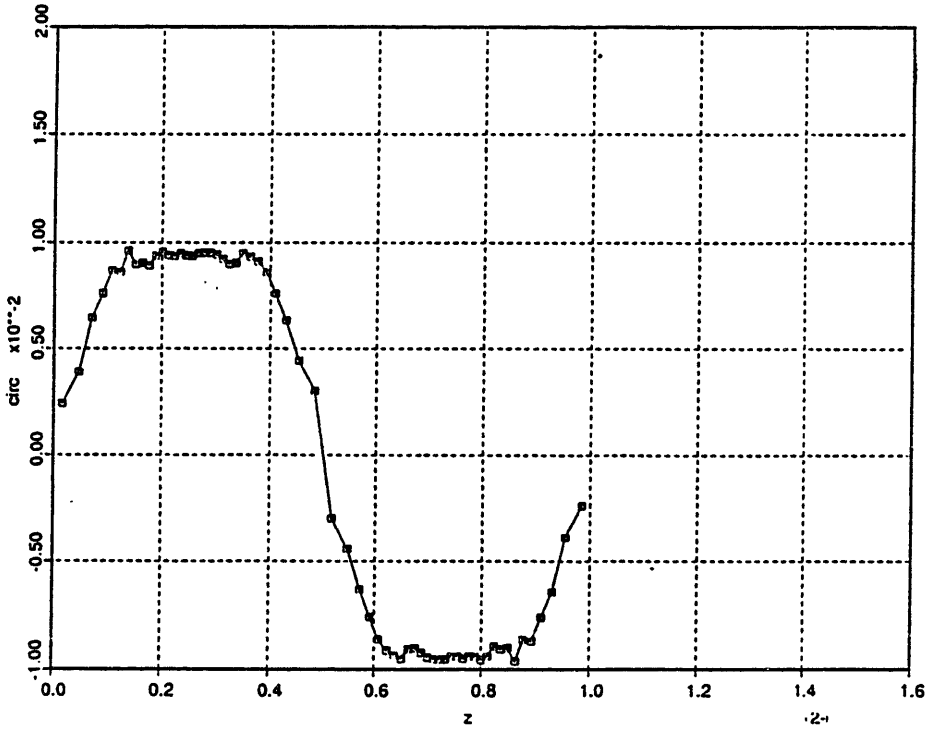

Figure 4.48: Circulation versus spanwise distance at lobe trailing edge.

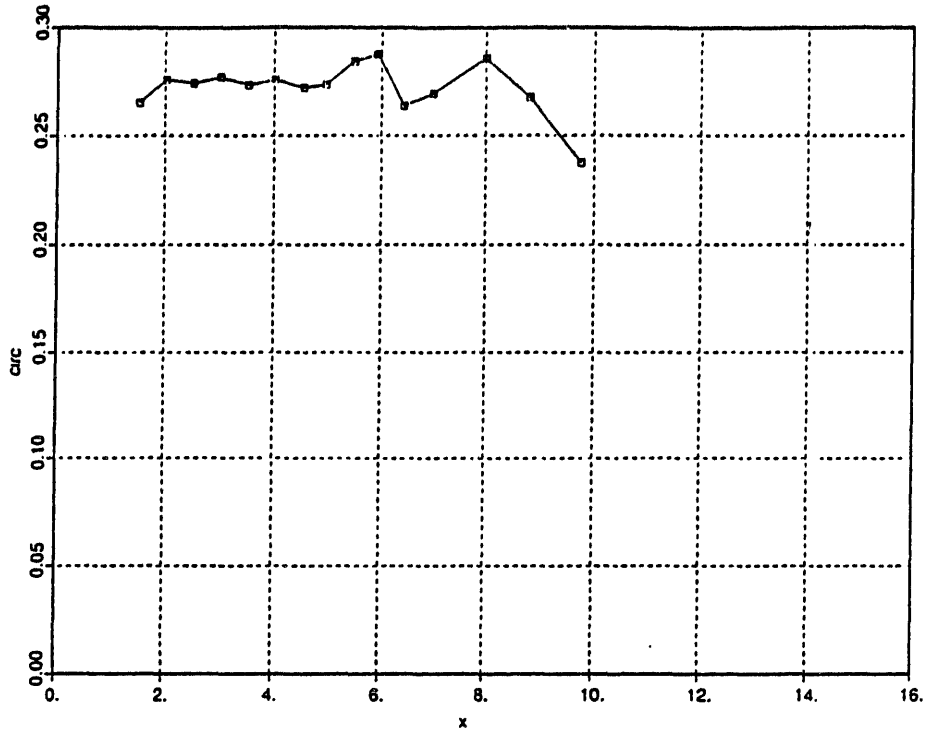

Figure 4.49: Circulation variation with axial distance

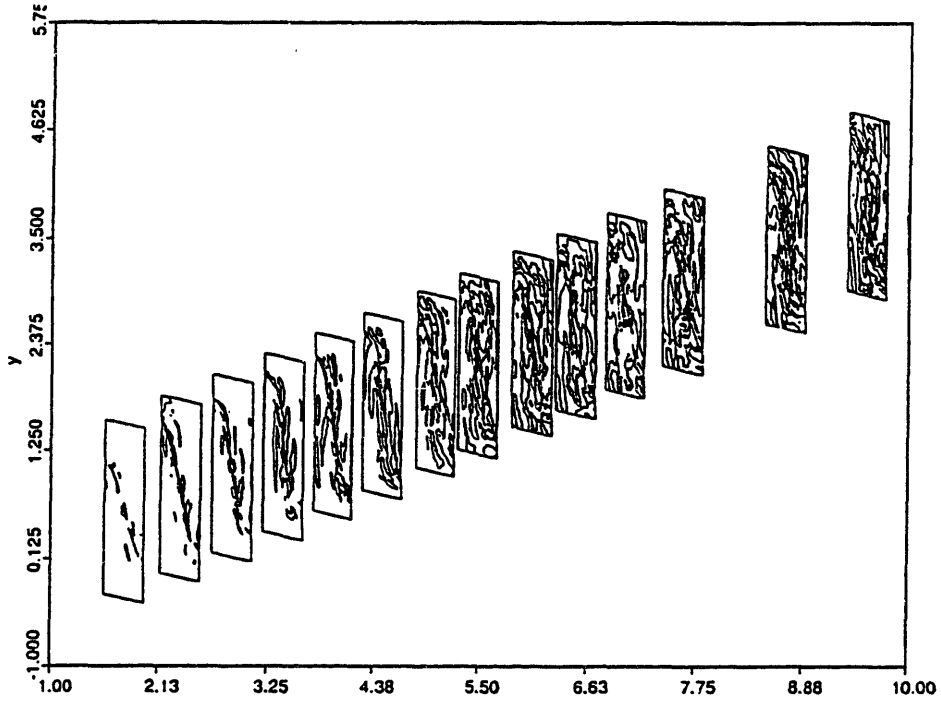

Figure 4.50: Contour plots of $\Delta P_t/P_\infty$ at various axial locations from lobe trailing edge to mixing duct exit. The axial locations are x/λ =1.48, 2.03, 2.52, 3.02, 3.53, 4.02, 4.55, 4.98, 5.51, 5.93, 6.42, 6.98, 7.63, 8.00, 8.81, 9.74. Eight contours from -7×10^{-2} to 7×10^{-2} are plotted in increments of 2×10^{-2}

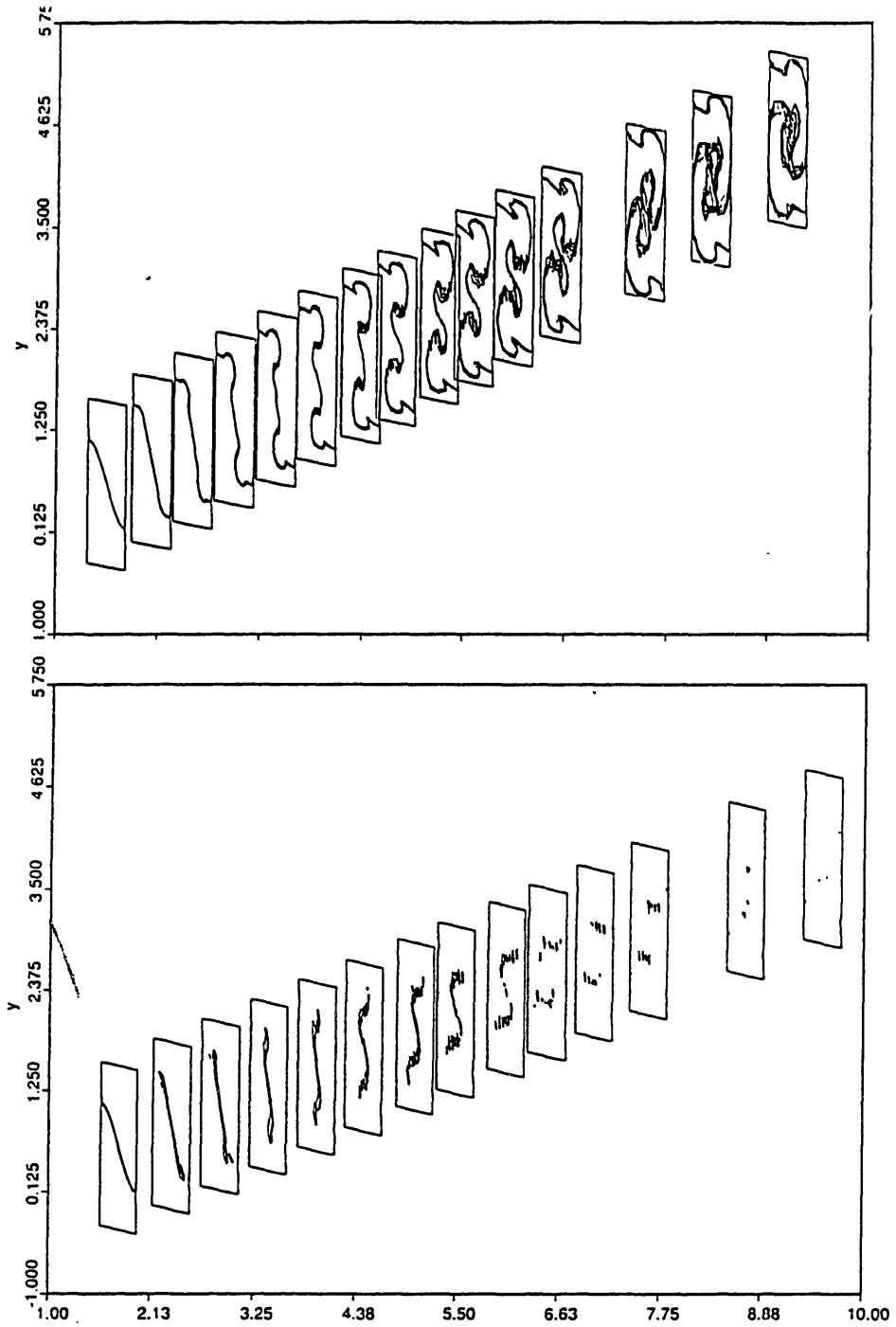

Figure 4.51: Contour plots of ψ, ω_x and c_p, at various axial locations from lobe trailing edge to mixing duct exit. The axial locations are x/λ =1.48, 2.03, 2.52, 3.02, 3.53, 4.02, 4.55, 4.98, 5.51, 5.93, 6.42, 6.98, 7.63, 8.00, 8.81, 9.74. Contours are as follows:

ψ: 5 contours from 0.3 to 0.7 in increments of .1;

ω_x: 6 contours from 2.5 to 27.5 in increments of 5

c_p: 8 contours from -.175 to +.175 in increments of .05

(continued overleaf)

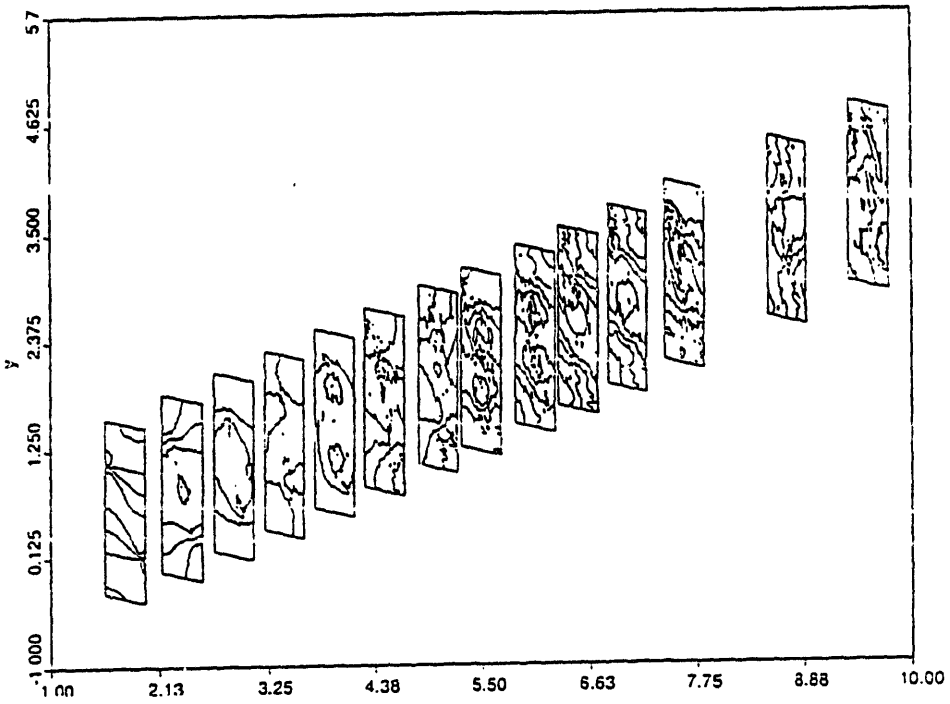

Figure 4.52: Secondary velocity vector field at axial locations $x/\lambda = 1.52, 5.51, 9.74$ (see over)

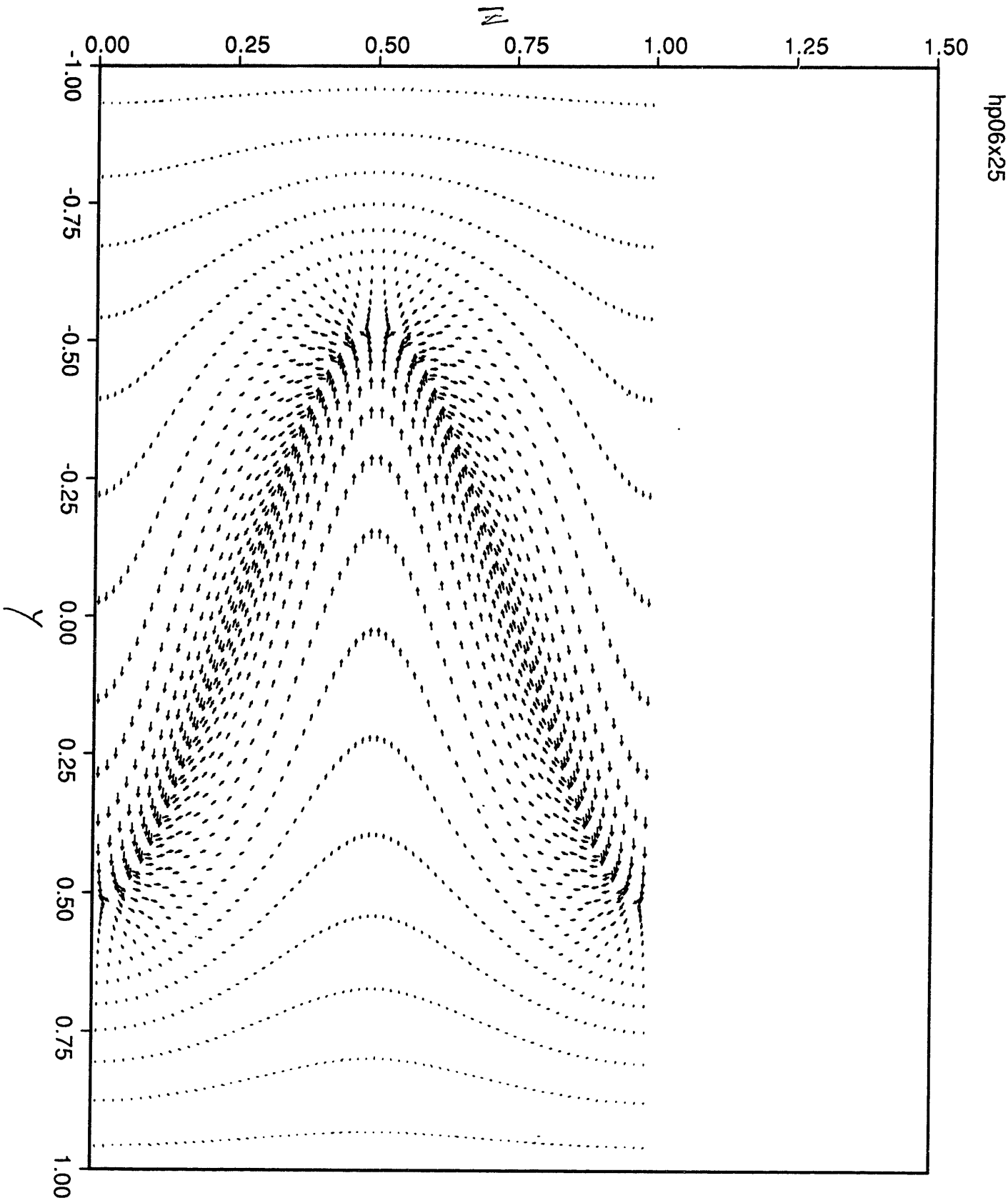
x
0.00
0.25
0.50
0.75
1.00
1.25
1.50
y
-1.00
-0.75
-0.50
-0.25
0.00
0.25
0.50
0.75
1.00
hp06x25

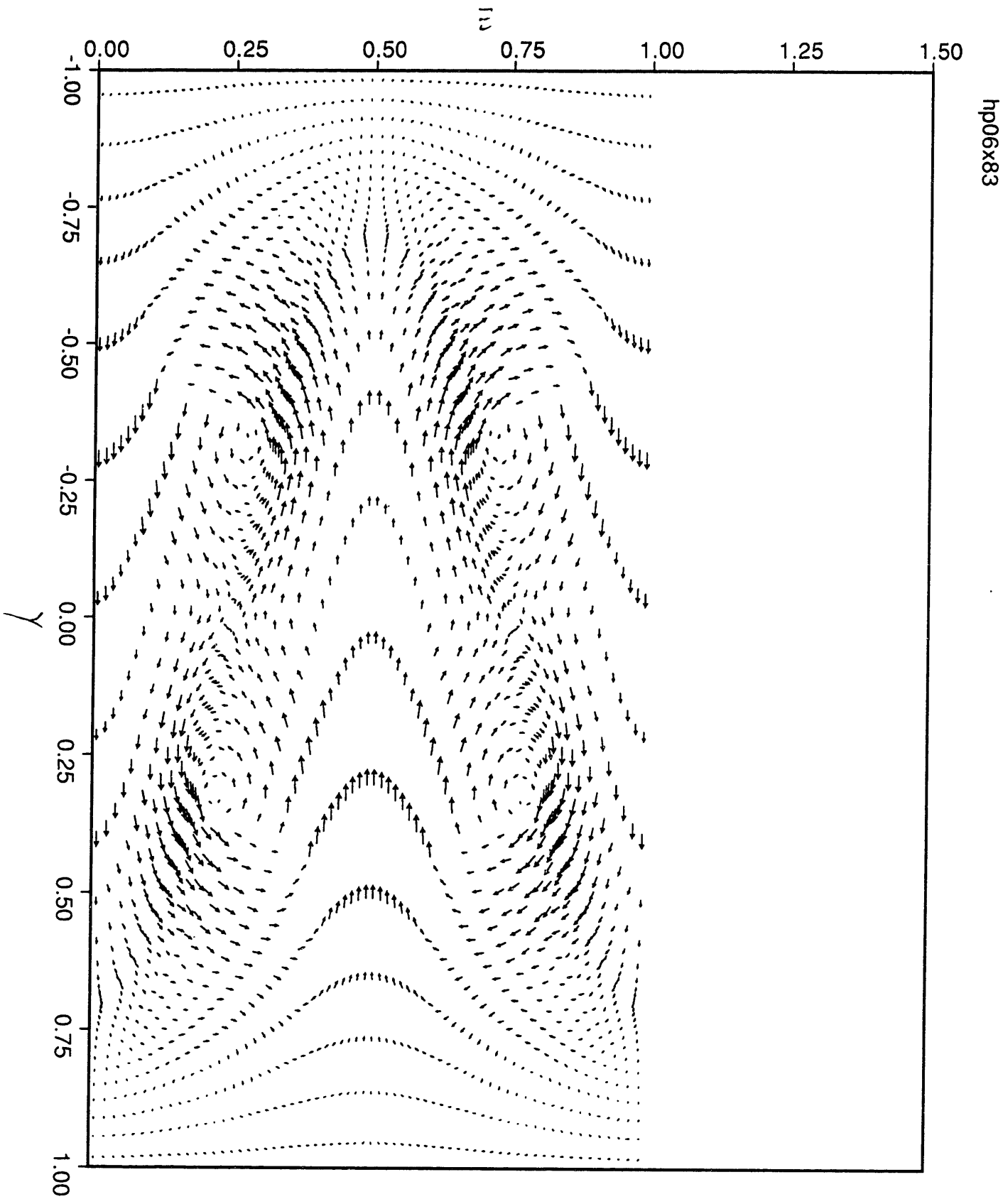
x
0.00
0.25
0.50
0.75
1.00
1.25
1.50
y
-1.00
-0.75
-0.50
-0.25
0.00
0.25
0.50
0.75
1.00
hp06x83

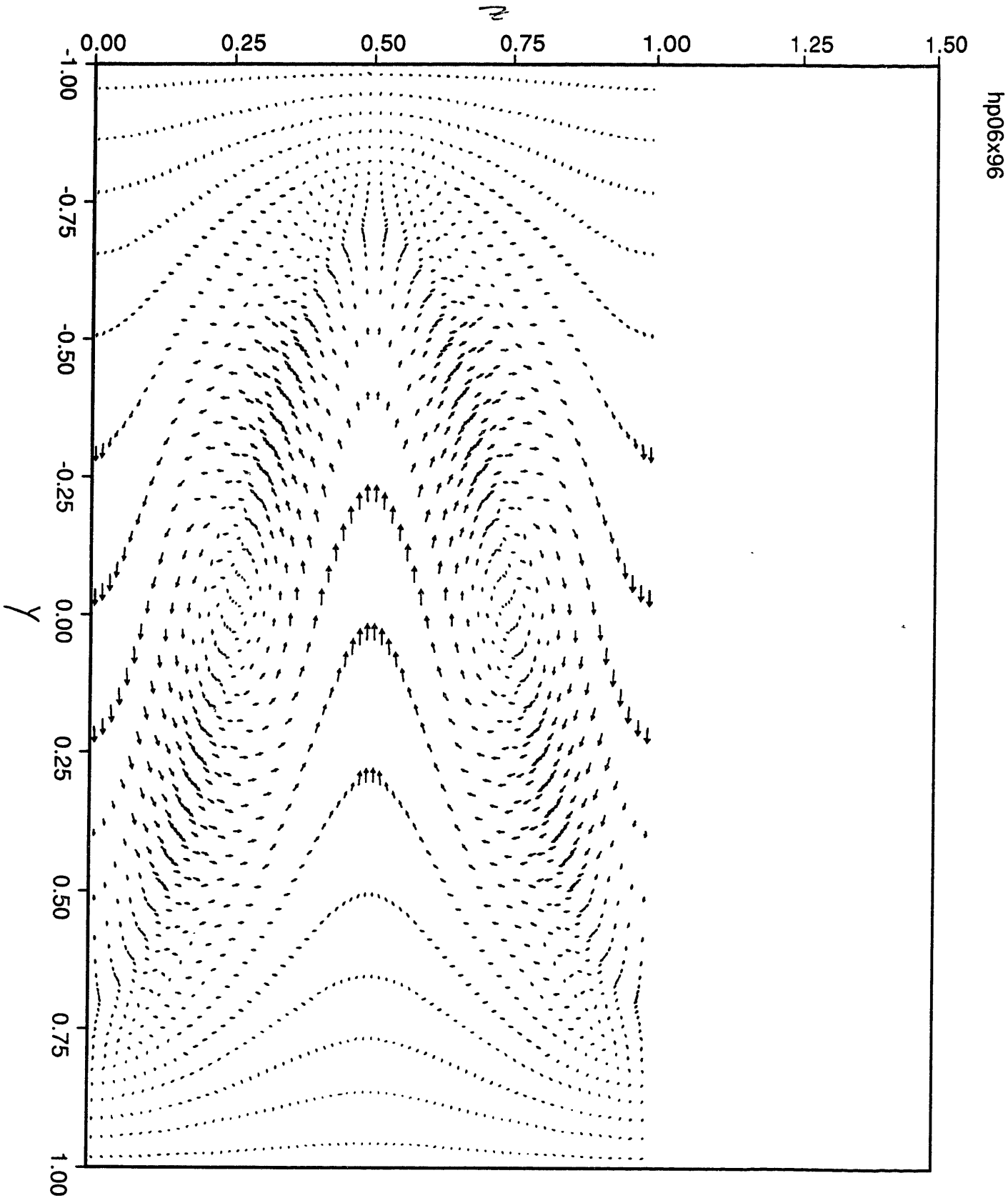
0.00
0.25
0.50
0.75
1.00
1.25
1.50
-1.00
-0.75
-0.50
-0.25
0.00
0.25
0.50
0.75
1.00
Y
hp06x96

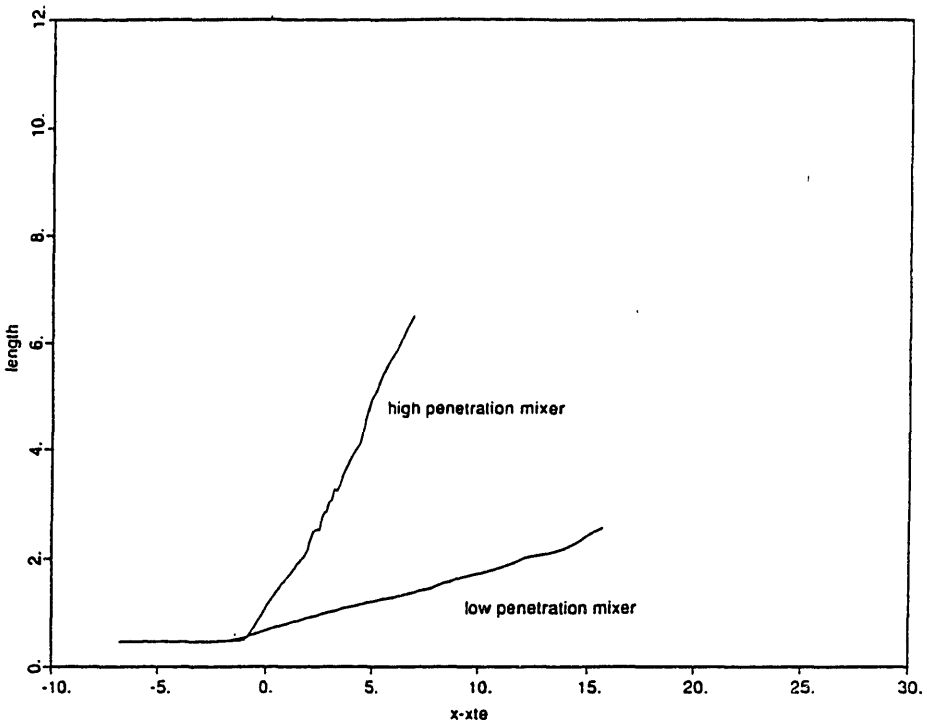

Figure 4.53: Length of $\psi = 0.5$ contour versus axial distance for subsonic high penetration calculation

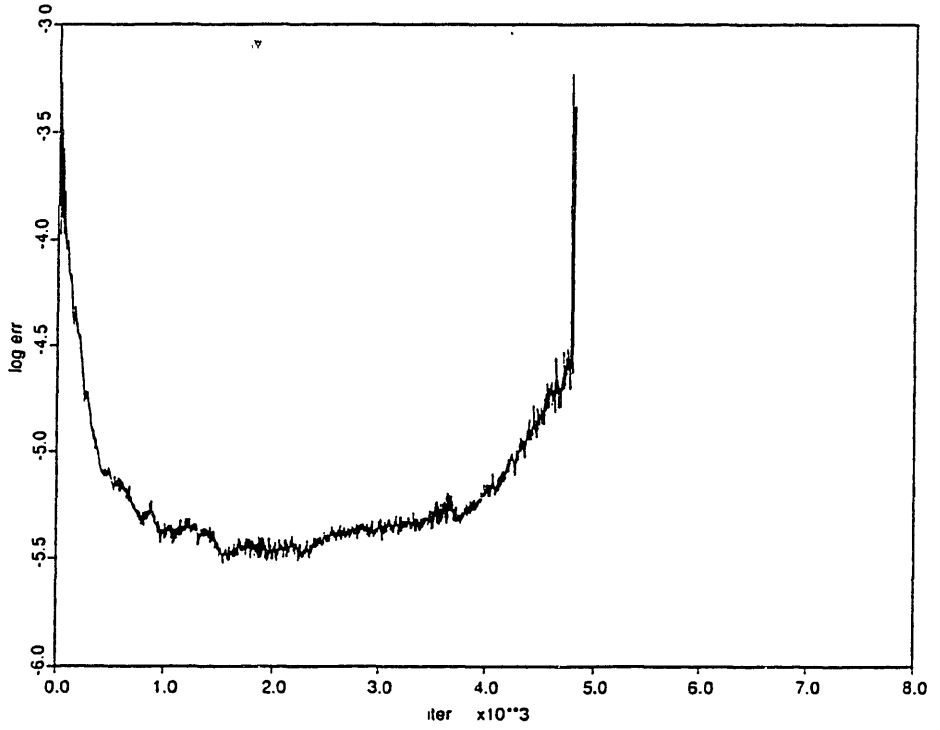

Figure 4.54: Convergence history for supersonic high penetration mixer case

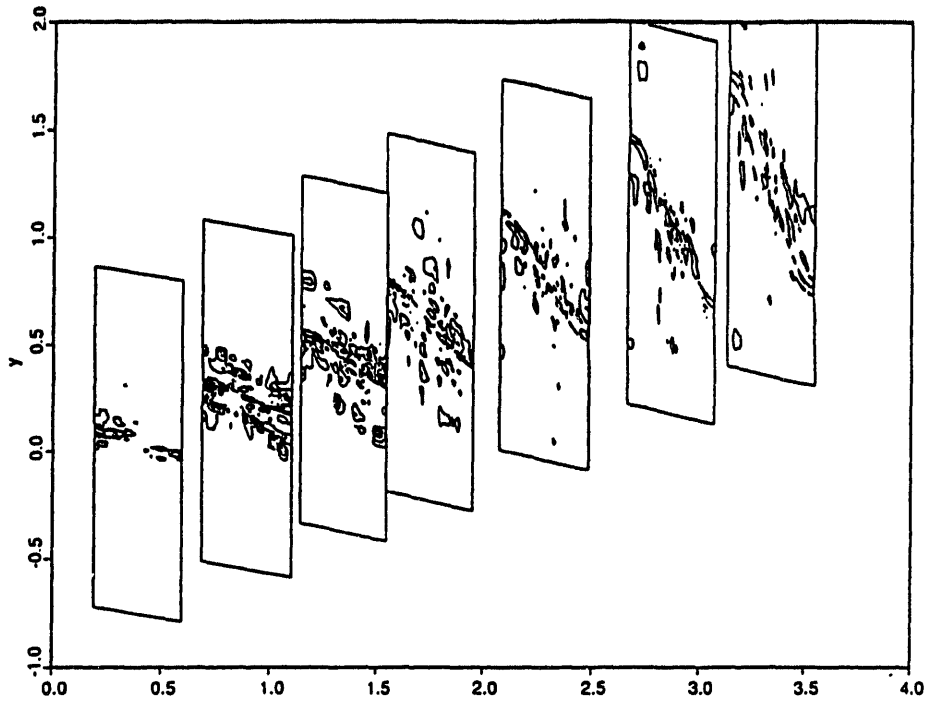

Figure 4.55: Threedimensional contour plot of total pressure change in flowfield around mixer. The first and last axial slices are located at the leading and trailing edges, respectively. The exact axial locations are x/λ =.08, 0.32, 0.53, 0.724, 0.98, 1.25, 1.48. Eight contours from -3.5×10^{-1} to $+3.5 \times 10^{-1}$ in increments of 1×10^{-1} are plotted

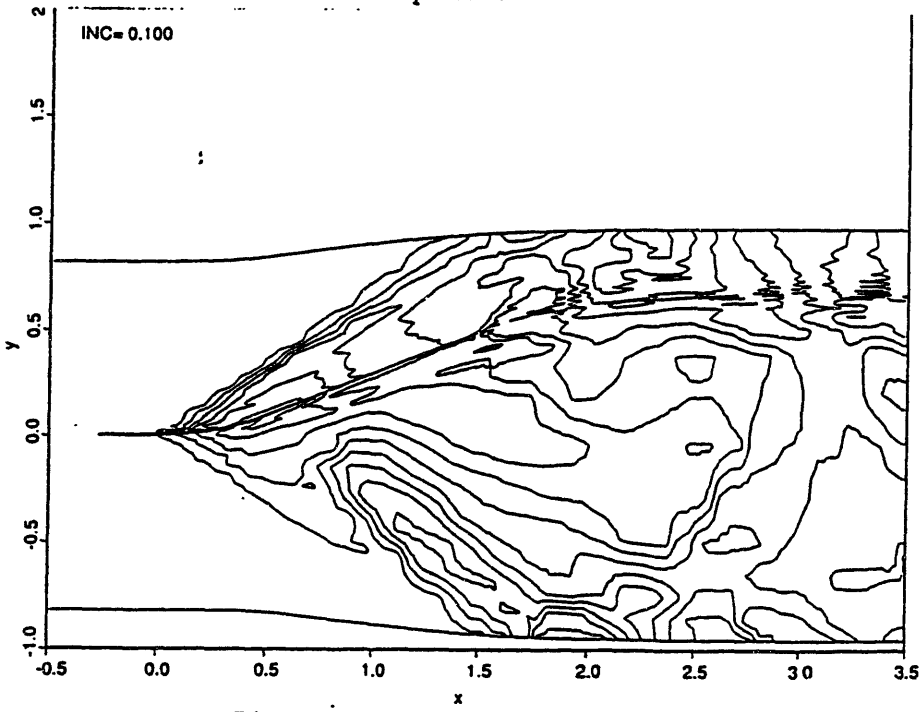

Figure 4.56: contour plot of ρ at $z = 0$

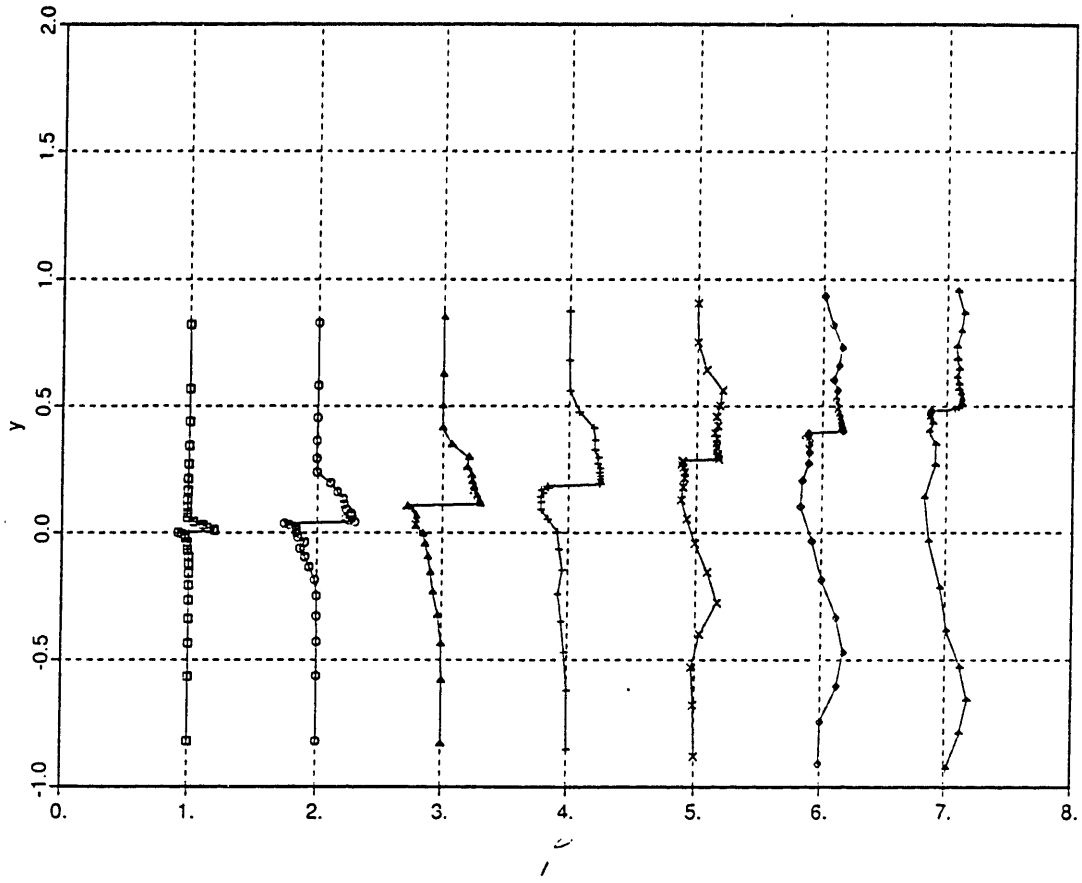

Figure 4.57: transverse profiles of ρ at $z = 0$ and axial locations :-

x/λ =.08, 0.32, 0.53, 0.724, 0.98, 1.25, 1.48

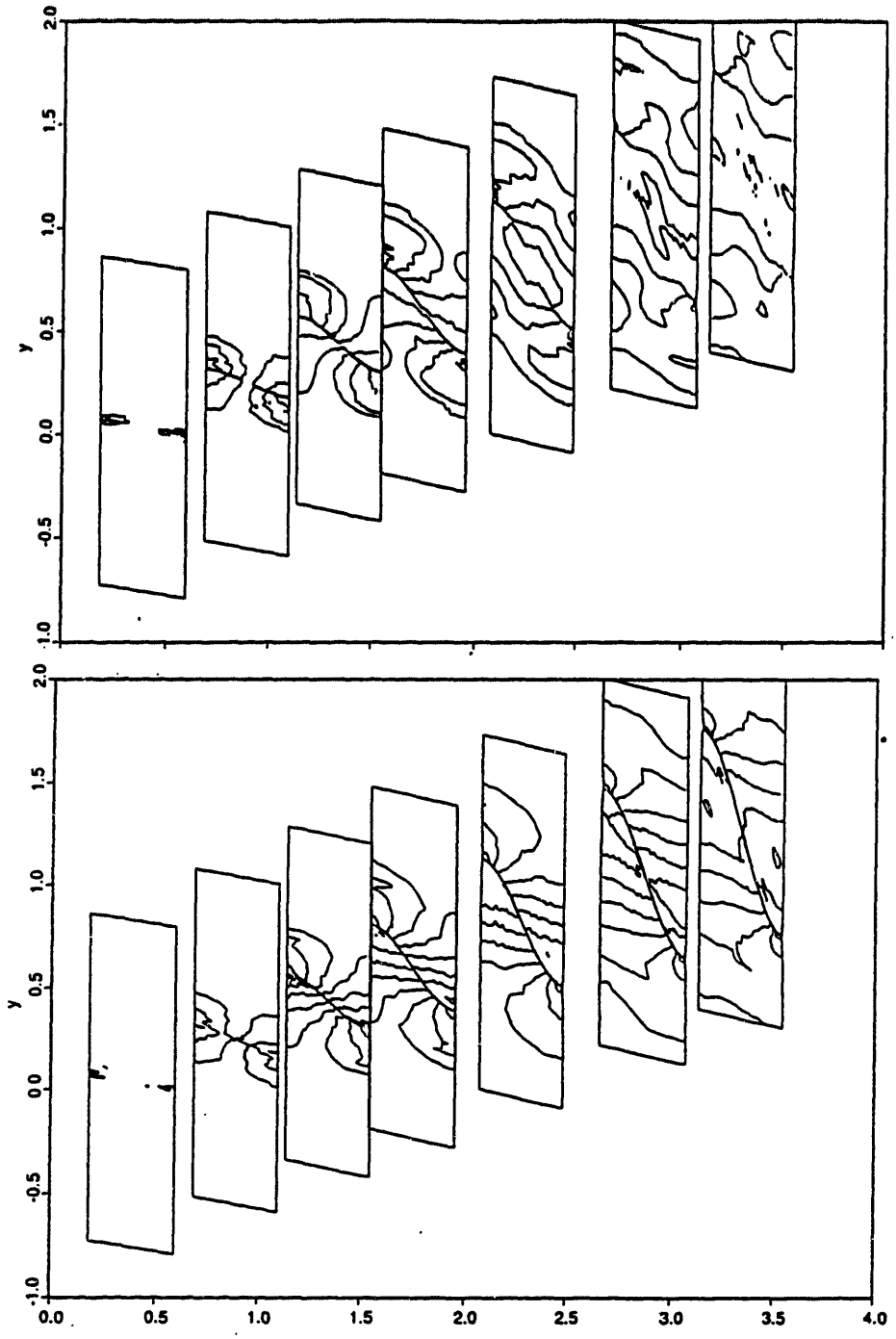

Figure 4.58: Three-dimensional contour plots of c_p, v_y and v_z. The first and last axial slices are located at the leading and trailing edges, respectively. The exact axial locations are $x/\lambda = .08, 0.32, 0.53, 0.724, 0.98, 1.25, 1.48..$ Contours are as follows:

c_p: 8 contours from -.35 to +.35 in increments of .1;

v_y: 10 contours from -.9 to +.9 in increments of .2;

v_z: 6 contours from -.5 to +.5 in increments of .2

(continued overleaf)

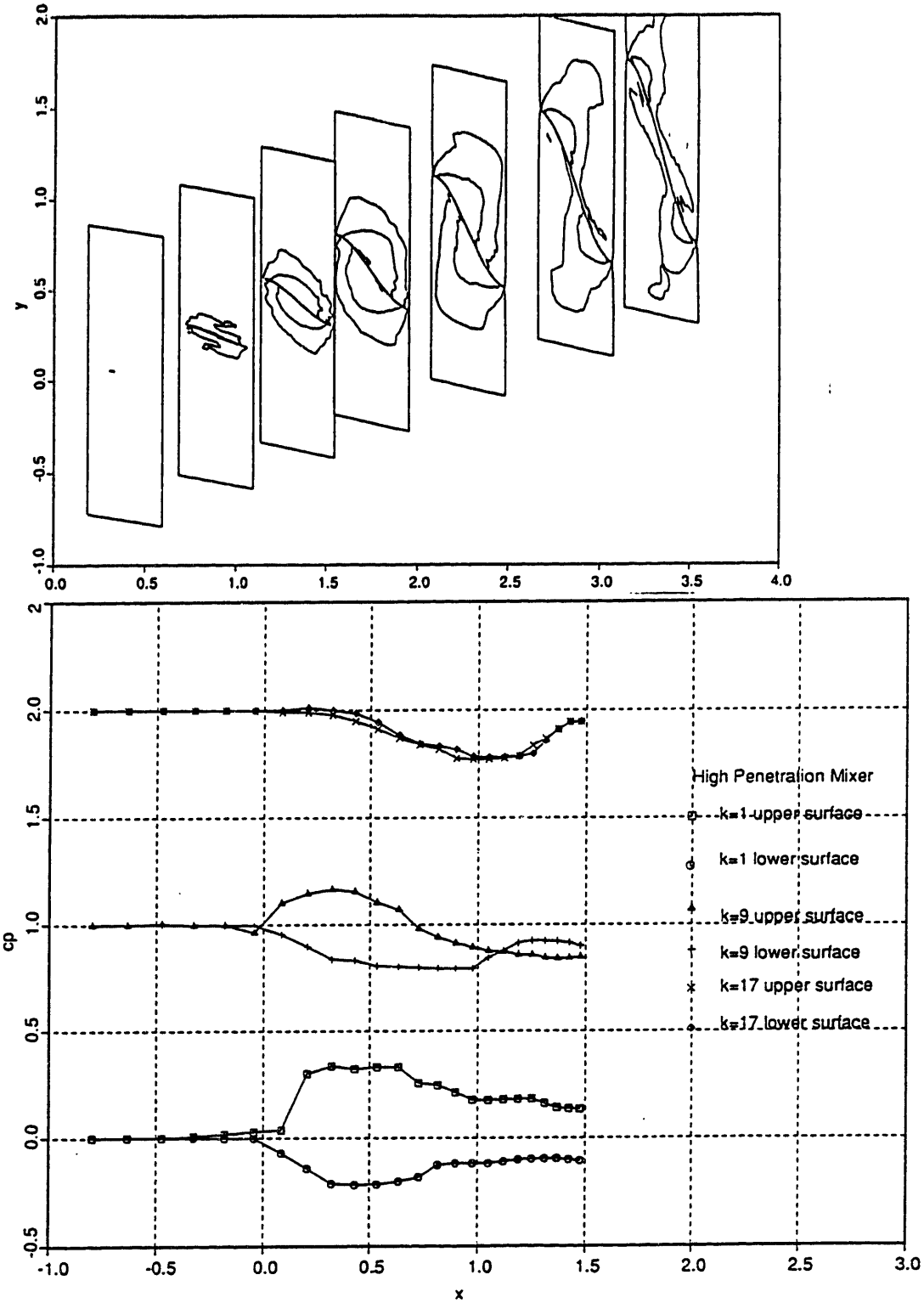

Figure 4.59: Axial variation of $c_{p_{upper}}$ and $c_{p_{lower}}$ for crest, quarterspan and midspan spanwise locations. These correspond to $\varsigma = 1, 9, 17$, respectively.

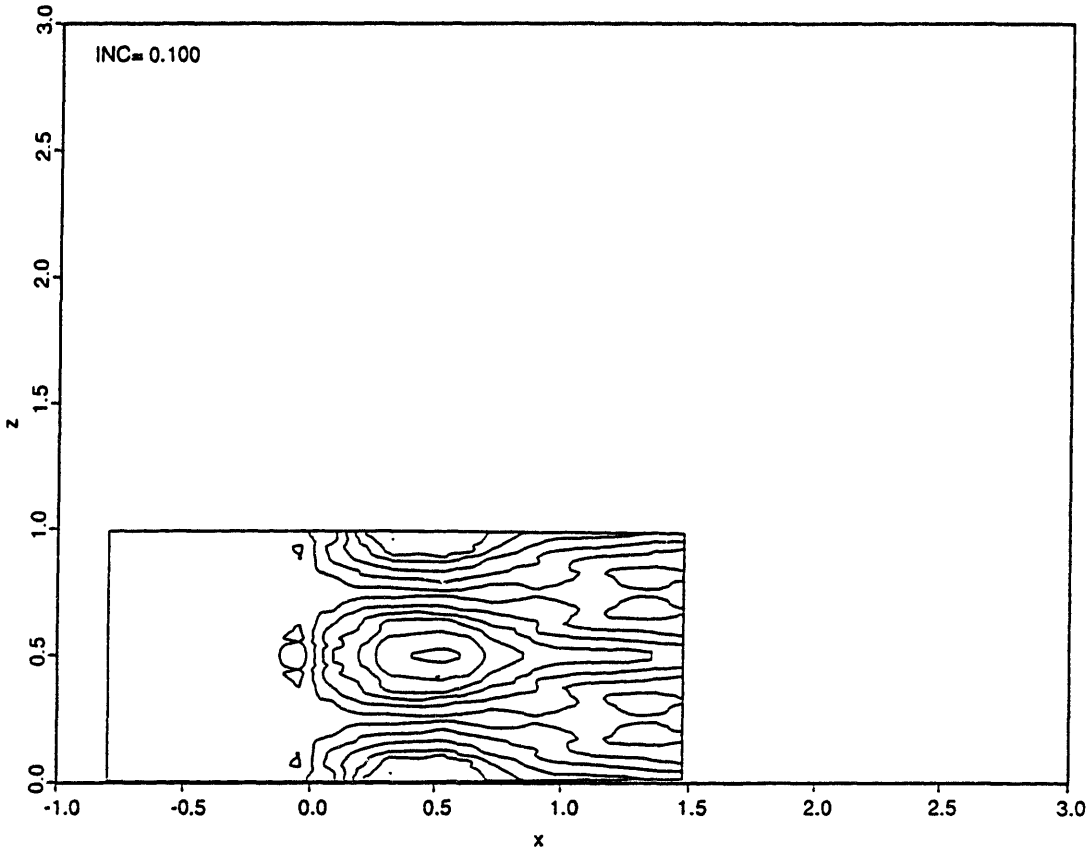

Figure 4.60: Loading $c_{p_{upper}} - c_{p_{lower}}$ on lobe surface projected onto a $y = consant$ surface. 12 Contours are plotted from -0.55 to 0.55 in increments of 0.05

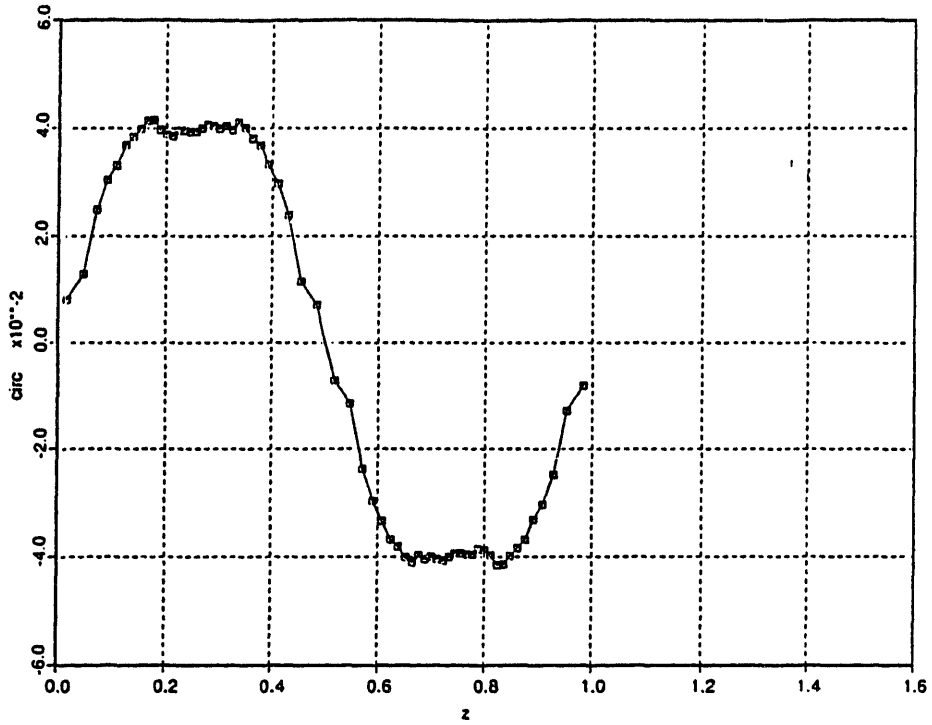

Figure 4.61: Circulation versus spanwise distance at lobe trailing edge for high penetration supersonic case.

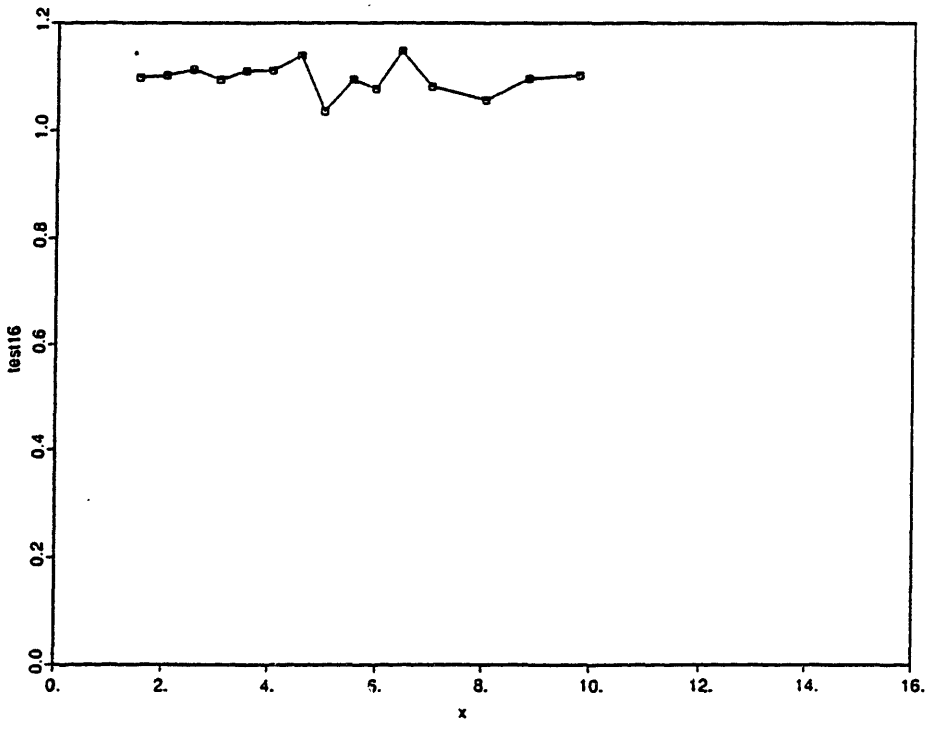

Figure 4.62: Circulation variation with axial distance for high penetration supersonic case.

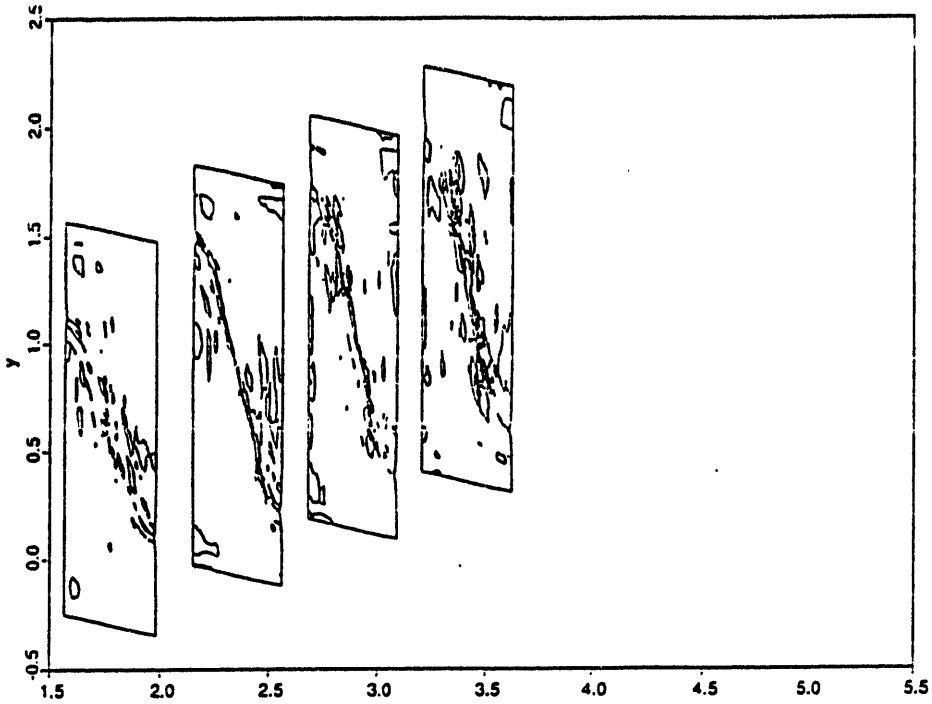

Figure 4.63: Contour plots of $\Delta P_t/P_\infty$ at various axial locations from lobe trailing edge to mixing duct exit. The axial locations are x/λ =1.48, 2.03, 2.52, 3.02, 3.53, 4.02, 4.55, 4.98, 5.51, 5.93, 6.42, 6.98, 7.63, 8.00, 8.81, 9.74. Sixteen contours from -7.5×10^{-1} to 7.5×10^{-1} are plotted in increments of 1×10^{-1}

Figure 4.64: Secondary velocity vector field at axial locations $x/\lambda = 1.52, 5.51$ (see over)

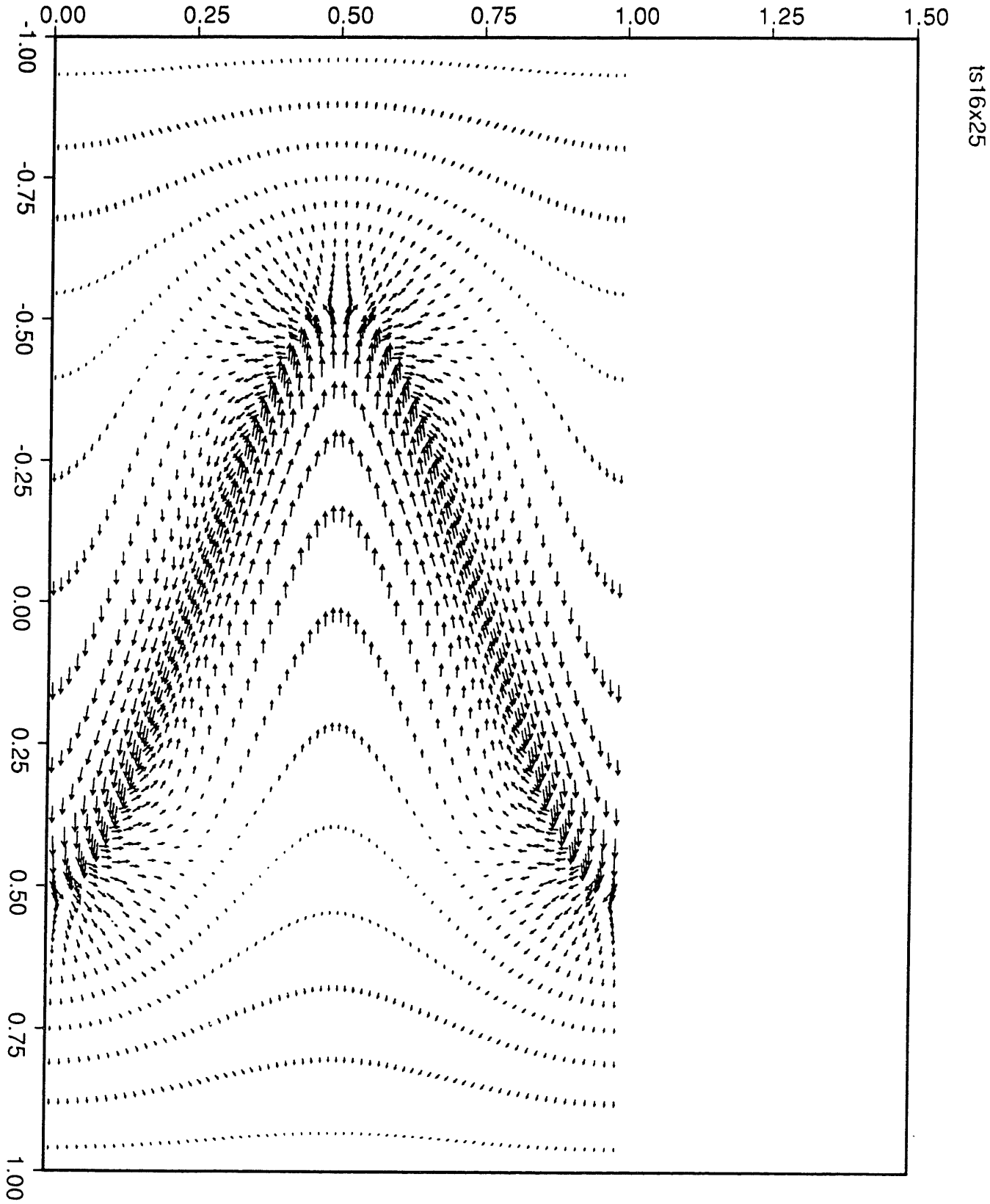
0.00
0.25
0.50
0.75
1.00
1.25
1.50
-1.00
-0.75
-0.50
-0.25
0.00
0.25
0.50
0.75
1.00
ts16x25

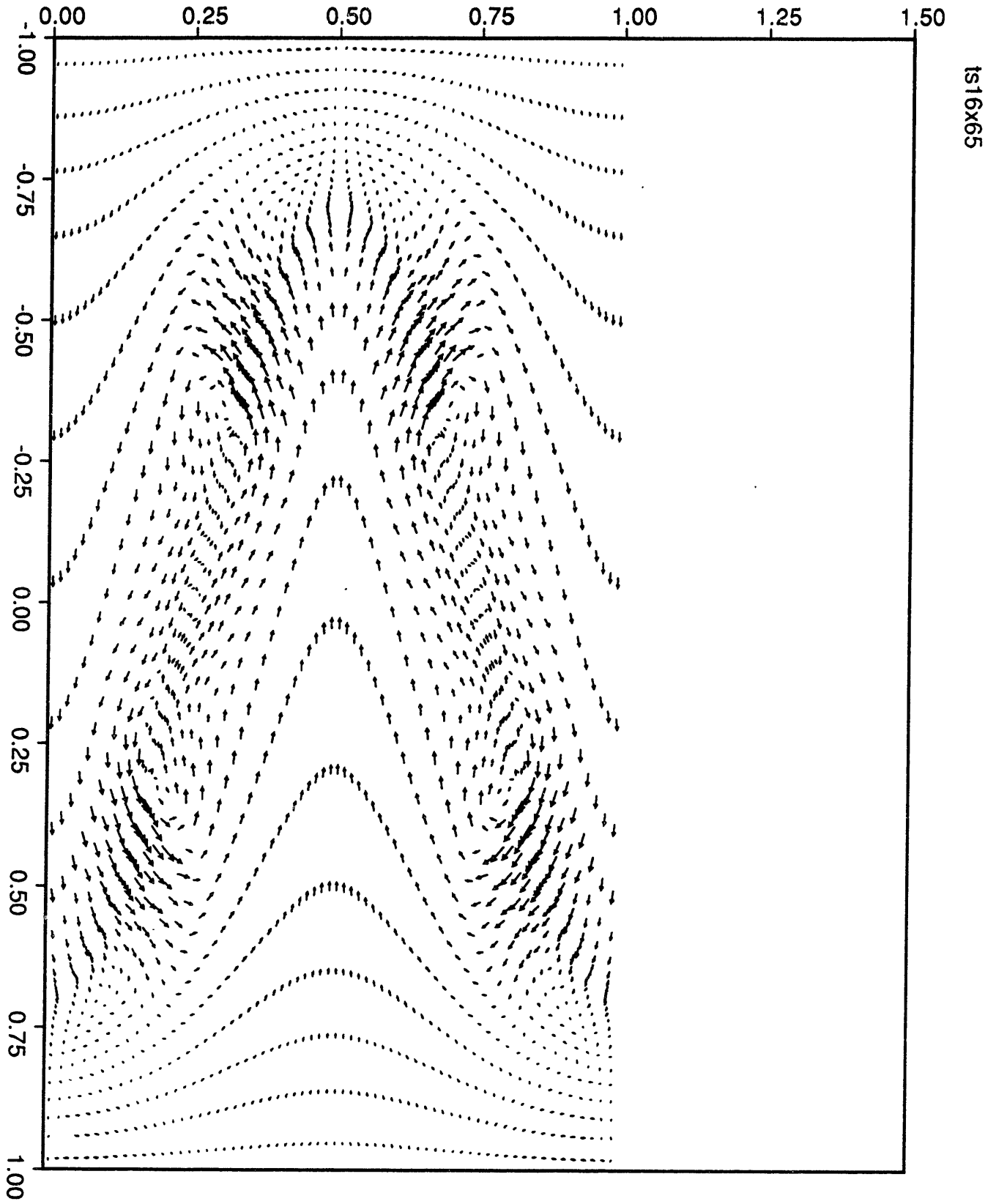
0.00
0.25
0.50
0.75
1.00
1.25
1.50
-1.00
-0.75
-0.50
-0.25
0.00
0.25
0.50
0.75
1.00
ts16x65

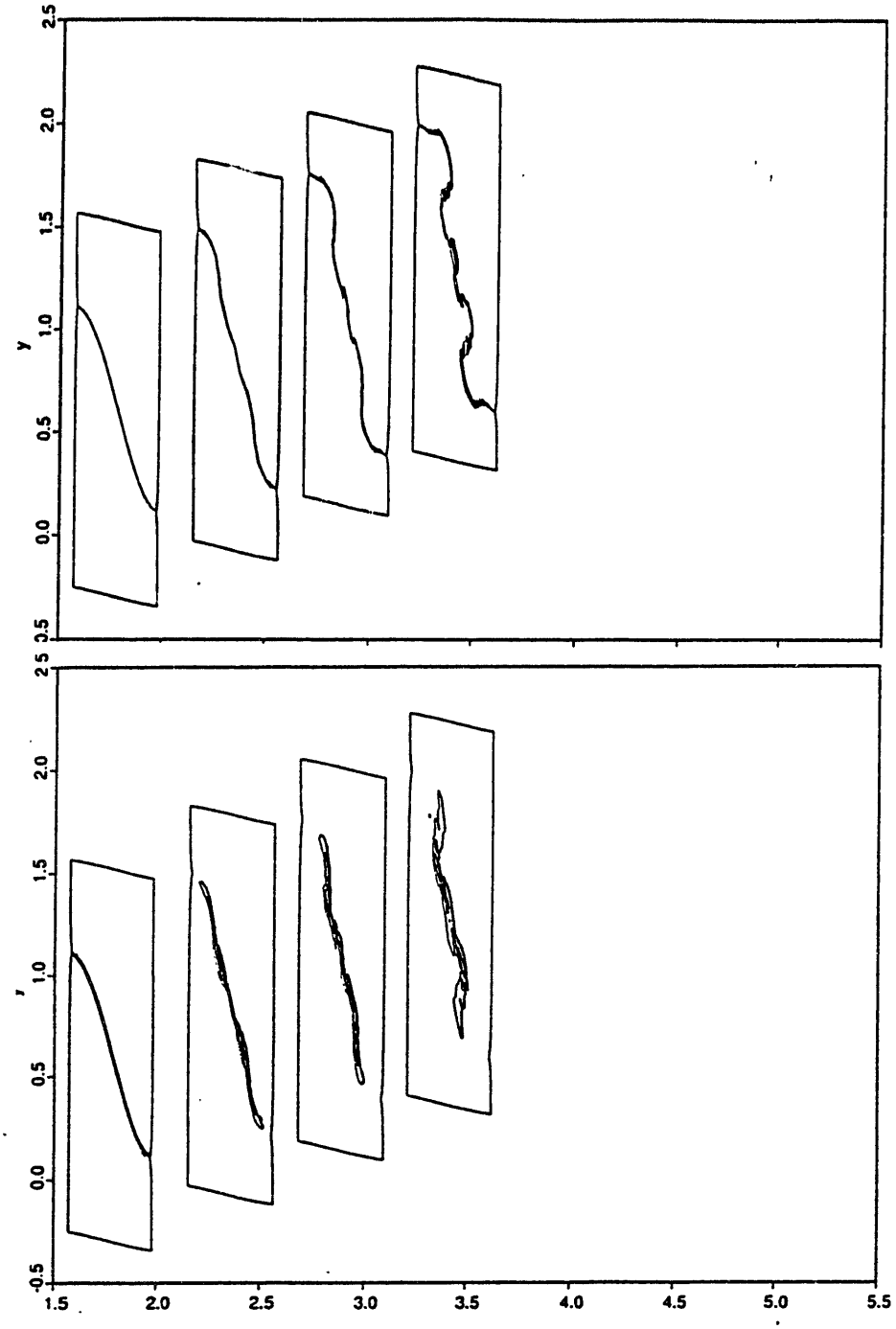

Figure 4.65: Contour plots of ψ, ω_z and c_p, at various axial locations from lobe trailing edge to mixing duct exit. The axial locations are x/λ =1.48, 2.03, 2.52, 3.02, 3.53, 4.02, 4.55, 4.98, 5.51, 5.93, 6.42, 6.98, 7.63, 8.00, 8.81, 9.74. Contours are as follows:

ψ: 5 contours from 0.3 to 0.7 in increments of .1;

ω_z: 6 contours from -10 to 110 in increments of 20

c_p: 8 contours from -.175 to +.175 in increments of .05

(continued overleaf)

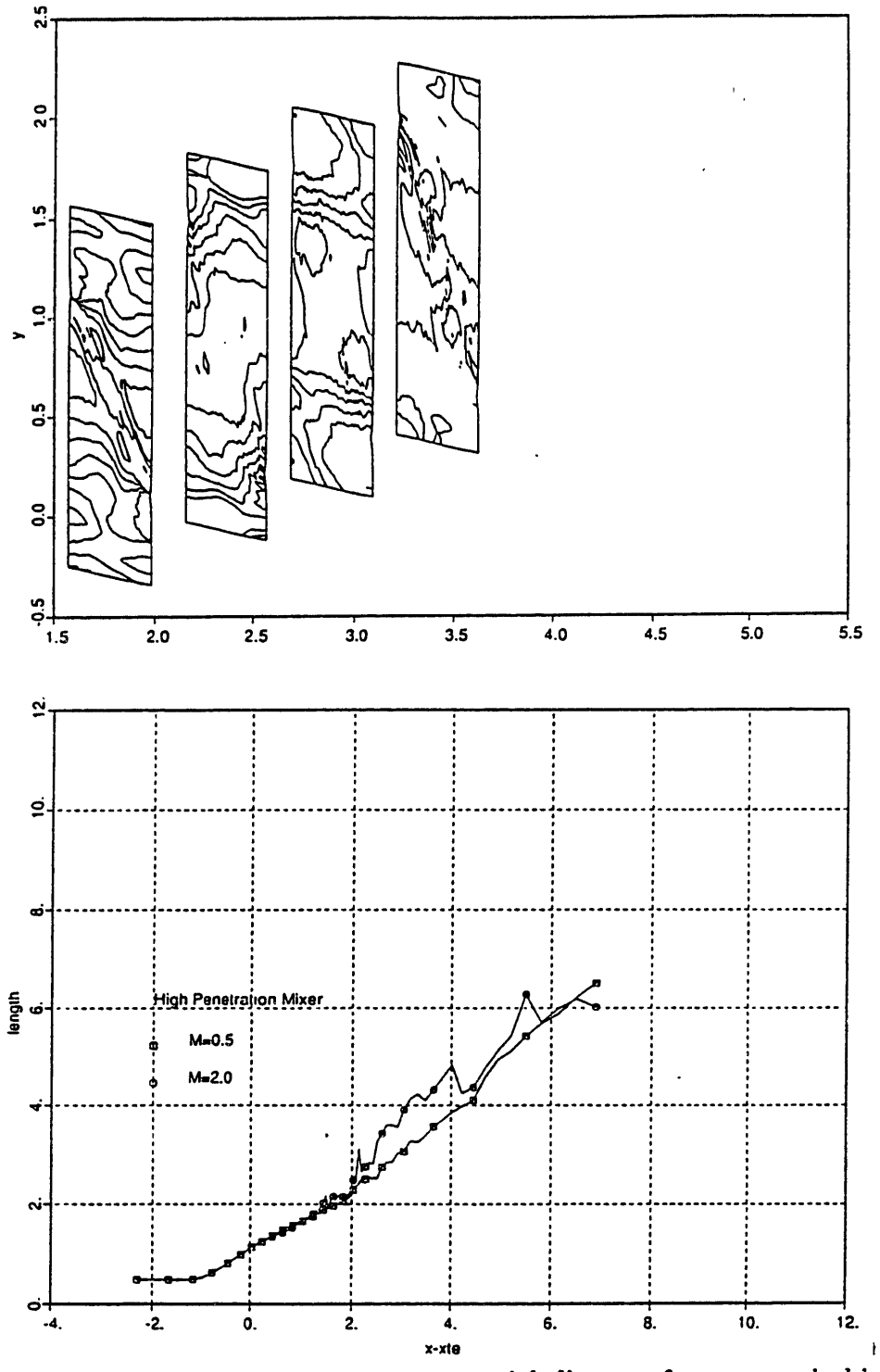

Figure 4.66: Length of $\psi = 0.5$ contour versus axial distance for supersonic high penetration calculation

Chapter 5

Conclusion

In this chapter, the conclusions from the work on the development of a numerical scheme for three-dimensional Euler flows based on Zalesak's Flux-Corrected Transport algorithm, and its use for the computational study of a three-dimensional lobed mixer, will be presented. The conclusions can be divided into two categories: contributions in terms of numerical aspects and contributions in terms of the fluid mechanical aspects.

5.1 Development of the Numerical Scheme

- A finite volume Flux-Corrected Transport algorithm, using Zalesak's fully multidimensional antidiffusive flux limiter in three-dimensional curvilinear coordinates has been developed for the numerical solution of the Euler Equations. This constitutes the first application of such an algorithm for computing inviscid flow in a three-dimensional curvilinear coordinate system. Computed results demonstrate the ability of the algorithm to predict flow features associated with

  (i) the generation and evolution of vortical flow in a lobed mixer and mixing duct

  (ii) shock waves in transonic and supersonic flow

- It is found that the use of the directional timestep technique to implement the Flux-Corrected Transport algorithm for computing flows in three-dimensional curvilinear coordinates yields results that are unacceptable for interrogative use

5.2 Fluid Mechanics of the Lobed Mixer

- Computed results agree well with experiments on a low penetration lobed mixer. Although this is not a severe test, the implication is that flow features associated with lobed mixers can be reliably predicted with the use of this Euler solver.

- Compressibility is only found to have marginal influence on the shed circulation for both low and high penetration mixer.

- When mixing is measured in terms of the availability of interface area separating the two streams, i.e. s_i, it is found that the mixing rate is not strongly affected by compressibility. This can be explained by the fact that even though the flow is supersonic in the axial direction, the flowfield in the crossflow plane driven by the presence of streamwise vortices remains essentially subsonic. (This fact is analogous to the successful use of the slender body approximation theory for slender delta wing flow.)

- The higher penetration mixer shows a factor of 6.5 increase in $\partial s_i/\partial x$ and a factor of 6.0 increase in trailing edge circulation compared to the low penetration lobed mixer. The mixing rate is thus increased by increasing the strength of the shed circulation, i.e. an increase in penetration angle leads to an increase in mixing rate. Computed trailing edge circulation agrees well with Paterson's scaling law [3].

- The computed results show that the shed vorticity evolves into a circular structure that resembles a vortex with a viscous core. For the high penetration mixer, roll-up initially occurs at the extremities of the vortex sheet before it takes on a circular shape.

- Comparison with a Trefftz plane analysis [7] for the low penetration mixer case shows that the potential field influence of the lobed mixer is small.

Chapter 6

Recommendations for Future Work

The recommendations for future work can be divided into two categories: (i) further improvements of the numerical algorithm and (ii) further investigation of the physical phenomena of the compressible mixing layer with strong streamwise vorticity through the use of this CFD code. The division is somewhat arbitrary, however, and many of the points fall between the two headings.

6.1 Improvement of CFD Algorithm

Solution quality could be improved by using a one-dimensional Zalesak limiter to prelimit all the antidiffusive fluxes. The present use of the Boris-Book limiter appears to have worked well particularly in the region close to the lobe trailing edge. However, further downstream of the trailing edge the vortex sheet no longer coincides with the η = const grid lines; this may cause clipping to occur due to the Boris-Book prelimiter which may result in the deterioration of the solution quality in that region. More importantly, the use of the Zalesak limiter for prelimiting purposes will allow prelimiting in every computational direction (ξ, η, ς) to be carried out. This is because the Zalesak limiter does not clip nearly as severely as the Boris-Book limiter and may not clip at all for this particular problem since it always has the solution from the previous timestep w^{n-1} to check for extrema (see Section2.5). Even if clipping does occur, the flexibility of the Zalesak limiter is such that means exist for preventing clipping. The details of the technique will not be discussed in detail here and the reader is referred to Zalesak's article [21] for further details. The ability to prelimit in all computational directions may preserve monotonicity in each direction and suppress small dispersive ripples that have been observed to arise with the present limiter.

Further investigation is needed into the selection of a low order scheme that remains effective

in fine and coarse regions of the grid. The low order method used for most of the calcultions reported herein, is the Euler method with zeroth order dissipation. One weakness observed with this method is that, because dissipative fluxes decrease with respect to convective fluxes in fine regions of the numerical grid, the flux correction process can become somewhat ineffective. The Rusanov method, discussed in Section 2.7, is a first order scheme designed to overcome this problem. This is done by multiplying the dissipative fluxes by a coefficient proportional to the local CFL number. A systematic method for selecting the low order dissipation coefficient should be developed in conjunction with this effort.

The effectiveness of the FCT scheme may be improved by correcting the antidiffusive fluxes after both the predictor and the corrector steps instead of just the corrector step as is the case with the present limiter. Although computationally more expensive, this may be more effective in suppressing dispersive errors, particularly in the vicinity of discontinuities as discussed in Section 3.1.1. Also, flux synchronization offers a means by which solution quality and computational performance can be improved. Although this is a relatively new field, much research is being done in this area and it is currently the state of the art in FCT circles. It is also relatively simple to code.

The use of Zip differencing [22], as discussed in Section 2.6 is likely to significantly improve the accuracy of the solution generated by the high order method acting alone. It will therefore also improve FCT solution quality in smooth regions in addition to regions where FCT is active (as found by Zalesak [22]). On the subject of the high order scheme, the possibility of using methods other than Leapfrog-Trapezoidal should eventually be investigated. A Runge-Kutta method could be used for the temporal discretization. (The attractiveness of the relaxed CFL condition ($CFL_{\max} = 2\sqrt{2}$) for a Fourth order Runge-Kutta method disappears when it is realized that Δt must also satisfy the CFL condition for the low order method.) A spectral method could be used for the spatial discretization. Zalesak's high order flux formulae [24] could also be used although it should be

borne in mind that for grids with large stretching, this is pointless as the flux formulae will remain first order.

The convergence rate to steady state could be improved if fourth order dissipation was used in the mixing duct as well as the lobe region. The problem is that if this is done in a straightforward manner, the vortex sheet will tend diffuse away. Some sort of switch could be used similar to the pressure switch used in many Euler solvers that turns on second order dissipation in the region of shocks. The most obvious way to implement this is with ψ as the argument of the switch. One of the many possibilities is

$$F^D_{i+1/2,j,k} = \gamma_4 s_{i+1/2,j,k} V_{i+1/2,j,k}(w_{i+2,j,k} - 3w_{i+1,j,k} + 3w_{i,j,k} - w_{i-1,j,k}) \tag{6.1}$$

where the switch is given by

$$s_{i+1/2,j,k} = \begin{cases} 0 & \text{if } |\psi_{i+1} - \psi_{i-2}| < 0.1 \\ 1 & \text{if } |\psi_{i+1} - \psi_{i-2}| \geq 0.1 \end{cases} \tag{6.2}$$

Since this formulation requires logical operations to be performed, it may not vectorize very well. If the detrimental effect on CPU time per iteration is excessive other alternatives should be looked at.

6.2 Physical Aspects

The highest priority item in this section is to generate a better numerical grid for the high penetration mixer (the low penetration mixer grid could also be improved). Aspect ratios (particularly in mixing duct, close to the outflow boundary) should be remain less than $\sim 5 - 10$ and stretching (particularly in the $\eta-$ direction) should be kept below $\sim 1.2 - 1.3$. The current grids waste resolution in regions far downstream of the lobe trailing edge because grid lines are clustered on the mid channel sinusoidal surface emanating from the lobe trailing edge. This surface does not coincide with the physical location of the vortex sheet beyond a certain distance from the trailing

edge. It would be better to have a uniform grid in these places. The problem is to come up with a way for the surface to undergo the transition from the trailing edge sinusoidal shape to a flat surface without losing resolution where it is needed.

For a/λ greater than 0.85, the present grid generator is not capable of generating a good quality grid and an improved grid generation scheme is required for these cases. The innovative method reported in [8] shows promise. Grids generated with this method should have improved skewedness properties although some resolution may be wasted where the η = const and ζ = const boundaries intersect at the symmetry boundary. This will allow the flow in the high penetration mixer used in the UTRC experimental investigation to be computed and will allow grids to be generated to model advanced mixers such as those with square profiles and rounded corners and mixers with past-vertical sidewalls.

The role of spanwise vorticity on the fluid dynamics of the mixing layer should be investigated since, in real applications, the two streams that are being mixed have different total pressures. For the fluid physics of the mixing layer to be properly modelled, the numerics will have to be able to "capture" any resulting Kelvin-Helmholtz instability. Fine resolution in the mixing layer will be needed and this will require some ingenuity in the grid generation scheme. Adaptive grids and mesh embedding [50] could be used to automatically produce the highest resolution where it is needed most but this will entail significant code alteration.

A more easily executed step would be to include molecular diffusion in the passive scalar equation. This will allow us to estimate the molecular mixing in a more tangible fashion. Along these lines, diffusion of momentum and temperature should eventually be modelled so that the bulk mixing properties of mixers between streams with different stagnation enthalpies can be calculated accurately. A more practical short term alternative to the full Navier-Stokes equations are the Thin-Layer Navier-Stokes equations in which viscous terms containing derivatives in the directions parallel to the body surface are neglected. The Thin layer approximation would allow modelling

of the boundary layers on the lobe surface and also allow separated and reverse flow regions to be computed in a straight forward fashion. This will prove useful for the problem of spanwise separation for lobes in which the spanwise flow has to pass over surfaces with severe curvature such as may be found in advance mixers with past-vertical sidewalls.

Bibliography

[1] Bernal, L.P., Roshko, A. "Streamwise Vortex Structure in Plane Mixing Layers" J. Fluid Mechanics (1986) 170 , pp.499-525

[2] Oates, G.C., "The Aerothermodynamics of Aircraft Gas Turbine Engines" AFAPL-TR-78-52

[3] Barber, T. Paterson, R.W., and Skebe, S.A. "Turbofan Forced Mixer Lobe Flow Modelling," NASA CR 4147, 1988

[4] Paterson, R.W. "Turbofan Forced Mixer-Nozzle Internal Flowfield, Part I - A Benchmark Experimental Study," NASA CR 3492, April, 1982

[5] Werle, M.J., Paterson, R.W.,"Flow Structure in a Periodic Axial Vortex Array" AIAA-87-0610, Reno, January, 1987

[6] Tillman, T.G., Patrick, W.P., Paterson, R.W. "Enhanced Mixing of Supersonic Jets" AIAA-88-3022, Boston, 1988

[7] Qiu, Y., Ph.D. Thesis, Department of Aeronautics and Astronautics, MIT, June, 1990

[8] Malecki, R., Lord, W., "Navier-Stokes Analysis of a Lobed Mixer and Nozzle" AIAA-90-1453, Reno, 1990

[9] Koutmos, P., McGuirk, J.J., "Turbofan Forced Mixer/Nozzle Temperature and Flow Field Modelling" Int. J. Heat Mass Transfer, Vol.32, No.6, pp.1141-1153, 1989

[10] Roe, P.L., "Characteristic-Based Schemes for the Euler Equations," in Ann. Rev. Fluid Mech. 1986, 18, 337-65

[11] Steger, J.L., Warming, R.F. "Flux-Vector Splitting of the Inviscid Gasdynamic Equations with Application to Finite Difference Methods," J. Comput. Phys. 40:263-293

[12] van Leer, B.M, "Flux-Vector Splitting for the Euler Equations," Lect. Notes in Phys. 170:507-512

[13] Osher, S., Solomon, F. "Upwind Difference Schemes for Hyperbolic Systems of Conservation Laws," Math. Comput. 38: 339-74

[14] Sod, G.A., "A Survey of Several Finite Difference Methods for Systems of Nonlinear Hyperbolic Conservation Laws," Journal of Computational Physics 27, 1-31 (1978)

[15] Spekreijse, S.P., "Multigrid Solution of the steady Euler Equations" Centrum voor Wiskunde en Informica, Amsterdam, 1988

[16] Allmaras, S.R., "A Coupled Euler/Navier-Stokes Algorithm for the 2-D Unsteady Transonic Shock/Boundary-Layer Interaction" GTL Report#196, March, 1989

[17] Boris, J.P. and Book, D.L., "Flux-Corrected Transport. I. SHASTA, A Fluid Transport Algorithm That Works," Journal of Computational Physics, Vol. 11, 1973, pp.38-69.

[18] Book, D.L., Boris, J.P. and Hain, K., "Flux-Corrected Transport II: Generalization of the Method," Journal of Computational Physics, Vol. 18, 1975, pp.248-283.

[19] Boris, J.P. and Book, D.L., "Flux-Corrected Transport III Minimal Error FCT Algorithms," Journal of Computational Physics, Vol. 20, 1976, pp.397-431.

[20] Boris, J.P. and Book, D.L., "Solutions of Continuity Equations by the Method of Flux-Corrected Transport," Methods in Computational Physics, Vol. 16, 1976, pp.85-129.

[21] Zalesak, S.T., "Fully Multidimensional Flux-Corrected Transport Algorithms for Fluids," Journal of Computational Physics, Vol. 31, 1979, 335-362

[22] Zalesak, S.T., "High Order Zip Differencing of Convective Terms" Journal of Computational Physics, Vol. 40, 1981, 497-508

[23] Lohner,R., Morgan,K.,Peraire,J.,Vahdati,M., "Finite Element Flux-Corrected Transport (FEM-FCT) for the Euler and Navier-Stokes Equations" Internationsl Journal for Numerical Methods in Fluids, Vol. 7, 1987, 1093-1109

[24] Zalesak, S.T., "Very High Order and Pseudospectral Flux- Corrected Transport (FCT) Algorithms for Conservation Laws," Advances in Computer Methods for Partial Differential Equations, Vol. 4, 1981, 126-134

[25] Zalesak, S.T., "A Physical Interpretation of the Richtmeyer Two-Step Lax-Wendroff Scheme, and its Generalization to Higher Spatial Order" Advances in Computer Methods for Partial Differential Equations, Vol. 5, 1984 pp. 491-496

[26] Grinstein, F.F., Oran, E.S. and Boris, J.P.,"Numerical Simulations of Asymmetric Mixing in Planar Shear Flows," Journal of Fluid Mechanics, Vol.165, 1986, pp.201-220

[27] Guirguis, R.H.,Grinstein, F.F, Young, T.R., Oran, E.S., Kailasanath, K., Boris, J.P."Mixing Enhancement in Supersonic Shear Layers," AIAA-87-0369,1987

[28] Anderson, D.A.,Tannehill, J.C.,Pletcher, R.H., "Computational Fluid Mechanics and Heat Transfer," Hemisphere Publishing Co., New York, NY, 1984

[29] Oran, E.S.,Boris, J.P., "Numerical Simulation of Reactive Flow," Elsevier Science Publishing Co., New York, NY, 1987

[30] MacCormack, R.W., "Numerical Solution of the Interaction of a Shock Wave with a Laminar Boundary Layer," Proc. of Second Int. Conf. on Num. Methods in Fluid Dynamics, Lecture Notes in Physics, Vol.8, 1971, pp.151-163

[31] Thomson, J.F.,Thames, F.C.,Mastin, C.W. "TOMCAT - A Code fir Numerical Generation of Boundery-Fitted Curvilinear Coordinate Systems on Fields Containing Any Number of Arbitrary Two- Dimensional Bodies" Journal of Computational Physics, Vol. 24, 1977, 274-302

[32] Kurihara, Y. "On the Use of Implicit and Iterative Methods for the Time Integration of the Wave Equation," Monthly Weather Review, Vol.93, Jan 1965, pp.33-46

[33] Grammeltvedt, A., "A Survey of Finite-Difference Schemes for the Primitive Equations for a Barotropic Fluid," Monthly Weather Review, Vol.97, 1969, pp.384-404

[34] Emery, A.F., "An Evaluation of Several Differencing Methods for Inviscid Fluid Flow Problems," Journal of Computational Physics, Vol. 2, 1968, 306-331

[35] Gentry, R.A., Martin, R.E., Daly, B.J., "An Eulerian Differencing Method for Unsteady Compressible Flow Problems" Journal of Computational Physics, Vol. 1, 1966, 87-118

[36] Rizzi,A.,"Numerical Implementation of Solid-Body Boundary Conditions for the Euler Equations," ZAMM, vol 58, pp T301-T304 1978

[37] Blumen, W.,"Shear Layer Instability of an Inviscid Compressible Fluid" J. Fluid Mech, vol 40, part 4, 1970, pp 769-781

[38] Blumen, W.,Drazen, P.G., Billings, D.F., "Shear Layer Instability of an Inviscid Compressible Fluid. Part 2" J. Fluid Mech, vol 71, part 2, 1975, pp 305-316

[39] Lasheras, J.C., Choi, H., "Three-dimensional instability of a plane shear layer: an experimental study of the formation and evolution of streamwise vortices," J. Fluid Mech, vol 189, 1988, pp 53-86

[40] Lasheras, J.C., Maxworthy, T. "Structure of the Vorticity Field in a Plane, Free Shear-Layer" in Turbulent Shear Flows 5 Springer-Verlag, 1986

[41] Koochesfahani, M.M., Dimotakis, P.E., Broadwell, J.E. "Chemically reacting turbulent shear layers" AIAA paper 83-0475, New York, 1983

[42] Lowery, P.S., Reynolds, W.C., "Numerical Simulation of a Spatially-Developing, Forced, Plane Mixing Layer," NASA Technical Report TF-26, Sept. 1986

[43] Ni, R.H.,"A Multiple-Grid Scheme for Solving the Euler Equations," AIAA J., Vol.20, No.11, Nov. 1981, pp 1565-1571

[44] Steger, and Sorenson, "Automatic Mesh-Point Clustering Near a Boundary in Grid Generation with Elliptic Partial Differential Equations" Journal of Computational Physics 33, 405-410 (1979)

[45] Liepmann, H.W.,Roshko, A., Elements of Gasdynamics, John Wiley, New York, 1957

[46] Lamb, H. Hydrodynamics, Dover Press, New York, 1945

[47] Landau, L.D., Lifshitz, E.M. Fluid Mechanics Pergamon, 1959

[48] Batchelor, G.K., An Introduction to Fluid Dynamics Cambridge University Press, 1967

[49] Marble, F.E., "Growth of a Diffusion Flame in the Field of a Vortex," in Recent Advances in the Aerospace Sciences Ed. C. Casci. pp 395-413

[50] Dannenhofer,J.F.,III "Grid Adaptation for Complex Two-Dimensional Transonic Flows," Sc.D. Thesis, Department of Aeronautics and Astronautics, MIT, May, 1987